

Applications of Discontinuous Galerkin Methods to Computational General Relativity

by

Scott Field

B.Sc. Physics, University of Rochester; Rochester, NY, 2006

B.Sc. Mathematics, University of Rochester; Rochester, NY, 2006

M.Sc. Physics, Brown University; Providence, RI, 2010

A dissertation submitted in partial fulfillment of the
requirements for the degree of Doctor of Philosophy
in the Department of Physics at Brown University

PROVIDENCE, RHODE ISLAND

May 2011

© Copyright 2011 by Scott Field

This dissertation by Scott Field is accepted in its present form
by the Department of Physics as satisfying the
dissertation requirement for the degree of Doctor of Philosophy.

Date _____

Jan S. Hesthaven, Ph.D., Advisor

Recommended to the Graduate Council

Date _____

Gerald Guralnik, Ph.D., Reader

Date _____

Ian Dell'Antonio, Ph.D., Reader

Approved by the Graduate Council

Date _____

Peter M. Weber, Dean of the Graduate School

Abstract of “Applications of Discontinuous Galerkin Methods to Computational General Relativity” by Scott Field, Ph.D., Brown University, May 2011

We discuss a discontinuous Galerkin (dG) method and its application to common partial differential equations which arise in the context of general relativity. First we consider extreme mass ratio binary (EMRB) systems. When modeling EMRBs as perturbations of a Schwarzschild black hole, the metric perturbations are described by the distributionally forced Regge–Wheeler–Zerilli (RWZ) equation. Despite the presence of jump discontinuities in the solution, our dG method achieves pointwise spectral accuracy. Particular attention is given to the common choice of trivial initial data, and we show such unphysical specification may lead to spurious solutions which contaminate the physical solution indefinitely. Unintended consequences of the persistent junk solution are considered as well as a simple prescription for removing it. Using our code we compute metric perturbations, gravitational waveforms, and self-force measurements from both circular and eccentric orbits.

Next, we present a dG method for evolving the spherically reduced Generalized Baumgarte–Shapiro–Shibata–Nakamura (GBSSN) system expressed in terms of second-order spatial operators. Our multi-domain method achieves global spectral accuracy and long-time stability on short computational domains. We discuss in detail both our scheme for the GBSSN system and its implementation. A theoretical and computational verification of the proposed scheme is given.

We conclude with a preliminary look at reduced basis (RB) methods for parameterized binary systems. Our algorithm aims to construct a compact RB space from which a particular solution can be quickly and accurately recovered. We apply the algorithm to compress the space of analytic chirp gravitational waveforms. Next, the RWZ equation is revisited, and we consider extensions of the algorithm to a dG solver along with numerical evidence that a RB space exists for EMRB waveforms.

CURRICULUM VITAE

Author

Scott Field, born on July 19th 1983 in Providence, RI, USA.

Education

University of Rochester, Rochester, NY.

Physics B.S., 2006. Advisor: Professor Arie Bodek.

Mathematics B.S., 2006.

Brown University, Providence RI.

Physics Ph.D, 2011 (in progress). Advisor: Professor Jan S. Hesthaven.

Physics M.Sc., 2010.

Publications

1. Scott Field, Chad Galley, Frank Herrmann, Jan Hesthaven, Evan Ochsner, and Manuel Tiglio. “Reduced basis catalogs for gravitational wave templates”
Submitted to Physics Review Letters
2. Scott Field, Jan Hesthaven, Stephen Lau, and Abdul Mroue. “Discontinuous Galerkin method for the spherically reduced BSSN system with second-order operators” Physical Review D, Volume 82, Issue 10, November 2010
3. Scott Field, Jan Hesthaven, and Stephen Lau. “Persistent junk solutions in time-domain modeling of extreme mass ratio binaries” Physical Review D,

Volume 81, Issue 12, June 2010

4. Scott Field, Jan Hesthaven, and Stephen Lau. “Discontinuous Galerkin method for computing gravitational waveforms from extreme mass ratio binaries” *Classical and Quantum Gravity* Volume 26, Number 16, 21, August 2009
5. Scott Field. “Search for Ξ_b and Σ_b with the CDF II Detector at Fermilab,” Undergraduate honors thesis, <http://hdl.handle.net/1802/2878> (5/2006)

ACKNOWLEDGEMENTS

Over the past five years many people have provided me with invaluable help and support. They have made my time at Brown an enjoyable and productive experience.

First and foremost, I thank Jan Hesthaven for being the foundation of my graduate years. When I first approached him about being my advisor, I was delighted by his enthusiasm and open-mindedness towards my interest in his research. As a professor of Applied Mathematics, Jan's research activities are centered on the development and numerical analysis of computational methods. I had some experience with this area, but there were many things to learn and his patience, encouragement, and teaching were essential for my transition. He has been a constant source of inspiration and ideas, while providing me significant freedom to explore my own ideas and interests. I feel lucky to have him as my advisor.

While in Jan's group I was fortunate to meet and work closely with Stephen Lau. Over the past few years Stephen has been much more than a collaborator, he has also provided me with mentorship and many useful physics discussions. When he moved to New Mexico I was the grateful recipient of his dining room table, where the majority of this dissertation was written.

In addition to Jan and Stephen I would like to thank my collaborators, Abdul Mroue, Chad Galley, Frank Herrmann, Evan Ochsner, and Manuel Tiglio from whom

I have learned many things. In particular, Manuel Tiglio has been an important driving force for recent work on reduced basis methods, and I am looking forward to continuing this work as a postdoctoral researcher in his group.

I would like to thank members of my PhD committee, Jan Hesthaven, Gerald Guralnik, and Ian Dell'Antonio for taking the time to read this dissertation and for thinking about my work.

While at Brown I have had the opportunity to meet many amazing individuals. There are too many to list, but I am sure they know who they are. I would like to thank them for stimulating discussions on physics and math, for thoughtful and patient responses to my questions, and for their company (especially outside of research).

The administrative staffs of both the physics and applied math departments have been amazing and I thank them for their help with many things.

Finally, I would like to thank all of my friends and family who have given me invaluable support in all aspects of life. I feel incredibly blessed to have spent the past five years studying in Providence, a city just a few miles from where I grew up, which has allowed me to frequently see many of them. I would especially like to thank my parents Edward and Elaine Field, my sister Kimberly Field, my wife Lauren Prusnofsky, and her parents Leslie and Vicki Prusnofsky for immeasurable encouragement.

Contents

Vitae	iv
Acknowledgments	vi
1 Introduction	1
2 Formulations and Approximations of General Relativity	9
2.1 Introduction	10
2.2 Differential Geometry and Conventions	10
2.3 General Relativity	14
2.3.1 Einstein Field Equation	14
2.3.2 Gravitational Waves	15
2.4 Gravitational Perturbation Theory for Non–Spinning Black Holes	17
2.4.1 Problem Setup	20
2.4.2 Polar Perturbations	23
2.4.3 Axial Perturbations	27
2.4.4 Perturbations at the Event Horizon and Future Null Infinity	31
2.4.5 Motion of the Compact Object	36
2.5 Splitting Spacetime into Space+Time	39
2.5.1 3+1 Decomposition	40
2.5.2 Extrinsic Geometry of the Foliation	43
2.5.3 Arnowitt–Deser–Misner Equations	44
2.6 The Generalized BSSN Formulation	46
2.6.1 Conformal–Traceless Decomposition and the GBSSN Variables	48
2.6.2 Interlude: Relationship to Traditional BSSN	49
2.6.3 GBSSN System	50
3 The Discontinuous Galerkin Method for Hyperbolic PDEs	53
3.1 Introduction	54
3.1.1 Notation, Norms, and Geometry	54
3.2 Hyperbolic PDEs and Stability	56

3.3	A Nodal Discontinuous Galerkin Method	61
3.3.1	Basic Ingredients of the Scheme	62
3.3.2	Properties of the Proposed DG Scheme	68
4	Extreme Mass Ratio Binaries	70
4.1	Introduction	71
4.2	RWZ Equations in the Presence of a Perturbing Particle	74
4.2.1	ODEs of Particle Motion	74
4.2.2	Zerilli–Moncrief (Polar) Source Term	76
4.2.3	Cunningham–Price–Moncrief (Axial) Source Term	77
4.2.4	Jump Conditions	80
4.2.5	Coordinate Transformation Adapted to Particle History	81
4.2.6	Wave Equation as a First–Order System	84
4.3	A DG Scheme for RWZ with Distributional Forcing	86
4.3.1	Discretization of (4.39)	86
4.3.2	Numerical Flux	88
4.4	Treatment of the Initial Boundary Value Problem	94
4.4.1	Initial Data with Source Smoothing	95
4.4.2	Boundary Conditions	95
4.4.3	Waveform Extraction	98
4.5	Numerical Experiments	98
4.5.1	Forced Wave Equation with Exact Initial Data	100
4.5.2	Longtime Accuracy of Radiation Boundary Conditions	103
4.5.3	Circular Orbits: Waveforms and Luminosities	104
4.5.4	Eccentric Orbits: Waveforms and Luminosities	106
5	Junk Solutions Seeded by Trivial Initial Data	109
5.1	Introduction	110
5.2	Jost Solution	113
5.2.1	Forced 1+1 Wave Equation	114
5.2.2	Master Wave Equations	117
5.2.3	Jost Solution and Radiation Boundary Conditions	121
5.3	Consequences of Impulsive Starting Conditions	123
5.3.1	Loss of Temporal Convergence	123
5.3.2	Inconsistent Modeling of the Axial Sector	125
5.3.3	Contamination of Waveforms	127
5.3.4	Self–Force Measurements	129
5.3.5	Consequences for Eccentric Orbits: Preliminary Results	133
5.4	Comments on the Generality of Jost Junk	135
6	GBSSN System in Spherical Symmetry	139
6.1	Introduction	140
6.2	Spherically Symmetric GBSSN Equations	144
6.2.1	Basic Variables and Spherically Reduced System	144
6.2.2	Abstract Expressions of the System	147

6.2.3	Hyperbolicity and Characteristic Fields	149
6.2.4	Construction of Initial Data	153
6.3	A DG Scheme for the GBSSN System	155
6.3.1	Discretization of the System (6.12)	156
6.3.2	Numerical Flux	158
6.3.3	Filtering	160
6.3.4	Model System	161
6.3.5	Stability of the Model System	163
6.4	Results from Numerical Simulations	170
6.4.1	Simulations of the Model System	172
6.4.2	Semi-Discrete Stability of Model PDE	174
6.4.3	Simulations of the GBSSN System	175
7	Reduced Basis Methods and Parameterized Problems	180
7.1	Gravitational Wave Searches and Catalogs	182
7.1.1	Generic Bottlenecks of High Dimensional Systems	182
7.1.2	A Reduced Basis to the Rescue	185
7.2	A Reduced Basis Method for PN Waveforms	186
7.2.1	Theoretical Description	186
7.2.2	Results for PN Waveforms	191
7.3	Preliminary Look at RBM for RWZ Equations	193
8	Conclusions	196
	Appendices	202
A	Derivation of the GBSSN System	203
A.1	Outline of Approach	204
A.2	GBSSN Evolution and Constraint Equations	204
A.2.1	GBSSN Constraints	205
A.2.2	Evolution Equation: Trace of the Extrinsic Curvature	207
A.2.3	Evolution Equation: Conformal Factor	208
A.2.4	Evolution Equation: Conformal Spatial Metric	208
A.2.5	Evolution Equation: Traceless Part of the Extrinsic Curvature	209
A.2.6	Evolution Equation: Conformal and Traceless Part of the Extrinsic Curvature	210
A.2.7	Evolution Equation: Conformal Connection Function	211
B	Distributional RWZ Jump Conditions	213
C	Exact Solutions to the Forced 1+1 Wave Equations	217
C.1	Problem Setup	218
C.2	Solution for $F(t) = 0, G(t) = \cos t$	218
C.3	Solution for $F(t) = \cos t, G(t) = 0$	219

D	Time-Independent Master Equations	221
D.1	Regge-Wheeler Equation	222
D.2	Zerilli Equation	224
E	Hyperbolicity of the First-order GBSSN System	228
F	Reduction of the GBSSN System to Spherical Symmetry	232
F.1	Problem Setup	233
F.2	Physical Ricci Tensor and Scalar	234
F.3	Reduced Constraint Equations	236
F.4	Reduced Evolution Equations	237
F.4.1	Trace of the Extrinsic Curvature	237
F.4.2	Conformal and Traceless Part of the Extrinsic Curvature	238
F.4.3	Spherically Symmetric GBSSN System	239

List of Tables

4.1	Compressed boundary kernels for $\ell = 2$, $r_b/(2M) = 500$, $\varepsilon = 10^{-10}$. . .	97
4.2	Gravitational radiation luminosities for EMRB in circular orbit . . .	105
4.3	Gravitational radiation luminosities for EMRB in eccentric orbit . . .	106
5.1	Basic set of parameters for an EMRB simulation	114
5.2	Circular orbit GW luminosities corrupted by Jost junk	129
5.3	Eccentric orbit GW luminosities corrupted by Jost junk	135
6.1	Characteristic speeds for spherically reduced GBSSN system	150
7.1	Comparison of catalog sizes constructed with reduced basis and template metric algorithms	193

List of Figures

3.1	Geometry for a typical discontinuous Galerkin scheme	61
4.1	Upwind numerical flux for an advection equation away from δ -singularity . . .	92
4.2	Upwind numerical flux for an advection equation at δ -singularity . . .	93
4.3	Solution of wave equation subject to distributional forcing	99
4.4	Temporal convergence of the linearly moving particle experiment . . .	101
4.5	Spectral convergence of the linearly moving particle experiment . . .	102
4.6	A transparent computational boundary for the RWZ equations	103
4.7	Path of particle orbiting a large mass- M black hole	107
4.8	Gravitational waveform generated by a particle in eccentric orbit . . .	108
5.1	Dependence of Jost junk on source smoothing parameters	113
5.2	Appearance of Jost junk in Regge-Wheeler equation forced by CPM source terms	118
5.3	Comparison between analytic and numerical Jost solutions	120
5.4	Loss of temporal convergence without temporal source smoothing . . .	124
5.5	Development of dynamical and Jost junk with and without smoothing	126
5.6	Behavior of dynamical and Jost junk as a time series	127
5.7	\dot{E}_p self-force measurement with and without smoothing	130
5.8	Snapshot of an instantaneous \dot{L}_p self-force measurement as a function of x with and without smoothing	132
5.9	Jost-like junk for eccentric orbits	133
5.10	Appearance of Jost junk with a finite difference method and Gaussian representation for Dirac deltas	136
6.1	Spectral convergence for model PDE with second order operators . . .	171
6.2	Scaling of maximum stable Δt with N for model PDE	173
6.3	Stability diagram for penalty parameters τ_u and τ_Q	174
6.4	Spectral convergence of constraint violations for $M = 1$ Kerr-Schild initial data	176
6.5	Spectral convergence of solution for $M = 1$ Kerr-Schild initial data . .	177
6.6	Spectral convergence of solution for $M = 1$ Kerr-Schild initial data . .	178
7.1	Parameter values chosen by the template metric method for the cat- alog of BNS and Initial LIGO	184
7.2	TM and RB comparison of error in approximating the space of wave- forms by a discrete catalog for BNS inspirals with Initial LIGO	190

7.3	Parameter values chosen by the reduced basis method for the catalog of BNS and Initial LIGO	192
7.4	Numerical evidence of a compact reduced basis space for EMRB waveforms modeled with RWZ equations	194

List of Algorithms

1	Greedy algorithm for building a reduced basis space	189
---	---	-----

Commonly Used...

Conventions

Geometrized units $G = c = 1$

Metric signature $(-, +, +, +)$

Greek indices $T_{\beta\dots}^{\alpha\dots}$ range over all possible values, typically running from 0 to 3

Latin indices $T_{j\dots}^i\dots$ range over a subset of possible values, typically running from 1 to 3 for spatial tensors. In the context of perturbation theory we will further distinguish between upper case Latin running from 0 to 1, and lower case running from 2 to 3

Notation

\pm **superscripts** Right X^+ and left X^- moving characteristic fields, or interior u_h^- and exterior u_h^+ numerical values relative to the subdomain D^k

$\bar{T}_{j\dots}^i\dots$ ‘Barred’ quantities are either conformal tensors (this rule is broken in Chapter 6, see footnote 1) or denote complex conjugation

f^T Transpose of a vector f

$[[u]]$ Analytic jump of u at a discontinuity

$[[u_h]]_{\mathbf{n}}$ Numerical jump of u_h at a subdomain interface defined with respect to a local normal \mathbf{n}

$\{\{u_h\}\}$ Numerical average of u_h at a subdomain interface

u_h Numerical approximation of u

u_h^k Numerical approximation of u restricted to the k th subdomain

\mathbf{u} Column vector representing the numerical degrees of freedom of u_h , typically nodal values

∇_α Covariant derivative on the full spacetime

D_i Induced covariant derivative on a submanifold

\mathcal{L}_X Lie derivative with respect to the vector field X^α

x Tortoise coordinate $x = r + 2M \ln\left(\frac{r}{2M} - 1\right)$ when discussing RWZ equations

$T_{\beta;\gamma}^\alpha$ Semicolon denotes covariant differentiation

$T_{\beta,\gamma}^\alpha$ Comma denotes partial differentiation

$T_{\beta;\gamma}^{\alpha}$ Colon denotes covariant differentiation on the two-sphere
 (ℓ, m) Spherical harmonic indices

Symbols

Ω Physical domain

Ω_h Computational domain

D^k Computational subdomain

K Number of subdomains covering Ω_h

N Polynomial order approximating a solution

M Mass of the Schwarzschild black hole

m_p Mass of the perturbing compact object or “particle”

E_p Energy of perturbing compact object

L_p Angular momentum of perturbing compact object

e Eccentricity of compact object’s orbit

p Semi-latus rectum of compact object’s orbit

Acronyms

PDE Partial differential equation

ODE Ordinary differential equation

EMRB Extreme mass ratio binary

ADM Arnowitt–Deser–Misner

(G)BSSN (Generalized) Baumgarte–Shapiro–Shibata–Nakamura

(L)dG Local discontinuous Galerkin

CFL Courant–Friedrichs–Lewy

LGL Legendre–Gauss–Lobatto

IP Interior penalty

RW Regge–Wheeler

RWZ Regge–Wheeler–Zerilli

RB(M) Reduced basis (method)
GW Gravitational wave
SVD Singular value decomposition
PSD Power spectral density
BNS Binary neutron star
BBH Binary black hole
LIGO Laser Interferometer Gravitational-Wave Observatory
LISA Laser Interferometer Space Antenna
GH Generalized harmonic
PN Post-Newtonian
TM Template metric

CHAPTER ONE

Introduction

Numerical general relativity is a young field which has seen tremendous progress in terms of both code sophistication and algorithm development over the last decade. During this time the simulation of large astrophysical events which emit gravitational waves have been carried out, leading to new insights of the theory and supporting data analysis efforts at large international experiments such as the Laser Interferometer Gravitational-Wave Observatory (LIGO), Virgo, and the proposed Laser Interferometer Space Antenna (LISA).

To date evidence for gravitational waves has been exclusively provided by binary pulsar systems. The most famous example, leading to a Nobel prize in 1993, comes from measuring the Hulse–Taylor pulsar’s orbital period over time. It was observed that the orbital period slowly decreases in agreement with the predicted energy loss due to gravitational wave emission. Such indirect evidence for gravitational waves certainly provides an important test of general relativity, but the very nature of the experiment yields only limited information.

Gravitational wave astrophysics to be carried out at LIGO, Virgo, and LISA will provide a powerful and unique astronomical tool as Einstein’s equations give precise predictions for gravitational wave signals. Critical to their success is the construction of an accurate catalog of gravitational waveform templates to be correlated with collected data through a process known as matched filtering. Thus, one of the most important goals of numerical relativity is the computation of gravitational waveforms. Of the many potential generators of gravitational waves, compact binary coalescences, which consist of a pair of Neutron stars and/or black holes inspiralling and merging, are considered to be one of the most promising sources. When the masses are nearly equal it is possible, although computationally expensive, to model the entire inspiral, merger and ringdown phases with the Einstein equation. The (generalized) Baumgarte–Shapiro–Shibata–Nakamura ([G]BSSN) system is one nu-

merically stable version of the Einstein equation we will consider. For extreme mass ratio binary (EMRB) systems solving the full system currently impossible. Instead we consider modeling the dynamics with a linearized Einstein equation in the form of the Regge–Wheeler–Zerilli (RWZ) equations.

The GBSSN (2.91) and RWZ (2.38,2.45) equations are examples of hyperbolic partial differential equations (PDEs), a particular classification to be considered in Sec. 3.2. Although hyperbolic PDEs are frequently encountered throughout science, there is no ‘one size fits all’ approach for their numerical simulation. An intelligent choice of numerical scheme may depend on numerous considerations. Are the equations linear or non-linear? Are the solutions non-smooth, or might a non-smooth feature develop? Are long time integrations needed? Is the geometry complicated or simple? Some questions may be more practical. How many months or years will it take to learn an existing code or develop a new one? With how much accuracy can the experimental counterpart measure physical quantities of interest? Simply by inspection, we note that the mathematical character of the GBSSN and RWZ equation is somewhat different and furthermore these equations are often used to describe different kinds of astrophysics. Thus we might expect different answers to the aforementioned questions, and in particular the utility of discontinuous Galerkin (dG) methods.

State of the art BSSN codes evolve nearly equal mass binary systems through inspiral, merger and ringdown of the remnant single black hole using finite difference methods with mesh refinement [53, 26, 52, 119, 82, 206, 49, 160, 86]. While these methods represent significant, and in fact ground breaking, progress of computational general relativity, dG methods have the potential to offer unique benefits for a wide class of problems. First, the high-order accuracy and robustness in the presence shocks, a hallmark feature in hydrodynamical simulations, has been

extensively demonstrated [70, 121, 224, 240, 187, 139]. Very recently, spherically symmetric general relativistic benchmark tests were performed and it was concluded that “discontinuous Galerkin methods could represent a new paradigm for the accurate numerical modeling in relativistic astrophysics” [189]. We wholeheartedly agree, and the work carried out in Chapter 6 is in part motivated by the advantage of dG methods to evolve both fluid and metric variables on the same computational grid with high accuracy. Second, a subset of dG methods known as local discontinuous Galerkin (LDG) methods provides a natural framework for stable discretization of second order spatial operators. Einstein’s equations naturally feature second order spatial derivatives, and discretizing an enlarged first order system results in extra computational overhead associated with the expanded system, and will introduce constraint violating auxiliary fields which may spoil numerical stability [212]. These issues are easily avoided by directly approximating the second-order operators. Finally, for intermediate and extreme mass ratio systems there is typically a large computational burden associated with the disparate length scales in the problem. To date the most ambitious mass ratio attempted has been 1:100 [154], which required significant computational resources and sampled a mere fraction of the dynamics. However, this bottleneck is mostly an artificial one. It is well known that there is a largest stable timestep associated with explicit numerical integration of a system of equations in time. This is known as the Courant–Friedrichs–Lewy (CFL) condition. Typically the step size scales with the grid spacing (a finite difference scheme) or distance between quadrature points (a dG or pseudospectral scheme). The length scale problem is then one of a stable timestep: if we have a region which needs to be resolved by a very fine grid, the global stable timestep is set by this particular region. Thus, when the mass ratios are large, the inefficiency of using a global *explicit* timestepping scheme can result in simulations running 10^2 - 10^7 times slower! A typical dG construction offers a novel solution. As each element is evolved nearly

independently we are free to choose different time integrators in different regions of the grid, meaning we are no longer tied to a global CFL condition. It has been shown that significant speedups are achievable with this approach [121, 105, 149].

Modeling EMRB systems with RWZ equations have historically relied on frequency domain codes [201]. A Fourier transform in time results in a system of ordinary differential equations (ODEs), and the source terms become a sum over frequencies. Frequency–domain codes are known to be very efficient for circular orbits where, for a given spherical harmonic index, only a single frequency appears. When the frequency spectrum is large (in the case of eccentric orbits) or continuous (realistic inspiral orbits) these codes become increasingly inefficient [177, 24] (see [125, 5, 23] for a recent revival of frequency–domain codes). Time–domain codes overcome this difficulty by simultaneously solving for all modes. Yet with time–domain approaches come a new set of issues such as potentially poor phase resolution for long integrations, resolving the particle (formally a Dirac delta), and minimizing artificial reflections from the outer physical boundary. Over the past decade numerous time–domain schemes have appeared and significant progress has been made [153, 204, 134, 61, 216, 229, 58]. Low–order methods have notoriously poor phase resolution properties. In contrast, dG methods typically allow for very good phase resolution. To treat the delta function some approaches, for example, may feature replacement by narrowly peaked Gaussian and consequently suffer from large oscillations and poor accuracy at the particle’s location. DG methods employ a multi–domain setup and this allows for a domain matching technique to overcome this difficulty. The key ingredient is that the singular δ -terms are taken into account as an additional numerical flux term defined at domain interfaces. There is no longer computational overhead in representing the particle and high accuracy is maintained at the particle’s location. Boundary conditions, although not part of a method, per

se, are an essential part of the RWZ initial boundary value problem. Using radiation outer boundary conditions developed by Lau [143] our code is the first to remove these artificial reflections.

The dG method is essentially unknown to the numerical general relativity community, but has been highly successful in the simulation of many other types of wave-dominated problems, such as electromagnetic scattering [123, 121, 105, 122, 71, 72], nonlinear hydrodynamics with Euler [70, 121, 224, 240, 187, 189] and Navier–Stokes equations [121, 25, 150], and magnetohydrodynamics [131, 148, 230, 145]. In particular, it seems that the computational efficiency, the high-order accuracy, and the general flexibility and robustness of dG methods could be fruitful for numerically solving the types of problems one encounters in gravitational wave simulations. Such simulations are often large and long-time problems, require good phase resolution, and generically involve different length scales and shock formation. It is the aim of this dissertation to begin migrating dG methods, which have been rapidly developing over the last decade in applied mathematics and engineering communities, to computational general relativity. This dissertation represents initial work towards this goal, and as such is mostly limited to systems which exhibit symmetries.

DG methods were first proposed by Reed and Hill in 1973 [191]. Nearly 20 years later stability for non-linear and time-dependent problems was demonstrated in a series of papers by Cockburn and Shu [68, 70, 69]. By the late 1990’s a solid foundation had been laid, and over the past decade significant theoretical and computational progress has continued. Although dG methods are now well developed, they are not as mature as more traditional finite difference, finite element, and finite volume methods. Thus, we have found it necessary to engage in both the designing of schemes as well as in their implementations. In the case of EMRB systems the main obstacle was rewriting the wave-like equation in first order form and then

treating a vectorized Dirac delta within a dG framework. Upon doing so we discovered that the enlarged system may admit a persistent distributional “junk” solution resulting from poor initial data, and Chapter 5 considers some consequences as well as providing a simple remedy. For the GBSSN system identification of the correct stabilizing numerical flux term was an essential step.

We begin in Chapter 2 by introducing the relevant differential geometry and notation needed to understand the physics. Next, perturbation theory of a non-spinning black hole is developed and the inhomogeneous RWZ equations (2.38,2.38) are motivated. These equations will be used in modeling EMRB systems. In the remainder of the chapter we return to the full Einstein equation, using a space+time decomposition followed by a conformal–traceless decomposition to arrive at the numerically stable GBSSN (2.6.3) system.

Additional introductory material is given in Chapter 3. We first define and discuss strongly hyperbolic PDEs. Motivation for well-posedness and stability of these systems, for both the continuum and semi-discrete problem, is also given. These concepts play an important role in understanding the properties of a PDE as well as informing the development of a numerical scheme. A nodal dG scheme is then proposed for a strongly hyperbolic toy PDE and this procedure is later employed in the discretization of both the RWZ (see Chapter 4) and GBSSN (see Chapter 6) systems.

Both Chapters 4 and 5 are concerned with the RWZ equation. Our numerical scheme, complete with radiation boundary conditions and waveform extraction, for the RWZ equation is given in Chapter 4. We also provide greater detail on the distributional source term and describe the RWZ equation as a first order system. A series of code diagnostics verify the theoretical properties of the method, and

we conclude the chapter by computing gravitational waveforms from circular and eccentric orbits. Chapter 5 looks at consequences of commonly chosen trivial initial data. We show such unphysical specification may lead to spurious solutions which contaminate the physical solution indefinitely as well as dynamical junk solutions which degrade accurate self-force computations. Using a new temporal smoothing technique we demonstrate that both persistent and dynamic junk can be removed.

In Chapter 6 we present a dG method for evolving the spherically reduced GBSSN system expressed in terms of second-order spatial operators. We discuss in detail both our scheme for the BSSN system and its implementation. We also consider a simple system which models the spherically reduced GBSSN system. This system is crucial for understanding the role of the dG penalty parameters and for the observed numerical stability, and an analytical proof that the model system is L_2 semi-discrete stable is given. We conclude the chapter by demonstrating our multi-domain method achieves global spectral accuracy and long-time stability on short computational domains.

A new opportunity offered by the dG method includes the utilization of a reduced basis (RB) approach as an efficient tool for high-dimensional parameterized problems ubiquitous in binary simulations. In Chapter 7 we switch gears a bit by offering a preliminary report towards the development of dG-RB methods for gravitational wave problems. In particular, we develop an algorithm that aims to construct a compact reduced basis space from which a particular solution can be quickly and accurately reconstructed. We apply the algorithm to compress the solution space of analytic chirp gravitational waveforms. Our approach has immediate consequences for gravitational wave searches, and we demonstrate improvement over the standard approach. We conclude the section by revisiting the RWZ equation, and consider possible extensions of the RB algorithm to our dG scheme.

CHAPTER TWO

Formulations and Approximations of General Relativity

2.1 Introduction

To motivate our problems of interest with sufficient background material, this chapter introduces the relevant physics and differential geometry utilized throughout the dissertation. Section 2.2 provides much of the essential differential geometry tools needed while developing relevant notation and conventions. Einstein’s field equations are presented with some discussion in section 2.3. These equations admit wave-like solutions and the basic features of these gravitational waves are outlined. Historical and technical background of gravitational perturbation theory is given in section 2.4. Extreme mass ratio binary (EMRB) systems are naturally described within the perturbative framework and we will use the developed theory, in particular the inhomogeneous Regge–Wheeler–Zerilli (RWZ) equations (2.38,2.38), to compute metric perturbations from such systems. Returning to the full Einstein equations, section 2.5 aims to express these as a Cauchy initial boundary value problem and culminates in the Arnowitt–Deser–Misner (ADM) formulation. The resulting ADM system (2.5.3) is poorly suited for numerical evolutions, and section 2.6 carries out a conformal–traceless decomposition of the ADM variables leading to the generalized Baumgarte–Shapiro–Shibata–Nakamura (GBSSN) system (2.6.3). Minor differences between the GBSSN system used in this dissertation and the more common BSSN system are highlighted throughout the section.

2.2 Differential Geometry and Conventions

Let M be a manifold equipped with a metric $g_{\alpha\beta}$. More specifically, in the context of general relativity, assume M is a 4-dimensional pseudo-Riemannian spacetime and g has a $(-, +, +, +)$ signature. Greek indices will range from 0 to 3, and Latin letters

will range from 1 to 3. Each point $p \in M$ is endowed with a tangent space $T_p M$ and a dual space $T_p^* M$. We will denote vectors and dual vectors by their components, V^α and V_α respectively. Products of vectors, dual vectors, and vector/dual pairs are performed in the usual way,

$$\langle V, W \rangle \equiv g(V, W) = g_{\alpha\beta} V^\alpha W^\beta = g^{\alpha\beta} V_\alpha W_\beta = V_\alpha W^\alpha = V^\alpha W_\alpha. \quad (2.1)$$

Here Einstein notation is used, that is repeated “dummy” indices are summed over all possible values.

To ensure a covariant derivative of an arbitrary tensor transforms as a tensor, we have the following general rule,

$$\nabla_\gamma T_{\beta\dots}^{\alpha\dots} \equiv \partial_\gamma T_{\beta\dots}^{\alpha\dots} + \Gamma_{\delta\gamma}^\alpha T_{\beta\dots}^{\delta\dots} - \Gamma_{\beta\gamma}^\delta T_{\delta\dots}^{\alpha\dots}, \quad (2.2)$$

and the metric connection coefficients are given in a coordinate basis by

$$\Gamma_{\beta\gamma}^\alpha = \frac{1}{2} g^{\alpha\delta} (g_{\delta\beta,\gamma} + g_{\delta\gamma,\beta} - g_{\beta\gamma,\delta}). \quad (2.3)$$

This choice of connection leads to the well-known identities $\Gamma_{\beta\delta}^\alpha = \Gamma_{\delta\beta}^\alpha$ and $\nabla_\gamma g_{\alpha\beta} = 0$. Comma and semi-colon notation will sometimes be used for partial and covariant differentiation,

$$\partial_\gamma T_{\beta\dots}^{\alpha\dots} = T_{\beta\dots,\gamma}^{\alpha\dots} \quad (2.4)$$

$$\nabla_\gamma T_{\beta\dots}^{\alpha\dots} = T_{\beta\dots;\gamma}^{\alpha\dots} \quad (2.5)$$

Along with partial and covariant differentiation, we shall often compute the Lie

derivative of a tensor field

$$\mathcal{L}_X T_{\beta\dots}^{\alpha\dots} = X^\gamma \partial_\gamma T_{\beta\dots}^{\alpha\dots} - T_{\beta\dots}^{\gamma\dots} \partial_\gamma X^\alpha + T_{\gamma\dots}^{\alpha\dots} \partial_\beta X^\gamma \quad (2.6)$$

$$= X^\gamma \nabla_\gamma T_{\beta\dots}^{\alpha\dots} - T_{\beta\dots}^{\gamma\dots} \nabla_\gamma X^\alpha + T_{\gamma\dots}^{\alpha\dots} \nabla_\beta X^\gamma \quad (2.7)$$

with respect to some vector field $X = X^\alpha \partial_\alpha$.

We will sometimes work with objects which are not tensors, but tensor densities. A tensor density transforms like a tensor with an overall factor of a Jacobian $J = |\partial x^\alpha / \partial y^\beta|$ to some power W . For example, a tensor density of weight W transforms as

$$T_{\beta\dots}^{\alpha\dots} = J^W \frac{\partial y^\alpha}{\partial x^\gamma} \dots \frac{\partial x^\delta}{\partial y^\beta} \dots T_\delta^\gamma. \quad (2.8)$$

The covariant and Lie derivative of a tensor density is given by

$$\nabla_\gamma T_{\beta\dots}^{\alpha\dots} = \partial_\gamma T_{\beta\dots}^{\alpha\dots} + \Gamma_{\delta\gamma}^\alpha T_{\beta\dots}^{\delta\dots} - \Gamma_{\beta\gamma}^\delta T_{\delta\dots}^{\alpha\dots} - W \Gamma_{\epsilon\gamma}^\epsilon T_{\beta\dots}^{\alpha\dots} \quad (2.9)$$

$$\mathcal{L}_X T_{\beta\dots}^{\alpha\dots} = X^\gamma \partial_\gamma T_{\beta\dots}^{\alpha\dots} - T_{\beta\dots}^{\gamma\dots} \partial_\gamma X^\alpha + T_{\gamma\dots}^{\alpha\dots} \partial_\beta X^\gamma + W T_{\beta\dots}^{\alpha\dots} \partial_\gamma X^\gamma \quad (2.10)$$

$$= X^\gamma \nabla_\gamma T_{\beta\dots}^{\alpha\dots} - T_{\beta\dots}^{\gamma\dots} \nabla_\gamma X^\alpha + T_{\gamma\dots}^{\alpha\dots} \nabla_\beta X^\gamma + W T_{\beta\dots}^{\alpha\dots} \nabla_\gamma X^\gamma. \quad (2.11)$$

Unlike partial differentiation, covariant derivatives need not commute. The Riemannian curvature tensor is an important quantity characterizing how covariant derivatives fail to commute at a point p and is defined by ¹

$$[\nabla_\alpha, \nabla_\beta] V_\delta \equiv V_\gamma R^\gamma_{\delta\beta\alpha} \quad \forall V_\delta \in T_p^* M. \quad (2.12)$$

¹An alternative definition is $[\nabla_\alpha, \nabla_\beta] V^\delta \equiv V^\gamma R^\delta_{\gamma\alpha\beta}$. Using symmetry properties of the curvature tensor and metric compatibility, these two definitions are identical.

$R^\gamma_{\delta\beta\alpha}$ is the only tensor which can be built from no more than two derivatives of the metric, and is linear in the second derivative [236]. Physically we may think of it as an expression of the gravitational field, or more precisely the intrinsic curvature of a manifold M . Noting that

$$[\nabla_\alpha, \nabla_\beta] V_\delta = (V_{\delta,\beta} - \Gamma_{\delta\beta}^\gamma V_\gamma)_{,\alpha} - \Gamma_{\beta\alpha}^\gamma (V_{\delta,\gamma} - \Gamma_{\delta\gamma}^\epsilon V_\epsilon) - \Gamma_{\delta\alpha}^\gamma (V_{\gamma,\beta} - \Gamma_{\gamma\beta}^\epsilon V_\epsilon) - (\alpha \leftrightarrow \beta), \quad (2.13)$$

and using the symmetry relationship $\Gamma_{\alpha\beta}^\delta = \Gamma_{\beta\alpha}^\delta$, the curvature tensor is given in a coordinate basis by

$$R^\gamma_{\delta\beta\alpha} = \Gamma_{\delta\alpha,\beta}^\gamma - \Gamma_{\delta\beta,\alpha}^\gamma + \Gamma_{\delta\alpha}^\epsilon \Gamma_{\epsilon\beta}^\gamma - \Gamma_{\delta\beta}^\epsilon \Gamma_{\epsilon\alpha}^\gamma. \quad (2.14)$$

From the Riemannian curvature tensor, $R^\alpha_{\beta\delta\gamma}$, we construct the Ricci tensor $R_{\alpha\beta} \equiv R^\delta_{\alpha\delta\beta}$ and scalar $R \equiv g^{\alpha\beta} R_{\alpha\beta}$. The curvature tensor may be expressed with explicit second derivatives of the metric plus lower order terms [236]. Contracting this form of the curvature tensor in a coordinate basis yields a particularly useful expression for the Ricci tensor [27]

$$R_{\alpha\beta} = \frac{1}{2} g^{\delta\epsilon} (g_{\delta\beta,\alpha\epsilon} + g_{\alpha\epsilon,\delta\beta} - g_{\delta\epsilon,\alpha\beta} - g_{\alpha\beta,\delta\epsilon}) + g^{\delta\epsilon} (\Gamma_{\alpha\epsilon}^\gamma \Gamma_{\gamma\delta\beta} - \Gamma_{\alpha\beta}^\gamma \Gamma_{\gamma\delta\epsilon}), \quad (2.15)$$

where $\Gamma_{\alpha\beta\delta} \equiv g_{\alpha\epsilon} \Gamma_{\beta\delta}^\epsilon$.

2.3 General Relativity

2.3.1 Einstein Field Equation

According to the theory of general relativity, in the presence of a stress–energy tensor $T_{\alpha\beta}$ the metric $g_{\alpha\beta}$ on M is given by Einstein’s equation

$$G_{\alpha\beta} \equiv R_{\alpha\beta} - \frac{1}{2}Rg_{\alpha\beta} = 8\pi\frac{G}{c^4}T_{\alpha\beta}. \quad (2.16)$$

In 4 dimensions, this is a non–linear system of 16 coupled PDEs, 6 of which are related by symmetry $G_{\alpha\beta} = G_{\beta\alpha}$. As the Ricci tensor and scalar are built from the metric, Einstein’s equation is in fact a second order PDE for $g_{\alpha\beta}$ and features nonlinear products of the metric and its derivatives. In mks units the constant $\frac{G}{c^4} \sim 10^{-44} s^2 m^{-1} kg^{-1}$ coupling the stress–energy tensor to the metric suggests that fast moving massive objects will be required to generate detectable gravitational wave signals.

Exact solutions of Einstein’s equation have been found, yet typically this is only possible for an idealized physical system (e.g. Schwarzschild and Kerr solutions being two prominent examples). It is more common, especially in the context of realistic astrophysical systems, that an exact solution is not known, and thus finding numerical solutions become important. When an approximate solution has been found, such as post–Newtonian gravitational waveforms, a numerical solution provides a direct check that the approximations are acceptable. Recently, numerical simulations have been used to calibrate semi–analytic models in the effective one body approach [77, 174, 168, 18]. In short, numerical simulations are an important part of modern research in both theoretical and experimental general relativity.

The primary goal of numerical general relativity is to find a solution $g_{\alpha\beta}$ to Eq. (2.16) for a given stress–energy tensor $T_{\alpha\beta}$. One approach, carried out in Sec. 2.4, linearizes the Einstein equation around a background solution and then one computes the metric perturbation. Another approach is to directly solve the fully non–linear PDE. It turns out that Eq. (2.16) is not suitable for numerical implementation, sections 2.5 and 2.6 are devoted to finding a suitable form.

2.3.2 Gravitational Waves

Regardless of the physical system under consideration or the relevant PDEs, the motivation is typically the same: what are the emitted gravitational waveforms? To answer this question we first discuss the general properties of these waves.

Consider weak field *radiative* solutions far from isolated sources so that, in a Cartesian coordinate system, we may write

$$g_{\alpha\beta} = \eta_{\alpha\beta} + h_{\alpha\beta} \tag{2.17}$$

where $\eta_{\alpha\beta} = \text{diag}(-1, 1, 1, 1)$ is the Minkowski metric and $h_{\alpha\beta}$ is comparatively small. Define the trace–reversed perturbation $\hat{h}_{\alpha\beta} = h_{\alpha\beta} - \frac{1}{2}\eta_{\alpha\beta}h^\mu{}_\mu$. One can show [163] it is always possible to find a coordinate transformation such that $\hat{h}_{\alpha\beta}$ is divergence free $\nabla_\alpha \hat{h}^{\alpha\beta} = 0$, and the linearized Einstein equation becomes

$$\nabla^\mu \nabla_\mu \hat{h}_{\alpha\beta} = 0 \tag{2.18}$$

a wave equation for the trace–reversed perturbation.

It is well known that the radiative part of the metric contains precisely two

degrees of freedom, whereas a generic perturbation $h_{\mu\nu}$ has 10 independent components. Clearly 8 components must contain unphysical information to be eliminated by a smart choice of coordinates. The physical significance of the two radiative modes becomes clear upon enacting a coordinate transformation which puts the perturbation $h_{\mu\nu}$ into the *transverse traceless* gauge. This gauge is in fact a sub-gauge of the divergence free condition, meaning it further restricts the form of $h_{\mu\nu}$ while keeping it divergence free. One can show it is always possible to construct such a transformation [163] and the resulting tensor is spatial, divergence free, traceless, and transverse to the direction of propagation [236, 163, 60]

$$h_{0\nu} = 0, \quad h^{\mu\nu}{}_{;\nu} = 0, \quad h^\mu{}_\mu = 0, \quad k^\mu h_{\mu\nu} = 0, \quad (2.19)$$

where k^μ denotes the direction of propagation. Note that some of these conditions are redundant, since for radiation we expect $h_{\mu\nu} \sim \exp(-ik^\mu x_\mu)$. Furthermore, as the perturbation is traceless $\hat{h}_{\alpha\beta} = h_{\alpha\beta}$. If $k^\mu = (1, 0, 0, 1)$ describes wavelike propagation in the z direction, the restrictions demanded by (2.19) suggest we write $h_{\mu\nu}$ as

$$h_{\mu\nu} = \begin{pmatrix} 0 & 0 & 0 & 0 \\ 0 & h_+ & h_\times & 0 \\ 0 & h_\times & -h_+ & 0 \\ 0 & 0 & 0 & 0 \end{pmatrix}. \quad (2.20)$$

The *plus* h_+ and *cross* h_\times modes encode fundamental degrees of freedom. A linear combination

$$h(t) = F_+(\theta, \phi, \psi)h_+ + F_\times(\theta, \phi, \psi)h_\times \quad (2.21)$$

will be directly measured by gravitational wave detectors, where (θ, ϕ) depend on the direction of the source and ψ depends on the orientation of the polarizations [220, 14].

It would not be an overstatement to suggest that, perhaps, one of the most important roles of numerical relativity is computing the plus and cross polarizations.

2.4 Gravitational Perturbation Theory for Non–Spinning Black Holes

The theory of Schwarzschild perturbations is well studied, and begins in 1957 with pioneering investigations of Regge and Wheeler [192]. Their work focused on the linear stability of the Schwarzschild solution written in the usual coordinates, which led them to develop the now standard framework for treating metric perturbations about a spherically symmetric spacetime. The approach consists of decomposing the perturbations into tensor spherical harmonics, which naturally split into *axial* (a.k.a. odd) and *polar* (a.k.a. even) parity sectors. A particular linear combination of the expansion coefficients, known as a *master function*, is then shown to satisfy a second order wave equation with an effective potential. Although Regge and Wheeler were unable to construct a master function for the polar parity sector [192], the technique proved to work here as well. This seminal work led to generations of research in gravitational perturbation theory.

The decades following 1957 played host to a series of important developments. We will now briefly summarize the most important and relevant advances, often focusing on those works which contributed to the ideas and techniques employed in this dissertation. Linear stability near the event horizon was conclusively demonstrated in 1970 by Vishveshwara [225] who worked in horizon penetrating Kruskal coordinates which were discovered a few years earlier [141]. In the same year, Zerilli constructed a master function and effective potential for the polar parity pertur-

bations [238]. Shortly thereafter, a new master function for the polar and axial perturbations were introduced by Moncrief [164] and Cunningham, Price, and Moncrief [73] respectively. These master functions are, up to a normalization constant, the preferred choice of modern treatments. The general theory was presented in a gauge-invariant framework by Moncrief in 1974 [164], and extended to a covariant and gauge-invariant formulation in 1980 by Gerlach [103]. Metric perturbations driven by dynamical matter fields were computed for collapsing stars [73, 74] and for the radial plunge of a compact object into the Schwarzschild black hole [239]. By considering second order perturbations, investigations into the nonlinear stability of the Schwarzschild solution were initiated by Tomita [222, 223]. Within the perturbation formalism the possibility of constructing a well defined average energy due to gravitational waves was recognized by Brill and Hartle [39]. Their insight was placed on a rigorous footing by Isaacson with the introduction of an effective gravitational wave stress-energy tensor [128, 129]. Thorne [219], Poisson [159, 177], Martel [157], and Brizuela [40] provided thorough treatments of the radiation field and associated energy and angular momentum luminosities. Perturbative treatments of the Kerr and Reissner-Nordström metrics were considered by Moncrief [165, 166] and Teukolsky [221] respectively.

Recent developments are primarily driven by the community’s goal to compute gravitational waveforms suitable for gravitational wave data analysis. Such waveforms must achieve an accuracy suitable for searching the data for a signal, meaningful parameter estimation, and precision tests of general relativity. It is important to identify and distinguish two very different sources of error which could lead to poor waveforms: numerical errors and modeling errors. For the present discussion we might be concerned that the linearized theory will introduce unacceptably large model errors. This is indeed the case when dealing with EMRB systems. As energy

is removed from the system via gravitational wave emission the smaller compact object will slowly inspiral and merge with the supermassive black hole. This phenomenon, known as radiation reaction, leads to a secular change in the characteristic frequency of the emitting system. Order of magnitude estimates suggest the phase slip between a waveform incorporating and neglecting this feature will be large on timescales of interest [79]. We are forced to conclude that waveforms which do not account for radiation reaction will result in a significantly reduced signal to noise ratio when data searches are performed. In the context of EMRB systems, a fully consistent second order (in perturbation theory) gravitational waveform from EMRB systems, so-called *Capra* waveforms, will include radiation reaction as well as other corrections which occur at second order.

This dissertation makes progress towards accurate and efficient computation of Capra waveforms by developing novel numerical methods for the physical problem at hand. Chapters 4 and 5, part of the original work of this dissertation, aims at reducing the numerical errors which would otherwise corrupt the suitability of Capra waveforms for data analysis *regardless of the model's accuracy*. Numerical errors can be just as dangerous as modeling errors. Comments about such errors are reserved for later.

Motivated by considerations above, we note a few recent developments of perturbation theory which are important for Capra waveforms. A complete covariant and gauge invariant formalism within the master function framework was provided by Sarbach and Tiglio [195]. Their work was later extended by Poisson and Martel to include covariant source terms arising from a stress–energy tensor [159]. Second order perturbations were further studied by Gleiser et al [104], and a gauge–invariant formalism for arbitrary second–order master functions was presented by Brizuela, Martín–García, and Tiglio [40]. Barack and Lousto reformulate the theory

of Schwarzschild black hole perturbations driven by compact objects in the Lorenz gauge [20], which is advantageous for self-force² computations. Computing self-force corrections to a perturbing particle’s geodesic orbit (to be discussed in Sec. 2.4.5) is an active area of research which comprises a major portion of current developments in perturbation theory.

The next few sections provide a brief introduction to the historied subject of Schwarzschild perturbation theory. We will focus on linear perturbations and later make use of our discussion in Chapters 4 and 5 when we numerically solve for the gravitational perturbations from EMRB systems. For additional discussion on Schwarzschild perturbations, we point the reader to any of the above references, in particular Refs. [192, 159, 204, 157]. The classic monograph by Chandrasekhar [62] gives a thorough description of gravitational perturbation theory up through the 1990’s.

2.4.1 Problem Setup

In the standard (t, r, θ, ϕ) coordinates, the Schwarzschild line-element reads

$$g_{\alpha\beta}^{Sch} dx^\alpha dx^\beta = g_{AB} dx^A dx^B + r^2 \Omega_{ab} dx^a dx^b = -f dt^2 + f^{-1} dr^2 + r^2 d\Omega^2, \quad (2.22)$$

where $f \equiv 1 - 2M/r$ and Ω_{ab} is the metric of the unit-radius round sphere; explicitly $d\Omega^2 = d\theta^2 + \sin^2 \theta d\phi^2$. We will use the convention that upper case Latin indices run over (t, r) whereas lower case run over (θ, ϕ) .

²The self-force is the instantaneous acceleration a compact object experiences due to its own metric perturbations. Objects experiencing a self-force will not execute geodesic motion of the background spacetime.

Assume the total metric may be written as a small perturbation $h_{\alpha\beta}$ to the background metric $g_{\alpha\beta}^{Sch}$ such that³

$$g_{\alpha\beta} = g_{\alpha\beta}^{Sch} + h_{\alpha\beta}. \quad (2.23)$$

Equations describing the metric perturbations are found by working to first order in $h_{\alpha\beta}$. For example, the inverse metric is $g^{\alpha\beta} = g_{Sch}^{\alpha\beta} - h^{\alpha\beta}$ because to first order in h we have $g^{\alpha\epsilon}g_{\epsilon\beta} = (g_{Sch}^{\alpha\epsilon} - h^{\alpha\epsilon})(g_{\epsilon\beta}^{Sch} + h_{\epsilon\beta}) = \delta^{\alpha}_{\beta}$. In this short computation we have employed the convention of simply dropping terms proportional to $O(h^2)$ when they arise. As a corollary tensors proportional to $h_{\alpha\beta}$ will have their indices raised and lowered using the unperturbed metric, which suggests we may interpret $h_{\alpha\beta}$ as a tensor field evolving on the background spacetime. Starting with Eqs. (2.3,2.14,2.16), a straightforward computation yields the perturbed connection, Ricci tensor, and Einstein tensor

$$\delta\Gamma_{\beta\gamma}^{\alpha} = \frac{1}{2}g_{Sch}^{\alpha\nu} (h_{\beta\nu;\gamma} + h_{\gamma\nu;\beta} - h_{\beta\gamma;\nu}) \quad (2.24)$$

$$\delta R_{\mu\nu} = \delta\Gamma_{\mu\nu;\beta}^{\beta} - \delta\Gamma_{\mu\beta;\nu}^{\beta} \quad (2.25)$$

$$\delta G_{\mu\nu} = \delta R_{\mu\nu} - \frac{1}{2}g_{\mu\nu}^{Sch} \delta R, \quad (2.26)$$

where $\delta R = g_{Sch}^{\alpha\beta} \delta R_{\alpha\beta}$ and covariant derivatives are taken with respect to $g_{\alpha\beta}^{Sch}$, although using $g_{\alpha\beta}$ clearly gives the same (first order) result. Although the background connection is not a tensor its first order variation is, and hence the covariant derivative of $\delta\Gamma_{\beta\delta}^{\alpha}$ is well defined. To derive the perturbed Einstein equation $\delta G_{\mu\nu}$ we have used the fact that when the background stress–energy tensor vanishes the

³At this stage it is important to realize the theory's gauge freedom has not yet been fixed even though the background coordinates have been. Physically equivalent spacetimes are related by coordinate transformations $(x^{\alpha})^{\text{new}} = (x^{\alpha})^{\text{old}} + \epsilon^{\alpha}$ obeying $\epsilon_{\alpha;\beta} \leq h_{\alpha\beta}$. This observation is simply a consequence of covariance, the transformation rule $h_{\alpha\beta}^{\text{new}} = h_{\alpha\beta}^{\text{old}} - \nabla_{\alpha}\epsilon_{\beta} - \nabla_{\beta}\epsilon_{\alpha}$, and the condition that in a new coordinate system the perturbations must remain small. A good discussion of this topic is found in Ref. [60].

background Ricci tensor and scalar vanishes as well. As

$$G_{\mu\nu} (g_{\alpha\beta}^{Sch} + h_{\alpha\beta}) = G_{\mu\nu} (g_{\alpha\beta}^{Sch}) + \delta G_{\mu\nu} (h_{\alpha\beta}) = \delta G_{\mu\nu} (h_{\alpha\beta}), \quad (2.27)$$

the metric perturbations are determined from $\delta G_{\mu\nu}$ alone.

Assume the perturbing stress-energy tensor $T^{\mu\nu}$ is due to the presence of a point particle of mass $m_p \ll M$,

$$T^{\mu\nu} = m_p \int \frac{1}{\sqrt{-g^{Sch}}} u^\mu u^\nu \delta^4(z^\alpha - z_p^\alpha(\tau)) d\tau. \quad (2.28)$$

In this expression we have introduced the proper time τ , the particle's path $z_p^\alpha(\tau)$, the particle's four-velocity $u_p^\alpha = \frac{dz_p^\alpha}{d\tau}$, and the coordinate Dirac delta function δ^4 . The linearized Einstein field equations for $h_{\alpha\beta}$ become

$$\delta G_{\mu\nu} = 8\pi T_{\mu\nu} \quad (2.29)$$

and we expect that $h_{\alpha\beta} \propto T_{\alpha\beta} \propto m_p$, thereby justifying $T^{\mu\nu}$ as a source for linear perturbations when $m_p \ll M$.

In principle we have our perturbation equations for $h_{\alpha\beta}$, yet further simplifications are possible. First note that we have not specified a gauge condition. In particular, working in the Regge-Wheeler gauge allows many components of $h_{\alpha\beta}$ to be set to zero. Furthermore, we will exploit the spacetime's spherical symmetry by decomposing the metric perturbations into a complete orthogonal basis of scalar, vector, and tensor spherical harmonics defined on the two-sphere. These harmonics transform as either $(-1)^\ell$ (polar parity) or $(-1)^{\ell+1}$ (axial parity) under parity transformations, corresponding to the simultaneous replacements $\phi \rightarrow \pi + \phi$ and $\theta \rightarrow \pi - \theta$ in spherical coordinates. Thus, the metric perturbations are naturally organized according to

their (ℓ, m) and parity family

$$h_{\alpha\beta}^{\ell m} = h_{\alpha\beta}^{\ell m, P} + h_{\alpha\beta}^{\ell m, A} \quad (2.30)$$

$$h_{\alpha\beta} = \sum_{\ell=0}^{\infty} \sum_{m=-\ell}^{\ell} h_{\alpha\beta}^{\ell m}. \quad (2.31)$$

This dissertation focuses on $\ell \geq 2$ metric perturbations⁴ resulting from a stress-energy tensor of the form (2.28). Nevertheless, we will not assume that form for $T^{\mu\nu}$ in this section. The perturbation equations of Sec. 2.4.2 and 2.4.3 are general, and the source terms which arise from a non-zero stress-energy tensor will be left opaque until Chapter 4. In what follows let x denote the tortoise coordinate

$$x = r + 2M \ln \left(\frac{r}{2M} - 1 \right). \quad (2.32)$$

For notational brevity, multipole (ℓ, m) labels are suppressed when they are clear from context.

2.4.2 Polar Perturbations

To decompose the polar perturbations, we first introduce the polar spherical harmonics

$$Y^{\ell m}, \quad Y_a^{\ell m} = Y_{:a}^{\ell m}, \quad Y_{ab}^{\ell m} = Y^{\ell m} \Omega_{ab}, \quad Z_{ab}^{\ell m} = Y_{:ab}^{\ell m} + \frac{\ell(\ell+1)}{2} Y^{\ell m} \Omega_{ab}, \quad (2.33)$$

where $Y^{\ell m}(\theta, \phi)$ are the ordinary scalar harmonics and a colon indicates covariant differentiation compatible with Ω_{ab} . $Y^{\ell m}(\theta, \phi)$ solves the eigenvalue problem

⁴The lower multipoles are not radiative and can be treated analytically [239].

$\Omega^{ab}Y_{:ab}^{\ell m} = -\ell(\ell + 1)Y^{\ell m}$, and a discussion of their utility may be found in any book on analytic solutions to spherically symmetric PDEs, for example [130]. The polar tensor harmonics are explicitly constructed in [159, 103, 219], and their orthogonality relations are

$$\int Y^{\ell m} \bar{Y}_{\ell' m'} d\Omega = \delta_{\ell\ell'} \delta_{mm'} \quad (2.34a)$$

$$\int Y_a^{\ell m} \bar{Y}_{\ell' m'}^a d\Omega = \ell(\ell + 1) \delta_{\ell\ell'} \delta_{mm'} \quad (2.34b)$$

$$\int Y_{ab}^{\ell m} \bar{Y}_{\ell' m'}^{ab} d\Omega = 2\delta_{\ell\ell'} \delta_{mm'} \quad (2.34c)$$

$$\int Z_{ab}^{\ell m} \bar{Z}_{\ell' m'}^{ab} d\Omega = \frac{1}{2} \frac{(\ell + 2)!}{(\ell - 2)!} \delta_{\ell\ell'} \delta_{mm'} \quad (2.34d)$$

where the bar denotes complex conjugation.

The polar harmonics form a complete basis for any rank 0, 1, or 2 tensor that transforms with polar parity. By considering the transformation properties of $h_{\alpha\beta}^{\ell m}$ under rotations⁵ and parity, the polar perturbations are expanded as

$$h_{AB}^P = \sum_{\ell \geq 2}^{\infty} \sum_{m=-\ell}^{\ell} p_{AB}^{\ell m} Y^{\ell m} \quad (2.35a)$$

$$h_{Ab}^P = \sum_{\ell \geq 2}^{\infty} \sum_{m=-\ell}^{\ell} p_A^{\ell m} Y_b^{\ell m} \quad (2.35b)$$

$$h_{ab}^P = r^2 \sum_{\ell \geq 2}^{\infty} \sum_{m=-\ell}^{\ell} K^{\ell m} Y_{ab}^{\ell m} + G^{\ell m} Z_{ab}^{\ell m}, \quad (2.35c)$$

where the newly defined fields are functions of t and r . It was noticed that a suitable coordinate (i.e. gauge) transformation, known as the Regge–Wheeler gauge, allows us to specify $p_A^{\ell m} = G^{\ell m} = 0$ [192]. The remaining harmonic coefficients $p_{AB}^{\ell m}$ and $K^{\ell m}$ are recovered by substituting (2.35) into (2.29) and using the orthogonality

⁵Subject to the assumption of spherical symmetry, the class of rotations under consideration are of the form $\theta^{\text{new}} = f(\theta, \phi)$ and $\phi^{\text{new}} = g(\theta, \phi)$ for a suitable choice of f and g .

relations of the polar harmonics. The result is a system of coupled PDEs for each (ℓ, m) mode [159]⁶

$$Q^{tt} = -K_{,rr} - \frac{3r - 5M}{r^2 f} K_{,r} + \frac{f}{r} p_{rr,r} + \frac{(\lambda_\ell + 2)r + 4M}{2r^3} p_{rr} + \frac{n_\ell}{r^2 f} K \quad (2.36a)$$

$$Q^{tr} = K_{,tr} + \frac{r - 3M}{r^2 f} K_{,t} - \frac{f}{r} p_{rr,t} - \frac{\lambda_\ell}{2r^2} p_{tr} \quad (2.36b)$$

$$Q^{rr} = -K_{,tt} + \frac{(r - M)f}{r^2} K_{,r} + \frac{2f}{r} p_{tr,t} - \frac{f}{r} p_{tt,r} + \frac{\lambda_\ell r + 4M}{2r^3} p_{tt} - \frac{f^2}{r^2} p_{rr} - \frac{n_\ell f}{r^2} K \quad (2.36c)$$

$$Q^t = p_{rr,t} - p_{tr,r} + \frac{1}{f} K_{,t} - \frac{2M}{r^2 f} p_{tr} \quad (2.36d)$$

$$Q^r = -p_{tr,t} + p_{tt,r} - f K_{,r} - \frac{r - M}{f r^2} p_{tt} + \frac{(r - M)f}{r^2} p_{rr} \quad (2.36e)$$

$$Q^b = -p_{rr,tt} + 2p_{tr,tr} - p_{tt,rr} - \frac{1}{f} K_{,tt} + f K_{,rr} + \frac{2(r - M)}{f r^2} p_{tr,t} + \frac{3M - r}{f r^2} p_{tt,r} + \frac{(M - r)f}{r^2} p_{rr,r} + \frac{2(r - M)}{r^2} K_{,r} + \frac{\lambda_\ell r^2 - 2(2 + \lambda_\ell)Mr + 4M^2}{2f^2 r^4} p_{tt} - \frac{\lambda_\ell r^2 - 4n_\ell Mr - 4M^2}{2r^4} p_{rr} \quad (2.36f)$$

$$Q^\sharp = \frac{1}{f} p_{tt} - f p_{rr}, \quad (2.36g)$$

where we have defined $n_\ell = (\ell + 2)(\ell - 1)/2$ and $\lambda_\ell = \ell(\ell + 1) = 2(n_\ell + 1)$, and the Q 's are projections of the stress-energy tensor onto the polar spherical harmonics [159].

The metric perturbations are clearly tensorial, nevertheless, they can be recon-

⁶The linearization (2.23) does not assume a particular gauge, while equations (2.36) hold in the Regge–Wheeler gauge. It turns out that $K^{\text{RW}} = K$ and $p_{AB}^{\text{RW}} = p_{AB}$, and so we will continue using K and p_{AB} with the understanding that we have chosen the Regge–Wheeler gauge. It is possible to express the perturbations as gauge invariant combinations, and the result is system (2.36) after making the replacement $K \rightarrow K^{\text{Gauge-Invariant}}$ and $p_{AB} \rightarrow p_{AB}^{\text{Gauge-Invariant}}$. We do not explore this freedom here.

structed from the Zerilli-Moncrief master function

$$\Psi^{\text{ZM}} = \frac{r}{n_\ell + 1} \left(K + \frac{f^2}{\Lambda_\ell} p_{rr} - \frac{fr}{\Lambda_\ell} K_{,r} \right), \quad (2.37)$$

where $\Lambda_\ell = n_\ell + 3M/r$ and we continue to suppress (ℓ, m) labels for the fields. One can show Ψ^{ZM} is a scalar under general coordinate transformations and gauge invariant under infinitesimal ones [159]. Definition (2.37) agrees, up to minor notational discrepancies, with modern treatments such as [159, 204, 151, 152, 89], and differs by a time derivative from Zerilli's original master function [239] and by an overall factor from Moncrief's [164]. Remarkably, the polar master function is governed by a forced scalar wave equation with the following form

$$-\partial_t^2 \Psi^{\text{ZM}} + \partial_x^2 \Psi^{\text{ZM}} - V_\ell^Z \Psi^{\text{ZM}} = S_{\ell m}^{\text{ZM}}(t, r), \quad (2.38a)$$

$$V_\ell^Z(r) = \frac{2f(r)}{(n_\ell r + 3M)^2} \left[n_\ell^2 \left(1 + n_\ell + \frac{3M}{r} \right) + \frac{9M^2}{r^2} \left(n_\ell + \frac{M}{r} \right) \right]. \quad (2.38b)$$

The source term's label highlights its generic dependence. In particular, $S_{\ell m}^{\text{ZM}}$ is built from linear combinations of the Q 's (see Sec. 4.2.2) and crucially depends on the chosen master function. When the stress–energy tensor's form is given by Eq. (2.28) we expect $S_{\ell m}^{\text{ZM}}$ to be distributional.

Each mode K , p_{rr} , p_{tt} , and p_{rt} may be reconstructed from Ψ^{ZM} and its derivatives, thus demonstrating that the master function contains all physical information about the metric perturbations $h_{\alpha\beta}^{\ell m, P}$. Using Eq. (2.37) we express p_{rr} and $\partial_r p_{rr}$ in terms of Ψ^{ZM} , K , and their derivatives. Upon substituting these expressions into Q^{tt} , one discovers that all terms proportional to $\partial_r K$ and $\partial_r^2 K$ cancel, leaving behind an equation for K . Then p_{rr} is found from the definition of Ψ^{ZM} . The Q^\sharp and Q^{tr}

components readily give p_{tt} and p_{rt} respectively. The result is:

$$K = f\Psi_{,r}^{\text{ZM}} + \frac{r\lambda_\ell\Lambda_\ell - 6Mf}{2\Lambda_\ell r^2}\Psi^{\text{ZM}} - \frac{2r^2 f^2}{\lambda_\ell\Lambda_\ell}Q^{tt} \quad (2.39a)$$

$$p_{rr} = \frac{\Lambda_\ell\lambda_\ell}{2rf^2}\Psi^{\text{ZM}} - \frac{\Lambda_\ell}{f^2}K + \frac{r}{f}K_{,r} \quad (2.39b)$$

$$p_{tt} = f^2 p_{rr} + fQ^\sharp \quad (2.39c)$$

$$p_{rt} = \frac{2r^2}{\lambda_\ell}K_{,tr} + \frac{2(r-3M)}{f\lambda_\ell}K_{,t} - \frac{2fr}{\lambda_\ell}p_{rr,t} - \frac{2r^2}{\lambda_\ell}Q^{tr}. \quad (2.39d)$$

We refer to Eqs. (2.39) as the polar metric reconstruction equations, and they hold only in the Regge–Wheeler gauge.

Having an explicit relationship between the master function Ψ^{ZM} and the metric perturbations is both satisfying and useful. For example, the reconstruction equations are needed to compute self-force corrections to the particle’s geodesic motion and can be used to define waveforms at future null infinity after a suitable gauge transformation has been enacted. Notice that the metric reconstruction equations feature Ψ^{ZM} , $\partial_t\Psi^{\text{ZM}}$, and their spatial derivatives. Therefore, any numerical scheme which promotes $\partial_t\Psi^{\text{ZM}}$ to an evolutionary variable will not have to compute a cumbersome and potentially inaccurate time derivative – which would typically require saving time histories and performing finite difference operations. Spatial derivatives are comparatively easy to compute, and for our numerical scheme accurate as well.

2.4.3 Axial Perturbations

To decompose the axial perturbations, we first introduce the axial spherical harmonics. With ϵ_{ab} the unit-sphere Levi–Civita tensor such that $\epsilon_{\theta\phi} = -\sin\theta$, the axial

spherical harmonics are

$$X_a^{\ell m} = \Omega^{bc} \epsilon_{ab} Y_{:c}^{\ell m}, \quad X_{ab}^{\ell m} = \frac{1}{2} (X_{a:b}^{\ell m} + X_{b:a}^{\ell m}), \quad (2.40)$$

where a colon indicates covariant differentiation compatible with Ω_{ab} and $Y^{\ell m}(\theta, \phi)$ are discussed in Sec. 2.4.2. The axial tensor harmonics are explicitly constructed in [159, 103, 219], and their orthogonality relations are

$$\int X_a^{\ell m} \bar{X}_{\ell' m'}^a d\Omega = \ell(\ell + 1) \delta_{\ell\ell'} \delta_{mm'} \quad (2.41a)$$

$$\int X_{ab}^{\ell m} \bar{X}_{\ell' m'}^{ab} d\Omega = \frac{1}{2} \frac{(\ell + 2)!}{(\ell - 2)!} \delta_{\ell\ell'} \delta_{mm'} \quad (2.41b)$$

where the bar continues to denote complex conjugation.

The axial harmonics form a complete basis for any rank 1 or 2 tensor which transforms with axial parity. By considering the transformation properties of $h_{\alpha\beta}^{\ell m}$ under rotations and parity, the axial perturbations as are expanded as

$$h_{BC}^A = 0 \quad (2.42a)$$

$$h_{Bc}^A = \sum_{\ell \geq 2}^{\infty} \sum_{m=-\ell}^{\ell} q_B^{\ell m} X_c^{\ell m} \quad (2.42b)$$

$$h_{bc}^A = \sum_{\ell \geq 2}^{\infty} \sum_{m=-\ell}^{\ell} q_2^{\ell m} X_{bc}^{\ell m}, \quad (2.42c)$$

where the newly defined fields are functions of t and r . It was noticed that a suitable coordinate (i.e. gauge) transformation will annul the angular h_{bc}^A perturbations [192]. Therefore, working in the Regge-Wheeler gauge allows us to set $q_2^{\ell m} = 0$. The remaining harmonic coefficient $q_B^{\ell m}$ can now be recovered by substituting (2.42) into (2.29) and using the orthogonality relations of the axial harmonics. The result is a

system of coupled PDEs for each (ℓ, m) mode [159]⁷

$$P^t = -q_{r,tr} + q_{t,rr} - \frac{2}{r}q_{r,t} - \frac{\lambda_\ell r - 4M}{r^3 f}q_t \quad (2.43a)$$

$$P^r = q_{r,tt} - q_{t,tr} + \frac{2}{r}q_{t,t} + \frac{2n_\ell f}{r^2}q_r \quad (2.43b)$$

$$P = -\frac{1}{f}q_{t,t} + f q_{r,r} + \frac{2M}{r^2}q_r, \quad (2.43c)$$

where the P 's arise from projections of the stress–energy tensor onto the axial spherical harmonics and are computed in Sec. 4.2.3.

The metric perturbations are clearly tensorial, nevertheless, they can be reconstructed from the Cunningham-Price-Moncrief master function

$$\Psi^{\text{CPM}} = \frac{r}{n_\ell} \left(q_{t,r} - q_{r,t} - \frac{2}{r}q_t \right). \quad (2.44)$$

One can show Ψ^{CPM} is a scalar under general coordinate transformations, and gauge invariant under infinitesimal ones [159]. Definition (2.44) agrees, up to minor notational discrepancies, with modern treatments such as [133, 159, 204, 151, 89], while differing from older discussions by either a time derivative [192, 239, 164] or an overall factor from Cunningham et al [73]. It was recognized by Tanaka and Jhingan [133] that Ψ^{CPM} is a particularly useful choice when one wishes to reconstruct the metric perturbations from algebraic combinations of the master function as opposed to integral relations which arise when using Regge and Wheeler's original master function [192]. Although they worked in the frequency domain, their insight proves useful here as well. Remarkably, the axial master function is governed by a forced

⁷The linearization (2.23) does not assume any particular gauge choice, while equations (2.43) hold in the Regge–Wheeler gauge. It turns out that $q_B^{\text{RW}} = q_B$, and so we will continue using q_B with the understanding that we have chosen the Regge–Wheeler gauge. It is possible to express the perturbations as gauge invariant combinations, and the result is system (2.43) after making the replacement $q_B \rightarrow q_B^{\text{Gauge-Invariant}}$. We do not explore this freedom here.

scalar wave equation with the following form

$$-\partial_t^2 \Psi^{\text{CPM}} + \partial_x^2 \Psi^{\text{CPM}} - V_\ell^{\text{RW}} \Psi^{\text{CPM}} = S_{\ell m}^{\text{CPM}}(t, r), \quad (2.45a)$$

$$V_\ell^{\text{RW}}(r) = \frac{f(r)}{r^2} \left[\ell(\ell + 1) - \frac{6M}{r} \right]. \quad (2.45b)$$

The source term's label highlights its generic dependence. In particular, $S_{\ell m}^{\text{CPM}}$ is built from a linear combination of the P 's (see Sec. 4.2.3) and crucially depends on the chosen master function. When the stress–energy tensor's form is given by Eq. (2.28) we expect $S_{\ell m}^{\text{CPM}}$ to be distributional.

Each mode q_r and q_t may be reconstructed from Ψ^{CPM} and its derivatives, thus demonstrating that the master function contains all physical information about the metric perturbations $h_{\alpha\beta}^{\ell m, A}$. To find q_r use the P^r component of the field equations and $\partial_t \Psi^{\text{CPM}}$. q_t can be recovered by using the linear combination $r\Psi_{,r}^{\text{CPM}} + \Psi^{\text{CPM}}$ to change $\partial_r q_t$ into $\partial_t q_r$. The P^t component readily gives q_t . The result is:

$$q_r = \frac{r}{2f} \Psi_{,t}^{\text{CPM}} + \frac{r^2}{2n_\ell f} P^r \quad (2.46a)$$

$$q_t = \frac{f}{2} (r\Psi_{,r}^{\text{CPM}} + \Psi^{\text{CPM}}) - \frac{r^2 f}{2n_\ell} P^t, \quad (2.46b)$$

where we have made use of the simplifying relation $\frac{2n_\ell r^2 f}{\lambda_\ell r - 4M - 2rf} = rf$. We will refer to Eqs. (2.46) as the axial metric reconstruction equations. Like much of this section, the utility and applicability of the axial metric reconstruction equations parallels the polar case which is discussed at the end of Sec. 2.4.2.

2.4.4 Perturbations at the Event Horizon and Future Null Infinity

The perturbative framework developed in the preceding sections can be used to compute gravitational waveforms expected to be observed at space and ground based gravitational wave observatories. Consider the gravitational radiation field far from the isolated sources. In Sec. 2.3.2, we considered the transverse traceless gauge as an appropriate setting for describing gravitational radiation. In a spherical coordinate system with waves propagating along a radial direction the corresponding plus $h_+ \equiv h_{\theta\theta}/r^2$ and cross $h_\times \equiv h_{\theta\phi}/(r^2 \sin^2 \theta)$ modes are defined to have the correct $O(r^{-1})$ asymptotic behavior.

Our numerical scheme solves the RWZ wave equations (2.45,2.38) for Ψ^{CPM} and Ψ^{ZM} , and so we seek h_+ and h_\times in terms of polar and axial master functions. First notice that the Regge–Wheeler gauge is not appropriate for this task. Harmonic coefficients of Z_{ab} and X_{ab} , which are precisely the traceless part of the radiation field, are identically set to zero $G = q_2 = 0$. In fact, one can show the harmonic coefficients do not have the correct asymptotic behavior for radiation in the Regge–Wheeler gauge [40]. Fortunately, the master functions are gauge invariant and in a suitable radiation gauge one can deduce the radiative perturbations to be [159, 40]

$$h_{ab}^{\ell m, P} = r \Psi_{\ell m}^{\text{ZM}} Z_{ab}^{\ell m}, \quad h_{ab}^{\ell m, A} = r \Psi_{\ell m}^{\text{CPM}} X_{ab}^{\ell m}. \quad (2.47)$$

This asymptotic result formally holds at future null infinity, although practically we are not able to evaluate our master functions there. The full metric perturbations

are then

$$h_{ab} = r \sum_{\ell \geq 2} \sum_{m=-\ell}^{\ell} (\Psi_{\ell m}^{\text{ZM}} Z_{ab}^{\ell m} + \Psi_{\ell m}^{\text{CPM}} X_{ab}^{\ell m}), \quad (2.48)$$

with plus and cross modes given by

$$h_+ = \frac{1}{r} \sum_{\ell \geq 2} \sum_{m=-\ell}^{\ell} (\Psi_{\ell m}^{\text{ZM}} Z_{\theta\theta}^{\ell m} + \Psi_{\ell m}^{\text{CPM}} X_{\theta\theta}^{\ell m}) \quad (2.49)$$

$$h_{\times} = \frac{1}{r \sin^2 \theta} \sum_{\ell \geq 2} \sum_{m=-\ell}^{\ell} (\Psi_{\ell m}^{\text{ZM}} Z_{\theta\phi}^{\ell m} + \Psi_{\ell m}^{\text{CPM}} X_{\theta\phi}^{\ell m}). \quad (2.50)$$

Notice that Eq. (2.48) implies $O(r)$ asymptotic behavior, corresponding to the expected $O(r^{-1})$ fall-off in an asymptotically Cartesian coordinate system.

Gravitational radiation will remove energy and angular momentum from the system. Where does it go? Some is transferred to the black hole and some escapes to future null infinity. From the metric perturbations we compute the energy contained in the gravitational radiation field by using Isaacson's effective stress-energy tensor [128, 129], given in the transverse traceless gauge by [163]

$$\begin{aligned} T_{\alpha\beta}^{\text{GW}} &= \frac{1}{32\pi} \langle \nabla_{\alpha} h_{\mu\nu} \nabla_{\beta} h^{\mu\nu} \rangle \\ &= \frac{1}{32\pi} \langle g_{Sch}^{\epsilon\mu} g_{Sch}^{\gamma\nu} \nabla_{\alpha} h_{\mu\nu} \nabla_{\beta} h_{\epsilon\gamma} \rangle. \end{aligned} \quad (2.51)$$

Brackets are a reminder to average $\nabla_{\alpha} h_{\mu\nu} \nabla_{\beta} h^{\mu\nu}$ over a volume of spacetime larger than the characteristic lengthscale of the wave. $T_{\alpha\beta}^{\text{GW}}$ is a perfectly reasonable stress-energy tensor when the perturbations are small and the characteristic wavelength of the gravitational radiation λ^{GW} is much shorter than the typical lengthscale on which curvature quantities vary \mathcal{R} . We speak of the short wavelength (often known as high frequency) approximation when $\lambda^{\text{GW}} \ll \mathcal{R}$. A non-vanishing invariant curvature

scale is provided by the Kretschmann invariant $R_{\alpha\beta\delta\gamma}R^{\alpha\beta\delta\gamma} \propto M^2/r^6$, or in units of length $(R_{\alpha\beta\delta\gamma}R^{\alpha\beta\delta\gamma})^{-1/4} \propto r^{3/2}M^{-1/2}$. As a specific example of relevance, when the background is flat \mathcal{R} is infinite. The Schwarzschild solution, the background considered in this dissertation, is asymptotically flat in the limit $r \rightarrow \infty$, thus $T_{\alpha\beta}^{\text{GW}}$ is well motivated in that limit. Intuitively, the short wavelength approximation is appropriate for radiation; far from isolated sources the gravitational radiation varies rapidly over typical lengthscales on which the background changes. Under this assumption and small perturbations one can show $T_{\alpha\beta}^{\text{GW}}$ obeys the ‘‘conservation’’ law [163, 128, 129, 236]

$$\nabla_{\alpha}T_{\text{GW}}^{\alpha\beta} = 0, \quad (2.52)$$

from which we can compute energy and angular momentum luminosities.

At a fixed t we seek the instantaneous energy flux through a two–sphere of large radius. Assume the two–sphere is the boundary of a hypersurface Σ and define $E^{\infty} = \int_{\Sigma} T^t_t \sqrt{-g^{\text{Sch}}} d^3x$, where we have temporarily dropped the ‘GW’ label. Let V^{α} be a Killing vector field. Together Killing’s equation $\nabla_{\alpha}V_{\beta} = -\nabla_{\beta}V_{\alpha}$ and the symmetry of $T^{\alpha\beta}$ imply

$$V_{\beta}\nabla_{\alpha}T^{\alpha\beta} = \nabla_{\alpha}(V^{\beta}T^{\alpha}_{\beta}) = 0. \quad (2.53)$$

If $V^{\alpha} = (1, 0, 0, 0)$ is the timelike Killing field, then by Gauss’ theorem

$$\begin{aligned} \int_{\Sigma} \nabla_{\alpha}T^{\alpha}_t \sqrt{-g^{\text{Sch}}} d^3x &= \int_{\Sigma} \partial_{\alpha} \left(\sqrt{-g^{\text{Sch}}} T^{\alpha}_t \right) d^3x \\ &= \int_{\Sigma} \partial_t T^t_t \sqrt{-g^{\text{Sch}}} d^3x + r^2 \int_{\partial\Sigma} T^r_t d\Omega. \end{aligned} \quad (2.54)$$

The time component of conservation law becomes

$$\dot{E}^\infty = -r^2 \int_{\partial\Sigma} T^{rt} d\Omega, \quad (2.55)$$

where the flat metric is used to raise indices at a large radius. In the distant wavezone the gravitational radiation is a function of retarded time $u = t - r$, and thus $\partial_t h = -\partial_r h$. This insight allows us to trade radial for time derivatives, and the energy luminosity becomes

$$\dot{E}^\infty = r^2 \int_{\partial\Sigma} T^{tt} d\Omega. \quad (2.56)$$

Evaluating the time–time component of Eq. (2.51) produces

$$\begin{aligned} \dot{E}^\infty &= \frac{1}{32\pi r^2} \int_{\partial\Sigma} \langle \Omega^{ae} \Omega^{bd} \partial_t h_{ab} \partial_t h_{cd} \rangle d\Omega \\ &= \frac{1}{32\pi} \int_{\partial\Sigma} \left\langle \sum_{\ell \geq 2} \sum_{m=-\ell}^{\ell} \left(\dot{\Psi}_{\ell m}^{\text{ZM}} Z_{ab}^{\ell m} + \dot{\Psi}_{\ell m}^{\text{CPM}} X_{ab}^{\ell m} \right) \times \right. \\ &\quad \left. \sum_{\ell' \geq 2} \sum_{m'=-\ell'}^{\ell'} \left(\dot{\Psi}_{\ell' m'}^{\text{ZM}} \bar{Z}_{\ell' m'}^{ab} + \dot{\Psi}_{\ell' m'}^{\text{CPM}} \bar{X}_{\ell' m'}^{ab} \right) \right\rangle d\Omega \\ &= \frac{1}{64\pi} \sum_{\ell \geq 2} \sum_{m=-\ell}^{\ell} \frac{(\ell+2)!}{(\ell-2)!} \langle |\dot{\Psi}_{\ell m}^{\text{ZM}}|^2 + |\dot{\Psi}_{\ell m}^{\text{CPM}}|^2 \rangle \\ &= \sum_{\ell \geq 2} \sum_{m=-\ell}^{\ell} \dot{E}_{\ell m}^\infty, \end{aligned} \quad (2.57)$$

where we have defined the energy in each mode

$$\dot{E}_{\ell m}^\infty = \frac{1}{64\pi} \frac{(\ell+2)!}{(\ell-2)!} \langle |\dot{\Psi}_{\ell m}^{\text{ZM}}|^2 + |\dot{\Psi}_{\ell m}^{\text{CPM}}|^2 \rangle. \quad (2.58)$$

\dot{E}^∞ is the gravitational energy luminosity computed at future null infinity. Bracket averaging is accomplished by time averaging Ψ at a fixed radial location for long time intervals. In practice, the averaging is done over some integer multiple of the

longest timescale associated with the wave. Similarly, one computes the gravitational angular momentum luminosity in each mode

$$\dot{L}_{\ell m}^{\infty} = \frac{im}{64\pi} \frac{(\ell+2)!}{(\ell-2)!} \left\langle \dot{\Psi}_{\ell m}^{\text{ZM}} \bar{\Psi}_{\ell m}^{\text{ZM}} + \dot{\Psi}_{\ell m}^{\text{CPM}} \bar{\Psi}_{\ell m}^{\text{CPM}} \right\rangle \quad (2.59)$$

as well as the total

$$\dot{L}^{\infty} = \sum_{\ell \geq 2} \sum_{m=-\ell}^{\ell} \dot{L}_{\ell m}^{\infty} \quad (2.60)$$

at future null infinity via the master functions [157, 159, 219, 40].

Although gravitational wave experiments are unable to directly access information near the event horizon, it is nonetheless interesting and important to compute the energy and angular momentum transferred to the Schwarzschild black hole. In the case of EMRB systems this loss contributes to the compact object's inspiral. Any radial null geodesic, such as gravitational radiation, will be blueshifted as it falls into the black hole, $\lambda^{\text{GW}} \rightarrow 0$ as $r \rightarrow 2M$ in Schwarzschild coordinates. We conclude Isaacson's short wavelength approximation is valid near the event horizon despite the invariant background lengthscale being $O(M)$. Our discussion at future null infinity applies, and the final result is identical to those luminosity expressions

$$\dot{E}_{\ell m}^{\text{BH}} = \frac{1}{64\pi} \frac{(\ell+2)!}{(\ell-2)!} \left\langle |\dot{\Psi}_{\ell m}^{\text{ZM}}|^2 + |\dot{\Psi}_{\ell m}^{\text{CPM}}|^2 \right\rangle \quad (2.61a)$$

$$\dot{L}_{\ell m}^{\text{BH}} = \frac{im}{64\pi} \frac{(\ell+2)!}{(\ell-2)!} \left\langle \dot{\Psi}_{\ell m}^{\text{ZM}} \bar{\Psi}_{\ell m}^{\text{ZM}} + \dot{\Psi}_{\ell m}^{\text{CPM}} \bar{\Psi}_{\ell m}^{\text{CPM}} \right\rangle, \quad (2.61b)$$

where all quantities are to be evaluated at $r = 2M$. A rigorous treatment of the event horizon with Eddington–Finkelstein coordinates is carried out in Ref. [177, 159, 157], where exactly expressions (2.61a,b) are derived.

By combining the above formulas, the net energy and angular momentum luminosity of the gravitational radiation is

$$\dot{E}^{\text{GW}} = \dot{E}^{\text{BH}} + \dot{E}^{\infty}, \quad \dot{L}^{\text{GW}} = \dot{L}^{\text{BH}} + \dot{L}^{\infty}. \quad (2.62)$$

Each equation holds for a particular choice of (ℓ, m) mode as well.

2.4.5 Motion of the Compact Object

Timelike Geodesics of Schwarzschild

To complete the problem's description we specify the stress–energy tensor (2.28) by fixing the particle's trajectory $z_p^\mu(\tau)$, our approach follows the standard arguments [62, 163, 60]. Recall $z_p^\mu(\tau) = (t_p(\tau), r_p(\tau), \theta_p(\tau), \phi_p(\tau))$ is the parameterization of the particle's four–trajectory in terms of proper time τ . Owing to the spherical symmetry of the line–element, we may assume, without loss of generality, that the particle trajectory lies in the equatorial plane $\theta_p(\tau) = \pi/2$. Existence of a Killing vector V^α implies a component of the particle's 4–velocity $V_\alpha u_p^\alpha$ is conserved along the particle's path (see problem 10.10 of Ref. [146]). ∂_t and ∂_ϕ are two such Killing vectors, and their associated conserved quantities are interpreted as the particle's energy per unit mass, $E_p = f u_p^t$, and angular momentum per unit mass, $L_p = r^2 u_p^\phi$. The radial velocity u_p^r is obtained by normalizing the 4–velocity to unity (when working in unit mass), which is also a constant of geodesic motion. Then the four–velocity $u_p^\mu = dz_p^\mu/d\tau$ components are:

$$u_p^t = E_p/f(r), \quad (u_p^r)^2 = E_p^2 - f(r) (1 + L_p^2/r^2), \quad u_p^\theta = 0, \quad u_p^\phi = L_p/r^2. \quad (2.63)$$

Given appropriate initial conditions and choice for the set (E_p, L_p) , these ODEs may be integrated to give $z_p^\mu(\tau)$. Details on this procedure as well as conditions for bounded orbits are provided in Sec. 4.2.1.

Orbits Perturbed by a Self-force

Schwarzschild geodesics correctly describe the small compact object's motion in the limit $m_p/M \rightarrow 0$. However, in the presence of metric perturbations the full spacetime is $g_{\alpha\beta}^{Sch} + h_{\alpha\beta}$ and thus the particle's motion will not be given by (2.63). Instead, the particle will experience a local self-force (i.e. accelerated motion pushing the particle off of its geodesic path) entirely due to $h_{\alpha\beta}$. The dissipative part of the self-force, in an averaged sense, is the radiation reaction. This identification can be understood by an energy-balancing argument: the energy emitted from the system is quadratic in the perturbations and causes a gradual inspiral which, from the point of view of the compact object that has no knowledge of future null infinity, is related to first order corrections of geodesic motion.

Although this effect has been recognized for decades, it was not until 1997 when two independent derivations of the gravitational self-force were presented by Mino, Sasaki, and Tanaka [162] and also Wald and Quinn [188]. An alternative, but equivalent, description was purposed by Detweiler and Whiting [81]. In the Detweiler-Whiting picture the particle follows a geodesic on $g_{\alpha\beta}^{Sch} + h_{\alpha\beta}^R$, where $h_{\alpha\beta}^R$ is the suitably regularized piece of $h_{\alpha\beta}$. For a detailed discussion of the theoretical and computational developments we point the reader to any of these excellent reviews [179, 21, 217].

Several existing techniques seek to capture self-force effects, thereby incorporat-

ing more realistic inspiral (and possibly plunge) into the model. Some of these approaches include effective one body formulations [77, 174, 168], effective field theory techniques [101, 102], post-Newtonian expansions [31], and adiabatic approximations [207, 209]. Because the metric perturbations are discontinuous at the particle, direct self-force calculations typically require a regularization technique. Mode-sum regularization has been carried out in the Lorenz gauge [22], in an approach where the metric perturbations are described by the full coupled system of 10 PDEs rather than the simpler master equation description developed in this section. In the Regge-Wheeler gauge, for which the metric reconstruction equations (2.39,2.46) hold, no regularization procedure has been proposed for generic orbits; however, direct field-regularization [228, 229] seems promising. For the restricted case of quasi-circular orbits⁸, Detweiler has shown how to calculate certain self-force quantities in the RW gauge [80]. Results based on this description agree with corresponding Lorenz gauge computations [193].

Detweiler’s approach obtains the particle’s energy and angular momentum evolution through local self-force calculations performed at the particle,

$$\dot{E}_p = -\frac{1}{2u_p^t} u_p^\alpha u_p^\beta \frac{\partial h_{\alpha\beta}}{\partial t}, \quad \dot{L}_p = \frac{1}{2u_p^t} u_p^\alpha u_p^\beta \frac{\partial h_{\alpha\beta}}{\partial \phi}, \quad (2.64)$$

where the perturbation $h_{\alpha\beta}$ is reconstructed from (2.39,2.46). These self-force equations have the desirable property of both being gauge independent and smooth at the particle, thus avoiding the need to regularize the discontinuity. When $h_{\alpha\beta} = 0$ we recover the Schwarzschild result that E_p and L_p are constants of motion, while for $h_{\alpha\beta} \neq 0$ neither ∂_t nor ∂_ϕ are Killing vectors of $g_{\alpha\beta}^{Sch} + h_{\alpha\beta}$.

⁸Circular orbits of the Schwarzschild black hole correspond to the condition $u_p^r = 0$. A quasi-circular orbit is one which would be circular if not for self-force effects. Section 4.2.1 discusses orbit classifications in greater detail.

Eqs. (2.64) are the dissipative part of the self-force; energy and angular momentum removed from the system through gravitational radiation is experienced by the particle as an instantaneous force which acts to decrease E_p and L_p . The particle's change in energy and angular momentum is related to the energy luminosity \dot{E}_{GW} and angular momentum luminosity \dot{L}_{GW} simply by [80]

$$\dot{E}_p = \dot{E}_{GW}, \quad \dot{L}_p = \dot{L}_{GW}, \quad (2.65)$$

which also hold for each (ℓ, m) mode of the metric perturbation.

2.5 Splitting Spacetime into Space+Time

This section provides an introductory discussion of the 3+1 decomposition of a 4-dimensional spacetime and the resulting Arnowitt–Deser–Misner (ADM) formulation of Einstein's field equations [16]. The ADM system is the traditional reformulation of the Einstein equations as an initial boundary value problem, and thus provides an important starting point for suitable form for numerical treatment. In particular, the GBSSN system described in Sec. 2.6 is derived directly from the ADM system in Appendix A. Like Einstein's equations themselves, the 3+1 decomposition is naturally geometrical and, thus, this section includes an overview of the important differential geometry material needed. Much of this section draws from [170, 235, 27, 183, 163].

2.5.1 3+1 Decomposition

We begin by assuming our spacetime M admits a foliation into non-intersecting three-surfaces Σ , and that each hypersurface Σ is a level set of a monotonic function τ (see chapter 4 of [170]) whose differential 1-form is

$$\Omega \equiv d\tau = \Omega_\alpha dx^\alpha. \quad (2.66)$$

Although Ω is not normalized to unity

$$|\Omega|^2 = g^{\alpha\beta} \Omega_\alpha \Omega_\beta \equiv -\alpha^{-2}, \quad (2.67)$$

we can build a timelike normal (to the hypersurface) vector

$$n^\alpha \equiv -\alpha g^{\alpha\beta} \Omega_\beta = -\alpha \Omega^\alpha \quad (2.68)$$

such that $n^\alpha n_\alpha = -1$. Our temporal coordinate freedom is encoded by an (as yet) unspecified function α , known as the lapse. With n^α we can form a projection operator $\gamma^\alpha_\beta : T_p M \rightarrow T_p \Sigma$,

$$\gamma^\alpha_\beta \equiv \delta^\alpha_\beta + n^\alpha n_\beta, \quad (2.69)$$

which projects a 4-vector's components onto the hypersurface's 3 dimensional tangent space. Each hypersurface Σ is a submanifold of M , and thus their tangent spaces are related by a direct sum decomposition $T_p M = T_p \Sigma \oplus (T_p \Sigma)^\perp$ [170]. For $V^\alpha \in T_p M$ we have the unique decomposition,

$$V^\alpha = (V^\alpha)^\parallel + (V^\alpha)^\perp, \quad (2.70)$$

where $(V^\alpha)^\parallel \equiv \gamma^\alpha_\beta V^\beta$ and $(V^\alpha)^\perp \equiv -(V^\beta n_\beta) n^\alpha$ are the components parallel and perpendicular to $T_p\Sigma$. For a general tensor all components are projected, for example as

$$(T_{\beta\dots}^{\alpha\dots})^\parallel = \gamma^\alpha_{\alpha'} \gamma^{\beta'}_\beta T_{\beta'\dots}^{\alpha'\dots} \quad (2.71)$$

The metric induced on Σ is simply $g_{\alpha\beta}$ restricted to accept vectors from $T_p\Sigma$. A convenient expression for the induced spatial metric

$$\gamma_{\alpha\beta} = (g_{\alpha\beta})^\parallel = g_{\alpha\beta} + n_\alpha n_\beta \quad (2.72)$$

may be found by projecting.

We now look for a timelike vectorfield t^α which is dual to the 1-form Ω , that is for which $t^\alpha \Omega_\alpha = 1$. As any spatial vector β^α satisfies $\beta^\alpha n_\alpha = 0$, the most general dual vector is of the form

$$t^\alpha = \alpha n^\alpha + \beta^\alpha. \quad (2.73)$$

The particular (yet to be) chosen β^α appearing in Eq. (2.73) is known as the shift vector, and it encodes the spatial coordinate degrees of freedom on each hypersurface. By choosing a set of basis vectors such that the zeroth vector is t^α and the others span $T_p\Sigma$ the components of the normal and shift are

$$\beta^\alpha = (0, \beta^i), \quad n^\alpha = \frac{1}{\alpha}(1, -\beta^i), \quad n_\alpha = (-\alpha, 0, 0, 0). \quad (2.74)$$

By appealing to the projection operator γ^α_β , the effect of our coordinate choice is to typographically convert the indices of all contravariant spatial vectors from Greek

letters to Latin letters. For example,

$$(V^\alpha)^\parallel = \gamma^\alpha_\beta V^\beta = V^\alpha - \alpha n^\alpha V^0 = (0, V^i + \beta^i V^0), \quad (2.75)$$

and so the zeroth component of any spatial contravariant tensor is zero. Hence, we will frequently write only Latin indices on spatial tensors with the understanding that the zeroth (time) component of such tensors is zero.

Our discussion and coordinate choice motivates us to write (see [27] for the construction) the metric as

$$ds^2 = g_{\alpha\beta} dx^\alpha dx^\beta = -(\alpha^2 - \gamma_{ij} \beta^i \beta^j) dt^2 + 2\gamma_{ij} \beta^j dt dx^i + \gamma_{ij} dx^i dx^j, \quad (2.76)$$

where the lapse α , shift β^i , and spatial metric γ_{ij} are precisely the objects previously introduced. One may consider (2.76) as the result of the 3+1 decomposition we have outlined in this subsection. The slices Σ are themselves differential 3-manifolds equipped with the metric γ_{ij} . As a well-defined metric, γ_{ij} is used to raise and lower the components of spatial tensors.

We are almost in a position to take the parallel and perpendicular components of the Einstein equation. First we need to determine how Σ lies in M , that is to say the extrinsic geometry of our foliation.

2.5.2 Extrinsic Geometry of the Foliation

Induced covariant derivative

If $v, w \in T_p\Sigma$, then in general $\nabla_v w \in T_pM$. Consider the unique decomposition $\nabla_v w = (\nabla_v w)^\parallel + (\nabla_v w)^\perp$. Define

$$D_v w \equiv (\nabla_v w)^\parallel, \quad (2.77)$$

then one can show that D is the induced covariant derivative on Σ [170], where we now have induced connection coefficients

$$\Gamma_{jk}^i = \frac{1}{2} \gamma^{il} (\gamma_{lj,k} + \gamma_{lk,j} - \gamma_{jk,l}) \quad (2.78)$$

as well as $D_k \gamma_{ij} = 0$.

Extrinsic curvature

The normal projection $(\nabla_v w)^\perp$ gives us something new – information about how the slices are embedded. Using the Leibniz product rule $v \langle n, w \rangle = \langle \nabla_v n, w \rangle + \langle n, \nabla_v w \rangle = 0$ produces

$$\langle \nabla_v w, n \rangle = - \langle \nabla_v n, w \rangle. \quad (2.79)$$

The Koszul formula for the last term is

$$\begin{aligned}
2 \langle \nabla_v n, w \rangle &= v \langle n, w \rangle + n \langle w, v \rangle - w \langle v, n \rangle \\
&\quad - \langle v, [n, w] \rangle + \langle n, [w, v] \rangle + \langle w, [v, n] \rangle \\
&= n \langle w, v \rangle - \langle v, [n, w] \rangle - \langle w, [n, v] \rangle. \tag{2.80}
\end{aligned}$$

This expression can be recognized as the Leibniz rule for a Lie derivative of the metric,

$$(\mathcal{L}_n \gamma)(v, w) = n \langle v, w \rangle - \langle v, [n, w] \rangle - \langle [n, v], w \rangle. \tag{2.81}$$

Thus the normal projection of the covariant derivative is

$$- \langle \nabla_v w, n \rangle = \frac{1}{2} (\mathcal{L}_n \gamma)(v, w). \tag{2.82}$$

Plugging the coordinate vector fields, $v = \partial_i$ and $v = \partial_j$, into the above expression results in the usual extrinsic curvature tensor, defined here as

$$K_{ij} \equiv -\frac{1}{2} \mathcal{L}_n \gamma_{ij}. \tag{2.83}$$

The extrinsic curvature tensor is sometimes referred to as the “velocity of the spatial metric,” and the tensors $\gamma_{ij}(\Sigma)$ and $K_{ij}(\Sigma)$ characterize each slice of the foliation [235]. What remains is how γ_{ij} and K_{ij} , and thus the slices Σ , evolve.

2.5.3 Arnowitt–Deser–Misner Equations

To facilitate projections of the Einstein equation onto parallel and perpendicular tangent spaces will require the Gauss, Codazzi, and Ricci equations [235, 27]. These

equations cover all possible projections of the Riemannian curvature tensor for M [170], and express the result in terms of the Riemannian curvature tensor for Σ , the extrinsic curvature, and the extrinsic curvature's covariant derivative. We simply state the result (see Refs. [235, 27] for a derivation) in the form of the ADM equations. These are the metric and extrinsic curvature evolution equations as well as Hamiltonian and Momentum constraints.

Eq. (2.83) is the evolution equation for the metric, while one for K_{ij} is found by using Ricci's equation and Einstein's equation (2.16) to give

$$\mathcal{L}_n \gamma_{ij} = -2K_{ij} \tag{2.84a}$$

$$\mathcal{L}_n K_{ij} = -\frac{1}{\alpha} D_i D_j \alpha + (R_{ij} - 2K_{ik} K^k_j + K K_{ij}) - 8\pi \left[S_{ij} - \frac{1}{2} \gamma_{ij} (S - \rho) \right]. \tag{2.84b}$$

We have defined the trace of the extrinsic curvature $K \equiv \gamma^{ij} K_{ij}$, the energy density $\rho \equiv n^\alpha n^\beta T_{\alpha\beta}$, the spatial projection of the stress–energy tensor $S_{ij} \equiv (T_{\alpha\beta})^\parallel$, and its trace $S \equiv \gamma^{ij} S_{ij}$.

The Hamiltonian (momentum) constraint is found by using the Einstein and Gauss (Codazzi) equations

$$\mathcal{H} \equiv R - K_{ij} K^{ij} + K^2 = 16\pi\rho \tag{2.85a}$$

$$\mathcal{M}_i \equiv D_j K^j_i - D_i K = 8\pi j_i, \tag{2.85b}$$

where $j_i \equiv -\gamma^\alpha_i n^\beta T_{\alpha\beta}$.

The ADM evolution equations are (2.84), subject to the constraints (2.85). We have not yet specified the lapse and shift. It is common to prescribe analytic forms

or evolution equations for these. We return to this issue in Sec. 2.6.3.

2.6 The Generalized BSSN Formulation

Early attempts to evolve the Einstein equations relied on the 3+1 decomposition developed in section 2.5. The resulting ADM system (2.5.3) proved only weakly hyperbolic when expressed in first-order form, a fact partly accounting for difficulties associated with its numerical evolution [136, 51]. Difficulties in evolving black hole solutions to the Einstein equations also stem from singularities, gauge conditions within the computational domain, and unstable constraint violation. The goal of accurate and stable numerical integration of the Einstein equations has continuously spurred the interest of numericists and theorists alike, leading to a wealth of new formalisms as in this non-exhaustive list [96, 200, 65, 1, 33, 155, 97, 95, 85, 127, 11, 34, 28, 232, 7, 98, 13, 120, 99, 233, 202, 234, 138, 109, 182, 41, 147, 172].

From the plethora of formalisms, numerical relativists currently use one of the following versions of the Einstein equations: the generalized harmonic (GH) system [93, 109, 182, 147], or the BSSN system [200, 28, 41]. Both the GH and BSSN have had remarkable success thanks to their numerical stability.

Additionally, there are three “flavors” of the BSSN system discussed in the literature: traditional, conformal, and covariant. As the name suggests, the traditional BSSN system (referred to simply as ‘the BSSN system’) was the first and most popular version of the three. Starting with the ADM equations, the BSSN system is constructed by performing a conformal-traceless decomposition of the metric and extrinsic curvature. The conformal metric determinant is set to unity. However,

as discussed in 2.6.2, the traditional system is neither conformal nor covariant, and many of the variables are tensor density weights.

To correct many of these deficiencies Ref. [41] recently purposed modifying the traditional BSSN system by relaxing the condition that the conformal metric's determinant be set to unity. The resulting GBSSN system features conformally invariant equations, and, besides the conformal connection, no tensor density weights. A later work considers a conformal and spatially-covariant (but not fully space-time covariant) BSSN system [43], which evolves BSSN variables relative to a background spacetime.

Apart from parenthetical remarks, this dissertation focuses exclusively on the GBSSN system. There are both practical and theoretical motivations for considering the GBSSN over the traditional system. Our aim is to purpose and study a new numerical method for evolving Einstein's equations (in particular a BSSN-like system), a task most easily accomplished in spherical symmetry. Yet, the traditional BSSN restricts the conformal metric's determinant to unity, and reduction to spherical symmetry is not straightforward (see [64] for a complete derivation). By contrast, in section 6.2 reduction to spherical symmetry is performed by assuming a particular ansatz and carrying out straightforward, although tedious, tensor operations.

In this section we discuss the GBSSN system in detail. The GBSSN variables are introduced with some discussion. Sec. 2.6.3 summarizes the system used in this dissertation along with our choice for gauge evolution equations. Evolution and constraint equations are deduced from the ADM system of equations using tensor analysis in appendix A.

2.6.1 Conformal–Traceless Decomposition and the GBSSN Variables

We begin by introducing the new variables. First we define a conformal spatial metric $\bar{\gamma}_{ij}$ and a conformal factor χ^{-n} as

$$\gamma_{ij} \equiv \chi^{-n} \bar{\gamma}_{ij} \quad \rightarrow \quad \gamma^{ij} = \chi^n \bar{\gamma}^{ij} \quad (2.86)$$

where n is a yet to be specified integer. With this definition the connection coefficients are expressible as

$$\begin{aligned} \Gamma_{jk}^i &= \frac{1}{2} \chi^n \bar{\gamma}^{im} \left[(\bar{\gamma}_{mj} \chi^{-n})_{,k} + (\bar{\gamma}_{mk} \chi^{-n})_{,j} - (\bar{\gamma}_{jk} \chi^{-n})_{,m} \right] \\ &= \bar{\Gamma}_{jk}^i - \frac{n}{2} \chi^{-1} (\delta^i_j \chi_{,k} + \delta^i_k \chi_{,j} - \bar{\gamma}^{im} \bar{\gamma}_{jk} \chi_{,m}) \end{aligned} \quad (2.87)$$

where the conformal connection coefficient has been introduced as

$$\bar{\Gamma}_{jk}^i \equiv \frac{1}{2} \bar{\gamma}^{im} [\bar{\gamma}_{mj,k} + \bar{\gamma}_{mk,j} - \bar{\gamma}_{jk,m}]. \quad (2.88)$$

Using the conformal connection we define the conformal covariant derivative \bar{D}_k , and note that the conformal metric satisfies $\bar{D}_k \bar{\gamma}_{ij} = 0$.

Next we decompose the extrinsic curvature K_{ij} into trace K and traceless \bar{A}_{ij} parts

$$K_{ij} = \chi^{-n} \left(\bar{A}_{ij} + \frac{1}{3} \bar{\gamma}_{ij} K \right), \quad (2.89)$$

which has been written with the conformal variable $\bar{A}_{ij} \equiv \chi^n A_{ij}$.

Finally, we introduce a set of conformal connection functions,

$$\bar{\Gamma}^i \equiv \bar{\gamma}^{jk} \bar{\Gamma}_{jk}^i = -\bar{\gamma}^{-1/2} (\bar{\gamma}^{1/2} \bar{\gamma}^{ij})_{,j} \quad (2.90)$$

and promote these to system variables. Along with the gauge variables α , β^i , and B^i (to be introduced in sec. 2.6.3), we take $\bar{\gamma}_{ij}$, \bar{A}_{ij} , K , $\bar{\Gamma}^i$, and χ as the GBSSN system variables. Indices of conformal variables are raised and lowered with the conformal metric, for example, $\bar{A}_{ij} = \bar{\gamma}_{im} \bar{\gamma}_{jn} \bar{A}^{mn}$.

2.6.2 Interlude: Relationship to Traditional BSSN

We are now in a position to discuss the GBSSN and traditional BSSN systems in greater detail. The characteristic difference is the tensorial type of χ^{-n} in each system. Physical variables γ_{ij} and A_{ij} are rank 2 tensors, whereas the tensorial properties of the conformal variables $\bar{\gamma}_{ij}$ and \bar{A}_{ij} will depend on χ^{-n} .

The traditional BSSN system assumes $\bar{\gamma} = 1$, which is viewed as an additional constraint. In the case of a unit conformal metric determinant we must have $\bar{\gamma}_{ij} = (\gamma)^{-1/3} \gamma_{ij}$, from which $\bar{\gamma} = \det(\gamma^{-1/3} \gamma_{ij}) = \gamma^{-1} \det(\gamma_{ij}) = 1$. As γ is a tensor density of weight 2, $\gamma^{-1/3}$ has a weight of $-2/3$. Thus, in the traditional BSSN system $\chi^{-n} = \gamma^{1/3}$ transforms as a scalar density of weight $2/3$; $\bar{\gamma}_{ij}$ and \bar{A}_{ij} transform as rank 2 tensors of weight $-2/3$.

Alternatively, in the GBSSN system χ^{-n} is introduced as an ordinary scalar, which we solve for by taking the determinant of conformal metric's definition $\chi^{-n} = (\gamma/\bar{\gamma})^{1/3}$. This distinction has three import implications. First, it is obvious from this discussion that both the variables and equations will be (slightly) different. For ex-

ample, terms proportional to $\mathcal{L}_n \ln \bar{\gamma}$ will appear throughout GBSSN (see Sec. 2.6.3), but are absent from traditional BSSN. Second, in GBSSN we must decide how $\bar{\gamma}$ evolves in time. Two natural choices are “Eulerian” and “Lagrangian” conditions [42]. Finally, the GBSSN system contains an additional equation and characteristic field, in particular the principle parts of GBSSN and traditional BSSN are different. Ref. [43, 42, 41] offers a more detailed discussion of these differences.

Although the traditional BSSN system, having arrived first, is more common, GBSSN is easier to work with as nearly all system variables are tensors with no density weight. Furthermore, removing the restriction of a unit conformal determinant could lead to a more robust system. Modern BSSN codes impose the unity condition by making the replacement $\bar{\gamma}_{ij} \rightarrow \bar{\gamma}_{ij} \bar{\gamma}^{-1/3}$ throughout the evolution. There are indications that this brute force approach of imposing constraints could spoil the numerical stability for spectral codes [167], however, a detailed understanding is still lacking. In our case, GBSSN is particularly useful as it permits a direct reduction to “spherical” coordinates.

2.6.3 GBSSN System

The GBSSN evolution equations can be derived by differentiating the system variables of Sec. 2.6.1 and using the ADM equations (2.84) and constraints (2.85). This program is carried out in Appendix A. The resulting equations must be supplemented with equations which specify how the gauge variables evolve. We will use the “1+log” and “T-driver” conditions [6] which have been employed in nearly all stable binary black hole evolutions [82, 206, 119, 52, 26, 53]. With this choice in mind, and setting the conformal factor exponent to $n = 1$, we will often refer of *the*

GBSSN system without ambiguity:

$$\mathcal{L}_n \alpha = -2K \quad (2.91a)$$

$$\mathcal{L}_n \beta^i = \frac{3}{4\alpha} B^i \quad (2.91b)$$

$$\hat{\partial}_0 B^i = \hat{\partial}_0 \bar{\Gamma}^i - \eta B^i \quad (2.91c)$$

$$\mathcal{L}_n \chi = \frac{\chi}{3} (\mathcal{L}_n \ln \bar{\gamma} + 2K), \quad (2.91d)$$

$$\mathcal{L}_n \bar{\gamma}_{ij} = \frac{1}{3} \bar{\gamma}_{ij} \mathcal{L}_n \ln \bar{\gamma} - 2\bar{A}_{ij}, \quad (2.91e)$$

$$\mathcal{L}_n K = -\frac{1}{\alpha} D^2 \alpha + \left(\bar{A}_{ij} \bar{A}^{ij} + \frac{1}{3} K^2 \right) + 4\pi (S + \rho), \quad (2.91f)$$

$$\mathcal{L}_n \bar{A}_{ij} = \frac{1}{3} \bar{A}_{ij} \mathcal{L}_n \ln \bar{\gamma} + K \bar{A}_{ij} - 2\bar{A}_{ik} \bar{A}^k{}_j + \chi \left(R_{ij} - \frac{1}{\alpha} D_i D_j \alpha - 8\pi S_{ij} \right)^{\text{TF}} \quad (2.91g)$$

$$\begin{aligned} \hat{\partial}_0 \bar{\Gamma}^i &= -\frac{1}{3} \bar{\Gamma}^i \hat{\partial}_0 \ln \bar{\gamma} - \frac{1}{6} \bar{\gamma}^{ij} \partial_j \hat{\partial}_0 \ln \bar{\gamma} - 2\bar{A}^{ij} \partial_j \alpha \\ &\quad - 2\alpha \left[8\pi \chi^{-1} j^i - \bar{A}^{jk} \bar{\Gamma}^i{}_{jk} + \frac{3}{2} \chi^{-1} \bar{A}^{ij} \partial_j \chi + \frac{2}{3} \bar{\gamma}^{ij} \partial_j K \right], \end{aligned} \quad (2.91h)$$

where $\hat{\partial}_0 = \alpha \mathcal{L}_n = \partial_t - \mathcal{L}_\beta$. A damping parameter η and auxiliary field B^i have been introduced. Motivations for these choices are discussed in [6].

Instead of imposing $\bar{\gamma} = 1$ as in the traditional BSSN system, we must specify how the conformal determinant evolves. Our particular choice, coined the ‘‘Lagrangian condition’’ in [41], specifies $\partial_t \ln \bar{\gamma} = 0$. Accordingly, throughout system (2.91) the following replacements are made $\hat{\partial}_0 \ln \bar{\gamma} \rightarrow -2\bar{D}_i \beta^i$.

In addition to the ADM Hamiltonian and momentum constraints (2.85), a new constraint arises from the introduction of conformal connection functions. System

(2.91) must satisfy

$$\mathcal{H} = R - \bar{A}_{ij}\bar{A}^{ij} + \frac{2}{3}K^2 = 16\pi\rho \quad (2.92a)$$

$$\mathcal{M}^k = D_j A^{jk} - \frac{2}{3}\gamma^{ki}D_i K = 8\pi j^k \quad (2.92b)$$

$$\mathcal{G}^i = \bar{\Gamma}^i - \bar{\gamma}^{jk}\bar{\Gamma}_{jk}^i. \quad (2.92c)$$

Along with the GBSSN evolution equations these are derived in Appendix A. Note that \mathcal{M}^k , which features both the physical spatial metric and covariant derivative, is expressed entirely with GBSSN system variables by Eq. A.9.

CHAPTER THREE

The Discontinuous Galerkin Method for Hyperbolic PDEs

3.1 Introduction

In the last chapter we encountered the relevant PDEs to be solved. This chapter develops the necessary tools to accomplish this task. In particular, we will discuss properties of hyperbolic PDEs and develop the basic building blocks of a nodal dG scheme for such systems. We begin by briefly introducing some definitions and terminology in Sec. 3.1.1. Section 3.2 defines the concept of strongly hyperbolic systems for a variety of PDEs while commenting on the the hyperbolicity of our RWZ and GBSSN systems. The importance of well-posedness at both the continuous and discrete level is noted, and an extended discussion of stability for strongly hyperbolic systems is given. A nodal dG scheme is then proposed for a strongly hyperbolic toy PDE system in Sec. 3.3. The model PDE is simple enough as to not obfuscate the dG construction while also being sufficiently realistic that the discretization procedure is directly applicable to our problems of interest. Problem specific choices, such as the numerical flux form and treatment of second order spatial operators, are delayed for future chapters.

3.1.1 Notation, Norms, and Geometry

We suppose our physical domain Ω is the closed interval $[a, b] \in \mathbb{R}^1$. We cover Ω with $K > 1$ non-overlapping intervals $\mathcal{D}^k = [a^k, b^k]$, where $a = a^1$, $b = b^K$, and $b^{k-1} = a^k$ for $k = 2, \dots, K$. The *computational domain* Ω_h is defined by the union

$$\Omega \simeq \Omega_h = \bigcup_{k=1}^K \mathcal{D}^k \tag{3.1}$$

over *subdomains* D^k . To succinctly represent the different domains let D be a placeholder for any of the three regions Ω , Ω_h , or D^k .

For any two square integrable functions $f, g : D \subset \mathbb{R}^1 \rightarrow \mathbb{R}^1$ define the L_2 inner product and norm on D by

$$(f, g)_D = \int_D fg dx, \quad \|f\|_D = \sqrt{(f, f)_D}, \quad (3.2)$$

and x is a spatial coordinate on D . When $D = \Omega_h$ these are referred to as the global broken inner product and norm

$$(f, g)_{\Omega_h} = \sum_{k=1}^K \int_{D^k} fg dx, \quad \|f\|_{\Omega_h} = \sqrt{(f, f)_{\Omega_h}}. \quad (3.3)$$

For any bounded function $f : D \subset \mathbb{R}^1 \rightarrow \mathbb{R}^1$ define the L_∞ norm

$$\|f\|_\infty = \max_{x \in D} |f(x)|, \quad (3.4)$$

which could be measured in $L_\infty(\Omega)$, $L_\infty(D^k)$, or $L_\infty(\Omega_h)$.

Sometimes we will work with vectors built from scalars. For any two square integrable column vectors $f, g : D \subset \mathbb{R}^1 \rightarrow \mathbb{R}^n$ define an inner product and norm on D componentwise

$$(f, g)_D = \int_D f^T g dx, \quad \|f\|_D = \sqrt{(f, f)_D}, \quad (3.5)$$

where f^T denotes the transpose of f .

3.2 Hyperbolic PDEs and Stability

Perhaps the most prominent example of a hyperbolic PDE is the wave equation $-\partial_t^2 u + \partial_x^2 u = 0$. The solutions describe information, or energy, moving along a given direction. For example, according to d'Alembert's formula, a solution to our wave equation may always be written as a sum of left and right traveling waves of a fixed shape $u(t, x) = F(x - t) + G(x + t)$, where F and G can be expressed in terms of initial data [113].

A general definition of hyperbolicity can be motivated as follows. Consider the initial value problem

$$\begin{aligned}\partial_t W &= AW' + B(t, x)W + S(t, x), \\ W(0, x) &= \hat{W}(x),\end{aligned}\tag{3.6}$$

where the prime stands for differentiation with respect to the spatial variable x , W is a column vector of length n , and A is an n -by- n matrix. Furthermore, assume the appropriate boundary conditions are supplied. The matrices B and S denote potential and inhomogeneous source terms respectively, and the *principle part* of (3.6) is identified by neglecting exactly these terms. System (3.6) is called *strongly hyperbolic* if the eigenvalues λ_i of A are all real and there exists a complete basis of eigenvectors [112]. For such systems A is diagonalizable $S^{-1}AS = \Lambda$ for an invertible matrix S and diagonal matrix Λ . Now define a column vector of *characteristic variables* $V \equiv S^{-1}W$ to express principle part of system (3.6) as

$$\begin{aligned}\partial_t V &= \Lambda V', \\ V(0, x) &= \hat{V}(x) = S^{-1}\hat{W}.\end{aligned}\tag{3.7}$$

Then, like the usual wave equation, the solution's components $V_i = \hat{V}_i(\lambda_i t + x)$ describe traveling waves of a fixed shape.

Extending the definition of strong hyperbolicity to a quasi-linear variable coefficient system is surprisingly straightforward. Consider the following initial value problem

$$\begin{aligned}\partial_t W &= A(t, x, W)W' + B(t, x, W)W + S(t, x), \\ W(0, x) &= \hat{W}(x),\end{aligned}\tag{3.8}$$

where the matrix $A(t, x, W)$ and solution W depend smoothly on their arguments, and appropriate boundary conditions have been supplied. System (3.8) is called strongly hyperbolic at a fixed (t_0, x_0) and W_0 if the eigenvalues of $A(t_0, x_0, W_0(t_0, x_0))$ are all real and there exists a complete basis of eigenvectors [112]. This criteria, which is employed in our analysis of the GBSSN system, is carried out as linearization followed by localization. We proceed with an example. Suppose $W_0(t, x)$ is a solution to system (3.8) and write

$$W(t, x) = W_0(t, x) + \epsilon w(t, x),\tag{3.9}$$

where $\epsilon \ll \|W_0(t, \cdot)\|_\infty$. Schematically, the perturbations satisfy a linear system

$$\epsilon \partial_t w = \epsilon A(t, x, W_0)w' + O(\epsilon^2) + (\text{Lower Order}),\tag{3.10}$$

where ‘Lower Order’ stands for all terms which are $O(\epsilon)$, but do not feature w' .

The principle part

$$\partial_t w = A(t, x, W_0)w',\tag{3.11}$$

is then analyzed with a localization principle [196]. Let $\hat{A}(t, x) = A(t, x, W_0)$ and perform a coordinate transformation $t = t_0 + \delta T$ and $x = x_0 + \delta X$ such that

$$\begin{aligned} w^\delta(T, X) &= w(t_0 + \delta T, x_0 + \delta X), \\ \partial_T w^\delta &= \hat{A}(t_0 + \delta T, x_0 + \delta X) \partial_X w^\delta, \end{aligned} \tag{3.12}$$

where x_0 and t_0 are the “frozen” coordinates and δ is a parameter. Taking the pointwise limit of $\delta \rightarrow 0$ results in

$$\partial_T w^\delta = \hat{A}(t_0, x_0) \partial_X w^\delta. \tag{3.13}$$

For a fixed point in space and time the principle part of system (3.8) linearized around W_0 reduces to a constant coefficient system of the form (3.6). Thus, in the limit $(\delta, \epsilon) \rightarrow 0$ the notion of strong hyperbolicity for a quasi-linear system (3.8) coincides with the constant coefficient case¹. Applying this criteria to a continuous range of solutions and coordinates identifies a region (t, x, W) of strong hyperbolicity.

A larger class of problems, which includes the GBSSN system, are given by

$$\begin{aligned} \partial_t W &= A(t, x, W)W'' + B(t, x, W, W')W' + C(t, x, W)W + S(t, x), \\ W(0, x) &= \hat{W}(x). \end{aligned} \tag{3.14}$$

These are second order in space first order in time PDEs where we continue to assume all matrices and solutions depend smoothly on their arguments. A straightforward extension of the aforementioned hyperbolicity discussion to the second order system (3.14) is achieved by considering possible (non-unique) *first order reductions*. As an initial attempt at first order reduction we define new fields $Q = W'$, which evolve

¹Our definition is sometimes referred to as *pointwise strongly hyperbolic* (see chapter 3 of Ref. [140] for a complete discussion).

according to $\partial_t Q = (\partial_t W)'$, and study the hyperbolicity of the enlarged system. If the enlarged (Q, W) system is strongly hyperbolic according to a previous definition, then system (3.14) is strongly hyperbolic provided that auxiliary constraints $Q = W'$ are satisfied. Refs. [140, 100, 110, 111] further discuss the concept of hyperbolicity in the context of second order systems.

From the preceding discussion we conclude that the RWZ equations are strongly hyperbolic, a first order reduction is explicitly presented in Sec. 4.2.6. Although Einstein's equation is not written in a form which is manifestly hyperbolic, in Chapter 2 we constructed an enlarged first order in time second order in space GBSSN system. Strong hyperbolicity of the spherically symmetric GBSSN system is demonstrated in Sec. 6.2.3. Gravitational waves impinging on the Earth are described by a wave equation for the tensor field perturbation (2.18), another strongly hyperbolic system.

We have defined strong hyperbolicity for constant coefficient, variable coefficient, quasi-linear, and second order systems. Why is it useful to know if an initial value problem is strongly hyperbolic²? There are a few important reasons for doing this. Before trying to solve an initial value problem it would be useful to know if such an undertaking makes sense. The problem is *well-posed* if it does. We say that the quasi-linear first order spatial system (3.8) is well-posed if [87, 112]:

1. The problem has a solution
2. The solution is unique
3. For constants α and K independent of initial data \hat{W} the solution's norm is bounded by the norm of the initial data as

²Further classifications of hyperbolicity may play an important role in a rigorous analysis, but will not be discussed here. As the primary focus of this dissertation is computational, our approach to hyperbolicity is one of practicality.

$$\|W(t, \cdot)\|_{\Omega} \leq Ke^{\alpha t} \|\hat{W}(\cdot)\|_{\Omega}. \quad (3.15)$$

We will always assume that a unique solution W exists. Condition (3) is known as *stability* and it demands that small changes to the initial data do not lead to large changes in the solution. Showing an initial value problem is strongly hyperbolic constitutes significant progress towards a stability bound; 1) a strongly hyperbolic linear PDE system in 1D is stable [140], and 2) for a non-linear system strong hyperbolicity at W_0 is often a necessary condition [112]. Additionally, the second order system (3.14) is well-posed if it admits a first order reduction which is well-posed and auxiliary constraints $Q = W'$ are satisfied. A stability bound for second order systems might feature those auxiliary variables Q which arise from the first order reduction [111].

Stability bounds play an essential role at both the continuum and discrete level. When constructing a stable numerical scheme it is important to understand semi-discrete stability, that is can we find a bound of the form (3.15) where the temporal coordinate is continuous and the spatial operator has been discretized. For a dG method the numerical flux, to be introduced in the next section, is intimately linked to the scheme's semi-discrete stability. A good choice of numerical flux is often informed by the system's characteristic variables and speeds, and for a wide class of problems the correct choice is known. But for GBSSN system a numerically stable choice is not obvious, and we rely upon both hyperbolicity and stability arguments while discretizing the GBSSN system.

Beyond considerations of stability, hyperbolicity may be important in other aspects of the numerics too. For example, the largest stable timestep scales with the maximum wavespeed of the system. When treating the RWZ equations, knowledge of the characteristic fields at the particle's location allows the correct jump information

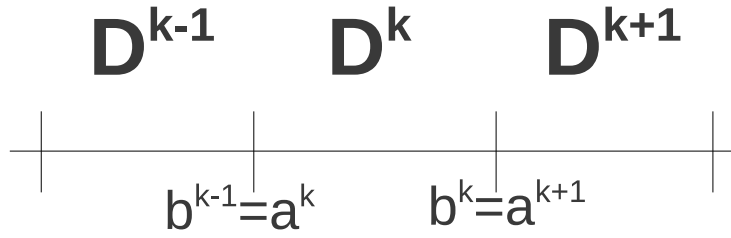


Figure 3.1: TREATMENT OF THE PHYSICAL GEOMETRY FOR A TYPICAL DG SCHEME. Subdomain D^k and its neighbors are shown.

implied by the δ -like singularity to be enforced.

3.3 A Nodal Discontinuous Galerkin Method

Following Refs. [121, 89, 91], this section develops a nodal discontinuous Galerkin method. Ultimately, we adopt a method-of-lines strategy, and here describe the relevant semi-discrete scheme which arises upon spatial approximation by the dG method. Temporal integration may then be carried out with a suitable ordinary differential integrator. DG methods incorporate and build upon finite-element, finite-volume and spectral methods, and in this section the reader will recognize the features our dG approach shares with these more traditional methods. For example, on each subdomain our approach features an integral formulation of Legendre collocation, and our technique for coupling subdomains draws on finite-volume methods. This section will focus on the practical elements which are applicable to both the GBSSN and RWZ systems, as well as on the properties of the scheme and general considerations.

3.3.1 Basic Ingredients of the Scheme

We began building our scheme back in Sec. 3.1.1 by defining a computational domain Ω_h as a collection of subdomains (sometimes called elements) D^k . Upon closer inspection, notice that we have significant freedom in choosing each D^k ; the only constraint is that our physical domain is covered and the boundaries of subdomains overlap. In general, the process of building Ω_h from Ω is *unstructured*.

In what follows let the variable coefficient initial value problem³

$$\begin{aligned}\partial_t W &= \Lambda(t, x)W', \\ W(0, x) &= \hat{W}(x),\end{aligned}\tag{3.16}$$

serve as a representative example for the nodal dG construction. W is a column vector of length n and Λ an n -by- n smooth diagonal matrix. Assume the system is strongly hyperbolic and each diagonal entry $\lambda_i(t, x)$ of Λ is real for all spacetime points considered.

On each subdomain D^k , we approximate each component of the system vector $W_i = \Psi$ by a local interpolating polynomial of degree N . For example,

$$\Psi_h^k(t, x) = \sum_{j=0}^N \Psi(t, x_j^k) \ell_j^k(x)\tag{3.17}$$

³Pedagogical treatments of dG often focus on systems in conservative form $\partial_t W = (\Lambda(t, x)W)'$. However, our problems of interest are given on non-conservative form and so we find this system to be of greater practical value.

approximates Ψ , where $\ell_j^k(x)$ is the j th Lagrange polynomial belonging to \mathbf{D}^k ,

$$\ell_j^k(x) = \prod_{\substack{i=0 \\ i \neq j}}^N \frac{x - x_i^k}{x_j^k - x_i^k}. \quad (3.18)$$

Evidently, the polynomial Ψ_h^k interpolates Ψ at the x_j^k . Throughout this dissertation, approximations are denoted by a subscript h . To define the nodes x_j^k , consider the affine mapping from the unit interval $[-1, 1]$ to \mathbf{D}^k ,

$$x^k(u) = a^k + \frac{1}{2}(1+u)(b^k - a^k), \quad (3.19)$$

and the $N+1$ Legendre–Gauss–Lobatto (LGL) nodes u_j . The u_j are the roots of the equation

$$(1 - u^2)P'_N(u) = 0, \quad (3.20)$$

where $P_N(u)$ is the N th degree Legendre polynomial, and the physical nodes are simply $x_j^k = x^k(u_j)$. In vector notation the approximation (3.17) takes the form

$$\Psi_h^k(t, x) = \mathbf{\Psi}^k(t)^T \boldsymbol{\ell}^k(x), \quad (3.21)$$

in terms of the column vectors

$$\mathbf{\Psi}^k(t) = [\Psi(t, x_0^k), \dots, \Psi(t, x_N^k)]^T, \quad \boldsymbol{\ell}^k(x) = [\ell_0^k(x), \dots, \ell_N^k(x)]^T. \quad (3.22)$$

An approximation W_h^k of the full system vector W is achieved by applying the above construction componentwise, with Ψ being the i^{th} component. Thus the column vector

$$\mathbf{W}^k(t) = [\mathbf{W}_1^k(t)^T, \dots, \mathbf{W}_n^k(t)^T]^T \quad (3.23)$$

contains $n(N + 1)$ degrees of freedom for which to be solved. The global solution

$$W_h(t, x) = \bigoplus_{k=1}^K W_h^k(t, x) \quad (3.24)$$

is obtained by direct sum.

On each open interval $(a^k, b^k) \subset \mathbf{D}^k$ and for each component of the equations in (3.16), we define local residuals measuring the extent to which our approximations satisfy the original continuum system. Dropping the subdomain label k on the polynomials and continuing with Ψ as a representative example, the local residual is

$$(R_\Psi)_h^k \equiv \partial_t \Psi_h - (\lambda_i \Psi')_h. \quad (3.25)$$

Here, for example, the second term reads⁴

$$(\lambda_i \Psi')_h = (\lambda_i)_h \partial_x \Psi_h, \quad (3.26)$$

and derivatives may be analytically computed by Eq. (3.18).

Recall the definition of a local inner product and consider the following expression $(\ell_j^k, (R_\Psi)_h^k)_{\mathbf{D}^k}$. Namely, the inner product between a residual and the j th Lagrange polynomial on \mathbf{D}^k . We call the requirement that this inner product vanish $\forall j$ the k th *Galerkin condition*. For each component of the system and for each k there is a corresponding Galerkin condition. We have achieved a spatial discretization of system (3.16), and in total there are $nK(N + 1)$ ordinary differential equations to be solved.

⁴ At this stage the expression is generically a polynomial of degree $2N - 1$. The conventions adopted in Eq. (3.25) prove useful while working with the residual. However, to obtain the final form of the numerical approximation we will ultimately replace all terms with degree- N polynomials.

Enforcement of the Galerkin conditions on each \mathbf{D}^k will not recover a meaningful global solution, since they provide no mechanism for coupling of the individual local solutions on the different intervals. Borrowing from the finite volume toolbox, we achieve coupling through integration by parts on x and introduction of the numerical flux at the interface between subdomains. Using integration by parts, we write

$$(\ell_j^k, (R_\Psi)_h^k)_{\mathbf{D}^k} = \int_{a^k}^{b^k} dx [\ell_j^k \partial_t \Psi_h^k + \ell_j^{k'} (\lambda_i \Psi)_h^k] - [(\lambda_i \Psi)_h^k] \ell_j^k \Big|_{a^k}^{b^k}, \quad (3.27)$$

where we have suppressed the coordinate dependence in all terms on the righthand side. In lieu of (3.27) with $(\ell_j^k, (R_\Psi)_h^k)_{\mathbf{D}^k} = 0$, we enforce the equation

$$(\ell_j^k, (R_\Psi)_h^k)_{\mathbf{D}^k} = \int_{a^k}^{b^k} dx [\ell_j^k \partial_t \Psi_h^k + \ell_j^{k'} (\lambda_i \Psi)_h^k] - (\lambda_i \Psi)^* \ell_j^k \Big|_{a^k}^{b^k}. \quad (3.28)$$

This equation features a numerical flux, $(\lambda_i \Psi)^*$, rather than the physical boundary flux, $(\lambda_i \Psi)_h^k$. We will often write the numerical flux without labels k and h for convenience. The numerical fluxes are determined by (as yet not chosen) functions

$$(\lambda_i \Psi)^* = (\lambda_i \Psi)^* ((\lambda_i \Psi)_h^+, (\lambda_i \Psi)_h^-) \quad (3.29)$$

where, for example, $(\lambda_i \Psi)_h^-$ is an interior boundary value [either $(\lambda_i \Psi)_h^k(t, a^k)$ or $(\lambda_i \Psi)_h^k(t, b^k)$] of the approximation defined on \mathbf{D}^k , and $(\lambda_i \Psi)_h^+$ is an exterior boundary value [either $(\lambda_i \Psi)_h^{k-1}(t, b^{k-1})$ or $(\lambda_i \Psi)_h^{k+1}(t, a^{k+1})$] of the approximation defined on either \mathbf{D}^{k-1} or \mathbf{D}^{k+1} . Choosing a functional form for $(\lambda_i \Psi)^*$ will couple adjacent subdomains and enforce semi-discrete stability, and is problem specific. Numerical flux expressions frequently feature the numerical average and jump defined at each subdomain interface, for example

$$\{\{\Psi\}\} = \frac{1}{2}(\Psi^+ + \Psi^-), \quad [[\Psi]]_{\mathbf{n}} = \mathbf{n}^+ \Psi^+ + \mathbf{n}^- \Psi^-. \quad (3.30)$$

Here $\mathbf{n}^-(\mathbf{n}^+)$ is the local outward pointing normal to the interior (exterior) subdomain and can be ± 1 . The numerical jump is not a predetermined analytical jump as defined in Eq. (4.21), and it has a different sign convention.

Returning to Eq. (3.28), we now employ an additional integration by parts to arrive at the integral statement

$$\int_{a^k}^{b^k} dx [\partial_t \Psi_h^k - (\lambda_i \Psi'_h)^k] \ell_j^k - [(\lambda_i \Psi)^* - (\lambda_i \Psi)_h] \ell_j^k \Big|_{a^k}^{b^k} = 0 \quad \forall j. \quad (3.31)$$

We refer to the dG scheme in weak (3.28) or strong (3.31) form to indicate if one or two integration by parts have been taken.

Remark: The term ‘nodal discontinuous Galerkin’ should now be clear. We seek a global discontinuous solution interpolated at nodal points and demand this solution satisfy a set of integral (Galerkin) conditions.

Let us now write the $N+1$ equations (3.31) in matrix form. To write down the matrix form, we first introduce the k th *mass* and *stiffness* matrices,

$$M_{ij}^k = \int_{a^k}^{b^k} dx \ell_i^k(x) \ell_j^k(x), \quad S_{ij}^k = \int_{a^k}^{b^k} dx \ell_i^k(x) \ell_j^{k'}(x). \quad (3.32)$$

These matrices belong to \mathbf{D}^k , and the corresponding matrices belonging to the reference interval $[-1, 1]$ are

$$M_{ij} = \int_{-1}^1 du \ell_i(u) \ell_j(u), \quad S_{ij} = \int_{-1}^1 du \ell_i(u) \ell_j'(u), \quad (3.33)$$

where $\ell_j(u)$ is the j th Lagrange polynomial determined by the LGL nodes u_j on $[-1, 1]$. These matrices are related by $M_{ij}^k = \frac{1}{2}(b^k - a^k)M_{ij}$ and $S_{ij}^k = S_{ij}$, whence only the reference matrices require computation and storage.

We will use the matrices M^k and S^k in obtaining an ODE system from (3.31). Towards this end, we first approximate products of polynomials, for example $(\lambda_i \Psi)_h^k$, by degree- N interpolating polynomials. Such approximations are achieved through pointwise representations in the following way (cf. footnote 4):

$$(\lambda_i \Psi)_h^k = (\lambda_i)_h^k \Psi_h^k \rightarrow \sum_{j=0}^N \lambda_i(t, x_j^k) \Psi(t, x_j^k) \ell_j^k(x). \quad (3.34)$$

Note that the expressions on the right and left are not equivalent due to aliasing error [124], and in Sec. 6.3.3 an exponential filter is introduced to control aliasing driven instability. Vector notation for this replacement will be

$$(\lambda_i \Psi)_h^k \rightarrow (\boldsymbol{\lambda}_i \boldsymbol{\Psi})_h(t)^T \boldsymbol{\ell}^k(r). \quad (3.35)$$

The dependence on coordinates has been retained on the right-hand side for clarity, but it is already awkward for this simple expression and will often be omitted. Operations among bold variables are always performed pointwise.

Carrying out the integrations in (3.31), which bring in M^k and S^k , we arrive at

$$\partial_t \boldsymbol{\Psi} = \boldsymbol{\lambda}_i D \boldsymbol{\Psi} + M^{-1} \boldsymbol{\ell}^k [(\lambda_i \Psi)^* - (\lambda_i \Psi)_h] \Big|_{a^k}^{b^k}, \quad (3.36)$$

where we have again suppressed the superscript k on all terms except $\boldsymbol{\ell}^k(r)$, and the subscript h is dropped on all boldfaced variables. As described in [121], the spectral collocation derivative matrix

$$(D^k)_{ij} = \left. \frac{d\ell_j^k}{dr} \right|_{x=x_i^k} \quad (3.37)$$

can also be expressed as $D^k = (M^k)^{-1} S^k$, which appears in (3.36). The remaining

semi-discrete evolution equations are similarly obtained.

3.3.2 Properties of the Proposed DG Scheme

Convergence and Error Estimates

To conclude the section we provide theoretical error estimates for our method. First, we invoke a slight change of viewpoint. Notice that the integral statement (3.31) is equivalent to finding a $\Psi_h^k \in V_N^k$ such that

$$\int_{a^k}^{b^k} dx [\partial_t \Psi_h^k - (\lambda_i \Psi')_h^k] v - [(\lambda_i \Psi)^* - (\lambda_i \Psi)_h] v \Big|_{a^k}^{b^k} = 0 \quad \forall v \in V_N^k. \quad (3.38)$$

Here V_N^k is the space of degree N polynomials defined on \mathbf{D}^k . Additionally, instead of approximating Ψ through interpolation (3.17) we now approximate it as a sum over a collection of Legendre polynomials which spans V_N^k . Under an affine mapping of \mathbf{D}^k to the unit reference interval $[-1, 1]$, appropriately normalized Legendre polynomials $P_n(u)$ form an orthonormal basis and we write

$$\Psi_{\text{Leg}}^k(t, u) = \sum_{i=0}^N a_n^k(t) P_n(u), \quad a_n^k(t) = \int_{-1}^1 \Psi P_n(u) du. \quad (3.39)$$

Appealing to the properties of P_n one can show the approximation error for a sufficiently smooth Ψ is given by [121]

$$\|\Psi - \Psi_{\text{Leg}}^k\|_{\mathbf{D}^k} \leq C(t) (h_k)^{N+1}, \quad (3.40)$$

where h_k is the length of \mathbf{D}^k . We see that the error decays exponentially with N , this property is often referred to as *spectral* convergence. However, our scheme's basis

functions are Lagrange interpolating polynomials. The Lebesgue constant

$$\Lambda = \max_{u \in [-1,1]} \sum_{i=0}^N |\ell_j(u)| \quad (3.41)$$

is a useful measure of interpolation error. If Ψ is the analytic function, Ψ_{Leg}^k it's expansion in Legendre polynomials, and Ψ_h^k the interpolation of Ψ_{Leg}^k , we can form a bound [121]

$$\|\Psi - \Psi_h^k\|_{\infty} \leq (1 + \Lambda) \|\Psi - \Psi_{\text{Leg}}^k\|_{\infty}. \quad (3.42)$$

Λ depends only on the chosen set of nodal points through the definition of ℓ_j (3.18), and the LGL set (3.20) minimizes Λ [121]. With this choice interpolation error remains small and we continue to expect convergence like

$$\|\Psi - \Psi_h^k\|_{\mathbb{D}^k} \leq \hat{C}(t) (h_k)^{N+1}. \quad (3.43)$$

CHAPTER FOUR

Extreme Mass Ratio Binaries

4.1 Introduction

An extreme mass ratio binary (EMRB) is a system comprised of small mass- m_p “particle” (possibly a main sequence star, neutron star, or stellar mass black hole) orbiting a large mass- M black hole, where the mass ratio $\mu = m_p/M \ll 1$. EMRB systems are expected to emit gravitational radiation in a low frequency band (10^{-5} to 10^{-1} Hz), and therefore offer the promise of detection by the joint NASA-ESA LISA project [169, 126]. A standard method for studying some EMRBs uses the perturbation theory of Schwarzschild black holes in an approximation which treats the particle as point-like and responsible for generating small metric perturbations which radiate away to infinity. These perturbations influence the trajectory of particle, resulting in deviation from geodesic motion. Nevertheless, as a first and useful approximation, one may compute the emitted gravitational radiation, assuming that the particle worldline is a timelike geodesic in the Schwarzschild spacetime.

For the scenario we consider, simulation of ERMBs entails numerical evolution of Schwarzschild perturbations. We now give a brief and unified summary of the main results from Sec. 2.4. Consider a small perturbation $h_{\alpha\beta}$ of the background Schwarzschild metric in standard coordinates, and the perturbation satisfies the linearized Einstein equation. The perturbation naturally decomposes into polar and axial parity sectors for each (ℓ, m) harmonic mode $h_{\alpha\beta}^{\ell m} = h_{\alpha\beta}^{\ell m, P} + h_{\alpha\beta}^{\ell m, A}$. Each parity sector can be reconstructed from a collection of scalar master functions. Both the polar and axial master functions are governed by forced scalar wave equations with

the following form generic form:¹

$$-\partial_t^2 \Psi_{\ell m} + \partial_x^2 \Psi_{\ell m} - V_\ell(r) \Psi_{\ell m} = f(r) [G_{\ell m}(t, r) \delta(r - r_p(t)) + F_{\ell m}(t, r) \delta'(r - r_p(t))]. \quad (4.1)$$

The coordinates here are the areal radius r , the Regge–Wheeler tortoise coordinate $x = r + 2M \ln(\frac{1}{2}r/M - 1)$, the time–dependent radial location $r_p(t)$ of the particle, and $f(r) = 1 - 2M/r$. In our scenario the stress–energy tensor $T_{\mu\nu}$ given in (2.28) corresponds to a material point particle, and is therefore a distribution. The distributional inhomogeneity on the right–hand side of (4.1) stems from $T_{\mu\nu}$, and it involves Dirac delta functions, as well as the ordinary functions $F_{\ell m}(t, r)$, $G_{\ell m}(t, r)$. The polar case corresponds to the Zerilli potential (2.38) and the Zerilli–Moncrief master function Ψ^{ZM} (2.37). The axial case corresponds to the Regge–Wheeler potential (2.45) and the Cunningham–Price–Moncrief master function Ψ^{CPM} (2.44).

A number of numerical methods for solving (4.1) as an initial boundary value problem, and therefore modeling EMRBs in the time–domain, have appeared in the literature. In particular, we note Lousto’s fourth–order algorithm [153] based on spacetime integration of (4.1) and careful Taylor series arguments, and Sopena and Laguna’s adaptive finite–element approach [204]. Jung, Khanna, and Nagle have applied a spectral collocation method to the perturbation equations for head–on collisions, using spectral filtering to handle the delta function terms [134] and a finite–difference domain at the outer boundary to reduce artificial boundary reflection [61]. To accelerate self–force computations Thornburg has proposed a finite

¹ We could instead work with the equation

$$-\partial_t^2 \Psi_{\ell m} + \partial_x^2 \Psi_{\ell m} - V_\ell(r) \Psi_{\ell m} = \mathcal{G}_{\ell m}(t) \delta(r - r_p(t)) + \mathcal{F}_{\ell m}(t) \delta'(r - r_p(t)),$$

where $\mathcal{G}_{\ell m}(t)$ and $\mathcal{F}_{\ell m}(t)$ depend only on t , and not on r . The relationships between $\mathcal{G}_{\ell m}(t)$ and $\mathcal{F}_{\ell m}(t)$ and our $G_{\ell m}(t, r)$ and $F_{\ell m}(t, r)$ follows from comparison between the right–hand sides of Eq. B.1 and the last equation.

difference method with Berger-Oliger adaptive mesh refinement [218, 216], and Vega, Diener, and Tichy are exploring a full 3+1 finite difference code [229]. Canizares and Sopuerta have proposed a multidomain spectral collocation method, with the particle location chosen between spectral elements [56, 58].

Clearly, the key difficulty to overcome is the distributional forcing; however, the problem should be amenable to a high-order accurate method, since —apart from possible transients— the solutions we seek to compute are everywhere smooth, except for jump discontinuities at the particle location. As a suitable high-order scheme for solving (4.1), we propose a dG method, and our approach shares some similarities with Refs. [204, 134, 56], in particular we also ensure that the particle always lies at the interface between domain intervals. Improving upon low-order methods, our method achieves *pointwise* spectral accuracy (see also Refs. [56, 58] which consider a scalar charged particle), in particular at the particle’s location. This work is one of the first applications of dG methods to the modeling of gravitational waves (see also [241]), and the first dG computation of gravitational metric perturbations driven by a point-particle.

Resolving the metric perturbation very close to the particle is paramount when computing the gravitational self-force. These computations comprise a major current effort within with EMRB modeling community, and much progress has already been made [19, 22, 56, 80, 218] (a representative, but far from exhaustive list). The major bottleneck towards an accurate and efficient self-force code is treatment of the delta function. Popular approaches, for example replacement by narrowly peaked Gaussian, all suffer from large oscillations and poor accuracy at the particle’s location making computations of the form (2.64) inaccurate and costly. In this chapter we describe our domain matching technique to overcome this difficulty, and self-force computations are presented in Sec. 5.3.4.

This chapter is organized as follows. Section 4.2 provides further background necessary to understand the physical model. In particular, this section presents ODEs used to describe the particle’s motion, constructs source terms found on the right hand side of (4.1), derives jump conditions in the master functions and their derivatives, and constructs a coordinate transformation adapted to the particle history. This background allows us to rewrite (4.1) as a first–order system which features only *undifferentiated* delta-functions in the forcing. Section 4.3 describes our dG scheme as applied to the first–order system obtained in the previous section. Here we focus on the numerical flux and on how delta function terms are incorporated into the numerical flux function. Specification of initial data and boundary conditions are given Sec. 4.4, along with our procedure for extracting gravitational waveforms to future null infinity. A series of code performance tests are summarized in section 4.5. Section 4.5 also provides physical results for circular and eccentric orbits.

4.2 RWZ Equations in the Presence of a Perturbing Particle

Throughout, we use an over–dot to denote $\partial/\partial t$ differentiation, and sometimes a prime for differentiation by argument. The labels $(\ell, m, \text{CPM/ZM})$ are often suppressed.

4.2.1 ODEs of Particle Motion

In Sec. 2.4.5 we derived a system of first order ODEs (2.63) describing the particle’s orbit for a fixed energy and angular momentum. As an alternative set to (E_p, L_p) , we

may instead work with (e, p) , the *eccentricity* constant e , *semi-latus rectum* constant p . These constants of the motion are related to our original set by [75, 157]

$$L_p^2 = \frac{p^2 M^2}{p - 3 - e^2}, \quad E_p^2 = \frac{(p - 2)^2 - 4e^2}{p(p - 3 - e^2)}. \quad (4.2)$$

Using the equation of motion $t_p(\tau)$, set $r_p(t) = r_p(\tau(t))$ for the radial coordinate of the particle expressed in terms of coordinate time, with similar expressions for $\theta_p(t)$ and $\phi_p(t)$. Introducing the parameterization $r_p(t) = pM/(1 + e \cos \chi(t))$, we obtain the particle trajectory $(r_p(t), \phi_p(t))$ by integration of the following system which describes timelike geodesic motion: [62, 204, 75, 157]

$$\frac{d\phi_p}{dt} = \frac{(p - 2 - 2e \cos \chi)(1 + e \cos \chi)^2}{Mp^{3/2}[(p - 2)^2 - 4e^2]^{1/2}} \quad (4.3a)$$

$$\frac{d\chi}{dt} = \frac{(p - 2 - 2e \cos \chi)(1 + e \cos \chi)^2 [p - 6 - 2e \cos \chi]^{1/2}}{Mp^2 [(p - 2)^2 - 4e^2]^{1/2}}. \quad (4.3b)$$

We use $\chi(t)$ rather than $r_p(t)$, since the former increases monotonically through radial turning points. In our scenario, integration of the system (4.3) is independent of (4.1). Therefore, we may view the particle path, and so the right-hand side of (4.1), as predetermined. We shall be interested in the parameter restriction $0 \leq e < 1$, for which the motion occurs between two turning points and the orbit is bounded. The r_{\min} and r_{\max} occur respectively at $pM/(1 + e)$ and $pM/(1 - e)$, and for $e = 0$ the orbit is circular. Measured in coordinate time t , an eccentric orbit executes a radial period in time T_r given by [75]

$$T_r = C \int_0^{2\pi} d\chi (1 + e \cos \chi)^{-2} \left[1 - \frac{2(3 + e \cos \chi)}{p} \right]^{-1/2} \left[1 - \frac{2(1 + e \cos \chi)}{p} \right]^{-1} \quad (4.4)$$

$$C = p^{3/2} M \left[\left(1 - \frac{2}{p} \right)^2 - \left(\frac{2e}{p} \right)^2 \right]^{1/2}.$$

When $e \neq 0$, we average physical quantities built from components of Isaacson's effective stress–energy tensor (2.51) over 4 radial periods, as defined by Eq. (4.68).

4.2.2 Zerilli–Moncrief (Polar) Source Term

The Zerilli–Moncrief source term is specified by

$$f(r)F_{\ell m}^{\text{ZM}}(t, r) = e_\ell(r)\bar{Y}^{\ell m}(t) \quad (4.5a)$$

$$f(r)G_{\ell m}^{\text{ZM}}(t, r) = a_\ell(r)\bar{Y}^{\ell m}(t) + b_\ell(r)\bar{Y}_\phi^{\ell m}(t) + c_\ell(r)\bar{Y}_{\phi\phi}^{\ell m}(t) + d_\ell(r)\bar{Z}_{\phi\phi}^{\ell m}(t), \quad (4.5b)$$

where the polar tensor harmonics are given in Sec. 2.4.2. Here, for example, $\bar{Y}^{\ell m}(t) \equiv \bar{Y}^{\ell m}(\pi/2, \phi_p(t))$. Moreover, the coefficients in (4.5) are given by [204, 157]

$$a_\ell(r) = \frac{8\pi m_p}{(1+n_\ell)} \frac{f^2(r)}{r\Lambda_\ell^2(r)} \left\{ \frac{6ME_p}{r} - \frac{\Lambda_\ell(r)}{E_p} \left[1 + n_\ell - \frac{3M}{r} + \frac{L_p^2}{r^2} \left(n_\ell + 3 - \frac{7M}{r} \right) \right] \right\} \quad (4.6a)$$

$$b_\ell(r) = \frac{16\pi m_p}{(1+n_\ell)} \frac{f^2(r)}{r^2\Lambda_\ell(r)} \frac{L_p}{E_p} u^r \quad (4.6b)$$

$$c_\ell(r) = \frac{8\pi m_p}{(1+n_\ell)} \frac{f^3(r)}{r^3\Lambda_\ell(r)} \frac{L_p^2}{E_p} \quad (4.6c)$$

$$d_\ell(r) = -32\pi m_p \frac{(\ell-2)!}{(\ell+2)!} \frac{f^2(r)}{r^3} \frac{L_p^2}{E_p} \quad (4.6d)$$

$$e_\ell(r) = \frac{8\pi m_p}{(1+n_\ell)} \frac{f^3(r)}{\Lambda_\ell(r)} \frac{1}{E_p} \left(1 + \frac{L_p^2}{r^2} \right), \quad (4.6e)$$

where $n_\ell = (\ell+2)(\ell-1)/2 = \Lambda_\ell(r) - 3M/r$, and u^r is determined by (2.63) and the sign of $\dot{r}_p(t)$. Due to the u^r factor, we may not, strictly speaking, interpret $b_\ell(r)$ as solely a function of r , but $f(r)u^r/E_p$ could also be reinterpreted as $\dot{r}_p(t)$ and paired with $\bar{Y}_\phi^{\ell m}(t)$.

4.2.3 Cunningham–Price–Moncrief (Axial) Source Term

The Cunningham–Price–Moncrief source term is specified by

$$f(r)F_{\ell m}^{\text{CPM}}(t, r) = C_\ell(r)\bar{X}_\phi^{\ell m}(t) \quad (4.7a)$$

$$f(r)G_{\ell m}^{\text{CPM}}(t, r) = A_\ell(r)\bar{X}_\phi^{\ell m}(t) + B_\ell(r)\bar{X}_{\phi\phi}^{\ell m}(t), \quad (4.7b)$$

where the axial tensor harmonics are given in Sec. 2.4.3. As before, (t) indicates evaluation on $(\theta, \phi) = (\pi/2, \phi_p(t))$, and the coefficients in the above expressions are as follows:

$$A_\ell(r) = 32\pi m_p \frac{(\ell - 2)!}{(\ell + 2)!} \frac{f^2(r)}{r^2} \frac{L_p}{E_p^2} \left[f(r) - 2E_p^2 - \left(1 - \frac{5M}{r}\right) \left(1 + \frac{L_p^2}{r^2}\right) \right] \quad (4.8a)$$

$$B_\ell(r) = 32\pi m_p \frac{(\ell - 2)!}{(\ell + 2)!} \frac{f^2(r)}{r^3} \frac{L_p^2}{E_p^2} u^r \quad (4.8b)$$

$$C_\ell(r) = 32\pi m_p \frac{(\ell - 2)!}{(\ell + 2)!} \frac{f^3(r)}{r} \frac{L_p}{E_p^2} \left(1 + \frac{L_p^2}{r^2}\right). \quad (4.8c)$$

As before, we may not truly interpret $B_\ell(r)$ as a function of r , but nevertheless keep this convenient notation. We note that our $A_\ell(r)$ does not agree with the corresponding factor $u_\ell(r)$ quoted in Ref. [204]; however, we find that $u_\ell(r) = A_\ell(r) - C'_\ell(r)$. Due to this discrepancy, we present our derivation of (4.8).

Derivation of the Axial Source Term

Our goal is to establish formulas (4.7, 4.8) for the Cunningham–Price–Moncrief source term,

$$S^{\text{CPM}} = G^{\text{CPM}}\delta(r - r_p(t)) + F^{\text{CPM}}\delta'(r - r_p(t)). \quad (4.9)$$

Here and in what follows, we suppress (ℓ, m) indices wherever possible. Our starting point is Martel and Poisson's expression for S^{CPM} in (t, r) coordinates,

$$S^{\text{CPM}} = \frac{2r}{(\ell-1)(\ell+2)} \left(f^{-1} \partial_t P^r + f \partial_r P^t + \frac{2M}{r^2} P^t \right). \quad (4.10)$$

This result appears in Appendix C of their expanded version of [159], where S_{odd} in that reference is our S^{CPM} . The vector $P^A = (P^t, P^r)$ is given by Eq. (5.10) of [159],

$$P^A = \frac{16\pi r^2}{\ell(\ell+1)} \int_{S^2} d\Omega T^{Ab} \bar{X}_b^{\ell m}, \quad (4.11)$$

but here with our index conventions.

The stress–energy tensor for a point particle (2.28) is

$$T^{\mu\nu} = m_p \int \frac{1}{\sqrt{-g^{\text{Sch}}}} u^\mu u^\nu \delta^4(z^\alpha - z_p^\alpha(\tau)) d\tau. \quad (4.12)$$

here with $g^{\text{Sch}} = -r^4 \sin^2 \theta$ the determinant of the background Schwarzschild metric. We now change coordinates $d\tau = (d\tau/dt)dt$, integrate over t , and use $u^t = dt/d\tau$, thereby finding

$$T^{\mu\nu} = m_p \frac{u^\mu u^\nu}{u^t r^2 \sin \theta} \delta(r - r_p(t)) \delta(\theta - \theta_p(t)) \delta(\phi - \phi_p(t)). \quad (4.13)$$

Combination of Eqs. (4.11) and (4.13), with the assumption of equatorial motion, then gives

$$P^A = \frac{16\pi m_p}{\ell(\ell+1)} \frac{u^A u^\phi}{u^t} \bar{X}_\phi(\pi/2, \phi_p(t)) \delta(r - r_p(t)). \quad (4.14)$$

Because we have not integrated over r , the four–velocity components u^μ here may be viewed either as functions solely of r , or solely of t upon replacing r by $r_p(t)$. Either viewpoint will yield the same derivatives $\partial_B P^A$ insofar as integration against

test functions is concerned, and we view the components u^μ as depending on r . The delta functions of course depend on both r and t . Having identified which terms depend on r and t , we then calculate

$$\partial_r P^t = \frac{16\pi m_p}{\ell(\ell+1)} (\partial_r u^\phi) \bar{X}_\phi \delta(r - r_p(t)) + \frac{16\pi m_p}{\ell(\ell+1)} u^\phi \bar{X}_\phi \partial_r \delta(r - r_p(t)) \quad (4.15)$$

$$\begin{aligned} \partial_t P^r = \frac{16\pi m_p}{\ell(\ell+1)} \frac{u^r u^\phi}{u^t} \times \\ \left\{ \left[\frac{u^\phi}{u^t} (\partial_\phi \bar{X}_\phi) - \partial_r \left(\frac{u^r}{u^t} \right) \bar{X}_\phi \right] \delta(r - r_p(t)) - \frac{u^r}{u^t} \bar{X}_\phi \partial_r \delta(r - r_p(t)) \right\}. \end{aligned} \quad (4.16)$$

To reach the last equation, we have replaced $\dot{\phi}_p(t)$ by u^ϕ/u^t , which is permissible due to the presence of the accompanying delta function. Moreover, we have also made the replacement

$$\dot{r}_p(t) \delta'(r - r_p(t)) \rightarrow \frac{u^r}{u^t} \delta'(r - r_p(t)) + \left(\frac{u^r}{u^t} \right)' \delta(r - r_p(t)), \quad (4.17)$$

where the prime denotes partial r -differentiation. Finally, substitution of the last two results into Eq. (4.10), along with Eq. (2.63) and the identity

$$\partial_r \left(\frac{u^r}{u^t} \right)^2 = \frac{2}{E_p^2} \frac{f^2(r)}{r} \left[\left(1 - \frac{5M}{r} \right) \left(1 + \frac{L_p^2}{r^2} \right) - f(r) \right] + \frac{4Mf(r)}{r^2}, \quad (4.18)$$

yields the desired results (4.7,4.8). We have also used $X_{\phi\phi}(\pi/2, \phi) = \partial_\phi X_\phi(\pi/2, \phi)$, that is ordinary partial differentiation suffices in the equatorial plane.

4.2.4 Jump Conditions

The forcing (4.1) induces jump conditions on the master function. Derived in Appendix B, these are the following:

$$(f_p^2(t) - \dot{r}_p^2(t)) [[\Psi]] = f_p(t)F(t, r_p(t)) \quad (4.19a)$$

$$\begin{aligned} 2\dot{r}_p(t)\partial_t [[\Psi]] + (\ddot{r}_p(t) - f_p(t)g_p(t)) [[\Psi]] + (f_p^2(t) - \dot{r}_p^2(t)) [[\partial_r \Psi]] \\ = f_p(t)G(t, r_p(t)) - g_p(t)F(t, r_p(t)) - f_p(t)F_r(t, r_p(t)), \end{aligned} \quad (4.19b)$$

where the subscript r in $F_r(t, r)$ denotes partial differentiation with respect to the second slot, and

$$f_p(t) = f(r_p(t)), \quad g_p(t) = f'(r_p(t)) \neq \partial_t f_p(t) \quad (4.20)$$

are shorthands. In (4.19) our notation for a time-dependent jump is, for example,

$$[[\Psi]](t) \equiv \lim_{\epsilon \rightarrow 0^+} [\Psi(t, r_p(t) + \epsilon) - \Psi(t, r_p(t) - \epsilon)]. \quad (4.21)$$

Defining the particle velocity as $v_p(t) = \dot{x}_p(t) = \dot{r}_p(t)/f_p(t)$, we see that (4.19a) has the form

$$f_p(t)(1 - v_p^2(t)) [[\Psi]] = F(t, r_p(t)), \quad (4.22)$$

confirming that the jump $[[\Psi]]$ is well-defined for a subluminal particle speed, $|v_p| < 1$. Therefore, we may safely make the substitution

$$[[\Psi]] = \frac{f_p(t)F(t, r_p(t))}{f_p^2(t) - \dot{r}_p^2(t)} \quad (4.23)$$

in all formulas which follow. Differentiation of (4.23) gives

$$\begin{aligned} \partial_t [[\Psi]] &= \frac{2f_p(t)\dot{r}_p(t)F(t, r_p(t)) [\ddot{r}_p(t) - f_p(t)g_p(t)]}{(f_p^2(t) - \dot{r}_p^2(t))^2} \\ &+ \frac{g_p(t)\dot{r}_p(t)F(t, r_p(t)) + f_p(t)F_t(t, r_p(t)) + f_p(t)\dot{r}_p(t)F_r(t, r_p(t))}{f_p^2(t) - \dot{r}_p^2(t)}. \end{aligned} \quad (4.24)$$

Finally, we may express (4.19b) as

$$\begin{aligned} [[\partial_r \Psi]] &= [- 2\dot{r}_p(t)\partial_t [[\Psi]] - (\ddot{r}_p(t) - f_p(t)g_p(t)) [[\Psi]] \\ &+ f_p(t)G(t, r_p(t)) - g_p(t)F(t, r_p(t)) - f_p(t)F_r(t, r_p(t))] / (f_p^2(t) - \dot{r}_p^2(t)), \end{aligned} \quad (4.25)$$

with the understanding that here $[[\Psi]]$ and $\partial_t [[\Psi]]$ respectively stand for (4.23) and (4.24). Again note that $f_p^2(t) - \dot{r}_p^2(t) > 1$ for a subluminal particle speed, whence the jumps $\partial_t [[\Psi]]$ and $[[\partial_r \Psi]]$ given by Eqs. (4.24) and (4.25) are finite. The formulas

$$[[\partial_t \Psi]] = \partial_t [[\Psi]] - \dot{r}_p(t) [[\partial_r \Psi]], \quad [[\partial_x \Psi]] = f_p(t) [[\partial_r \Psi]] \quad (4.26)$$

prove useful later.

4.2.5 Coordinate Transformation Adapted to Particle History

Now assume that $x \in [a, b]$ specifies the computational domain and the time-dependent particle location $x_p = x_p(t)$ obeys $a < x_p(t) < b, \forall t$. We enact the

coordinate transformation

$$t = \lambda \tag{4.27}$$

$$x = a + \frac{x_p - a}{\xi_p - a}(\xi - a) + \frac{(b - x_p)(\xi_p - a) - (x_p - a)(b - \xi_p)}{(\xi_p - a)(b - \xi_p)(b - a)}(\xi - a)(\xi - \xi_p), \tag{4.28}$$

with the understanding that $x_p = x_p(\lambda)$ is explicitly time-dependent. The transformation obeys the following criteria: (i) t and λ label the same time slices; (ii) $x(\lambda, \xi_p) = x_p(\lambda)$, with $\xi_p = \text{constant}$ and $a < \xi_p < b$; (iii) $x(\lambda, a) = a$ and $x(\lambda, b) = b$. We further require (iv) that the transformation is invertible on $[a, b]$. This will only hold provided the point

$$\xi_{\text{critical}} = \frac{(\xi_p + a)(\xi_p - x_p(\lambda)) + (x_p(\lambda) - a)(b - \xi_p)}{(\xi_p - x_p(\lambda))} \tag{4.29}$$

lies outside of the interval $[a, b]$. This is not a restriction of our method *per se*, and a coordinate transformation satisfying conditions (i) through (iv) may always be found. We have chosen to work with this one only for its simplicity.

Differentiations of (4.28) yield

$$\frac{\partial x}{\partial \lambda} = \frac{(\xi - a)(b - \xi)x'_p(\lambda)}{(\xi_p - a)(b - \xi_p)} \tag{4.30}$$

$$\frac{\partial x}{\partial \xi} = \frac{(2\xi - \xi_p - a)(\xi_p - x_p(\lambda)) + (x_p(\lambda) - a)(b - \xi_p)}{(\xi_p - a)(b - \xi_p)} \tag{4.31}$$

$$\frac{\partial^2 x}{\partial \xi^2} = \frac{2(\xi_p - x_p(\lambda))}{(\xi_p - a)(b - \xi_p)}, \tag{4.32}$$

and these expressions appear in later formulas.

Under the coordinate transformation, the line-element (2.22) acquires a shift vector,

$$ds^2 = -N^2 d\lambda^2 + L^2 (d\xi + \beta^\xi d\lambda)^2 + r^2 (d\theta^2 + \sin^2 \theta d\phi^2). \quad (4.33)$$

Here $N = f^{1/2}$, $L = f^{1/2} \partial x / \partial \xi$, with f understood as $f(r(x(\lambda, \xi)))$. The shift vector is

$$\beta^\xi = \frac{\partial x / \partial \lambda}{\partial x / \partial \xi} = \frac{(\xi - a)(b - \xi)x'_p(\lambda)}{(2\xi - \xi_p - a)(\xi_p - x_p(\lambda)) + (x_p(\lambda) - a)(b - \xi_p)}, \quad (4.34)$$

and we will also need

$$\frac{\partial \beta^\xi}{\partial \xi} = \frac{(A\xi^2 + B\xi + C)x'_p(\lambda)}{[(2\xi - \xi_p - a)(\xi_p - x_p(\lambda)) + (x_p(\lambda) - a)(b - \xi_p)]^2}, \quad (4.35)$$

where $A = 2(x_p(\lambda) - \xi_p)$, $B = 2(ab + \xi_p^2 - (a + b)x_p(\lambda))$, and $C = (a^2 + b^2)x_p(\lambda) - a(b - \xi_p)^2 - b(a^2 + \xi_p^2)$. The velocity variable $v = L\beta^\xi/N = \partial x / \partial \lambda$ obeys

$$v(\lambda, a) = 0, \quad v(\lambda, \xi_p) = x'_p(\lambda), \quad v(\lambda, b) = 0. \quad (4.36)$$

Since $|x'_p(\lambda)| < 1$, we have $|v(\lambda, \xi)| < 1$ uniformly in ξ , assuming appropriately chosen ξ_p , a , and b . The vector field $\partial / \partial \lambda$ is not the Killing direction, and it does not point orthogonal to the constant- λ slices. To relate the $\partial / \partial \lambda$ direction to the unit-normal² u of the slicing, first consider $g_{\lambda\lambda} = -N^2 + L^2(\beta^\xi)^2 = -N^2(1 - v^2) = -(N/\gamma)^2$, where $\gamma = (1 - v^2)^{-1/2}$ is the relativistic factor. Therefore, the vector field

$$\bar{u} = \gamma N^{-1} \partial / \partial \lambda \quad (4.37)$$

is normalized, and one of its integral curves is the particle history. From standard formulas

$$N^{-1}(\partial / \partial \lambda - \beta^\xi \partial / \partial \xi) = \gamma^{-1} \bar{u} - v L^{-1} \partial / \partial \xi, \quad (4.38)$$

²Here we use coordinate-free abstract notation for the *vector fields* u , \bar{u} , and n .

so that $\bar{u} = \gamma u + v\gamma n$. Here $g(n, n) = L^{-2}g_{\xi\xi} = 1$, whence $n = L^{-1}\partial/\partial\xi$ is a normalized spacelike vector field. These formulas show that the spacetime dependent parameter v determines a local boost in the tangent space of each spacetime point in the coordinate domain. At $\xi = \xi_p$ this boost relates the slice normal u to the particle direction.

4.2.6 Wave Equation as a First–Order System

Retaining the same letter Ψ to denote the wave field $\Psi(\lambda, r(x(\lambda, \xi)))$ in the new coordinates, we introduce the variable Φ which is *almost* $\partial_\xi\Psi$. Away from the particle's location $\Phi = \partial_\xi\Psi$ is the gradient, and at ξ_p we remove the δ –singularity implied by the inhomogeneous source term. Notice that $\partial_x\Psi = f\partial_r\Psi$ in the old system corresponds to $(\partial x/\partial\xi)^{-1}\Phi$ in the new system. The following first–order system in the (λ, ξ) coordinates corresponds to the original second–order wave equation (4.1):

$$\partial_\lambda\Psi = \beta^\xi\Phi - \Pi \tag{4.39a}$$

$$\partial_\lambda\Pi = \beta^\xi\partial_\xi\Pi - (\partial x/\partial\xi)^{-1}\partial_\xi[(\partial x/\partial\xi)^{-1}\Phi] + V(r)\Psi + J_1\delta(\xi - \xi_p) \tag{4.39b}$$

$$\partial_\lambda\Phi = \partial_\xi(\beta^\xi\Phi) - \partial_\xi\Pi + J_2\delta(\xi - \xi_p), \tag{4.39c}$$

where Eq. (4.39a) defines the variable Π . The λ –dependent functions

$$J_1 = -\beta^\xi[[\Pi]] + (\partial x/\partial\xi)^{-2}[[\Phi]], \quad J_2 = -\beta^\xi[[\Phi]] + [[\Pi]]. \tag{4.40}$$

implement the jump conditions collected in Section 4.2.4, where in terms of (4.26)

$$[[\Pi]] = -[[\partial_t\Psi]], \quad [[\Phi]] = (\partial x/\partial\xi)[[\partial_x\Psi]]. \tag{4.41}$$

The jumps (4.40) can be recovered by integrating (4.39) against a test function over the region $(\xi_p - \epsilon, \xi_p + \epsilon)$, performing an integration by parts, and taking the $\epsilon \rightarrow 0^+$ limit. Smooth terms vanish in the limit. Thus, the system (4.39), with this choice of J_1 and J_2 , is the first order form of (4.1) provided certain distributional constraints hold as per the discussion in Sec. 3.2.

Distributional Constraints

The first order reduction (4.39) of the RWZ equations (4.1) involve two new auxiliary fields Π and Φ and functions J_1 and J_2 . Notice J_1 and J_2 have been recovered under the assumption $\partial_\lambda \Phi$ and $\partial_\lambda \Pi$ vanished in the limit $\epsilon \rightarrow 0^+$. Hence, in our approach, from Φ and Π we have removed delta function terms arising from the distributional inhomogeneity³.

To make this point clear, consider the case of circular orbits for which $\beta^\xi = 0$, $(\partial x / \partial \xi) = 1$, $\lambda = t$ and $\xi = x$. Define $\tilde{\Phi} = \partial_x \Psi$ to hold for distributions, then $\Phi = \tilde{\Phi} - [[\Psi]] \delta(x - x_p)$ is the δ -free piece (Eq. (B.4) gives an explicit construction). As ∂_t is tangential to particle motion, $\Pi = -\partial_t \Psi$ is already δ -free and the evolution equations are

$$\partial_t \tilde{\Phi} = -\partial_x \Pi, \tag{4.42a}$$

$$\partial_t \Phi = -\partial_x \Pi - [[\partial_t \Psi]] \delta(x - x_p), \tag{4.42b}$$

where we have used $\partial_t [[\Psi]] = [[\partial_t \Psi]]$ for circular orbits. Working with Φ leads to

³Because ∂_λ is tangential to the particle's path, ∂_λ will not create any δ -singularity at the particle's location. Hence, when considering terms like $\partial_\lambda \Phi$ we only need to look for a Dirac delta lurking in Φ .

our system (4.39) and the distributional constraint

$$\Phi = \partial_x \Psi - [[\Psi]] \delta(x - x_p), \quad (4.43)$$

while a preference for $\tilde{\Phi}$ results in system (5.29) and the distributional constraint

$$\tilde{\Phi} = \partial_x \Psi. \quad (4.44)$$

In practice the constraint (4.43) is neither enforced nor checked (and for eccentric orbits it is not even constructed) at ξ_p . Away from ξ_p , including points infinitesimally close, we check $\Phi = \partial_x \Psi$ and convergence to an exact solution.

4.3 A DG Scheme for RWZ with Distributional Forcing

Our spatial discretization follows the approach and notation of Sec. 3.3, and our intention here is to apply those techniques to (4.39). Special attention is paid to the treatment of the distributional source term. In what follows, we use the shorthands $x_\xi = \partial x / \partial \xi$ and $x_{\xi\xi} = \partial^2 x / \partial \xi^2$.

4.3.1 Discretization of (4.39)

The computational domain Ω_h is the closed ξ -interval $[a, b]$. We cover Ω_h with $K > 1$ non-overlapping intervals D^k . We further assume that the particle location $\xi_p = b^{k_p} = a^{k_p+1}$ lies at the endpoint shared by D^{k_p} and D^{k_p+1} , with $1 \leq k_p < K$. On

each interval D^k , we approximate each component of the system vector (Ψ, Π, Φ) by a local Lagrange interpolating polynomial belonging to D^k and interpolating at the LGL nodal points.

On each interval D^k and for each solution component, we define local residuals,

$$(R_\Psi)_h^k = \partial_\lambda \Psi_h^k - (\beta^\xi \Phi)_h^k + \Pi_h^k \quad (4.45a)$$

$$(R_\Pi)_h^k = \partial_\lambda \Pi_h^k - \partial_\xi (\beta^\xi \Pi)_h^k + (\Pi \partial_\xi \beta^\xi)_h^k + \partial_\xi (x_\xi^{-2} \Phi)_h^k + (x_\xi^{-3} x_{\xi\xi} \Phi)_h^k - (V \Psi)_h^k \quad (4.45b)$$

$$(R_\Phi)_h^k = \partial_\lambda \Phi_h^k - \partial_\xi (\beta^\xi \Phi)_h^k + \partial_\xi \Pi_h^k, \quad (4.45c)$$

measuring the extent to which our approximations satisfy the original system of PDE. We define these residuals on open intervals $(a^k, b^k) \subset D^k$, but have assumed that the particle location $\xi_p = b^{k_p} = a^{k_p+1}$ lies at an endpoint. Therefore, in the residuals (4.45) we have not yet included the δ -function contributions appearing in (4.39).

Galerkin conditions arise from the inner products between each residual (4.45) and all $\ell_j^k(\xi)$. Integrating once by parts, introducing the numerical fluxes, and recalling definitions of the mass and stiffness matrix (3.32) results in a nodal form of the semi-discrete equations

$$\partial_\lambda \Psi_h^k - (\beta^\xi \Phi)_h^k + \Pi_h^k = 0 \quad (4.46a)$$

$$\begin{aligned} \partial_\lambda \Pi_h^k + (D_M^k)^T (\beta^\xi \Pi)_h^k - (D_M^k)^T (x_\xi^{-2} \Phi)_h^k + (x_\xi^{-3} x_{\xi\xi} \Phi)_h^k - (V \Psi)_h^k \\ = (M^k)^{-1} [(\beta^\xi(\lambda, \xi)(\Pi_h^k)^* - x_\xi^{-2}(\lambda, \xi)(\Phi_h^k)^*) \ell^k(\xi)] \Big|_{a^k}^{b^k} \end{aligned} \quad (4.46b)$$

$$\partial_\lambda \Phi_h^k + (D_M^k)^T (\beta^\xi \Phi)_h^k - (D_M^k)^T \Pi_h^k = (M^k)^{-1} [(\beta^\xi(\lambda, \xi)(\Phi_h^k)^* - (\Pi_h^k)^*) \ell^k(\xi)] \Big|_{a^k}^{b^k}. \quad (4.46c)$$

The weak (single integration by parts) dG form features the transpose of the operator

$$D_M^k = M^k D^k (M^k)^{-1}, \quad (4.47)$$

instead of the spectral collocation derivative matrix D^k . Using the relationship $(D^k)^T = (S^k)^T (M^k)^{-1}$ we conclude $(D_M^k)^T = (M^k)^{-1} (S^k)^T$. All adjacent vectors in these expressions, e. g. $(\beta^\xi \Phi)_h^k$, $(\mathbf{V}\Psi)_h^k$, and $(\mathbf{x}_\xi^{-3} \mathbf{x}_{\xi\xi} \Phi)_h^k$, should be interpreted as a single vector obtained via component-by-component products.

4.3.2 Numerical Flux

To define the vector $(f_\Pi, f_\Phi)^T$ of physical fluxes, we write (4.39b,c) as

$$\partial_\lambda \begin{pmatrix} \Pi \\ \Phi \end{pmatrix} + \partial_\xi \begin{pmatrix} f_\Pi \\ f_\Phi \end{pmatrix} = \text{lower order terms}. \quad (4.48)$$

This equation determines the physical and numerical fluxes as follows:

$$\begin{pmatrix} f_\Pi \\ f_\Phi \end{pmatrix} \equiv \begin{pmatrix} -\beta^\xi & x_\xi^{-2} \\ 1 & -\beta^\xi \end{pmatrix} \begin{pmatrix} \Pi \\ \Phi \end{pmatrix}, \quad \begin{pmatrix} (f_\Pi^k)^* \\ (f_\Phi^k)^* \end{pmatrix} \equiv \begin{pmatrix} -\beta^\xi & x_\xi^{-2} \\ 1 & -\beta^\xi \end{pmatrix} \begin{pmatrix} (\Pi_h^k)^* \\ (\Phi_h^k)^* \end{pmatrix}. \quad (4.49)$$

The combinations of $(\Pi_h^k)^*$ and $(\Phi_h^k)^*$ which appear in (4.46b,c) are precisely $-(f_\Pi^k)^*$ and $-(f_\Phi^k)^*$, as must be the case since these terms have arisen through integration by parts. In this subsection we construct the required boundary expressions for $(f_\Pi^k)^*$ and $(f_\Phi^k)^*$. Our numerical flux must be robust, ensure stability, and be capable of handling the analytic discontinuities at the particle location. Numerical experiments suggest that inclusion of a Dirac delta function renders inadequate otherwise suitable numerical fluxes, such as the central and Lax–Friedrichs fluxes [121]. How-

ever, as we will see, a suitably modified upwind numerical flux successfully handles the delta functions in the system (4.39), recovering optimal convergence. We begin by constructing the standard upwind flux corresponding to no particle, and then incorporate the particle's effect into the flux through the addition of an extra term.

An upwind numerical flux passes information across an interface in the direction of propagation. To construct the upwind numerical fluxes, we first diagonalize the matrix appearing in (4.49) as follows:

$$\begin{pmatrix} -\beta^\xi & x_\xi^{-2} \\ 1 & -\beta^\xi \end{pmatrix} = T \begin{pmatrix} -\beta^\xi + x_\xi^{-1} & 0 \\ 0 & -\beta^\xi - x_\xi^{-1} \end{pmatrix} T^{-1}, \quad T^{-1} = \begin{pmatrix} 1 & x_\xi^{-1} \\ 1 & -x_\xi^{-1} \end{pmatrix}. \quad (4.50)$$

Application of T^{-1} on the system vector $(\Pi, \Phi)^T$ of fundamental fields yields the system vector $(\Pi + \Phi/x_\xi, \Pi - \Phi/x_\xi)^T$ of characteristic fields. For our problem, the first characteristic field $\Pi + \Phi/x_\xi$ propagates rightward with speed $-\beta^\xi + x_\xi^{-1}$ relative to the $\partial/\partial\lambda$ time axis, while the second characteristic field $\Pi - \Phi/x_\xi$ propagates leftward with speed $-\beta^\xi - x_\xi^{-1}$. Respectively, the upwind fluxes at a left endpoint

a^k ($k \neq k_p + 1$) and at a right endpoint b^k ($k \neq k_p$) then take the following forms:

$$\begin{pmatrix} (f_{\Pi}^k)^* \\ (f_{\Phi}^k)^* \end{pmatrix}_{\text{left}} = T \begin{pmatrix} 0 & 0 \\ 0 & -\beta^\xi - x_\xi^{-1} \end{pmatrix} T^{-1} \begin{pmatrix} \Pi_h^- \\ \Phi_h^- \end{pmatrix} + T \begin{pmatrix} -\beta^\xi + x_\xi^{-1} & 0 \\ 0 & 0 \end{pmatrix} T^{-1} \begin{pmatrix} \Pi_h^+ \\ \Phi_h^+ \end{pmatrix} \quad (4.51a)$$

$$\begin{pmatrix} (f_{\Pi}^k)^* \\ (f_{\Phi}^k)^* \end{pmatrix}_{\text{right}} = T \begin{pmatrix} 0 & 0 \\ 0 & -\beta^\xi - x_\xi^{-1} \end{pmatrix} T^{-1} \begin{pmatrix} \Pi_h^+ \\ \Phi_h^+ \end{pmatrix} + T \begin{pmatrix} -\beta^\xi + x_\xi^{-1} & 0 \\ 0 & 0 \end{pmatrix} T^{-1} \begin{pmatrix} \Pi_h^- \\ \Phi_h^- \end{pmatrix}. \quad (4.51b)$$

Eqs. (4.51a,b) formalize the intuitive concept behind the upwind numerical flux. In these equations triple-product matrices operate on the interior and exterior solution. The first matrix operation transforms the fields to characteristic fields, the second projects out one of the characteristic fields, and the third transforms back to the fundamental fields. As a result, information from a right-moving field, say, influences the subdomain to the right, but not the subdomain to the left. One can show the effect of the upwind choice is to penalize (i.e. add a negative contribution to) the semi-discrete energy statement, thus ensuring semi-discrete stability for the method.

To achieve succinct expressions for the upwind flux which hold at both left and right endpoints, recall our definitions (3.30) for the numerical average and jump

$$\{\{\Phi\}\} = \frac{1}{2}(\Phi^+ + \Phi^-), \quad [[\Phi]]_{\mathbf{n}} = \mathbf{n}^+ \Phi^+ + \mathbf{n}^- \Phi^-, \quad (4.52)$$

where the jump is defined with respect to a local outward-pointing normal \mathbf{n} of a subdomain. These definitions yield the following concise formulas (valid at left or

right endpoints):

$$(f_{\Pi}^k)^* = \{\{-\beta^\xi \Pi_h + x_\xi^{-2} \Phi_h\}\} + \frac{1}{2} \left[[x_\xi^{-1} \Pi_h - x_\xi^{-1} \beta^\xi \Phi_h] \right]_{\mathbf{n}} \quad (4.53a)$$

$$(f_{\Phi}^k)^* = \{\{\Pi_h - \beta^\xi \Phi_h\}\} + \frac{1}{2} \left[[x_\xi^{-1} \Phi_h - x_\xi \beta^\xi \Pi_h] \right]_{\mathbf{n}}. \quad (4.53b)$$

At all interior endpoints (a^k for $k \neq 1, k_p + 1$, and b^k for $k \neq k_p, K$) we will use this numerical flux which is determined by the local numerical solutions. We also use this upwind form at a physical boundary (that is, a^1 or b^K), but in this case a boundary condition supplies the exterior solution.

Turning now to the endpoints $a^{k_p+1} = b^{k_p}$ corresponding to the particle location, we modify the standard upwind flux (4.53) following the *generalized* discontinuous Galerkin method for scalar equations outlined in [88], which we now extend to the system (4.39). Consider a Dirac delta function located at the interface between elements \mathbf{D}^{k_p} and \mathbf{D}^{k_p+1} , and the weak form of the resulting system (4.39). The relevant new terms to consider have the form

$$\int_{\mathbf{D}^{k_p}} d\xi J_{1,2} \delta(\xi - \xi_p) \ell_j^{k_p}(\xi), \quad \int_{\mathbf{D}^{k_p+1}} d\xi J_{1,2} \delta(\xi - \xi_p) \ell_j^{k_p+1}(\xi). \quad (4.54)$$

Upon evaluation, each of these terms appears similar in form to a boundary flux. The discontinuous Galerkin method provides a self-consistent way to evaluate these integrals and then add the results to the numerical flux. We only require the usual selection property of the delta function when integrated over the *union* $\mathbf{D}^{k_p} \cup \mathbf{D}^{k_p+1}$, and we are free to choose how the individual integrals over \mathbf{D}^{k_p} and \mathbf{D}^{k_p+1} contribute to the total integral. In fact, the dynamics of (4.39) suggest a preferred distributional splitting. To see why, consider the scalar advection equation $(\partial_\lambda + v \partial_\xi) \Psi = J(\xi, \lambda) \delta(\xi - \xi_p)$, with $v > 0$. Since this equation corresponds to rightward propagation, the natural choice for the associated distributional splitting

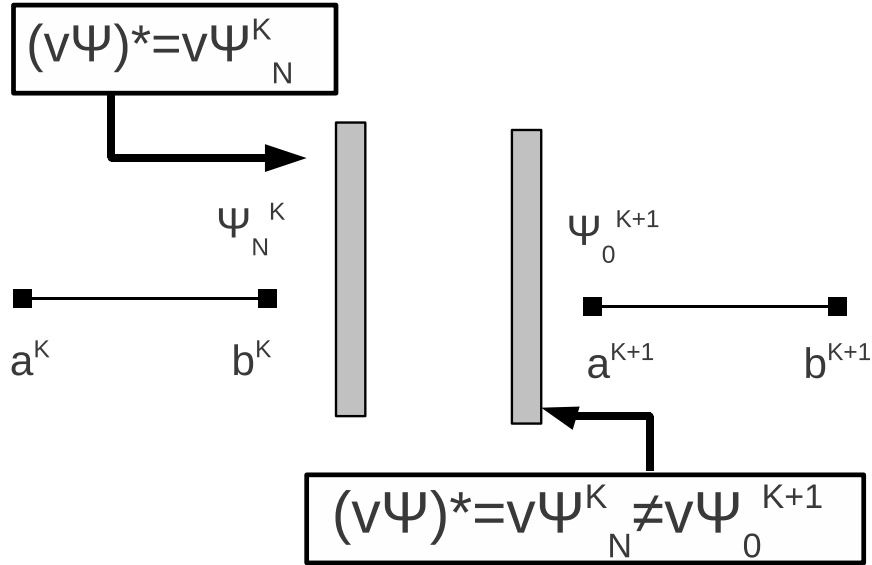


Figure 4.1: NUMERICAL FLUX FOR AN ADVECTION EQUATION AWAY FROM δ -SINGULARITY. At an interface between D^k and D^{k+1} an upwind numerical flux passes information from left to right.

of the delta function term is

$$\int_{D^{k_p}} d\xi J \delta(\xi - \xi_p) \ell_j^{k_p}(\xi) = 0, \quad \int_{D^{k_p+1}} d\xi J \delta(\xi - \xi_p) \ell_j^{k_p+1}(\xi) = J(\xi_p, t) \delta_{0,j}. \quad (4.55)$$

For this case, notice that the delta function only “sees” a single Lagrange polynomial, namely $\ell_0^{k_p+1}(\xi)$ on the rightward interval. Figures 4.1 and 4.2 show the upwind numerical flux for the advection equation with and without a Dirac delta.

To enact an upwind splitting of the delta functions appearing the system (4.39), we simply use the matrix T^{-1} already defined in (4.50) to isolate the two propagating characteristic modes of the system. Consistent with propagation of these modes, at

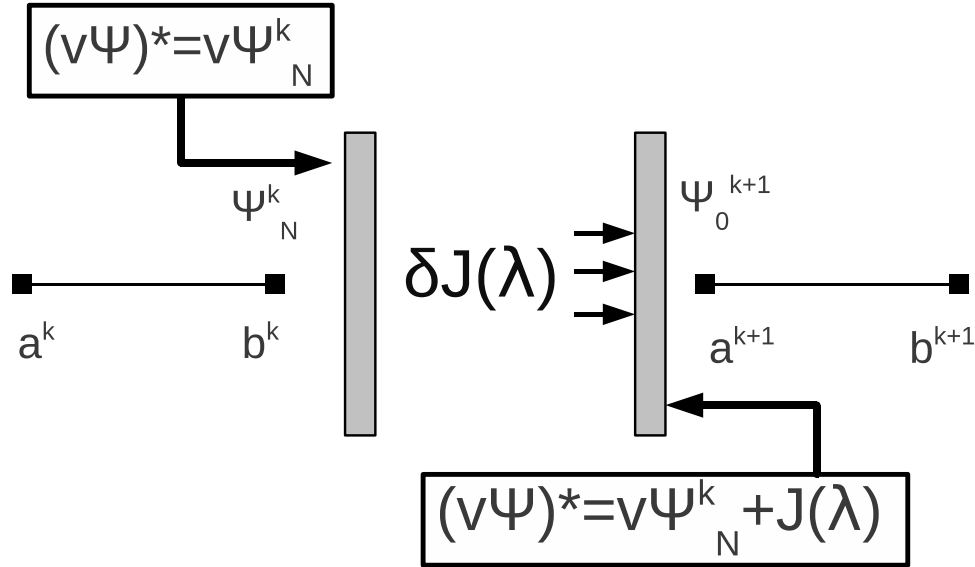


Figure 4.2: NUMERICAL FLUX FOR AN ADVECTION EQUATION AT δ -SINGULARITY. At the interface we continue to use an upwind numerical flux (cf. Fig. 4.1), while only the D^{k+1} subdomain “sees” the Dirac delta.

the particle location we modify the fluxes given in Eqs. (4.51a,b),

$$\begin{pmatrix} (f_{\Pi}^{k_p+1})^* \\ (f_{\Phi}^{k_p+1})^* \end{pmatrix}_{\text{left, modified}} = \begin{pmatrix} (f_{\Pi}^{k_p+1})^* \\ (f_{\Phi}^{k_p+1})^* \end{pmatrix}_{\text{left}} + T \begin{pmatrix} 1 & 0 \\ 0 & 0 \end{pmatrix} T^{-1} \begin{pmatrix} J_1 \\ J_2 \end{pmatrix} \quad (4.56a)$$

$$\begin{pmatrix} (f_{\Pi}^{k_p})^* \\ (f_{\Phi}^{k_p})^* \end{pmatrix}_{\text{right, modified}} = \begin{pmatrix} (f_{\Pi}^{k_p})^* \\ (f_{\Phi}^{k_p})^* \end{pmatrix}_{\text{right}} + T \begin{pmatrix} 0 & 0 \\ 0 & -1 \end{pmatrix} T^{-1} \begin{pmatrix} J_1 \\ J_2 \end{pmatrix}. \quad (4.56b)$$

The correctness of this prescription can be seen as follows. Integration of the system (4.39) over the union $D^{k_p} \cup D^{k_p+1}$ followed by a subsequent integration by parts on each interval generates the following boundary terms at the particle location (and on the right-hand side of the equal sign):

$$\begin{pmatrix} f_{\Pi} \\ f_{\Phi} \end{pmatrix} \Big|_{(\lambda, a^{k_p+1})} - \begin{pmatrix} f_{\Pi} \\ f_{\Phi} \end{pmatrix} \Big|_{(\lambda, b^{k_p})} + \begin{pmatrix} J_1 \\ J_2 \end{pmatrix}. \quad (4.57)$$

The two physical fluxes in this equation of course cancel each other out, leaving only

the vector $(J_1, J_2)^T$. Our modifications (4.56a,b) of the numerical flux are tailored to mimic this result. While the difference of the left/right numerical fluxes at the particle location will not, in general, cancel each other out (due to numerical error), notice that by subtracting (4.56b) from (4.56a) we generate precisely the vector $(J_1, J_2)^T$. This argument can be made more rigorous through an analysis based on integrating the two local numerical solutions on \mathbf{D}^{k_p} and \mathbf{D}^{k_p+1} against the Lagrange polynomials $\ell_N^{k_p}(\xi)$ and $\ell_0^{k_p+1}(\xi)$. Finally, using the general expressions (4.53a,b), we may likewise succinctly express the modified numerical flux at the particle location as

$$\begin{pmatrix} (f_{\Pi}^k)^* \\ (f_{\Phi}^k)^* \end{pmatrix}_{\text{modified}} = \begin{pmatrix} (f_{\Pi}^k)^* \\ (f_{\Phi}^k)^* \end{pmatrix} + \frac{1}{2}T \begin{pmatrix} 1 - \mathbf{n}^- & 0 \\ 0 & -1 - \mathbf{n}^- \end{pmatrix} T^{-1} \begin{pmatrix} J_1 \\ J_2 \end{pmatrix}, \quad (4.58)$$

where either $k = k_p$ or $k = k_p + 1$ in this equation.

4.4 Treatment of the Initial Boundary Value Problem

The issues of initial data and boundary conditions are not part of the dG method *per se*, but we must, nevertheless, specify both to complete our numerical scheme. This section also discusses a simple waveform extraction technique to approximate future null infinity.

4.4.1 Initial Data with Source Smoothing

We adopt trivial (zero) initial data, and avoid the issue of an impulsively started problem by smoothly “switching on” the source terms. Precisely, the source terms are switched on smoothly via the following prescription:

$$F_{\ell m}(t, r) \rightarrow \begin{cases} \frac{1}{2}[\operatorname{erf}(\sqrt{\delta}(t - t_0 - \tau/2) + 1)]F_{\ell m}(t, r) & \text{for } t_0 \leq t \leq t_0 + \tau \\ F_{\ell m}(t, r) & \text{for } t > t_0 + \tau, \end{cases} \quad (4.59)$$

and the same for $G_{\ell m}(t, r)$. Typically, the initial time $t_0 = 0$, and the timescale τ is much shorter than the final time of the run. Choosing suitable τ and δ , one achieves smooth and consistent start-up to machine precision. Note that this prescription does initially affect the form of $\partial_t F_{\ell m}(t, r)$.

The importance of switching on the source terms is crucial. All of the next chapter is devoted to issues stemming from an impulsively started problem, which appears to be especially problematic for spectral methods [132, 90]. Delaying the discussion until then, here we simply assume these issues have been correctly addressed by temporal source smoothing.

4.4.2 Boundary Conditions

At the boundaries we impose outgoing radiation boundary conditions. Both potentials (2.38, 2.45) behave differently in the $\xi \rightarrow -\infty$ and $\xi \rightarrow \infty$ limits, whence we treat the cases $\xi = a$ and $\xi = b$ differently. Since

$$1 - 2Mr^{-1} = 2Mr^{-1} \exp(-r/(2M)) \exp(x/(2M)) \quad (4.60)$$

in the $x \rightarrow -\infty$, $r \rightarrow 2M^+$ limit both potentials are exponentially small. Therefore, with a being sufficiently negative, $|V^{\text{RW,Z}}(r)|$ is zero to machine precision when r corresponds to $\xi \simeq a$, and as an excellent approximation we may use the Sommerfeld boundary condition

$$(\partial_t \Psi - \partial_x \Psi)(\lambda, a) = 0 \rightarrow \Pi(\lambda, a) + \Phi(\lambda, a)/x_\xi(\lambda, a) = 0. \quad (4.61)$$

In the $x, r \rightarrow \infty$ limit, both the Zerilli and Regge–Wheeler potentials (2.38,2.45) behave like $V^{\text{RW,Z}} = \ell(\ell + 1)r^{-2} + O(r^{-3})$. Therefore, were we to adopt a naive Sommerfeld condition at $\xi = b$, the slow fall-off of the potential would corrupt the benefits of our high-order accurate method. Instead, we implement the radiation boundary condition described in [143],

$$-\Pi(\lambda, b) + \Phi(\lambda, b)/x_\xi(\lambda, b) = \frac{f(r_b)}{r_b} \int_0^\lambda \Omega_\ell^{\text{RW,Z}}(\lambda - \lambda', r_b) \Psi(\lambda', b) d\lambda', \quad (4.62)$$

where $r_b = r(x(\lambda, b)) = r(b)$ and $\Omega_\ell^{\text{RW,Z}}$ is a time-domain boundary kernel. As indicated, this kernel is different for the Regge–Wheeler (here spin-2) and Zerilli cases, although we suppress this dependence wherever possible.

We approximate the time-domain boundary kernel $\Omega_\ell \simeq \Xi_\ell$ as a sum of exponentials

$$\Xi_\ell(t, r_b) = \sum_{k=1}^d \Xi_{\ell,k}(t, r_b), \quad \Xi_{\ell,k}(t, r_b) = \frac{\gamma_{\ell,k}(r_b/(2M))}{2M} \exp\left(\frac{t\beta_{\ell,k}(r_b/(2M))}{2M}\right). \quad (4.63)$$

The parameters $\gamma_{\ell,k}(r_b/(2M))$ and $\beta_{\ell,k}(r_b/(2M))$ determine the approximation kernel $\Xi_\ell(t, r_b)$, and they depend on the Regge–Wheeler or Zerilli case, the orbital index ℓ , and the dimensionless boundary radius $r_b/(2M)$. The approximation Ξ_ℓ is designed so that its Laplace transform agrees with the transform of Ω_ℓ to relative supremum

k	$\text{Re}\beta_{2,k}^{\text{RW}}(500)$	$\text{Im}\beta_{2,k}^{\text{RW}}(500)$	k	$\text{Re}\beta_{2,k}^{\text{Z}}(500)$	$\text{Im}\beta_{2,k}^{\text{Z}}(500)$
1	-1.25849067540E-02	0	1	-1.25789030971E-02	0
2	-8.23918644025E-03	0	2	-8.23529461921E-03	0
3	-5.49064917188E-03	0	3	-5.48806353366E-03	0
4	-3.62410271081E-03	0	4	-3.62239165593E-03	0
5	-2.32805739548E-03	0	5	-2.32695433490E-03	0
6	-1.42584745587E-03	0	6	-1.42517041551E-03	0
7	-8.04688157035E-04	0	7	-8.04304980721E-04	0
8	-3.83719341654E-04	0	8	-3.83535015275E-04	0
9	-2.99532499571E-03	1.73407822255E-03	9	-2.99383340672E-03	1.73321233868E-03

k	$\text{Re}\gamma_{2,k}^{\text{RW}}(500)$	$\text{Im}\gamma_{2,k}^{\text{RW}}(500)$	k	$\text{Re}\gamma_{2,k}^{\text{Z}}(500)$	$\text{Im}\gamma_{2,k}^{\text{Z}}(500)$
1	-8.36957985819E-09	0	1	-8.35513276685E-09	0
2	-2.95922379193E-07	0	2	-2.95425498144E-07	0
3	-2.97720676842E-06	0	3	-2.97239482588E-06	0
4	-8.13540247121E-06	0	4	-8.12342297064E-06	0
5	-1.40566197350E-06	0	5	-1.40379108037E-06	0
6	-5.02202428400E-08	0	6	-5.01539234399E-08	0
7	-1.01094068265E-09	0	7	-1.00959570760E-09	0
8	-7.70486047714E-12	0	8	-7.69439666825E-12	0
9	-2.99056309897E-03	1.73610608573E-03	9	-2.98758843820E-03	1.73437449497E-03

Table 4.1: Compressed kernels for $\ell = 2$, $r_b/(2M) = 500$, $\varepsilon = 10^{-10}$. There are $d = 10$ poles and strengths, and complex conjugation of the ninth entries gives the tenth entries. Zeros correspond to outputs from the compression algorithm which are less than 10^{-30} in absolute value.

error ε along the axis of imaginary Laplace frequency, and the parameters $\gamma_{\ell,k}$ and $\beta_{\ell,k}$ are the outputs from the Alpert–Greengard–Hagstrom compression algorithm [10, 143]. Theoretically, ε is a long-time bound on the relative convolution error in the time domain, and it measures the accuracy of the boundary condition. Table 4.1 collects the $\ell = 2$ kernels for $r_b = 1000M$ and $\varepsilon = 10^{-10}$. We evolve the constituent pieces of the approximate convolution via temporal integration of the ODE

$$\begin{aligned}
\frac{d}{d\lambda} \int_0^\lambda \Xi_{\ell,k}(\lambda - \lambda', r_b) \Psi(\lambda', b) d\lambda' = \\
\frac{\beta_{\ell,k}}{2M} \int_0^\lambda \Xi_{\ell,k}(\lambda - \lambda', r_b) \Psi(\lambda', b) d\lambda' + \Xi_{\ell,k}(0, r_b) \Psi(\lambda, b),
\end{aligned} \tag{4.64}$$

carrying out the integration along side, and coupled with, the numerical evolution of the system (4.39). With this boundary condition, we are free to choose essentially any boundary $\xi = b$, so long as it lies to the right of the source. Our outer radiation boundary condition is especially useful when studying eccentric orbits, for which one must average quantities over many periods.

4.4.3 Waveform Extraction

Practically one must devise a way to extract the waveforms at future null infinity from the finite computation domain. Formally the luminosity Eqs. (2.58, 2.59) hold there, and to a good approximation these are the waveforms gravitational wave detectors measure. This problem has been solved for waves on flat spacetime by Abrahams and Evans [2, 3]. For $\ell = 2$ the procedure is as follows. We record a master scalar Ψ at the outer boundary $x = b$ as a time series, and then integrate $\Psi(t, b) \simeq \ddot{f}(t-b) + 3\dot{f}(t-b)b^{-1} + 3f(t-b)b^{-2}$ as if it were exact, thereby recovering the profile $f(t)$ and its derivatives. We perform a similar extraction on Π . The Abrahams–Evans procedure is not exact for the perturbation equations we consider. Nevertheless, upon substitution of the approximate expansion $\ddot{f}(t-x) + 3\dot{f}(t-x)x^{-1} + 3f(t-x)x^{-2}$ into one of the (homogeneous) master equations (4.1), we find a residual which is $O(r^{-3} \log(\frac{1}{2}r/M))$.

4.5 Numerical Experiments

Before applying our method to physical problems we perform a series of diagnostic tests to confirm the expected theoretical properties of the scheme. We are interested in demonstrating the global spectral convergence of the scheme (especially at the analytic discontinuity), 4th order convergence of the classic Runge–Kutta integrator, and the long–time accuracy of our radiation boundary conditions. We conclude the section by applying our method to circular and eccentric orbits and compare our results to existing results from the literature.

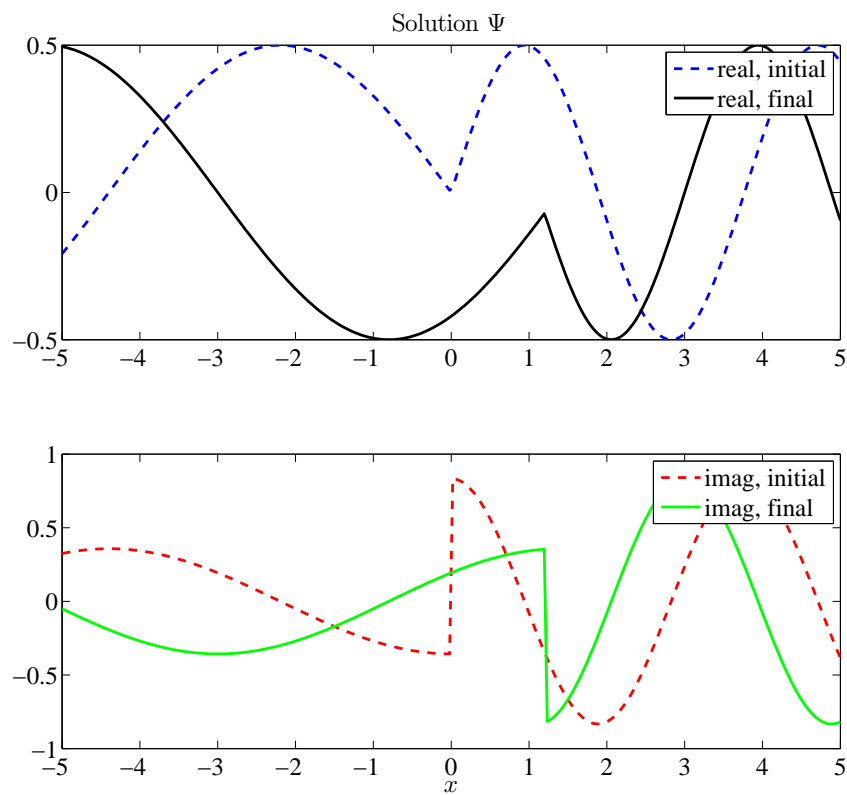


Figure 4.3: Ψ -COMPONENT OF THE SOLUTION. The Π and Φ components are qualitatively similar.

4.5.1 Forced Wave Equation with Exact Initial Data

For a fixed velocity v obeying $|v| < 1$, we consider the model

$$-\partial_t^2 \Psi + \partial_x^2 \Psi = \cos t \delta(x - vt) + i \cos t \delta'(x - vt). \quad (4.65)$$

Appendix C shows that

$$\Psi(t, x) = -\frac{1}{2} \sin \vartheta + \frac{1}{2} i \gamma^2 [v + \operatorname{sgn}(x - vt)] \cos \vartheta, \quad \vartheta = \gamma^2 (t - xv - |x - vt|) \quad (4.66)$$

is an exact particular solution to (4.65) and we will check the convergence of our numerically generated solution against these exact solutions. Here $\gamma = (1 - v^2)^{-1/2}$ is the usual relativistic factor. After expressing (4.65) as a first order system and adopting our dG scheme, we obtain the same equations as in (4.46), except now with a zero potential vector \mathbf{V} . Our domain is comprised of two subdomains: D^1 to the left of the particle location $x_p(t) = vt$, and D^2 to the right of $x_p(t)$. At $x_p(t)$, the interface between D^1 and D^2 , we use Eq. (4.58) for the numerical fluxes $(f_{\Pi}^k)^*$ and $(f_{\Phi}^k)^*$. At the physical boundary points we choose fluxes which enforce simple Sommerfeld boundary conditions,

$$\Pi(\lambda, a) + \Phi(\lambda, a)/x_{\xi}(\lambda, a) = 0, \quad \Pi(\lambda, b) - \Phi(\lambda, b)/x_{\xi}(\lambda, b) = 0. \quad (4.67)$$

Working with the global domain $[a, b] = [-5, 5]$, we choose $v = 0.4$ and the final time $t_F = 3.0$. For these choices the critical ξ value (4.29) always lies outside of the global domain, although clearly the example becomes pathological for a final time t_F near 12.5 (when the particle crosses the outer boundary). Fig. 4.3 shows the Ψ component of the solution vector, and the Φ and Π components also feature moving discontinuities. Fig. 4.4 documents the accuracy after several evolutions,

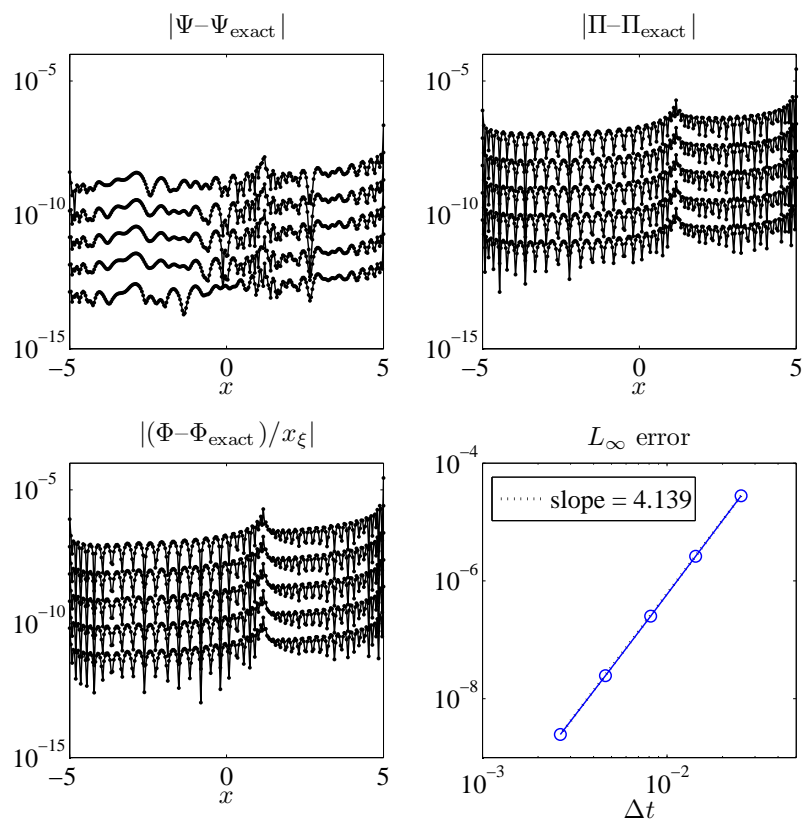


Figure 4.4: TEMPORAL CONVERGENCE OF THE LINEARLY MOVING PARTICLE EXPERIMENT. Errors have been computed relative to a uniformly spaced x -grid and over all fields. The dotted line is a least-squares fit of the data points (the round circles).

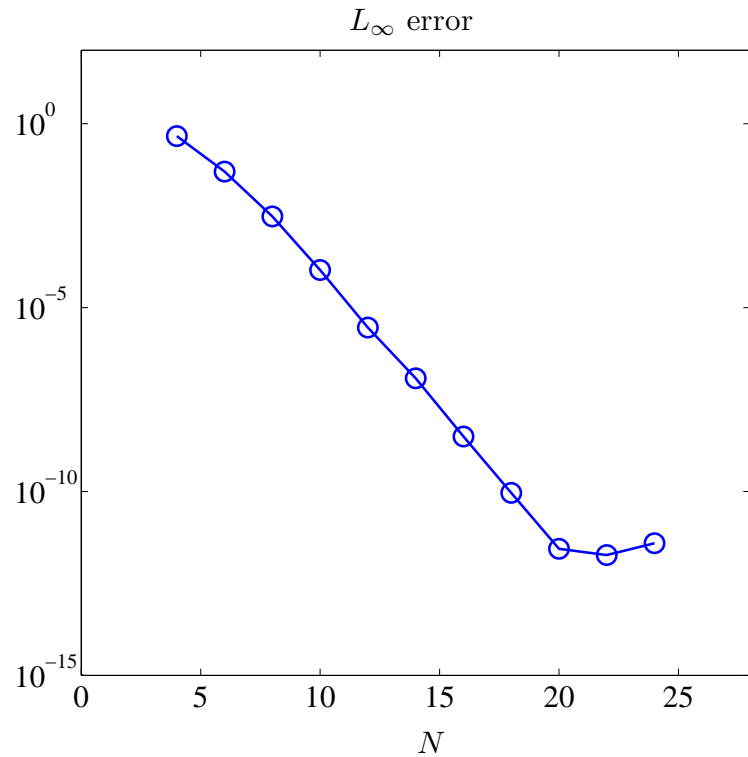


Figure 4.5: SPECTRAL CONVERGENCE OF THE LINEARLY MOVING PARTICLE EXPERIMENT. Again, errors have been computed relative to a uniformly spaced x -grid and over all fields.

each with $N = 26$ points, performed with decreasing temporal resolution in order to exhibit the fourth-order accuracy of the temporal Runge-Kutta integration. To compute errors, we have used the polynomial representations of the two local solutions, each computed with respect to the coordinates (λ, ξ) , to interpolate onto a uniformly spaced x -grid with 256 points where L_∞ errors have been calculated. Fig. 4.5 demonstrates the spectral convergence of our method for this problem, in particular at the particle's location. Here N is the number of points on each of the two subdomains, and for each N we have chosen a Δt to ensure stability.

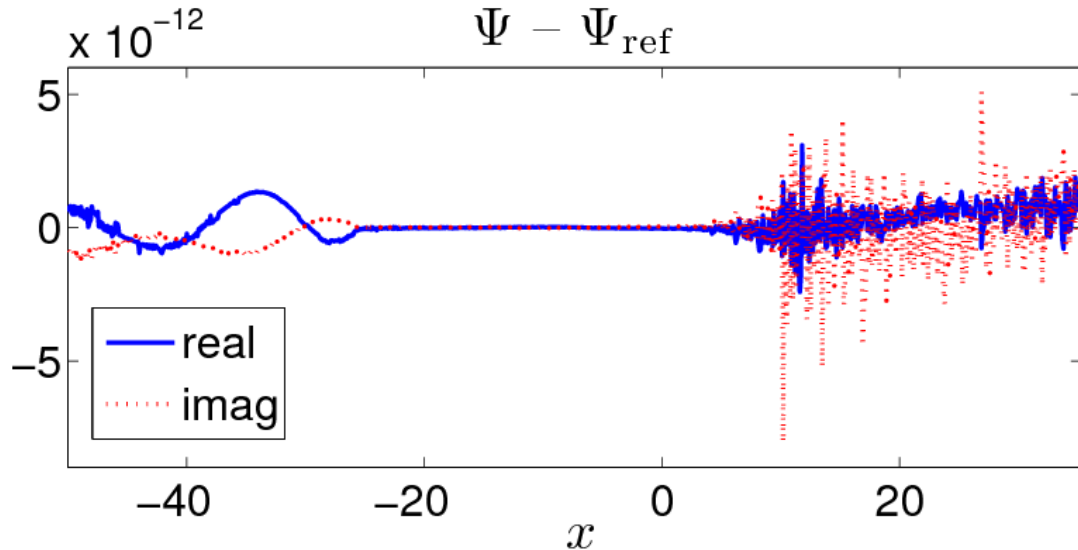


Figure 4.6: EFFECT OF RADIATION BOUNDARY CONDITIONS ON THE SOLUTION Ψ . The experiment described in the text produces a solution Ψ whose magnitude is of order 1, thus the boundary effects are seen to result in very small relative errors.

4.5.2 Longtime Accuracy of Radiation Boundary Conditions

This experiment involves the $\ell = 2$, $m = 2$ polar problem and a circular orbit with $p = 7.9456$, $M = 1$, and $m_p = 1$. We choose trivial initial data at $t_0 = 0$, with a smoother defined by $\tau = 10$ and $\delta = 10$. Integrating to final time $t_F = 90$, we first generate an accurate reference solution Ψ_{ref} on the domain $[-100, 100]$, using 65+55 subdomains (65 to the left of the particle and 55 to the right) with $N = 37$ nodal points on each. Here and below, we choose the time step Δt to ensure stability. At both endpoints $x = \pm 100$ we place Sommerfeld boundary conditions on Ψ_{ref} , as physically no radiation reaches the endpoints by the final time.

The experiment is to generate a second numerical solution Ψ on the shorter domain $[-50, b]$, where $b = 30 + 2 \log(15 - 1) \simeq 35.2$. We again evolve to final time $t_F = 90$, now with the convolution radiation boundary condition (4.62) placed at the outer endpoint $x = b$. The relevant Zerilli kernel is defined in Table II of Ref. [143].

This kernel corresponds to $r_b/(2M) = 15$ and the tolerance $\varepsilon = 10^{-10}$. At the inner endpoint $x = -50$ we again adopt a Sommerfeld boundary condition. For 30+15 subdomains with 33 points on each, the corresponding Ψ is then compared against the reference solution Ψ_{ref} in the L_∞ norm. After interpolation onto a uniformly spaced grid with 853 points, we have found that $\|\Psi - \Psi_{\text{ref}}\|_\infty \simeq 8.2314 \times 10^{-12}$. Fig. 4.6 displays a wavelike reflection off of the left boundary, which can be made arbitrarily small by extending the boundary further to the left, and numerical errors on the right.

4.5.3 Circular Orbits: Waveforms and Luminosities

This subsection compares our numerical results for circular orbits to those obtained by other authors. For brevity we restrict ourselves to $\ell = 2$, but note that our method maintains its performance for higher ℓ . For our simulations, we have chosen⁴ $M = 1 = m_p$, with $\xi_{\text{max}} = x_{\text{max}} = 1000 + 2\log(500 - 1) \simeq 1012$ and $\xi_{\text{min}} = x_{\text{min}} = -200$ as the outer and inner boundaries. We have used 45+200 subdomains, each with $N = 21$ points, and a smoother defined by $\tau = 1000$ and $\delta = 0.0002$. For these choices, we have integrated to $t_F = 2500$ with time step $\Delta t = 0.005$. With these parameters we compute waveforms with a relative error of better than 10^{-8} . Radiation boundary conditions (4.62) have been enforced through Table 4.1. Other parameters or non-uniformly placed subdomains may prove advantageous, but we have not explored all possibilities.

We first describe what we have measured. The luminosities of gravitational energy and angular momentum across an arbitrarily large spherical surface are de-

⁴By dividing Eq. (4.1) by m_p we can solve for the per-particle-mass perturbation Ψ/m_p (from the coding standpoint, this is equivalent to setting $m_p = 1$). Physical waveforms and other quantities can then be recovered via multiplication by appropriate powers of m_p .

Energy luminosity $(\dot{E}_{2m} + \dot{E}_{2,-m})/m_p^2$					
m	dG, read off	dG, extract	FE	FR	FD
1	$8.17530620 \times 10^{-7}$	8.1633×10^{-7}	8.1662×10^{-7}	8.1633×10^{-7}	8.1623×10^{-7}
2	$1.70685914 \times 10^{-4}$	1.7062×10^{-4}	1.7064×10^{-4}	1.7063×10^{-4}	1.7051×10^{-4}

Angular momentum luminosity $(\dot{L}_{2m} + \dot{L}_{2,-m})/m_p^2$					
m	dG, read off	dG, extract	FE	FR	FD
1	$1.83102416 \times 10^{-5}$	1.8283×10^{-5}	1.8289×10^{-5}	1.8283×10^{-5}	1.8270×10^{-5}
2	$3.82285415 \times 10^{-3}$	3.8215×10^{-3}	3.8219×10^{-3}	3.8215×10^{-3}	3.8164×10^{-3}

Table 4.2: $\ell = 2$ LUMINOSITIES FOR A CIRCULAR ORBIT WITH $(p, e) = (7.9456, 0)$.

terminated from the master functions $\Psi_{\ell m}^{\text{CPM}}(u + x, r)$ and $\Psi_{\ell m}^{\text{Z}}(u + x, r)$. We view the retarded time $u = t - x$ as fixed, but with r, x arbitrarily large. Note that $x \sim r$, as $r \rightarrow \infty$. In the $r \rightarrow \infty$ limit we have the energy and angular momentum luminosities across an infinite-radius spherical surface given by Eqs. (2.58, 2.59). The individual multipole contributions ($\dot{E}_{\ell m}$ and $\dot{L}_{\ell m}$) to the total energy and angular momentum luminosities decay exponentially with ℓ [157, 178, 78]. A few simplifications concerning $\dot{E}_{\ell m}$ and $\dot{L}_{\ell m}$ are worth noting. First, due to the fact that the particle moves in the equatorial plane, the following conditions hold: $\ell + m$ even $\implies \Psi^{\text{CPM}} = 0$ and $\ell + m$ odd $\implies \Psi^{\text{ZM}} = 0$. To establish these conditions, note, for example, that when $\ell + m$ is even the axial source terms $F_{\ell m}^{\text{CPM}}$ and $G_{\ell m}^{\text{CPM}}$ are identically zero. Second, from the behavior of the master functions under the mapping $m \rightarrow -m$, we have $\dot{E}_{\ell, m} = \dot{E}_{\ell, -m}$ and $\dot{L}_{\ell, m} = \dot{L}_{\ell, -m}$ [157].

We will either simply “read off” waveforms at $r_{\text{max}} = 1000$ or use the extraction technique. Table 4.2 compares our dG, circular-orbit, and $\ell = 2$ energy and angular momentum luminosities to results obtained by other numerical methods described in the literature. Such a comparison is not straightforward as the finite-element (FE) results of Sopena and Laguna [204] involved reading off the master functions at $x = 2000$, while the finite-difference (FD) results of Martel [157] involved read-off at $x = 1500$ (here we always assume $M = 1$). The frequency-domain (FR) results of

Total $\ell = 2$ energy luminosity $m_p^{-2} \sum_{m=-2}^2 \langle \dot{E}_{2m} \rangle$			
Orbit parameters	dG, read off	dG, extract	FR
$e = 0.18891539, p = 7.50477840$	2.59367×10^{-4}	2.59296×10^{-4}	2.59296×10^{-4}
$e = 0.76412402, p = 8.75456059$	1.57146×10^{-4}	1.57120×10^{-4}	1.57131×10^{-4}

Total $\ell = 2$ angular momentum luminosity $m_p^{-2} \sum_{m=-2}^2 \langle \dot{L}_{2m} \rangle$			
Orbit parameters	dG, read off	dG, extract	FR
$e = 0.18891539, p = 7.50477840$	4.91165×10^{-3}	4.91018×10^{-3}	4.91016×10^{-3}
$e = 0.76412402, p = 8.75456059$	2.09297×10^{-3}	2.09220×10^{-3}	2.09221×10^{-3}

Table 4.3: TOTAL $\ell = 2$ LUMINOSITIES FOR ECCENTRIC ORBITS.

Poisson, as reported in [157], for the wave forms at infinity rely on the appropriate boundary value problems in the frequency domain, and of the three should afford the most direct comparisons.

4.5.4 Eccentric Orbits: Waveforms and Luminosities

This subsection compares our numerical results for eccentric orbits to the frequency (FR) domain results of Tanaka *et al* [201] (rather than Poisson’s frequency domain results). We again choose 45+200 subdomains, each with $N = 21$ points, and $\Delta t \simeq 0.01$. Due to the incommensurate radial T_r and azimuthal T_ϕ periods, we encounter the standard difficulty in obtaining measurements from eccentric-orbit simulations. Ideally, we would average measured luminosities over an infinite time, but will content ourselves with averaging over 4 radial cycles. Given a time series $A(t)$, we compute its corresponding average as

$$\langle A \rangle \equiv \frac{1}{T_2 - T_1} \int_{T_1}^{T_2} dt A(t), \quad T_2 - T_1 = 4T_r. \quad (4.68)$$

Table 4.3 compares our total $\ell = 2$ angular momentum and energy luminosities to the frequency (FR) domain results of Ref. [201]. In that reference the authors

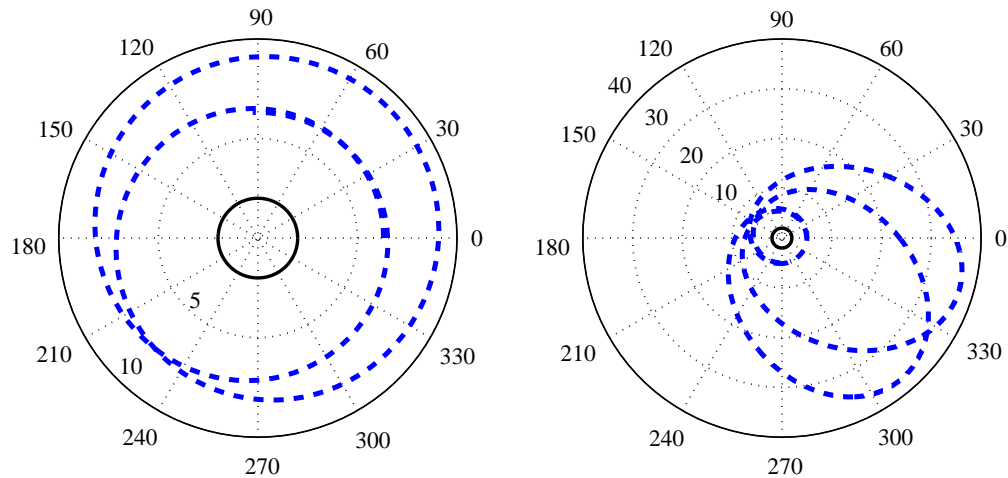


Figure 4.7: ORBITAL PATHS. The left panel shows one orbital period for $(e, p) = (0.18891539, 7.50477840)$. The right panel shows two orbital periods for $(e, p) = (0.76412402, 8.75456059)$. In each case the dark inner circle is the horizon. We have used the (r, ϕ) system to construct these polar plots.

claim a relative numerical error of better than 10^{-4} , which we have confirmed. We have retained enough significant digits in (e, p) to match the parameters (E_p, L_p) chosen in that reference. While we achieve relative errors of better than 10^{-4} for our *averaged* and *extracted* luminosities, we achieve single precision accuracy for our waveforms as a time series at $x = b$. Figure 4.7 exhibits the orbital paths for the two cases considered in this subsection, and Fig. 4.8 shows the corresponding waveforms.

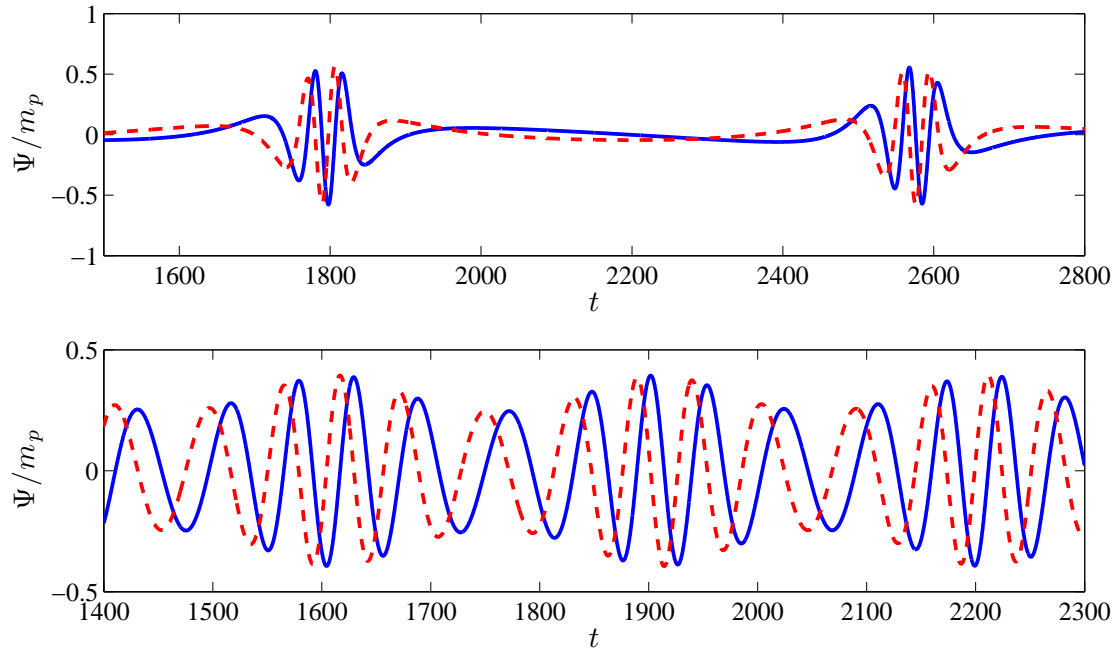


Figure 4.8: WAVEFORMS FOR $\ell = 2$, $m = 2$. The top panel shows the $(e, p) = (0.76412402, 8.75456059)$ extracted waveform, and the bottom panel the $(e, p) = (0.18891539, 7.50477840)$ extracted waveform. Solid blue lines and dashed red lines respectively correspond to real and imaginary parts.

CHAPTER FIVE

Junk Solutions Seeded by Trivial Initial Data

5.1 Introduction

A common approach for computing EMRB waveforms is to numerically solve Eq. (4.1) as a time-domain initial boundary value problem with prescribed initial data. This was carried out in the previous chapter with a nodal dG method. In our discussion of initial data we briefly alluded to unintended consequences which have been appropriately handled. We now return to this issue with our full attention.

The exact initial data for generic point-particle trajectories is non-trivial, and the most common choice is therefore to set both Ψ and its time derivative to zero. (See Refs. [158, 184, 54, 55] for the construction of more realistic data.) Inspection of (4.1) shows that trivial data is inconsistent with the jump conditions stemming from the delta function terms in the inhomogeneity. Thus, trivial data results in an impulsive (i. e. discontinuous in time) start-up. This chapter addresses the main question of if, and when, a *physical* solution eventually emerges from such trivial initial data. Ideally, we would have both the correct source terms and initial conditions. Without the exact initial data, we consider modifying the source terms according to the procedure outlined in Sec. 4.4.1 such that they are consistent with the choice of trivial initial data.

To appreciate some of the issues associated with the main question above, consider a particle in a fixed circular orbit. The energy \dot{E}^∞ and angular momentum \dot{L}^∞ luminosities for gravitational waves at future null infinity are then constant in time and obey the relation $\dot{E}^\infty = \Omega \dot{L}^\infty$, where Ω is the angular orbital velocity of the particle. However, verification of this relationship is limited by a finite computational domain, leading to an $O(r^{-1})$ error (see Ref. [237] for a recent suggestion towards overcoming this limitation). Therefore, numerical verification of $\dot{E}^\infty = \Omega \dot{L}^\infty$ is a

useful diagnostic only in the distant wave-zone. In the near-zone we might also test “ $\dot{E} = \Omega \dot{L}$ ”, now constructing the luminosities with self-force quantities via Eq. 2.64; however, because Ψ is discontinuous at the particle location, self-force measurements will involve large errors unless due care is taken. For generic quasi-periodic orbits, selection of a meaningful set of diagnostics is not straightforward. In particular, we can neither infer steady-state behavior throughout the computational domain, nor can we claim to have a solution which solves the hypothetical “true” initial value boundary problem. These difficulties are due to the inconsistent initial conditions. That is, we are really solving a problem different from the physical one. As a partial resolution of these issues, we examine a direct test condition which is necessary to claim that a physically correct solution has been achieved everywhere in the computational domain. This is a simple self-consistency condition relating Ψ^{CPM} and the Regge-Wheeler (RW) Ψ^{RW} master functions. Each master function describes the same physical axial perturbations, and violations of this relationship are necessarily due to numerical errors and/or incorrect initial conditions.

We will refer to errors seeded by the initial conditions as “junk”. One type of junk either propagates off the computational domain or decays away. We collectively refer to such junk radiation, junk quasi-normal ringing, and junk Price tails as *dynamical junk*. The key observation of this chapter is that trivial initial conditions *may* also give rise to a static distributional junk solution Ψ_{Jost} , which we refer to as *Jost junk*. In terms of the “Schrödinger operator” $H = -\partial_x^2 + V$, a Jost solution satisfies $H\Psi_{\text{Jost}}^\pm = \nu^2\Psi_{\text{Jost}}^\pm$, with $\Psi_{\text{Jost}}^\pm \sim \exp(\pm i\nu x)$ as $x \rightarrow \infty$ [83]. In this chapter, we are exclusively interested in “zero-energy” Jost solutions for which $\nu = 0$, in which case Ψ_{Jost} does not behave exponentially at infinity (see below). Therefore, in what follows a Jost function satisfies a “zero-energy”, time-independent, Schrödinger equation $(-\partial_x^2 + V)\Psi_{\text{Jost}} = 0$ to the left and right of the particle, and, as it turns out,

is discontinuous at the particle location. We find that Ψ_{Jost} has a non-negligible effect in the wave-zone, yet is often small enough to be buried into the $O(r^{-1})$ error associated with a waveform “read-off” in the far-field.

We will adopt trivial initial conditions throughout, but allow for temporally smoothed source terms according to (4.59). Our chief goal is to study the properties of the numerical solutions computed with and without smoothed source terms, especially in the context of the Jost solution. To carry out numerical simulations, we have primarily used the nodal Legendre discontinuous Galerkin method described in Chapter. 4. In addition, some of our results have independently verified with a nodal Chebyshev method (similar to the one described in Refs. [56, 57]), which also features multiple subdomains and upwinding¹. Our nodal Chebyshev method treats the jump discontinuities at the particle location in the same fashion as outlined in Ref. [89] for the nodal dG method. Both our dG and Chebyshev methods solve a first order system representing (4.39). Most of this chapter considers circular orbits, for which $\lambda = t$, $\xi = x$, and the shift vector $\beta^\xi = 0$. Thus, for circular orbits, our system (4.39) becomes

$$\begin{aligned}\partial_t \Psi &= -\Pi \\ \partial_t \Pi &= -\partial_x \Phi + V(r)\Psi + J_1 \delta(x - x_p) \\ \partial_t \Phi &= -\partial_x \Pi + J_2 \delta(x - x_p),\end{aligned}\tag{5.1}$$

where the time-dependent jump factors are $J_1 = [[\partial_x \Psi]]$ and $J_2 = -[[\partial_t \Psi]]$. Also, in the case of circular orbits, the variables Π and Φ are $-\partial_t \Psi$ and $\partial_x \Psi$, respectively.

This Chapter is organized as follows. Section 5.2 focuses on the Jost solution, from both empirical and analytical standpoints. Here we present analytic formulas

¹Comments towards the generality of our observations will be addressed, but in general the central issue is *how* the δ -singularity is handled and not the underlying numerical scheme.

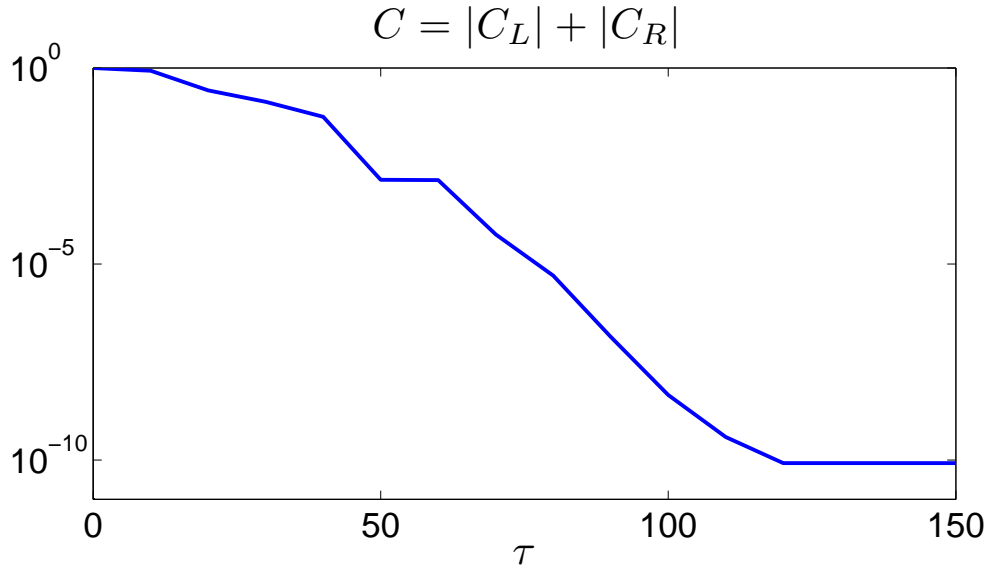


Figure 5.1: DEPENDENCE OF C ON SMOOTHING PARAMETERS. We have empirically determined that $|C_L| = \frac{1}{2} = |C_R|$ for an impulsive start-up, corresponding to $C = 1$ at the leftmost point. The parameter δ is different for each τ ; $\delta = 2$ for $\tau = 10$ and $\delta = 0.0058$ for $\tau = 150$.

for Jost solutions and compare them with numerical results. Section 5.3 considers several practical consequences of impulsive start-up for EMRB modeling with circular orbits: violation of the axial consistency condition, contamination of waveform luminosities, and influence on self-force measurements. This section also gives a preliminary report on consequences for eccentric orbits. Universality of our results are considered in Sec. 5.4, where we touch upon finite-difference methods and alternative first order reductions. Longer calculations appear in Appendix D.

5.2 Jost Solution

To better explain the origin of the Jost junk solution, we first consider a toy model: the ordinary 1+1 wave equation with distributional forcing. We then examine the Jost solution for the master wave equations, with a forcing determined by a circular orbit.

a, b :	Endpoint of computational domain $[a, b]$.
S_L, S_R :	Number of subdomains to left and right of particle.
N :	Number of points on each subdomain.
τ, δ :	Smoothing parameters introduced in Eq. (4.59).
$\Delta t, t_F$:	Timestep and final time.
$M = 1$:	Schwarzschild mass parameter.
$m_p = 1$:	Particle mass.

Table 5.1: BASIC SET OF PARAMETERS FOR A NUMERICAL SIMULATION. This set is not complete, but in what follows we often refer to these variables. For all simulations we continue to set $M = 1 = m_p$, where the choice $m_p = 1$ is equivalent to working with per-particle-mass perturbations Ψ/m_p .

5.2.1 Forced 1+1 Wave Equation

We return to the forced wave equation model (4.65), written as a first order system (5.1) with $V = 0$, for which an exact particular solution is known. For this model, junk radiation propagates off the computational domain with speeds ± 1 . However, when numerically solving this equation subject to (incorrect) trivial initial conditions, we observe that the numerical solution no longer converges to the particular solution. For simulations involving (5.1), we have used the dG method with (cf. Table 5.1) $a = -100$, $b = 100$, $S_L = 10$, $S_R = 10$, $N = 27$, and $\Delta t = 0.01$. To compute errors relative to the exact solution, we have first interpolated onto a uniformly spaced x -grid with 5121 points. Furthermore, to better model the circular orbit scenario for EMRBs, we have taken $v = 0$.

With the exact solution used to generate initial conditions at $t = 0$, the nodal dG method exhibits spectral convergence throughout the computational domain (see Sec. 4.5.1). However, with trivial initial conditions, only the corresponding numerical derivatives, $\Pi_{\text{numerical}}$ and $\Phi_{\text{numerical}}$, converge to the correct values, whereas $\Psi_{\text{numerical}}$ itself is off by a constant value on each subdomain. Let us write

$$\Psi_{\text{numerical}} = (\Psi_L + C_L) \Theta(-x) + (\Psi_R + C_R) \Theta(x), \quad (5.2)$$

where $\Theta(x)$ is the Heaviside function and the exact solution from (4.66) is

$$\begin{aligned}\Psi_L &= -\frac{1}{2}\sin(t+x) - \frac{1}{2}i\cos(t+x) \\ \Psi_R &= -\frac{1}{2}\sin(t-x) + \frac{1}{2}i\cos(t-x).\end{aligned}\tag{5.3}$$

We introduce the time-independent 1+1 Jost junk solution

$$\Psi_{\text{Jost}} = C_L\Theta(-x) + C_R\Theta(x),\tag{5.4}$$

in order to express the numerical solution as $\Psi_{\text{numerical}} = \Psi_{\text{exact}} + \Psi_{\text{Jost}}$.

We examine the dependence of $C = |C_L| + |C_R|$ on the smoothing parameters (τ, δ) , defined analogously to those in (4.59), but here introduced to smooth our toy source term $\cos t\delta(x) + i\cos t\delta'(x)$. We restrict the parameter space by first choosing τ , and then finding the smallest δ such that $\frac{1}{2}[\text{erf}(\sqrt{\delta}(t - t_0 - \tau/2) + 1)]$ is less than 10^{-16} when $t = 0$ and greater than $1 - 10^{-16}$ when $t = \tau$. These requirements ensure that the start-up phase is smooth to machine precision, while providing the most gradual rate at which the distributional source terms are turned-on. Figure 5.1 shows that the troublesome constant term is arbitrarily well suppressed by the smoothing procedure. However, we find that the value of C remains fixed when varying the timestep. The final run time for each data point in the plot is $t_F = \tau + 150$. No essential difference exists between the $v = 0$ and $v \neq 0$ cases, except that for the latter case we must ensure that the particle does not get too close to the boundary. Let Ψ_{smooth} represent $\Psi_{\text{numerical}}$ obtained with smoothing, and $\Psi_{\text{impulsive}}$ represent $\Psi_{\text{numerical}}$ obtained without smoothing. Then we have shown $\Psi_{\text{smooth}} \simeq \Psi_{\text{exact}}$, so that

$$\Psi_{\text{Jost}} \simeq \Psi_{\text{impulsive}} - \Psi_{\text{smooth}}\tag{5.5}$$

is another expression for the Jost solution, valid up to method error.

Jost Junk as a Time–dependent Constraint Violating Solution

The Jost junk solution does not instantaneously appear during our scheme’s first timestep $0 \rightarrow \Delta t$, nor can it be found in our (trivial) initial conditions. Instead, we must wait a finite time for it to have completely developed, although it may seem counterintuitive to speak of a developing static solution. To confront this paradox, consider a natural time–dependent generalization of the static Jost junk solution (5.4):

$$\Psi_{\text{Jost}} = C_L \Theta(-x) \Theta(t+x) + C_R \Theta(x) \Theta(t-x), \quad (5.6)$$

which solves the second order wave equation

$$(-\partial_t^2 + \partial_x^2) \Psi_{\text{Jost}} = [[\Psi_{\text{Jost}}]] \Theta(t) \delta'(x). \quad (5.7)$$

Numerical evidence indicates (5.6) is the generate time–dependent Jost junk. At late times, after which the advecting Heaviside propagates off the numerical grid, (5.6) agrees with the time–independent Jost junk solution (5.4) from the previous section. Observe that:

1. $\Psi_{\text{Jost}} = 0$ for $t \leq 0$, and thus compatible with trivial initial data for Ψ .
2. $\Psi_{\text{exact}} + \Psi_{\text{Jost}}$ does not solve the 2nd order 1+1 wave equation (4.65) at $x = 0$.
3. At sufficiently late times $\partial_t \Psi_{\text{Jost}} = 0$ and $\partial_x \Psi_{\text{Jost}} = [[\Psi_{\text{Jost}}]] \delta(x)$.

Our second and third observations suggest Ψ_{Jost} may act to violate the distributional constraint discussed in Sec. 4.2.6, although a complete understanding is still lacking. For the remainder of the chapter we will continue to focus on time–independent Jost junk and it’s consequence without identifying the generating mechanism.

5.2.2 Master Wave Equations

The first numerical experiment in this subsection involves the axial sector with V^{RW} given by (2.45) and assumes CPM source terms (4.7). To empirically verify that an impulsive start-up also leads to a Jost solution in this setting, we will form and plot the expression (5.5). Later on, we will give analytic expressions for static Jost solutions. Our smoothing parameters are $\tau = 150$ and $\delta = 0.0058$. We compute the $(\ell, m) = (3, 2)$ metric perturbations for a particle in circular orbit initially at $(r, \phi) = (7.9456, 0)$. Other parameters (cf. Table 5.1) are $a \simeq -202.16$, $b = 60 + 2 \log(29) \simeq 66.73$, $S_L = 30$, $S_R = 8$, $N = 26$, $\Delta t \simeq 0.03$, and $t_F = 600$. Figure 5.2 shows the result. The plots suggest that the Jost junk solution affects $\Psi_{\text{impulsive}}^{\text{CPM}}$ and its spatial derivatives.

For both axial and polar perturbations generated by circular orbits, we now present the analytic form of the Jost solution, suppressing throughout the analysis both orbital ℓ and azimuthal m indices. For circular orbits we have observed empirically that the Jost junk solution can be written as

$$\Psi_{\text{Jost}}^{\text{axial/polar}} = C_L v_L^{\text{axial/polar}} \Theta(-x) + C_R v_R^{\text{axial/polar}} \Theta(x), \quad (5.8)$$

where C_L and C_R are complex constants. The functions $v_{L,R}^{\text{axial/polar}}$ satisfy a Schrödinger equation $Hv = 0$ defined by the operator

$$H^{\text{axial/polar}} = -\partial_x^2 + V^{\text{RW/Z}}, \quad (5.9)$$

where V^{RW} is given in Eq. (2.45) and V^{Z} is given in Eq. (2.38). The functions $v_L^{\text{axial/polar}}$ satisfy the Schrödinger equation to the left of the particle, and the functions $v_R^{\text{Axial/Polar}}$ the equation to the right. The relevant solutions to $Hv = 0$ decay either

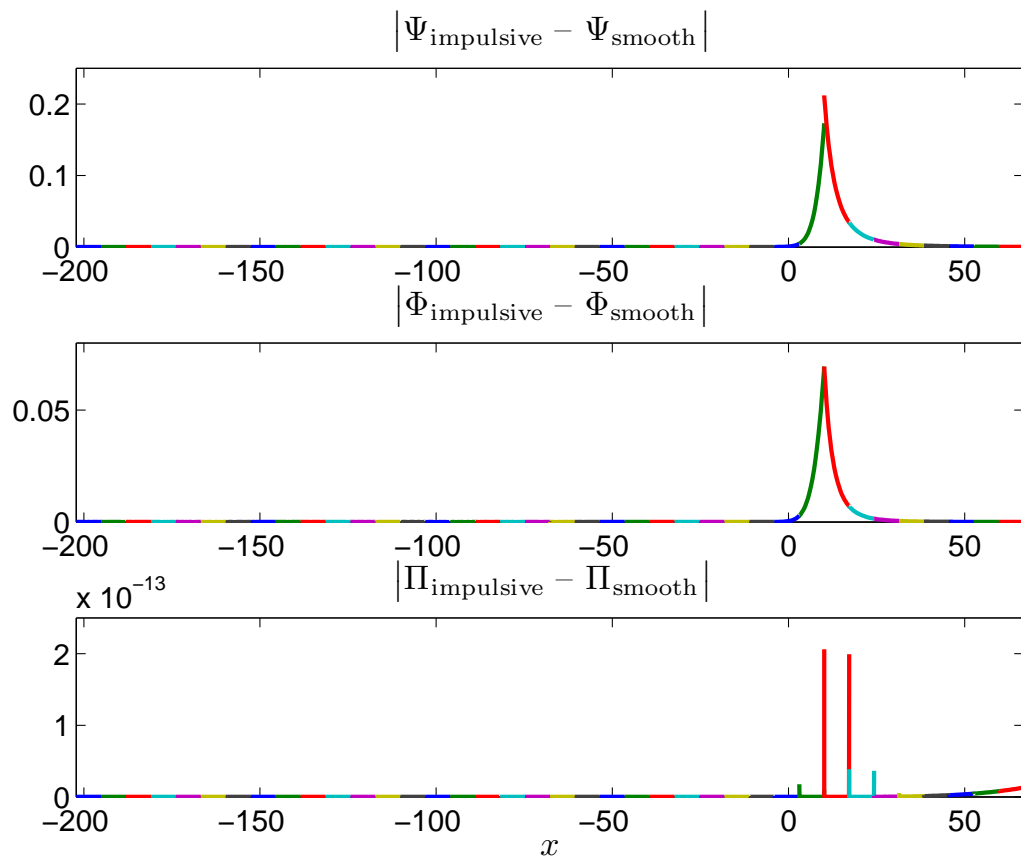


Figure 5.2: DIFFERENCE BETWEEN SMOOTHLY AND IMPULSIVELY STARTED CPM FIELDS. Here $\ell = 3$, $m = 2$, and the snapshot is taken at $t = 600$.

as $r \rightarrow 2M^+$ or $r \rightarrow \infty$.

We derive expressions for all four functions $v_{L,R}^{\text{axial/polar}}$ in Appendix D, adopting the dimensionless radius $\rho = (2M)^{-1}r$ as the basic variable. Here we record the set of axial functions,

$$v_L^{\text{axial}}(\rho) = \rho^{-\ell} {}_2F_1(\ell + j + 1, \ell - j + 1; 1; (\rho - 1)/\rho) \quad (5.10a)$$

$$v_R^{\text{axial}}(\rho) = \rho^{-\ell} {}_2F_1(\ell + j + 1, \ell - j + 1; 2(\ell + 1); \rho^{-1}), \quad (5.10b)$$

where for gravitational perturbations the spin $j = 2$. Evidently, up to transformations of the dependent and independent variables, the equation $H^{\text{axial}}v = 0$ is the hypergeometric equation. The equation $H^{\text{polar}}v = 0$ involves an extra regular singular point, and its normal form is a particular realization of the Heun equation. Nevertheless, by exploiting certain intertwining relations between the polar and axial master functions [12], we are likewise able to express $v_{L,R}^{\text{polar}}$ in terms of the classical Gauss-hypergeometric function ${}_2F_1$. The Appendix D gives further details.

To complete our analytic expressions for the Jost solutions, we still must determine C_L and C_R . Recall our notation for a time-dependent jump for circular orbits,

$$[[\Psi]](t) = \lim_{\epsilon \rightarrow 0^+} [\Psi(t, r_p + \epsilon) - \Psi(t, r_p - \epsilon)]. \quad (5.11)$$

For trivial data (that is $\Psi = 0$) the analytic jump (4.23)

$$[[\Psi_{\text{analytic}}]](t) = \frac{F(t, r_p)}{f_p} \quad (5.12)$$

will in general not be satisfied at $t = 0$. We find empirically that the jump in Ψ_{Jost} exactly cancels $[[\Psi_{\text{analytic}}]](0)$, while the jump in $\partial_x \Psi_{\text{Jost}}$ is zero. The system of

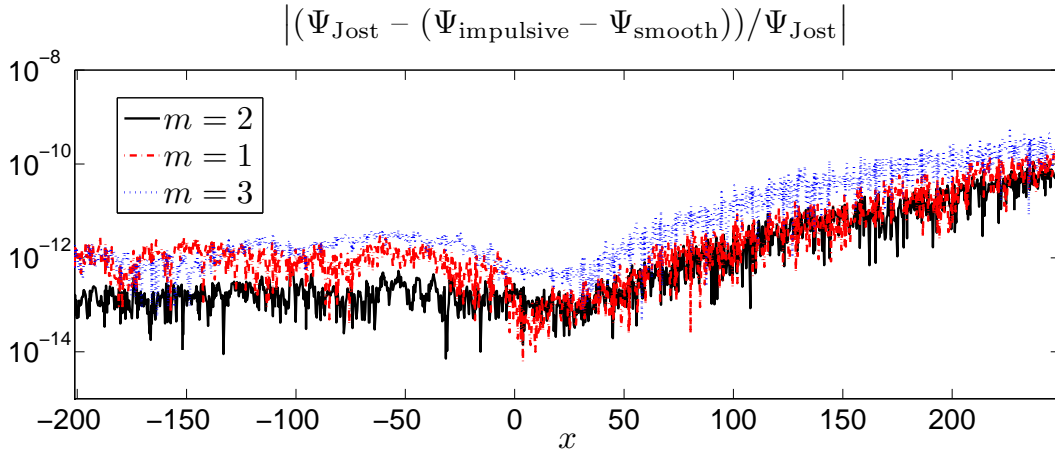


Figure 5.3: COMPARISON BETWEEN ANALYTIC AND NUMERICAL JOST SOLUTIONS. CPM and ZM modes respectively correspond to $(\ell, m) = (3, 2)$ and $(\ell, m) = (3, 1), (3, 3)$.

equations used to determine our constants is therefore

$$\begin{aligned} v_R(r_p)C_R - v_L(r_p)C_L &= -\frac{F(0, r_p)}{f_p} \\ v'_R(r_p)C_R - v'_L(r_p)C_L &= 0, \end{aligned} \tag{5.13}$$

which has a solution

$$\begin{aligned} C_R &= -\frac{F(0, r_p)}{f_p} \left(\frac{v'_L}{v_R v'_L - v_L v'_R} \right)_p \\ C_L &= C_R \left(\frac{v'_R}{v'_L} \right)_p. \end{aligned} \tag{5.14}$$

Recall that Ψ_{Jost} may be numerically approximated as $\Psi_{\text{impulsive}} - \Psi_{\text{smooth}}$ [cf. Eq. (5.5)]. Figure 5.3 depicts the relative error $|(\Psi_{\text{Jost}} - (\Psi_{\text{impulsive}} - \Psi_{\text{smooth}})) / \Psi_{\text{Jost}}|$ for $\ell = 3$ perturbations, with Ψ_{Jost} given by (5.8). To generate this figure, we have used nearly the same set-up as described for Fig. 5.2, but with the outer boundary $b = 240 + 2 \log(119)$ and final time $t_F = 3100$.

5.2.3 Jost Solution and Radiation Boundary Conditions

We wish to examine the extent to which the right analytic Jost solutions $v_R^{\text{axial/polar}}$ satisfy radiation boundary conditions adopted for our numerical simulations. Unfortunately, for blackhole perturbations the issue would seem difficult to address analytically. Therefore, we consider the analogous issue for the flatspace radial wave equation.

Consider a flatspace multipole solution $r^{-1}\Psi(t, r)Y_{\ell m}(\theta, \phi)$ to the ordinary 3+1 wave equation, and assume the multipole is initially of compact support in radius r . Exact non-reflecting boundary conditions relative to a sufficiently large outer boundary radius b then take the form [10]

$$\left(\frac{\partial\Psi}{\partial t} + \frac{\partial\Psi}{\partial r}\right)\Big|_{r=b} = \frac{1}{b^2} \sum_{j=1}^{\ell} k_{\ell,j} \int_0^t \exp(b^{-1}k_{\ell,j}(t-t'))\Psi(t', b)dt'. \quad (5.15)$$

Here $\{k_{\ell,j} : j = 1, \dots, \ell\}$ are the roots of the modified cylindrical Bessel function $K_{\ell+1/2}(x)$, also known as MacDonald's function. All $k_{\ell,j}$ lie in the left-half plane. Moreover, the scaled roots $k_{\ell,j}/(\ell+1/2)$ accumulate on a fixed transcendental curve as ℓ grows [10, 143], so the exponentials $\exp(b^{-1}k_{\ell,j}t)$ tend to decay more quickly in time $t > 0$ for larger ℓ .

For the flatspace setting at hand, the Jost solution satisfies

$$v'' - \frac{\ell(\ell+1)}{r^2}v = 0, \quad (5.16)$$

and two appropriate linearly independent solutions are the following:

$$v_L(r) = r^{\ell+1}, \quad v_R(r) = r^{-\ell}. \quad (5.17)$$

We therefore examine to what extent $v_R(r)$ satisfies (5.15). Straightforward calculation yields

$$\begin{aligned} \left. \left(\frac{\partial v_R}{\partial r} \right) \right|_{r=b} &= -b^{-1} v_R(b) \sum_{j=1}^{\ell} \exp(b^{-1} k_{\ell,j} t) \\ &+ \frac{1}{b^2} \sum_{j=1}^{\ell} k_{\ell,j} \int_0^t \exp(b^{-1} k_{\ell,j} (t-t')) v_R(b) dt'. \end{aligned} \quad (5.18)$$

The function $v_R(r)$ does not satisfy the non-reflecting condition (5.15); however, the violation of (5.15) decays exponentially fast. For blackhole perturbations we likewise expect that $v_R^{\text{axial/polar}}(\rho)$ violates our radiation boundary conditions only by exponentially decaying terms, and have seen some evidence of this behavior in our numerical simulations.

We have also observed persistent junk solutions when adopting the Sommerfeld condition at the outer boundary b along with impulsive start-up. We differentiate between two scenarios: the first involving a detector which is not in causal contact with the outer boundary b during the simulation, and a second with the detector located at b . For the first scenario, the static junk solution which develops and persists around the detector is precisely Ψ_{Jost} . For the second, we also observe a persistent junk solution, but one which is distorted from Ψ_{Jost} in a boundary layer near b . Such distortion presumably arises since Ψ_{Jost} satisfies the outer Sommerfeld condition only up to an $O(r^{-\ell-1})$ error term.

5.3 Consequences of Impulsive Starting Conditions

5.3.1 Loss of Temporal Convergence

In this scenario we again consider the forced wave equation (4.65) with $v = 0$ and trivial initial data $\Psi = \Pi = \Phi = 0$. We will compute errors over all fields, after interpolation onto a reference grid, and against the exact solution. Before computing errors for the Ψ variable when adopting trivial initial data we first subtract off the analytic Jost junk solution (5.4).

Our first test involves the minimal two domain set up with smoother parameters given by $t_0 = 0$, $\tau = 3$, and $\delta = 10$. For these choices, the source is switched on (to machine precision) and is fully on by $t = 3$. Resolution of the transition requires relatively many points, and we have chosen $N = 61$ on each subdomain. For the final time $t_F = 10$, we demonstrate the anticipated 4th order temporal convergence in the left panel of Fig. 5.4. We note that, as indicated in the figure, convergence is abruptly lost without the smoother. However, even without the smoother, by adopting multiple subdomains we also recover convergence to the exact solution (of course assuming $t_F > 5$, so that the initial incorrect profiles can fully propagate off the domain). Indeed, the right panel of Fig. 5.4 documents the results for the same problem, but now without smoothing and 20 subdomains, each with $N = 7$ points. We explain this observation by noting that for $N = 1$ our dG method formally becomes a finite-volume method. Therefore, many low-order elements corresponds to a more dissipative numerical flux, and the extra dissipation smooths the oscillations stemming from our impulsively started problem.

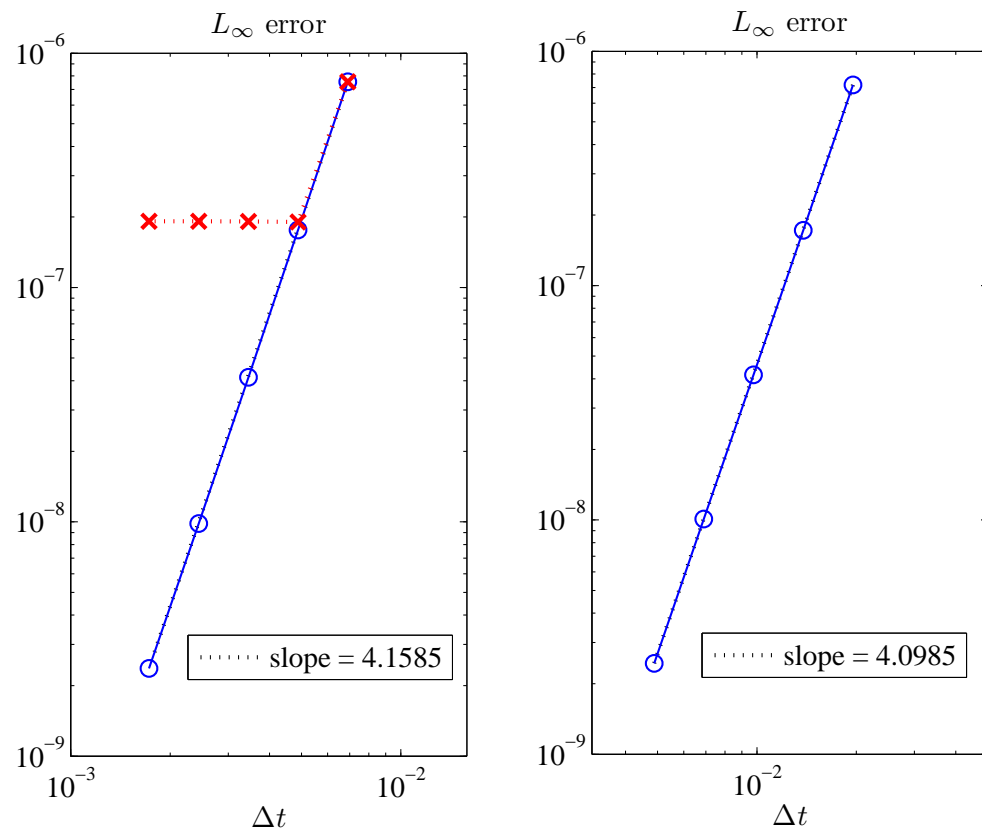


Figure 5.4: TEMPORAL CONVERGENCE WITH TRIVIAL INITIAL DATA. The left panel compares the two-domain experiment run with and without the smoother, denoted by circles and crosses respectively. The right panel corresponds to multiple subdomains and no smoother. As described in the text, on each subdomain the Jost junk solution is subtracted off before computing errors.

5.3.2 Inconsistent Modeling of the Axial Sector

Thus far we have studied axial perturbations by solving for Ψ^{CPM} . Axial perturbations are equally well described by the Regge–Wheeler master function [157]

$$\Psi^{\text{RW}} = -\frac{f}{r}q_r. \quad (5.19)$$

In fact both Ψ^{CPM} and Ψ^{RW} solve the generic wave equation (4.1) with potential V^{RW} . However, the wave equations for Ψ^{CPM} and Ψ^{RW} have different distributional source terms [159, 89, 157]. As shown in [159], these master functions obey

$$\Psi^{\text{RW}} + \frac{1}{2}\Pi^{\text{CPM}} = 0, \quad r \neq r_p(t), \quad (5.20)$$

and we refer to this formula as the *axial consistency condition*. For circular orbits this condition becomes $\Psi^{\text{RW}} - \frac{1}{2}\partial_t\Psi^{\text{CPM}} = 0$, $r \neq r_p$. We now numerically examine the extent to which the axial consistency condition is violated when the master functions $\Psi^{\text{RW,CPM}}$ are obtained with and without smoothing.

For all experiments we again enforce Sommerfeld boundary conditions at the left physical boundary, and radiation outer boundary conditions on the right boundary. Now our smoothing parameters are $t_0 = 0$, $\tau = 100$, and $\delta = 0.05$. We compute the $(\ell, m) = (2, 1)$ metric perturbations for a particle in circular orbit initially at $(r, \phi) = (7.9456, 0)$. Other parameters (cf. Table 5.1) are $a = -200$, $b = 30 + 2\log(14) \simeq 35.28$, $S_L = 22$, $S_R = 3$, $N = 31$, $\Delta t = 0.01$, and $t_F = 800$. We first plot $|\Psi^{\text{RW}} + \frac{1}{2}\Pi^{\text{CPM}}|$ at various times. The left panels in Fig. 5.5 show results with smoothing. Although the consistency condition is initially violated, the expression eventually relaxes to a small value once the dynamical junk has propagated off the domain. The right panels in Fig. 5.5 show result without smoothing. Even at late

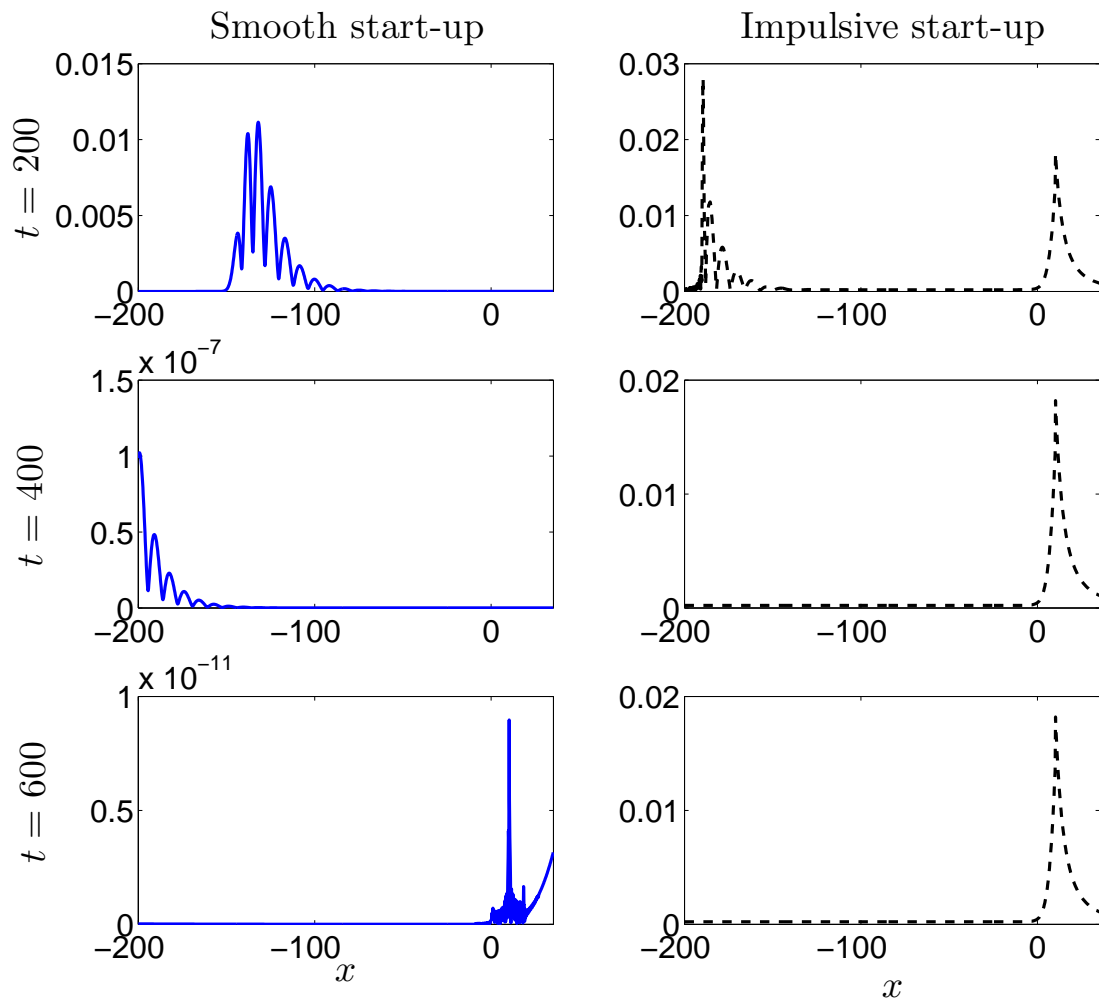


Figure 5.5: SNAPSHOTS OF $|\Psi^{\text{RW}} + \frac{1}{2}\Pi^{\text{CPM}}|$ WITH AND WITHOUT SMOOTHING. The left three panels correspond to smooth start-up and the right three to impulsive start-up. The times at the far left correspond to both sets of panels. Ψ^{RW} is of order 10^{-2} near r_p .

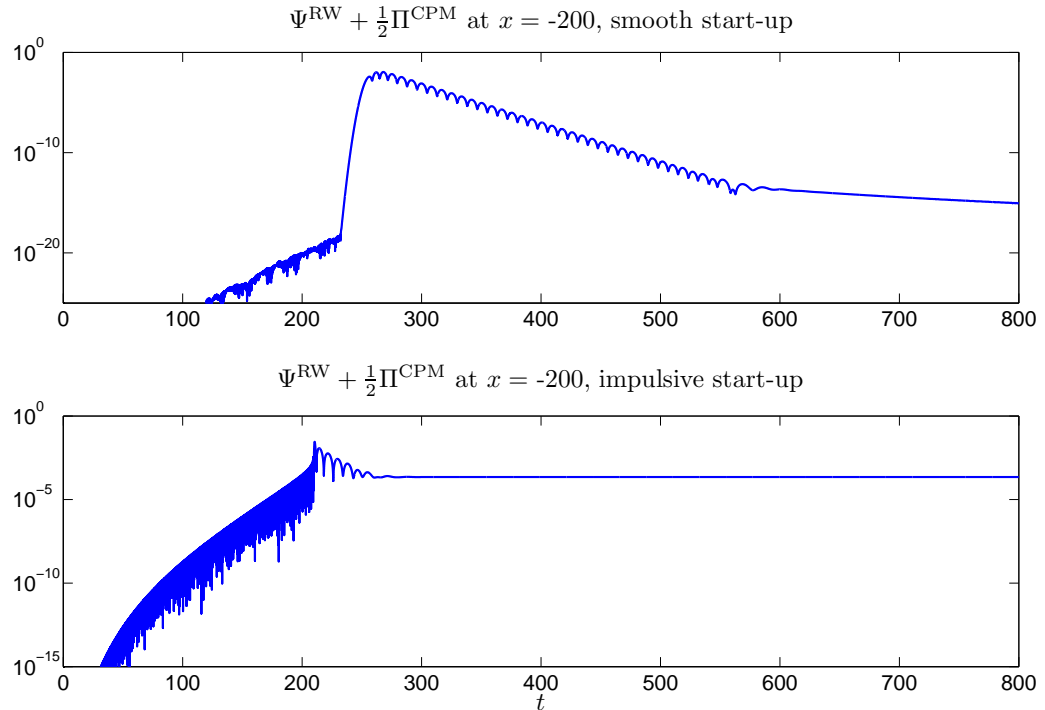


Figure 5.6: TIME SERIES AT $x = -200$ FOR $|\Psi^{\text{RW}} + \frac{1}{2}\Pi^{\text{CPM}}|$ WITH AND WITHOUT SMOOTHING. Ψ^{RW} is of order 10^{-4} at $x = -200$.

times violation in the axial consistency condition is now evident. The plots in Fig. 5.6 depict $|\Psi^{\text{RW}} + \frac{1}{2}\Pi^{\text{CPM}}|$ recorded as a time series at $x = -200$. The plot for smooth start-up indicates that quasinormal ringing and Price decay tails characterize the late-stage dynamical junk, although this ringing is suppressed with more smoothing (e. g. with $\tau = 150$, $\delta = 0.0058$). The plot for impulsive start-up suggests that a static Jost junk solution $\Psi_{\text{impulsive}}^{\text{RW}} - \Psi_{\text{smooth}}^{\text{RW}}$ persists indefinitely (as Π^{CPM} should be unaffected by a similar Jost solution in Ψ^{CPM}).

5.3.3 Contamination of Waveforms

For a given (ℓ, m) multipole either read off at a finite radius or measured at null infinity through an approximate extraction, we can apply standard formulas to estimate

the energy and angular momentum carried away by the gravitational waves. We continue to work with the axial perturbations, with formulas featuring only CPM and RW master functions. The energy and angular momentum luminosities are computable from Ψ^{CPM} by Eqs. (2.58, 2.59), or Ψ^{RW} [159, 204, 157] by

$$\dot{E}_{\ell m}^{\text{RW}} = \frac{1}{16\pi} \frac{(\ell+2)!}{(\ell-2)!} |\Psi_{\ell m}^{\text{RW}}|^2, \quad \dot{L}_{\ell m}^{\text{RW}} = \frac{im}{16\pi} \frac{(\ell+2)!}{(\ell-2)!} \Psi_{\ell m}^{\text{RW}} \int \bar{\Psi}_{\ell m}^{\text{RW}} dt. \quad (5.21)$$

In the distant wave-zone we expect $\dot{E}_{\ell m}^{\text{CPM}} = \dot{E}_{\ell m}^{\text{RW}}$ and $\dot{L}_{\ell m}^{\text{CPM}} = \dot{L}_{\ell m}^{\text{RW}}$. However, Sec. 5.3.2 has shown that impulsive start-up can result in violation of the axial consistency condition (5.20), and such violation in turn results in discrepancies between the above luminosity formulas. As seen in Sec. 5.2.2, whether simulations are based on Ψ^{CPM} or Ψ^{RW} , an impulsive start-up generates a Jost junk solution, even at long distances from the source. Although dynamical junk is also present, its effect is negligible in the wave-zone at late times.

Table 5.2 collects summed luminosities for $(\ell, m) = (2, \pm 1)$ waveforms. The top set of numbers are unaveraged and recorded at time $t_F = 2750$, while the bottom set have been averaged between $t = 2500$ and $t_F = 2500 + 4T_\phi$, where $T_\phi = 2\pi p^{3/2} \simeq 140.7246$. Other parameters (cf. Table 5.1) are $a \simeq -190.34$, $b = 1000 + 2 \log(499) \simeq 1012.43$, $S_L = 30$, $S_R = 150$, $N = 26$, and $\Delta t = 0.038$. For smoothing we use $\tau = 150$ and $\delta = 0.0058$. For circular orbits we expect $\langle \dot{Q}_{\text{smooth}} \rangle = \dot{Q}_{\text{smooth}}$, where brackets denote time averaging for a generic luminosity \dot{Q} . Relative errors are computed by

$$\dot{Q}_{\text{error}} = \frac{|\dot{Q}_{\text{smooth}} - \dot{Q}_{\text{impulsive}}|}{|\dot{Q}_{\text{smooth}}|}. \quad (5.22)$$

For the CPM luminosities computed with smoothing, time averaging has little effect. However, it does enhance the accuracy of the RW luminosities computed with smoothing. Indeed, inspection of the bottom section of Table 5.2 shows that the

\dot{Q}	\dot{Q}_{smooth}	$\dot{Q}_{\text{impulsive}}$	\dot{Q}_{error}
\dot{E}^{CPM}	$8.17530620 \times 10^{-7}$	$8.17530623 \times 10^{-7}$	3.466×10^{-9}
\dot{E}^{RW}	$8.17530652 \times 10^{-7}$	$8.18248752 \times 10^{-7}$	8.783×10^{-4}
\dot{L}^{CPM}	$1.83102415 \times 10^{-5} + i3.2 \times 10^{-14}$	$1.82972897 \times 10^{-5} - i1.2 \times 10^{-8}$	9.968×10^{-4}
\dot{L}^{RW}	$1.83047467 \times 10^{-5} - i2.1 \times 10^{-8}$	$1.66825388 \times 10^{-5} + i8.1 \times 10^{-7}$	9.969×10^{-2}
$\langle \dot{E}^{\text{CPM}} \rangle$	$8.17530620 \times 10^{-7}$	$8.17530620 \times 10^{-7}$	2.837×10^{-10}
$\langle \dot{E}^{\text{RW}} \rangle$	$8.17530617 \times 10^{-7}$	$8.17531431 \times 10^{-7}$	9.966×10^{-7}
$\langle \dot{L}^{\text{CPM}} \rangle$	$1.83102416 \times 10^{-5} - i1.4 \times 10^{-15}$	$1.83102416 \times 10^{-5} + i3.4 \times 10^{-14}$	2.073×10^{-9}
$\langle \dot{L}^{\text{RW}} \rangle$	$1.83102415 \times 10^{-5} + i4.1 \times 10^{-13}$	$1.82927679 \times 10^{-5} + i7.0 \times 10^{-9}$	1.029×10^{-3}

Table 5.2: $\ell = 2$ LUMINOSITIES RECORDED AT $r = 1000$. Entries result from addition of $m = 1$ and $m = -1$ luminosities, and they correspond to a circular orbit with $(r, \phi) = (7.9456, 0)$ initially. \dot{Q}_{error} as been computed with more precision than reported for the table entries.

CPM and RW entries in the \dot{Q}_{smooth} column are in excellent agreement.

Relative to the true luminosity which would be recorded at null infinity, even the exact \dot{E}^{CPM} read off at $r = 1000$ would have an $O(r^{-1})$ error, but here we have viewed the read-off value as the true one. Because \dot{E}^{CPM} is unaffected by the Jost junk solution, $\dot{E}_{\text{error}}^{\text{CPM}}$ estimates error stemming from both the method and any residual dynamical junk. The other luminosities are affected by the Jost junk solution; however, as shown in the Appendix, errors which stem from the Jost solution decay faster than $1/r$. Therefore, these errors should be smaller than the $O(r^{-1})$ errors associated with using the read-off luminosities as approximations to the ones at null infinity.

5.3.4 Self-Force Measurements

Incorporation of self-force effects constitutes an important approach towards modeling realistic gravitational waveforms. For quasi-circular orbits the dissipative part of the self-force is given by (2.64). For perturbations described by the CPM masterfunction and with the Regge-Wheeler gauge, the non-zero contributions (for each

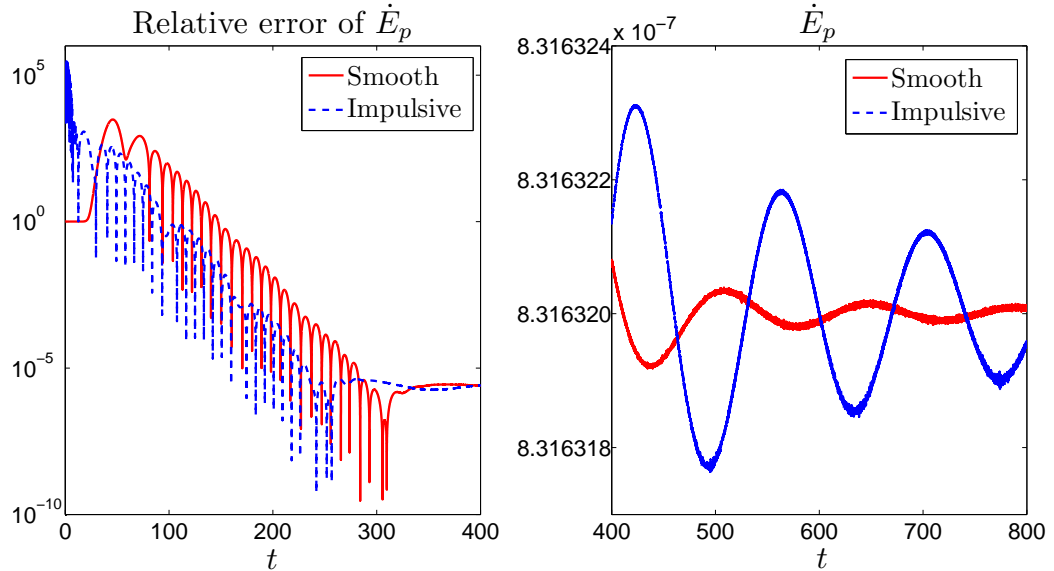


Figure 5.7: \dot{E}_p TIME SERIES FOR SUMMATION OF $\ell = 2$ AND $m = \pm 1$ MODES. In the right panel the curve corresponding to impulsive start-up has the larger amplitude (due to small fluctuations this curve does not appear dashed as indicated in the legend).

mode) involve the axial metric reconstruction Eqs. (2.46)

$$\begin{aligned} \frac{\partial h_{t\phi}}{\partial t} &= \frac{f}{2} \left(r \frac{\partial^2 \Psi}{\partial t \partial r} + \frac{\partial \Psi}{\partial t} \right) X_\phi \\ \frac{\partial h_{t\phi}}{\partial \phi} &= \frac{f}{2} \left(r \frac{\partial \Psi}{\partial r} + \Psi \right) X_{\phi\phi} \end{aligned} \quad (5.23)$$

in a source free region. When numerically forming these expressions, we replace $\partial_t \Psi$ and $\partial_r \Psi$ by $-\Pi$ and $f^{-1}\Phi$.

We now fix $\tau = 100$ and $\delta = 0.014$ to achieve a smooth start-up, run to the final time $t_F = 800$, and pick $\Delta t = 0.005$. Other parameters are the same as those in Sec. 5.3.2. We compute \dot{E}_p and \dot{L}_p for $(\ell, m) = (2, \pm 1)$ perturbations. Because \dot{E}_p is computed with time derivatives of Ψ^{CPM} , the static Jost junk solution does not impact its measurement. We therefore expect that

$$\dot{E}_p(\Psi_{\text{impulsive}}^{\ell m}) \simeq \dot{E}_p(\Psi_{\text{smooth}}^{\ell m}). \quad (5.24)$$

However, an impulsive start-up appears to generate more dynamical junk at late times. Figure 5.7 depicts \dot{E}_p , recorded as a time series, for both impulsive and smooth start-ups. A separate experiment based on waveform read-off near the blackhole and waveform extraction at the outer boundary determines that the energy carried away by the gravitational waves is $\dot{E}_{GW} \simeq 8.3163 \times 10^{-7}$. The relative errors in the left panel of Fig. 5.7 are computed as $|\dot{E}_p - \dot{E}_{GW}|/\dot{E}_{GW}$, and are limited by the accuracy of \dot{E}_{GW} . We therefore do not expect agreement beyond a relative error of 10^{-5} , although clearly such error will settle to a constant value. The time series for both the impulsive and smooth start-up exhibit large oscillations which persist until about $t = 400$. However, beyond $t = 400$ the impulsive start-up series shows larger oscillations.

\dot{L}_p depends on both Ψ^{CPM} and its spatial derivative Φ^{CPM} , whence the Jost junk solution will impact its self force measurement. With smoothing, the time series plot for \dot{L}_p looks similar to one for \dot{E}_p in Fig. 5.7, and is not shown. We note that our self-force \dot{L}_p measurement agrees with a separate experiment which finds that the angular momentum carried away by gravitational waves is $\dot{L}_{GW} \simeq 1.8626 \times 10^{-5}$. Figure 5.8 shows that \dot{L}_p is typically discontinuous at the particle for an impulsive start-up. Even with an impulsive start-up, the \dot{L}_p measurement yields the correct value when averaged over an orbital period T_ϕ , and it is continuous across the particle (with the correct value) when the particle returns to its initial orbital angle.

These phenomena are a consequence of the axial Jost junk solution (5.8). For t fixed, Eq. (2.64) shows that $\dot{L}_p(\Psi)$ depends linearly on Ψ . Therefore, $\dot{L}_p(\Psi_{\text{Jost}}^{\ell m} + \Psi_{\text{smooth}}^{\ell m}) = \dot{L}_p(\Psi_{\text{Jost}}^{\ell m}) + \dot{L}_p(\Psi_{\text{smooth}}^{\ell m})$, so we can focus on $\dot{L}_p(\Psi_{\text{Jost}}^{\ell m})$ alone. The expressions (5.14) for $C_{L,R}$ are linear in $F(0, r_p)$, which is in turn proportional to the conjugate of an axial vector spherical harmonic X_ϕ . Motivated by this observation, we “factor off” the conjugate, writing $\Psi_{\text{Jost}}^{\ell m} = \eta_\ell(x) \bar{X}_\phi^{\ell m}(\phi_0)$, where ϕ_0 is

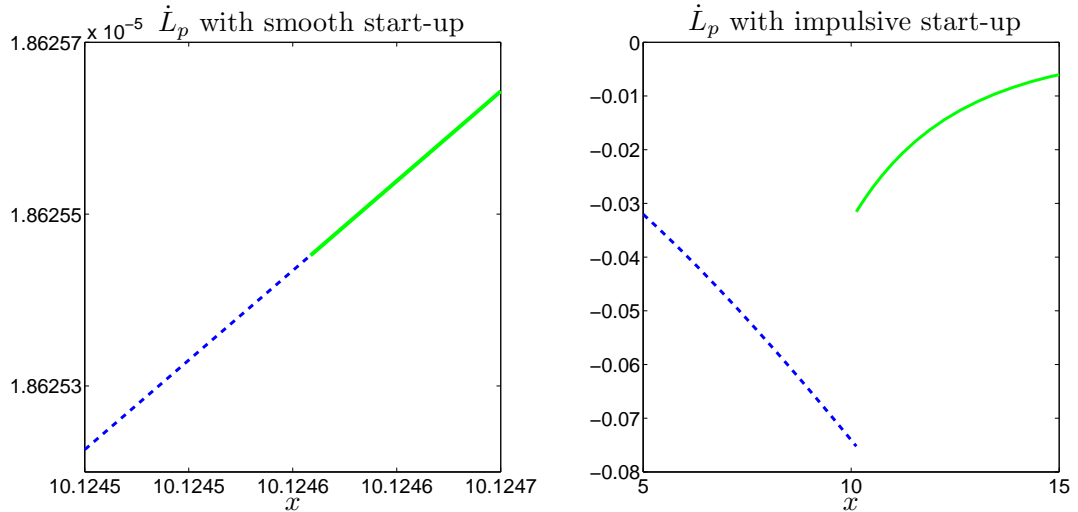


Figure 5.8: $t = 800$ SNAPSHOT OF REAL PART OF \dot{L}_p FOR $\ell = 2$ AND $m = 1$. The particle is located at the interface between the two subdomains.

the particle's initial orbital angle and $\eta_\ell(x)$ is a real discontinuous function solely of x . The expression (2.64) for \dot{L}_p involves $\partial h_{t\phi}/\partial\phi$, which by (5.23) is proportional to $X_{\phi\phi}$. In the equatorial plane $X_{\phi\phi}^{\ell m} = \partial_\phi X_\phi^{\ell m} = imX_\phi^{\ell m}$, and we conclude that $\dot{L}_p(\Psi_{\text{Jost}}^{\ell m}) = im\xi_\ell(x)\bar{X}_\phi^{\ell m}(\phi_0)X_\phi^{\ell m}(\phi_p(t))$, where $\xi_\ell(x)$ is a real discontinuous function solely of x . Therefore, when the particle returns to its initial position (that is, when $\phi_p(t) = \phi_0$), the value of $\dot{L}_p(\Psi_{\text{Jost}}^{\ell m})$ is pure imaginary and $\dot{L}_p(\Psi_{\text{Jost}}^{\ell m}) + \dot{L}_p(\Psi_{\text{Jost}}^{\ell, -m}) = 0$. For perturbations generated by a particle in circular orbit, we have seen that $\Psi_{\text{impulsive}}^{\ell m} \simeq \Psi_{\text{Jost}}^{\ell m} + \Psi_{\text{smooth}}^{\ell m}$ to high accuracy. Combination of this expression and the above arguments for axial perturbations then gives

$$\sum_{|m| \leq \ell} \dot{L}_p(\Psi_{\text{impulsive}}^{\ell m}) \simeq \sum_{|m| \leq \ell} \dot{L}_p(\Psi_{\text{smooth}}^{\ell m}), \quad (5.25)$$

when $\phi_p(t) = \phi_0$. Moreover, one finds $\langle \dot{L}_p(\Psi_{\text{Jost}}^{\ell m}) \rangle = 0$ for time averaging over an orbital period T_ϕ .

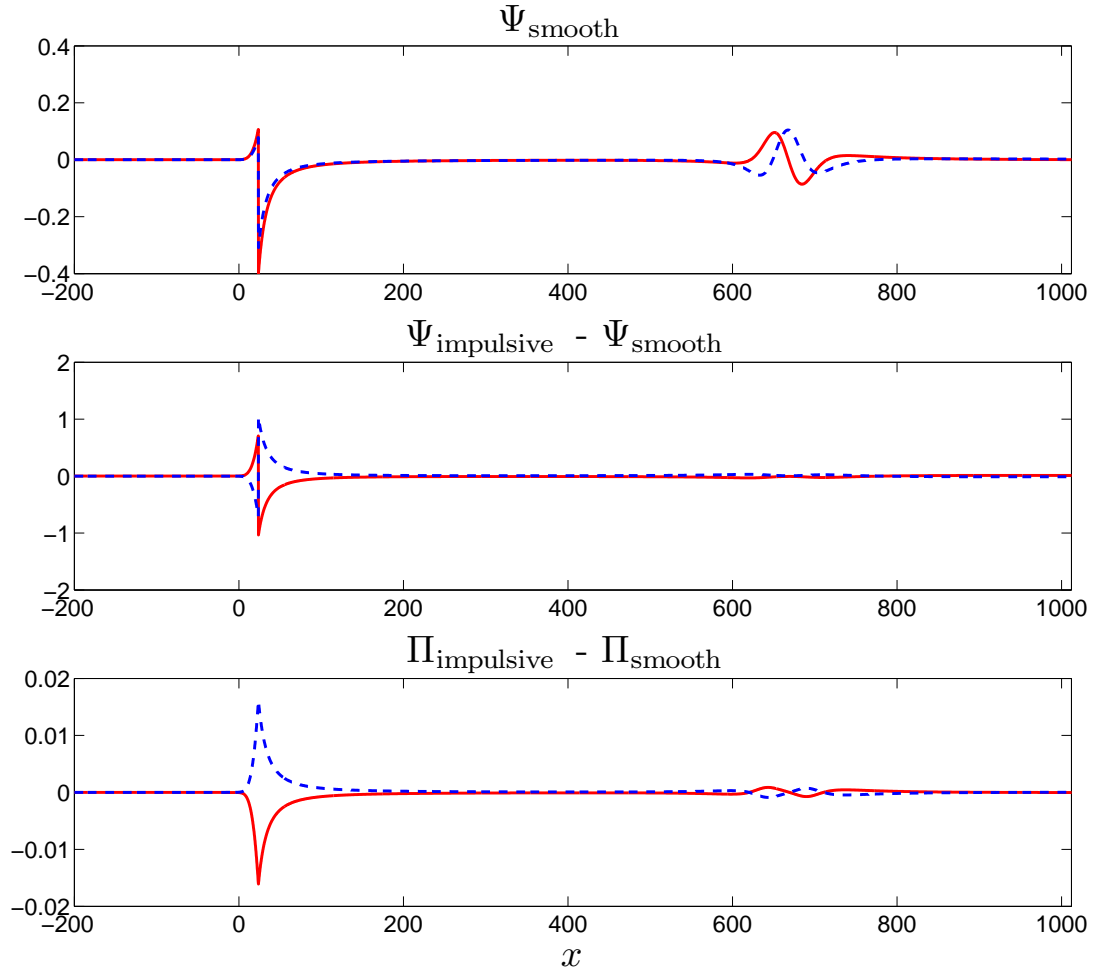


Figure 5.9: DIFFERENCE BETWEEN CPM FIELDS WITH AND WITHOUT SMOOTHING FOR AN ECCENTRIC ORBIT. Here we plot both real (dashed) and imaginary (solid) parts at $t_F = 3000$.

5.3.5 Consequences for Eccentric Orbits: Preliminary Results

This section considers a particle in an eccentric orbit using the full moving particle setup developed in Chapter 4. The orbit's eccentricity and semi-latus rectum are ($e = 0.76412402, p = 8.75456059$), and we choose $\chi = 0.2$ and $\phi = \pi/4$ to fix the particle's initial position. We simulate the resulting $(\ell, m) = (2, 1)$ perturbation with (cf. Table 5.1) $a = -200$, $b = 1012.43$, $S_L = 22$, $S_R = 100$, $N = 31$, $\Delta t = 0.02$,

and $t_F = 3000$. We again take $\tau = 150$, $\delta = 0.0058$ as the smoothing parameters. A coordinate transformation is used to keep the particle at a fixed location between subdomains. Thus, before making comparisons, we first interpolate all fields onto a uniform x -grid (tortoise coordinate) with 6063 points.

Fig. 5.9 shows the difference between fields for smooth and impulsive start-ups. The two numerical solutions are clearly different, although for the case of eccentric orbits we have no analytical understanding of the resulting “junk solution”² presumably seeded by impulsive start-up. Empirically, we find that this solution satisfies

$$[[\Psi_{\text{junk}}]](t) = -[[\Psi_{\text{analytic}}]](0) \quad (5.26a)$$

$$[[\Phi_{\text{junk}}]](t) = 0 \quad (5.26b)$$

$$[[\Pi_{\text{junk}}]](t) = 0, \quad (5.26c)$$

where $[[\Psi_{\text{analytic}}]](t) = f_p(t)F(t, r_p(t))/(f_p^2(t) - \dot{r}_p^2(t))$ is derived in Sec. 4.2.4. These time independent jump conditions are the same as for the circular orbit Ψ_{Jost} solution. With our choice of numerical parameters the axial consistency condition is satisfied to better than a 1×10^{-6} relative error throughout the entire domain for a smooth start-up. For an impulsive start-up the condition is violated to the order of the solution itself. We conclude that, as for circular orbits, the junk solution generated by an impulsive start-up leads to an inconsistent modeling of the axial sector.

Table 5.3 collects energy and angular momentum luminosities. These luminosities have been averaged from $t = 1700$ to $t_F = 1700 + 4T_r$, where $T_r \simeq 780.6256$ is the radial period from (4.4). Unlike the circular orbit case, the discrepancy between

²At present, we are uncertain if the generated junk solution fulfills the formal definition of a Jost solution. Thus, in the context of eccentric orbits we simply refer to the persistent solution as the “junk solution”.

\dot{Q}	\dot{Q}_{smooth}	$\dot{Q}_{\text{impulsive}}$	\dot{Q}_{error}
$\langle \dot{E}_{2,2}^{\text{ZM}} \rangle$	1.559917×10^{-4}	1.559484×10^{-4}	2.775789×10^{-4}
$\langle \dot{E}_{2,1}^{\text{CPM}} \rangle$	1.153983×10^{-6}	1.236758×10^{-6}	7.172983×10^{-2}
$\langle \dot{E}_{2,1}^{\text{RW}} \rangle$	1.153983×10^{-6}	1.872073×10^{-6}	6.222709×10^{-1}
$\langle \dot{E}_{2,1}^{\text{CPM}} \rangle + \langle \dot{E}_{2,2}^{\text{ZM}} \rangle$	1.571457×10^{-4}	1.571852×10^{-4}	2.512000×10^{-4}
$\text{Re}\langle \dot{L}_{2,2}^{\text{ZM}} \rangle$	2.078556×10^{-3}	2.076811×10^{-3}	8.395251×10^{-4}
$\text{Re}\langle \dot{L}_{2,1}^{\text{CPM}} \rangle$	1.441737×10^{-5}	1.537876×10^{-5}	6.668276×10^{-2}
$\text{Re}\langle \dot{L}_{2,1}^{\text{RW}} \rangle$	1.441749×10^{-5}	1.662726×10^{-5}	1.532701×10^{-1}
$\text{Re}\langle \dot{L}_{2,1}^{\text{CPM}} \rangle + \text{Re}\langle \dot{L}_{2,2}^{\text{ZM}} \rangle$	2.092973×10^{-3}	2.092190×10^{-3}	3.744004×10^{-4}

Table 5.3: $\ell = 2$ LUMINOSITIES FOR A PARTICLE WITH AN ORBIT GIVEN BY ($e = 0.76412402, p = 8.75456059$). Entries result from the addition of $|m|$ and $-|m|$ luminosities.

waveforms corresponding to smoothly and impulsively started fields may be larger than usual $O(1/r)$ error associated with read-off at a finite radial location rather than infinity. Moreover, the junk solution would seem determined by the initial orbital parameters. Indeed, the values $\dot{Q}_{\text{impulsive}}$ and errors quoted in our table strongly depend upon such choices.

5.4 Comments on the Generality of Jost Junk

A number of time-domain methods exist for solving Eq. (4.1) as an initial boundary value problem, including those described in [21, 157, 153, 204, 134, 56, 57]. These methods vary in both the underlying numerical scheme (e.g. finite difference, finite element, pseudospectral, and spectral) as well as their treatment of the distributional source terms (e.g. Gaussian representation, analytic integration, domain matching). Numerical simulation of metric perturbations may also involve other choices (e.g. gauge, number of spatial dimensions, choice of numerical variables). Moreover, similar time-domain methods exist for solving the forced Teukolsky equation describing particle-driven perturbations of the Kerr geometry (see for example

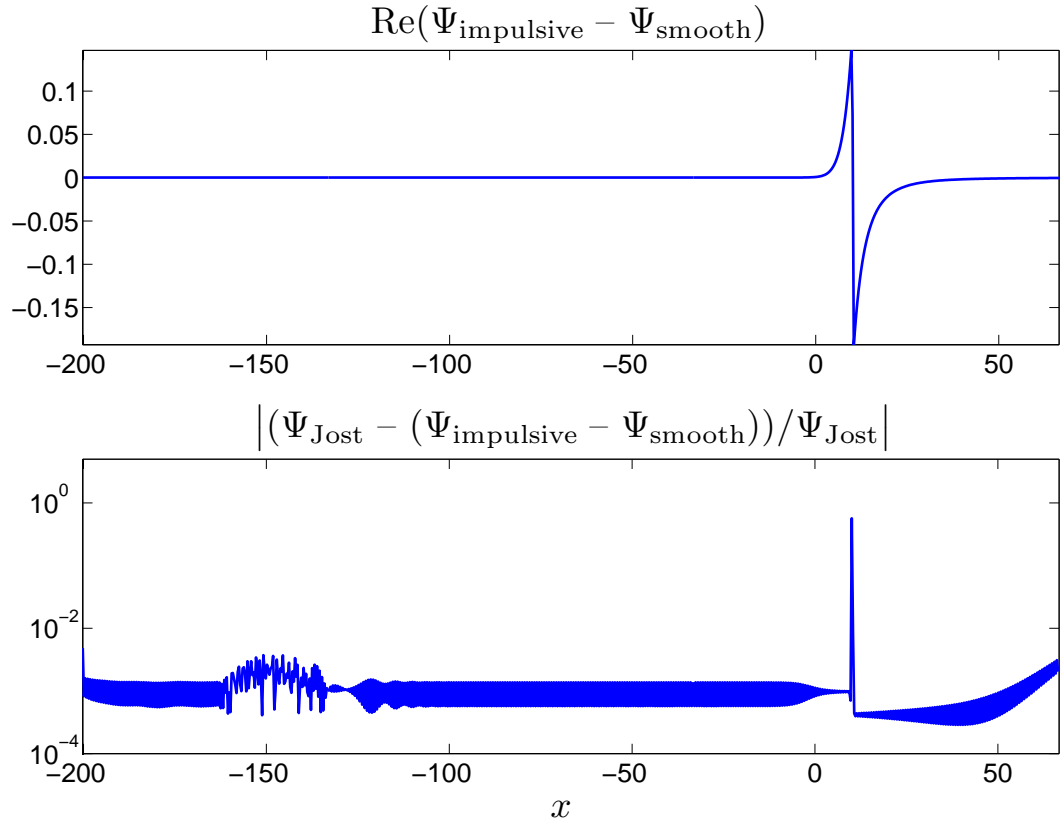


Figure 5.10: DIFFERENCE BETWEEN SMOOTHLY AND IMPULSIVELY STARTED FIELDS USING A FINITE-DIFFERENCE METHOD. As in Subsection 5.2.2, we consider Ψ^{CPM} for $\ell = 3$ and $m = 2$. The bottom plot depicts the relative error between the numerical and analytical Jost solutions.

Refs. [8, 207, 209]). For all of these methods, the issue of impulsive start-up would seem pertinent, although clearly we cannot examine each method. Nevertheless, we now attempt to provide at least partial insight into the ubiquity of static junk solutions.

As mentioned earlier, the results and observations of this chapter have been independently confirmed with each of our two numerical methods: the nodal Legendre dG and Chebyshev schemes. However, as these schemes are rather similar, we now briefly consider a finite-difference scheme for solving (4.39), based on fourth, sixth, and eighth order stencils for the spatial derivatives. To stabilize sixth and eighth order stencils, we have followed Ref. [114]. Furthermore, we replace the Dirac delta

functions in (5.1) by narrow Gaussians. Precisely, for $\sigma = 0.1$ we make the replacement

$$J(x, t)\delta(x - x_p) \rightarrow J(x, t)\frac{1}{\sqrt{2\pi\sigma}}\exp\left(-\frac{(x - x_p)^2}{2\sigma^2}\right) \quad (5.27)$$

for both the J_1 and J_2 terms in (5.1). With essentially the same experimental setup described in Subsection 5.2.2, we repeat that experiment using 4000 points and sixth order spatial differences. The results, shown in Fig. 5.10, clearly indicate the presence of a static “Jost junk” solution. A larger choice for σ gives rise to a rounder transition near the particle. However, the following shows that such contamination is not a generic feature. We introduce a variable $\tilde{\Phi}$ obeying

$$\Phi = \tilde{\Phi} - [[\Psi]]\delta(x - x_p), \quad (5.28)$$

so that the system formally becomes

$$\begin{aligned} \partial_t \Psi &= -\Pi \\ \partial_t \Pi &= -\partial_x \tilde{\Phi} + V(r)\Psi + J_1\delta(x - x_p) + J_3\delta'(x - x_p) \\ \partial_t \tilde{\Phi} &= -\partial_x \Pi, \end{aligned} \quad (5.29)$$

where $J_3 = [[\Psi]] = F(t, r_p)/f_p$. If we now replace the δ, δ' terms in the new system by appropriate Gaussians, *then we do not observe a persistent Jost junk solution* when trivial initial conditions are supplied (neither in finite-difference nor dG simulations).

Persistent junk solutions arise from the combination of inconsistent initial data and the distributional forcing terms which define the EMRB model. In particular, we observe that development of a Jost junk solution depends on how the distributional forcing is treated rather than the underlying numerical method. Therefore, whether or not they contaminate simulations should be considered on a case-by-case basis. Domain matching approaches which enforce jump conditions without approx-

imation (considered in this chapter) exhibit a Jost junk solution in the absence of smooth start-up. With first order variables such approaches correspond to system (5.1) rather than (5.29). Treatment of system (5.29) with Gaussian representations for δ, δ' exhibits no persistent junk solution, although such an approach necessarily introduces large method error relative to the exact distributional model and features variables with δ -like behavior near the “particle” (Gaussian peak). The issue of a static junk solution for schemes which discretize the second order equation (4.1) deserves further consideration, although, if present, then the particular Jost junk solution observed in this chapter would likely be of relevance.³

³For a static solution to have gone unnoticed, it would seem reasonable to expect decay as either $r \rightarrow 2M^+$ or $r \rightarrow \infty$. Such solutions will necessarily be discontinuous, and presumably such discontinuities could only “hide” at the particle, requirements that fix the form of the static solution up to the constants C_L and C_R introduced in Section 5.2.2.

CHAPTER SIX

GBSSN System in Spherical Symmetry

6.1 Introduction

This chapter details a discontinuous Galerkin method for the GBSSN system, which is a close cousin of the traditional BSSN system currently used by numerical relativity groups. A full discussion of both systems is given in 2.6, and we remind the reader that the essential difference is that GBSSN does not require the conformal metric's determinant be set to unity.

To provide context we briefly consider the generalized harmonic (GH) system [93, 109, 182, 147] and the traditional BSSN system [200, 28, 41], these are the two most widely used systems to evolve comparable mass binary black hole systems. Using a finite-difference approach with adaptive mesh refinement, Pretorius [180, 182, 181] used a constraint-suppressing second-order form of the GH system (suggested by Gundlach et al. [109]) to evolve a binary through inspiral, merger and ringdown. Lindblom et al. [147] recast the second-order GH system into a first-order symmetric-hyperbolic evolution system with constraint suppression comparable to that of the second-order system. This first-order GH system has been used to successfully simulate binary black holes evolution with nodal spectral (pseudospectral) methods [35, 198, 205]. More recently, Ref. [212] has introduced a new penalty method for nodal spectral evolutions of spatially second-order wave equations. This work provides a foundation for solution of the second-order GH system via spectral methods, and has been used to evolve the Kerr solution [213] and the inspiral of binaries. Typically written in a spatially second-order form, the BSSN system [28] has seen widespread use by numerical relativity groups that employ finite-difference techniques to evolve binaries. Ref. [214] presented a nodal spectral code to evolve the BSSN system in second-order form. The system proved unstable when tested on a single black hole. In more recent work [215], longer evolutions were obtained

through the adoption of better gauge conditions, filtering methods, and more distant outer boundaries. The BSSN system has also been evolved in a first-order strongly-hyperbolic formulation for a single black hole with nodal spectral methods [167]. Such evolutions of a single black hole exhibited instabilities similar to those reported in Ref. [215].

Corresponding to the two versions of the Einstein equations discussed in the last paragraph are two distinct techniques for the treatment of singularities in numerical relativity. Evolutions based on the GH system have used black hole excision, whereby the interior of an apparent horizon is removed (excised) from the computational domain. This technique relies on horizon-tracking and gauge conditions which ensure that inner boundaries of the computational domain are pure out-flow, whence no inner boundary conditions are needed. Evolutions based on the BSSN system have relied on the moving-punctures technique [53, 26], also coined “natural excision.” Technically much easier to implement than excision, this technique features mild central singularities which evolve freely in the computational domain. Initially these puncture points may represent either asymptotically flat regions or “trumpets.” Hannam et al. first discussed cylindrical asymptotics in moving puncture evolutions [115, 116], see also [42, 29, 117, 45, 46].

Relative to the alternative systems previously discussed, the (G)BSSN system in second order form affords an easier treatment of singularities and features a relatively small number of geometric variables directly related to the foliation of spacetime into spacelike hypersurfaces. However, to date, spectral methods for black hole binaries have been successfully implemented only for the first-order GH system. The binary black hole problem is essentially a smooth one (singularities reside on sets of measure zero censored by horizons), and spectral methods exhibit well-established advantages over finite-difference methods for long-time simulation of such problems

[124]. Therefore, the development and analysis of a stable spectral implementation of the full BSSN system is a worthwhile goal in numerical relativity, and the motivation behind the pioneering investigations reported in Refs. [214, 215, 167].

In Refs. [41, 42], Brown introduced the spherically reduced GBSSN system as a test bed for tractable examination of theoretical and computational issues involved in solving this system. Indeed, appealing to the simplicity of this system, he offered geometrical and physical insights into the nature of the moving-puncture technique and its finite-difference implementation [42, 45, 46] (see also [29, 117]). Here, we exploit this system to a similar end, using it as a simplified setting in which to develop spectral methods for the stable integration of the GBSSN system. Precisely, we develop and test a nodal discontinuous Galerkin method [121] for integration of the spherically reduced GBSSN system. While Brown’s chief focus lay with moving punctures, for further simplicity we adopt the excision technique. Clearly, the problem we consider is not as daunting as the one confronted by both Tichy and Mroue [214, 215, 167]. Nevertheless, our method is robustly stable, and therefore might serve as a stepping stone toward a stable dG-based formulation for the full (G)BSSN system.

Nodal dG schemes are both well-suited and well-developed for hyperbolic problems [121]. Although mostly used for hyperbolic problems expressed as first-order systems, dG methods have also been applied to systems involving second-order spatial operators, typically via dG *interior penalty* (IP) methods [208, 63, 107, 108, 122, 199]. (Refs. [100, 110, 111] discuss the concept of hyperbolicity [140] in the context of such systems.) Penalty methods of a different type were exploited in Ref. [212] for the wave equation written in second order form. *Local discontinuous Galerkin* (LDG) schemes, developed initially by Shu and coworkers [67, 226, 227], constitute an alternate approach for integration of spatially second-order systems.

LDG schemes feature essentially the same auxiliary variables as those appearing in traditional first-order reductions, however in LDG schemes such variables are not evolved and arise only as local variables. The basic difference between dG-IP and LDG methods is the manner in which subdomains are coupled. The method we described for the spherically reduced GBSSN system is essentially an LDG scheme.

This chapter is organized as follows. Section 6.2 collects the relevant equations and develops some further notation useful for expressing the spherically reduced GBSSN system in various abstract forms. This section also considers a discussion of hyperbolicity and constructs the relevant initial data. Section 6.3 presents our nodal dG scheme in detail and considers a simple system which models the spherically reduced GBSSN system, giving an analytical proof that the model system is L_2 stable in the semi-discrete sense. Section 6.4 documents the results of several numerical simulations testing our scheme. Appendix F details the reduction of the 3+1 GBSSN to spherical symmetry, and appendix E constructs the characteristic fields and speeds of our system.

6.2 Spherically Symmetric GBSSN Equations

6.2.1 Basic Variables and Spherically Reduced System

Consider a general spherically symmetric line element¹,

$$ds^2 = -\alpha^2 dt^2 + \chi^{-1} g_{rr} (dr + \beta^r dt)^2 + \chi^{-1} g_{\theta\theta} (d\theta^2 + \sin^2 \theta d\phi^2), \quad (6.1)$$

along with the spherically symmetric *Ansatz*:

$$\Gamma^a = \begin{pmatrix} \Gamma^r \\ -\cos \theta / (g_{\theta\theta} \sin \theta) \\ 0 \end{pmatrix}, \quad A_{ab} = A_{rr} \begin{pmatrix} 1 & 0 & 0 \\ 0 & -g_{\theta\theta} / (2g_{rr}) & 0 \\ 0 & 0 & -g_{\theta\theta} \sin^2 \theta / (2g_{rr}) \end{pmatrix}. \quad (6.2)$$

The ansatz A_{ab} is motivated by the line element (6.1) and definition $\bar{K}_{ij} = -\frac{1}{2} \mathcal{L}_n \bar{g}_{ij}$. Notice that \bar{K}_{ij} contains two pieces of information, namely \bar{K}_{rr} and $\bar{K}_{\theta\theta}$, and upon a conformal traceless decomposition these become K and A_{rr} . Of course we could have chosen $A_{\theta\theta}$ as our preferred variable, which is related to A_{rr} through the trace-free condition².

Section 2.6.3 presented the full 3+1 GBSSN system with 1+log and Γ -driver gauge conditions. Appendix F derives the spherically symmetry version of this sys-

¹ Two potentially confusing notational changes are made in this chapter. First, we deviate from the convention of Chapter 2 by now using $g_{\alpha\beta}$ for the spatial metric. Second, we now denote physical tensors, for example \bar{g}_{rr} , with a ‘bar’ and conformal tensors, for example g_{rr} , without a ‘bar’. This switch will reduce the notational burden when we discretize the GBSSN system. Also, our notation changes agree with Refs. [42, 91].

² A_{ij} is traceless by virtue of the ansatz, and at the analytic level is traceless by definition. However, suppose we abandon our ansatz by permitting both A_{rr} and $A_{\theta\theta}$ as system variables. Numerical errors would then result in $A^i_i \neq 0$. Thus an advantage of the ansatz is seen to exactly enforce the trace-free constraint, although in principle this does not need to be done.

tem given our ansatz, although not with the notational conventions of this chapter (cf. footnote 1). There it is found that the basic GBSSN variables χ , g_{rr} , $g_{\theta\theta}$, A_{rr} , K , Γ^r , α , β^r , and B^r satisfy the (Lagrangian-form) GBSSN system:

$$\partial_t \alpha = \beta^r \alpha' - 2\alpha K - (\partial_t \alpha)_0 \quad (6.3a)$$

$$\partial_t \beta^r = \beta^r \beta^{r'} + \frac{3}{4} B^r - (\partial_t \beta^r)_0 \quad (6.3b)$$

$$\partial_t B^r = \beta^r B^{r'} + \lambda(\partial_t \Gamma^r - \beta^r \Gamma^{r'}) - \eta B^r - (\partial_t B^r)_0 \quad (6.3c)$$

$$\partial_t \chi = \beta^r \chi' + \frac{2}{3} K \alpha \chi - \frac{\beta^r g'_{rr} \chi}{3g_{rr}} - \frac{2\beta^r g'_{\theta\theta} \chi}{3g_{\theta\theta}} - \frac{2}{3} \beta^{r'} \chi \quad (6.3d)$$

$$\partial_t g_{rr} = \frac{2}{3} \beta^r g'_{rr} + \frac{4}{3} g_{rr} \beta^{r'} - 2A_{rr} \alpha - \frac{2g_{rr} \beta^r g'_{\theta\theta}}{3g_{\theta\theta}} \quad (6.3e)$$

$$\partial_t g_{\theta\theta} = \frac{1}{3} \beta^r g'_{\theta\theta} + \frac{A_{rr} g_{\theta\theta} \alpha}{g_{rr}} - \frac{g_{\theta\theta} \beta^r g'_{rr}}{3g_{rr}} - \frac{2}{3} g_{\theta\theta} \beta^{r'} \quad (6.3f)$$

$$\begin{aligned} \partial_t A_{rr} = & \beta^r A'_{rr} + \frac{4}{3} A_{rr} \beta^{r'} - \frac{\beta^r g'_{rr} A_{rr}}{3g_{rr}} - \frac{2\beta^r g'_{\theta\theta} A_{rr}}{3g_{\theta\theta}} + \frac{2\alpha \chi (g'_{rr})^2}{3g_{rr}^2} - \frac{\alpha \chi (g'_{\theta\theta})^2}{3g_{\theta\theta}^2} \\ & - \frac{\alpha (\chi')^2}{6\chi} + \frac{2}{3} g_{rr} \alpha \chi \Gamma^{r'} - \frac{\alpha \chi g'_{rr} g'_{\theta\theta}}{2g_{rr} g_{\theta\theta}} + \frac{\chi g'_{rr} \alpha'}{3g_{rr}} + \frac{\chi g'_{\theta\theta} \alpha'}{3g_{\theta\theta}} - \frac{\alpha g'_{rr} \chi'}{6g_{rr}} - \frac{\alpha g'_{\theta\theta} \chi'}{6g_{\theta\theta}} \\ & - \frac{2}{3} \alpha' \chi' + \frac{\alpha \chi''}{3} - \frac{2}{3} \chi \alpha'' - \frac{\alpha \chi g''_{rr}}{3g_{rr}} + \frac{\alpha \chi g''_{\theta\theta}}{3g_{\theta\theta}} - \frac{2\alpha A_{rr}^2}{g_{rr}} + K \alpha A_{rr} - \frac{2g_{rr} \alpha \chi}{3g_{\theta\theta}} \end{aligned} \quad (6.3g)$$

$$\partial_t K = \beta^r K' + \frac{\chi g'_{rr} \alpha'}{2g_{rr}^2} - \frac{\chi g'_{\theta\theta} \alpha'}{g_{rr} g_{\theta\theta}} + \frac{\alpha' \chi'}{2g_{rr}} - \frac{\chi \alpha''}{g_{rr}} + \frac{3\alpha A_{rr}^2}{2g_{rr}^2} + \frac{1}{3} \alpha K^2 \quad (6.3h)$$

$$\begin{aligned} \partial_t \Gamma^r = & \beta^r \Gamma^{r'} + \frac{A_{rr} \alpha g'_{\theta\theta}}{g_{rr}^2 g_{\theta\theta}} + \frac{2\beta^{r'} g'_{\theta\theta}}{3g_{rr} g_{\theta\theta}} + \frac{A_{rr} \alpha g'_{rr}}{g_{rr}^3} - \frac{4\alpha K'}{3g_{rr}} - \frac{2A_{rr} \alpha'}{g_{rr}^2} - \frac{3A_{rr} \alpha \chi'}{g_{rr}^2 \chi} \\ & + \frac{4\beta^{r''}}{3g_{rr}} - \frac{\beta^r (g'_{\theta\theta})^2}{g_{rr} (g_{\theta\theta})^2} + \frac{\beta^r g''_{rr}}{6(g_{rr})^2} + \frac{\beta^r g''_{\theta\theta}}{3g_{\theta\theta} g_{rr}}, \end{aligned} \quad (6.3i)$$

where the prime stands for partial r -differentiation. Eqs. (6.3) have been specialized to matter-free regions of spacetime by setting $j^r = S_{ij}^{\text{TF}} = S = \rho = 0$ in the more general version of Sec. F.4.3. Throughout this chapter we refer to Eqs. (6.3) as the GBSSN system, although some minor modifications (beyond the vacuum condition) have been introduced³. First, $(\partial_t \alpha)_0$ designates a constant term which

³All modifications take place in the gauge evolution equations, whence the physics is unaffected. Such freedom is simply a reflection of our ability to choose coordinates as we wish.

ensures that the right-hand side of the α evolution equation (6.3a) vanishes at the initial time. This source term as well as the analogous terms appearing in the evolution equations (6.3b,c) for β^r and B^r are needed to enable a static evolution of the Schwarzschild solution in Kerr-Schild coordinates. Second, the parameter λ (perhaps with functional dependence) modifies the hyperbolicity of the first-order system [6], allowing for an “adjustable” excision surface. For this GBSSN system, we have three constraints: the Hamiltonian constraint \mathcal{H} , the momentum constraint \mathcal{M}_r , and the conformal connection constraint \mathcal{G}^r resulting from the definition of the conformal connection Γ^r . These constraints are given in Appendix F.3, reproduced here for convenience:

$$\begin{aligned} \mathcal{H} = & -\frac{3A_{rr}^2}{2g_{rr}^2} + \frac{2K^2}{3} - \frac{5(\chi')^2}{2\chi g_{rr}} + \frac{2\chi''}{g_{rr}} + \frac{2\chi}{g_{\theta\theta}} \\ & - \frac{2\chi g_{\theta\theta}''}{g_{rr}g_{\theta\theta}} + \frac{2\chi' g_{\theta\theta}'}{g_{rr}g_{\theta\theta}} + \frac{\chi g_{rr}' g_{\theta\theta}'}{g_{rr}^2 g_{\theta\theta}} - \frac{\chi' g_{rr}'}{g_{rr}^2} + \frac{\chi (g_{\theta\theta}')^2}{2g_{rr} g_{\theta\theta}^2} \end{aligned} \quad (6.4a)$$

$$\mathcal{M}_r = \frac{A'_{rr}}{g_{rr}} - \frac{2K'}{3} - \frac{3A_{rr}\chi'}{2\chi g_{rr}} + \frac{3A_{rr}g'_{\theta\theta}}{2g_{rr}g_{\theta\theta}} - \frac{A_{rr}g'_{rr}}{g_{rr}^2} \quad (6.4b)$$

$$\mathcal{G}^r = -\frac{g'_{rr}}{2g_{rr}^2} + \frac{g'_{\theta\theta}}{g_{rr}g_{\theta\theta}} + \Gamma^r. \quad (6.4c)$$

Eqs. (6.3e,f) also ensure that the determinant factor $g/\sin^2\theta = g_{rr}(g_{\theta\theta})^2$ remains fixed throughout an evolution.

6.2.2 Abstract Expressions of the System

We define the following vectors built with system variables:

$$u = \begin{pmatrix} \chi \\ g_{rr} \\ g_{\theta\theta} \\ \alpha \\ \beta^r \end{pmatrix}, \quad v = \begin{pmatrix} B^r \\ A_{rr} \\ K \\ \Gamma^r \end{pmatrix}, \quad Q = \begin{pmatrix} \chi' \\ g'_{rr} \\ g'_{\theta\theta} \\ \alpha' \\ \beta^{r'} \end{pmatrix}. \quad (6.5)$$

Introduction of Q might seem unnecessary at this stage, but proves useful in the construction of our discontinuous Galerkin scheme. In terms of the vectors u , v , and Q we further define

$$W_{u:v} = \begin{pmatrix} u \\ v \end{pmatrix}, \quad W_{v:Q} = \begin{pmatrix} v \\ Q \end{pmatrix}, \quad W = W_{u:Q} = \begin{pmatrix} u \\ v \\ Q \end{pmatrix}. \quad (6.6)$$

Here we now have introduced “colon notation” [106] to represent (sub)vectors and (sub)matrices⁴, although we employ the notation over block rather than individual elements. In the first-order version of the system (6.3) the components of Q are promoted to independent fields, in which case the corresponding principal part features

⁴This should not be confused with our earlier usage of a colon for covariant derivative on the two-sphere.

$$\partial_t B^r = \beta^r B^{r'} - \frac{4\lambda\alpha}{3g_{rr}} K' + \frac{4\lambda}{3g_{rr}} Q'_{\beta^r} + \frac{\lambda\beta^r}{6(g_{rr})^2} Q'_{g_{rr}} + \frac{\lambda\beta^r}{3g_{\theta\theta}g_{rr}} Q'_{g_{\theta\theta}} \quad (6.7a)$$

$$\partial_t A_{rr} = \beta^r A'_{rr} + \frac{2}{3}g_{rr}\alpha\chi\Gamma^{r'} + \frac{1}{3}\alpha Q'_\chi - \frac{2}{3}\chi Q'_\alpha - \frac{\alpha\chi}{3g_{rr}} Q'_{g_{rr}} + \frac{\alpha\chi}{3g_{\theta\theta}} Q'_{g_{\theta\theta}} \quad (6.7b)$$

$$\partial_t K = \beta^r K' - \frac{\chi}{g_{rr}} Q'_\alpha \quad (6.7c)$$

$$\partial_t \Gamma^r = \beta^r \Gamma^{r'} - \frac{4\alpha K'}{3g_{rr}} + \frac{4}{3g_{rr}} Q'_{\beta^r} + \frac{\beta^r}{6(g_{rr})^2} Q'_{g_{rr}} + \frac{\beta^r}{3g_{\theta\theta}g_{rr}} Q'_{g_{\theta\theta}} \quad (6.7d)$$

$$\partial_t Q_\chi = \beta^r Q'_\chi + \frac{2}{3}\alpha\chi K' - \frac{\beta^r\chi}{3g_{rr}} Q'_{g_{rr}} - \frac{2\beta^r\chi}{3g_{\theta\theta}} Q'_{g_{\theta\theta}} - \frac{2}{3}\chi Q'_{\beta^r} \quad (6.7e)$$

$$\partial_t Q_{g_{rr}} = \frac{2}{3}\beta^r Q'_{g_{rr}} + \frac{4}{3}g_{rr} Q'_{\beta^r} - 2\alpha A'_{rr} - \frac{2g_{rr}\beta^r}{3g_{\theta\theta}} Q'_{g_{\theta\theta}} \quad (6.7f)$$

$$\partial_t Q_{g_{\theta\theta}} = \frac{1}{3}\beta^r Q'_{g_{\theta\theta}} + \frac{g_{\theta\theta}\alpha}{g_{rr}} A'_{rr} - \frac{g_{\theta\theta}\beta^r}{3g_{rr}} Q'_{g_{rr}} - \frac{2}{3}g_{\theta\theta} Q'_{\beta^r} \quad (6.7g)$$

$$\partial_t Q_\alpha = \beta^r Q'_\alpha - 2\alpha K' \quad (6.7h)$$

$$\partial_t Q_{\beta^r} = \beta^r Q'_{\beta^r} + \frac{3}{4}B^{r'}, \quad (6.7i)$$

where all lower-order terms on the right-hand side have been dropped. This sector of principal parts of the first-order system has the form

$$\partial_t W_{v:Q} + \tilde{A}(u)W'_{v:Q} = 0, \quad (6.8)$$

where (minus) the explicit form of the 9-by-9 matrix $\tilde{A}(u)$ is given in (E.1). The first-order version of (6.3) takes the nonconservative form

$$\partial_t W + \mathcal{A}(u)W' = \mathcal{S}(W), \quad \mathcal{A}(u) = \left(\begin{array}{c|c} 0_{5 \times 5} & 0_{5 \times 9} \\ \hline 0_{9 \times 5} & \tilde{A}(u) \end{array} \right), \quad (6.9)$$

where $\mathcal{S}(W)$ is a vector of lower order terms built with all components of W . Partition of $\tilde{A}(u) = \mathcal{A}(u)_{v:Q,v:Q}$ into blocks corresponding to the v and Q sectors yields

$$\tilde{A}(u) = \left(\begin{array}{c|c} \tilde{A}(u)_{vv} & \tilde{A}(u)_{vQ} \\ \hline \tilde{A}(u)_{Qv} & \tilde{A}(u)_{QQ} \end{array} \right). \quad (6.10)$$

Using these blocks, we then define the 9-by-9 matrix

$$A(u) = \mathcal{A}(u)_{u:v,v:Q} = \left(\begin{array}{c|c} 0_{5 \times 4} & 0_{5 \times 5} \\ \hline \tilde{A}(u)_{vv} & \tilde{A}(u)_{vQ} \end{array} \right), \quad (6.11)$$

and express (6.3) as

$$\partial_t W_{u:v} + A(u)W'_{v:Q} = S(W) \quad (6.12a)$$

$$Q = u', \quad (6.12b)$$

where $S(W) = \mathcal{S}(W)_{u:v}$.

6.2.3 Hyperbolicity and Characteristic Fields

Although our numerical scheme deals directly with the second-order spatial operators appearing in (6.3), we first consider the hyperbolicity of the corresponding first-order system (6.9). Our definitions and method for analysis directly follows the discussion in Sec. 3.2. The characteristic fields and their speeds are found by instantaneously “freezing” the fields u in $\mathcal{A}(u)$ to some value u_0 , corresponding to a linearization around a uniform state. Below we continue to write u for simplicity with the understanding that u is really the background solution u_0 . Of primary interest is the range of u_0 for which the system is strongly hyperbolic [100, 110, 111, 140].

field	speed
X_1	$\mu_1 = 0$
$X_{2,3}$	$\mu_{2,3} = -\beta^r$
X_4^\pm	$\mu_4^\pm = -\beta^r \pm \sqrt{2\alpha\chi/g_{rr}}$
X_5^\pm	$\mu_5^\pm = -\beta^r \pm \alpha\sqrt{\chi/g_{rr}}$
X_6^\pm	$\mu_6^\pm = -\beta^r \pm \sqrt{\lambda/g_{rr}}$

Table 6.1: CHARACTERISTIC SPEEDS. These speeds are the *coordinate* speeds, measured with respect to $\partial/\partial t$ and to be distinguished from *proper* speeds measured by observers who are at rest in the space-like hypersurface (for a discussion see Ref. [45]). These coordinate speeds are the eigenvalues listed in E.2.

Appendix E shows that the characteristic fields corresponding to (6.3) are as follows: (i) all components of u (each with speed 0), and (ii) the fields

$$X_1 = g_{\theta\theta}Q_{g_{rr}} + 2g_{rr}Q_{g_{\theta\theta}} \quad (6.13a)$$

$$X_2 = g_{rr}\Gamma^r + \frac{2}{\chi}Q_\chi - \frac{1}{2g_{rr}}Q_{g_{rr}} - \frac{1}{g_{\theta\theta}}Q_{g_{\theta\theta}} \quad (6.13b)$$

$$X_3 = \frac{g_{rr}}{\lambda}B^r + \frac{2}{\chi}Q_\chi - \frac{1}{2g_{rr}}Q_{g_{rr}} - \frac{1}{g_{\theta\theta}}Q_{g_{\theta\theta}} \quad (6.13c)$$

$$X_4^\pm = \pm\sqrt{\frac{2\alpha g_{rr}}{\chi}}K + Q_\alpha \quad (6.13d)$$

$$X_5^\pm = \mp\frac{3}{\sqrt{g_{rr}\chi}}A_{rr} \pm 2\sqrt{\frac{g_{rr}}{\chi}}K + 2g_{rr}\Gamma^r + \frac{1}{\chi}Q_\chi - \frac{1}{g_{rr}}Q_{g_{rr}} + \frac{1}{g_{\theta\theta}}Q_{g_{\theta\theta}} \quad (6.13e)$$

$$X_6^\pm = -\frac{3}{4}\frac{g_{rr}}{\lambda}B^r \pm \frac{\alpha\sqrt{\lambda g_{rr}}}{(2\alpha\chi - \lambda)}K - \frac{\beta^r}{8(\beta^r g_{rr} \mp \sqrt{\lambda g_{rr}})}Q_{g_{rr}} \\ - \frac{\beta^r g_{rr}}{4g_{\theta\theta}(\beta^r g_{rr} \mp \sqrt{\lambda g_{rr}})}Q_{g_{\theta\theta}} + \frac{\alpha\chi}{(2\alpha\chi - \lambda)}Q_\alpha \pm \sqrt{\frac{g_{rr}}{\lambda}}Q_{\beta^r}, \quad (6.13f)$$

with the speeds listed in Table 6.1. To ensure strong hyperbolicity we must necessarily require

$$\lambda > 0, \quad (\beta^r)^2 g_{rr} - \lambda \neq 0, \quad 2\alpha\chi - \lambda \neq 0, \quad (6.14)$$

as shown in in Appendix E where further conditions are also given. When $\lambda = 1$ the hyperbolicity condition of Ref. [42] is recovered. In fact, the system could be recast as symmetric hyperbolic. Indeed, as it involves one spatial dimension, the

relevant symmetrizer can be constructed via polar decomposition of the diagonalizing similarity transformation. However, we will not exploit this possibility.

This system admits an inner excision boundary provided

$$\beta^r \geq \max \left(\sqrt{\frac{2\alpha\chi}{g_{rr}}}, \sqrt{\frac{\alpha^2\chi}{g_{rr}}}, \sqrt{\frac{\lambda}{g_{rr}}} \right) \quad (6.15)$$

holds at the inner boundary. This condition ensures each characteristic field has a nonpositive speed at the inner boundary, and therefore the inner boundary is an excision boundary at which no boundary conditions are needed. The extra flexibility afforded by the parameter λ could be used to maintain rigorous hyperbolicity by moving the points at which the conditions in (6.14) are violated outside of the computational domain. Furthermore, for $\lambda = 1$ Eq. (6.15) conceivably fails or is only satisfied close to $r = 0$ where field gradients are prohibitively large. The troublesome X_6^+ gauge mode has a positive speed $-\beta^r + \sqrt{\lambda/g_{rr}}$. Indeed, for the conformally flat Kerr-Schild system considered in section 6.4.3 an inner excision boundary is only possible provided λ is small enough.

The transformation (6.13) can be inverted in order to express the fundamental

fields in terms of the characteristic fields:

$$B^r = -\frac{1}{6} \frac{\lambda}{g_{rr}g_{\theta\theta}} \left[\frac{(\beta^r)^2}{(\beta^r)^2 g_{rr} - \lambda} \right] X_1 + \frac{2}{3} \frac{\lambda\alpha\chi}{g_{rr}(2\alpha\chi - \lambda)} (X_4^+ + X_4^-) - \frac{2}{3} \frac{\lambda}{g_{rr}} (X_6^+ + X_6^-) \quad (6.16a)$$

$$A_{rr} = \frac{1}{3} \sqrt{\frac{g_{rr}\chi}{2\alpha}} (X_4^+ - X_4^-) - \frac{\sqrt{g_{rr}\chi}}{6} (X_5^+ - X_5^-) \quad (6.16b)$$

$$K = \sqrt{\frac{\chi}{8\alpha g_{rr}}} (X_4^+ - X_4^-) \quad (6.16c)$$

$$\Gamma^r = -\frac{1}{6} \frac{1}{g_{rr}g_{\theta\theta}} \left[\frac{(\beta^r)^2}{(\beta^r)^2 g_{rr} - \lambda} \right] X_1 + \frac{1}{g_{rr}} (X_2 - X_3) + \frac{2}{3} \frac{\alpha\chi}{g_{rr}(2\alpha\chi - \lambda)} (X_4^+ + X_4^-) - \frac{2}{3} \frac{1}{g_{rr}} (X_6^+ + X_6^-) \quad (6.16d)$$

$$Q_\chi = \frac{1}{12} \frac{\chi}{g_{rr}g_{\theta\theta}} \left[\frac{4(\beta^r)^2 g_{rr} - 3\lambda}{(\beta^r)^2 g_{rr} - \lambda} \right] X_1 + \frac{\chi}{2} X_3 - \frac{1}{3} \frac{\alpha\chi^2}{(2\alpha\chi - \lambda)} (X_4^+ + X_4^-) + \frac{\chi}{3} (X_6^+ + X_6^-) \quad (6.16e)$$

$$Q_{g_{rr}} = \frac{2(\beta^r)^2 g_{rr} - 3\lambda}{6g_{\theta\theta}((\beta^r)^2 g_{rr} - \lambda)} X_1 + \frac{4}{3} g_{rr} X_2 - g_{rr} X_3 + \frac{2}{3} \frac{\alpha\chi g_{rr}}{(2\alpha\chi - \lambda)} (X_4^+ + X_4^-) - \frac{1}{3} g_{rr} (X_5^+ + X_5^-) - \frac{2}{3} g_{rr} (X_6^+ + X_6^-) \quad (6.16f)$$

$$Q_{g_{\theta\theta}} = \left[\frac{1}{4g_{rr}} + \frac{(\beta^r)^2}{12((\beta^r)^2 g_{rr} - \lambda)} \right] X_1 - \frac{2}{3} g_{\theta\theta} X_2 + \frac{1}{2} g_{\theta\theta} X_3 - \frac{1}{3} \frac{\alpha\chi g_{\theta\theta}}{(2\alpha\chi - \lambda)} (X_4^+ + X_4^-) + \frac{1}{6} g_{\theta\theta} (X_5^+ + X_5^-) + \frac{1}{3} g_{\theta\theta} (X_6^+ + X_6^-) \quad (6.16g)$$

$$Q_\alpha = \frac{1}{2} (X_4^+ + X_4^-) \quad (6.16h)$$

$$Q_{\beta^r} = \frac{\beta^r \lambda}{8g_{rr}g_{\theta\theta}((\beta^r)^2 g_{rr} - \lambda)} X_1 - \frac{\lambda}{(2\alpha\chi - \lambda)} \sqrt{\frac{\alpha\chi}{8g_{rr}}} (X_4^+ - X_4^-) + \frac{1}{2} \sqrt{\frac{\lambda}{g_{rr}}} (X_6^+ - X_6^-). \quad (6.16i)$$

We will refer to this inverse transformation when discussing outer boundary conditions for our numerical simulations in Sec. 6.4.3.

6.2.4 Construction of Initial Data

We now construct initial data which is well suited for testing the nodal dG scheme. At a minimum the initial data should be spherically symmetric, and additionally we focus on solutions which are analytically known for all times. With such solutions we can perform straightforward and unambiguous convergence tests in addition to monitoring constraint violations. We wish to treat the singularity via excision, thus we further demand that for some region of the spacetime the excision conditions (6.15) are satisfied. Here we consider the classic Kerr-Schild solution, although many others are possible [137].

Schwarzschild Solution in Conformal Kerr-Schild Coordinates

In Kerr-Schild coordinates, here the system directly related to *incoming* Eddington-Finkelstein null coordinates, the line element for the Schwarzschild solution reads

$$ds^2 = -\alpha^2 dt^2 + (1 + 2M/R)(dR + \beta^R dt)^2 + R^2 d\theta^2 + R^2 \sin^2 \theta d\phi^2, \quad (6.17)$$

where R is the area radius, $\alpha = (1 + 2M/R)^{-1/2}$ is the lapse, and $\beta^R = 2M/(R + 2M)$ is the shift vector. The physical spatial metric⁵ \bar{g}_{ab} is the spatial part of this line element.

To define the corresponding solution to the GBSSN system, we use equation $g_{ab} = \chi \bar{g}_{ab}$ to define the following relationship between line elements:

$$dr^2 + r^2(d\theta^2 + \sin^2 \theta d\phi^2) = \chi[(1 + 2M/R)dR^2 + R^2 d\theta^2 + R^2 \sin^2 \theta d\phi^2], \quad (6.18)$$

⁵We remind the reader that throughout this chapter physical quantities have a ‘bar’ while conformal ones have no ‘bar’ (cf. footnote 1).

so that

$$\chi \left(1 + \frac{2M}{R}\right) \left(\frac{dR}{dr}\right)^2 = 1, \quad \chi R^2 = r^2. \quad (6.19)$$

Then we have

$$\left(1 + \frac{2M}{R}\right)^{1/2} \frac{dR}{R} = \frac{dr}{r}, \quad (6.20)$$

with integration yielding

$$r = \frac{R}{4} \left(1 + \sqrt{1 + \frac{2M}{R}}\right)^2 e^{2-2\sqrt{1+2M/R}}, \quad (6.21)$$

where the constant of integration has been chosen so that the $R, r \rightarrow \infty$ limits are consistent. The second relation in (6.19) shows that

$$\chi = \frac{1}{16} \left(1 + \sqrt{1 + \frac{2M}{R}}\right)^4 e^{4-4\sqrt{1+2M/R}}, \quad \chi^{-4} = \frac{2e^{\sqrt{1+2M/R}-1}}{1 + \sqrt{1 + 2M/R}}. \quad (6.22)$$

The extrinsic curvature tensor is specified by the expression for K given in (6.25h), the identity $K = K_R^R + 2K_\theta^\theta$, and

$$K_\theta^\theta = \left(1 + \frac{2M}{R}\right)^{-1/2} \frac{2M}{R^2}. \quad (6.23)$$

Since $K_R^R = K_r^r$, we compute that

$$K_r^r = K - 2K_\theta^\theta = - \left(1 + \frac{2M}{R}\right)^{-1/2} \left(\frac{R+M}{R+2M}\right) \frac{2M}{R^2}. \quad (6.24)$$

Next, since $K_{rr} = \bar{g}_{rr} K_r^r = \chi^{-1} K_r^r$, we have $K_r^r = A_{rr} + \frac{1}{3} g_{rr} K$. This implies

$A_{rr} = K_r^r - \frac{1}{3}K$, from which we get (6.25g). In all we have

$$\alpha = \left(1 + \frac{2M}{R}\right)^{-1/2} \quad (6.25a)$$

$$\beta^r = \beta^R \frac{dr}{dR} = \chi^{1/2} \left(1 + \frac{2M}{R}\right)^{-1/2} \frac{2M}{R} \quad (6.25b)$$

$$g_{rr} = 1 \quad (6.25c)$$

$$g_{\theta\theta} = r^2 = \chi R^2 \quad (6.25d)$$

$$\chi = \frac{1}{16} \left(1 + \sqrt{1 + \frac{2M}{R}}\right)^4 e^{4-4\sqrt{1+2M/R}} \quad (6.25e)$$

$$B^r = 0 \quad (6.25f)$$

$$A_{rr} = - \left(1 + \frac{2M}{R}\right)^{-1/2} \frac{4M}{3R^2} \left(\frac{2R+3M}{R+2M}\right) \quad (6.25g)$$

$$K = \left(1 + \frac{2M}{R}\right)^{-3/2} \left(1 + \frac{3M}{R}\right) \frac{2M}{R^2} \quad (6.25h)$$

$$\Gamma^r = -\frac{2}{r} = -\frac{2}{\chi^{1/2}R}. \quad (6.25i)$$

To differentiate these expressions with respect to r , we use the identity

$$\frac{dR}{dr} = \chi^{-1/2} \left(1 + \frac{2M}{R}\right)^{-1/2} \quad (6.26)$$

along with the chain rule.

6.3 A DG Scheme for the GBSSN System

This section describes the nodal discontinuous Galerkin method used to numerically solve (6.3), and builds upon the basic dG scheme ingredients of Sec. 3.3. To approximate (6.3), we follow the general procedure first introduced in Ref. [25]. Our approach defines local auxiliary variables $Q = u'$, and rewrites the spatially second-

order system (6.3) as the first-order system (6.12a). Once we use (6.12b) to eliminate Q from (6.12a), we recover the *primal* equations (6.3). The auxiliary variable approach was later generalized and coined the *local discontinuous Galerkin* (LDG) method in Ref. [67]. We may refer to our particular scheme as an LDG method, but note that many variations exist in the literature. We stress that in LDG methods Q is *not* evolved and is introduced primarily to assist in the construction of a stable scheme.

Equations (6.11) and (6.12a) imply that the physical flux function is

$$F(W) = \begin{pmatrix} F_u(W) \\ F_v(W) \end{pmatrix} \equiv A(u)W_{v:Q} = \begin{pmatrix} 0_{5 \times 1} \\ f(W) \end{pmatrix}, \quad f = \begin{pmatrix} f_{B^r} \\ f_{A_{rr}} \\ f_K \\ f_\Gamma \end{pmatrix}. \quad (6.27)$$

Only the evolution equations for B^r , A_{rr} , K , and Γ^r give rise to non-zero components in F , and we have collected these non-zero components into a smaller vector $f = F_v$. Inspection of (6.7) determines these components. For example, from (6.7c) we find

$$f_K = -\beta^r K + \frac{\chi}{g_{rr}} Q_\alpha. \quad (6.28)$$

6.3.1 Discretization of the System (6.12)

The computational domain Ω_h is the closed r -interval $[a, b]$. We cover Ω_h with $K > 1$ non-overlapping intervals D^k . On each interval D^k , we approximate each component of the system vector W by an interpolating polynomial of degree N belonging to D^k and interpolating at the LGL nodal points. Notice that although $Q = u'$, Q_h and u'_h

are not necessarily the same.

On each open interval $(a^k, b^k) \subset \mathbf{D}^k$ and for each component of the equations in (6.12), we define local residuals measuring the extent to which our approximations satisfy the original continuum system. Dropping the subdomain label k on the polynomials and focusing on the K equation as a representative example, the local residual corresponding to (6.3h) is⁶

$$\begin{aligned} -(R_K)_h^k \equiv & -\partial_t K_h + (\beta^r K^r)_h - \left(\frac{\chi Q'_\alpha}{g_{rr}} \right)_h + \left(\frac{\chi Q_{g_{rr}} Q_\alpha}{2g_{rr}^2} \right)_h - \left(\frac{\chi Q_{g_{\theta\theta}} Q_\alpha}{g_{rr} g_{\theta\theta}} \right)_h \\ & + \left(\frac{Q_\alpha Q_\chi}{2g_{rr}} \right)_h + \left(\frac{3\alpha A_{rr}^2}{2g_{rr}^2} \right)_h + \left(\frac{1}{3} \alpha K^2 \right)_h. \end{aligned} \quad (6.29)$$

We similarly construct the remaining eight residuals, e.g. $(R_{g_{rr}})_h$ and $(R_{\Gamma^r})_h$, as well as five residuals corresponding to (6.12b). For example, one of these remaining five is

$$(R_{Q_\alpha})_h^k \equiv -Q_{\alpha,h} + \alpha'_h. \quad (6.30)$$

The Galerkin conditions give rise to $9K(N+1)$ coupled ODES for (6.12a) and $5K(N+1)$ for (6.12b). Integrating twice by parts, introducing the numerical fluxes, and recalling definitions of the mass and stiffness matrix (3.32) we arrive at a nodal form of the semi-discrete equation

$$\begin{aligned} \partial_t \mathbf{K} = & \beta^r D \mathbf{K} - \frac{\chi D Q_\alpha}{g_{rr}} + \frac{1}{2} \frac{\chi Q_{g_{rr}} Q_\alpha}{g_{rr}^2} - \frac{\chi Q_{g_{\theta\theta}} Q_\alpha}{g_{rr} g_{\theta\theta}} \\ & + \frac{1}{2} \frac{Q_\alpha Q_\chi}{g_{rr}} + \frac{3}{2} \frac{\alpha A_{rr}^2}{g_{rr}^2} + \frac{1}{3} \alpha K^2 + M^{-1} \ell^k (f_{K,h} - f_K^*) \Big|_{a^k}^{b^k}. \end{aligned} \quad (6.31)$$

The superscript k is suppressed on all terms except $\ell^k(r)$ and the subscript h is dropped on all boldfaced variables. Eq. (6.31) features a component f_K^* of the nu-

⁶Non-linear products and quotients of polynomials are discussed in Sec. 3.3.

merical flux. The numerical flux is determined by (as yet not chosen) functions⁷

$$f^* = f^*(W^+, W^-), \quad (6.32)$$

where, recall, W^- is an interior boundary value of the approximation defined on D^k , and W^+ is an exterior boundary value of the approximation defined on either D^{k-1} or D^{k+1} . Eight other semi-discrete evolution equations are similarly obtained, with nine in total (one for each component of $W_{u:v}$). Additionally, we have

$$Q_\alpha = D\alpha + M^{-1}\ell^k(\alpha^* - \alpha_h)\Big|_{a^k}^{b_k}, \quad (6.33)$$

which again features a component α^* of the numerical flux. Four other auxiliary equations are similarly obtained, with five in total (one for each component of $Q = W_{Q:Q}$). The auxiliary variables are constructed and used at each stage of temporal integration, *but are not evolved variables*.

6.3.2 Numerical Flux

To complete our dG scheme we must specify functional forms for the components of the numerical flux introduced in the previous section. We distinguish between the physical fluxes (components of f) and the auxiliary fluxes (components of u) arising from the definition of the auxiliary variables. These choices are not independent as the resulting scheme must be stable and consistent. Our choice follows [37] which considered diffusion problems. Additional analysis of this flux choice appears in [15, 121].

⁷ In the context of the dG method here, + and - denote “exterior” and “interior”, and have no relation to the \pm using to denote the characteristic fields and speeds in Table 6.1. For characteristic fields and speeds, + and - mean “right-moving” and “left-moving”.

Let us first consider the numerical fluxes corresponding to the physical fluxes and of the form (6.32). The numerical flux vector is a function of the system and auxiliary variables interior and exterior to a subdomain. A common choice for f^* is

$$f^* = \{\{f_h\}\} + \frac{\tau}{2} [[v_h]]_{\mathbf{n}}, \quad K\text{-component of } f^*: f_K^* = \{\{f_{K,h}\}\} + \frac{\tau}{2} [[K_h]]_{\mathbf{n}}, \quad (6.34)$$

where, as an example, we have also shown the component of f^* corresponding to the analysis above. The numerical average $\{\{f_{K,h}\}\}$ and jump $[[K_h]]_{\mathbf{n}}$ across a local outward-pointing normal \mathbf{n} to a subdomain is defined in Eq. (3.30). Here τ is a position dependent penalty parameter (fixed below). The role of τ is to “penalize” (i. e. yield a negative contribution to the L_2 energy norm) jumps across an interface. An appropriate choice of τ will ensure stability, and we now provide some motivation for the choice (6.36) of τ we make below.

Were we treating the fully first-order system (6.9), the local Lax-Friedrichs flux would often be a preferred choice due to its simplicity [121]. In this case, the constant ω in the numerical flux formula $\mathcal{F}^* = \{\{\mathcal{F}_h\}\} + \frac{1}{2}\omega [[W_h]]_{\mathbf{n}}$ obeys $\omega \geq \max|\mu(\nabla_W \mathcal{F}(W))|$. Here, $\mathcal{F}(W) = \mathcal{A}(u)W$, the notation $\mu(\cdot)$ indicates the spectral radius of the matrix within, and the max is taken over interior W^- and exterior W^+ states. Motivated by (6.8), we adopt a similar but simpler prescription, substituting the field gradient

$$\nabla_{W_{v:Q}} \tilde{A}(u) W_{v:Q} = \tilde{A}(u) \quad (6.35)$$

for $\nabla_W \mathcal{F}(W)$. Precisely, we assume the scaling

$$\tau(b^k) = \tau(a^{k+1}) = \tau^{k+1/2} \equiv C \cdot \max|\mu(\tilde{A}(u))|, \quad (6.36)$$

where $C = O(1)$ is a constant chosen for stability. Larger values of C will result in schemes with better stability properties, whereas too large a value will impact

the CFL condition. At the interface point $I^{k+1/2} \equiv D^k \cap D^{k+1}$, the vector u_h has two representations: u^- at b^k and u^+ at a^{k+1} . The max in (6.36) is taken over the corresponding two sets of field speeds. More precisely, the speeds in Table 6.1 are computed for both u^- and u^+ , and the maximum taken over all resulting speeds. For the auxiliary variables, a penalized central flux is used. The definition with one representative component is

$$u^* = \{\{u_h\}\} - \frac{1}{2}[[u_h]]_{\mathbf{n}}, \quad \alpha\text{-component of } u^*: \alpha^* = \{\{\alpha_h\}\} - \frac{1}{2}[[\alpha_h]]_{\mathbf{n}}, \quad (6.37)$$

with similar expressions for the remaining components.

We stress the following point. Since the interior coupling between subdomains is achieved through the numerical flux forms (6.36) and (6.37), the inverse transformation (6.16) expressing the fundamental fields in terms of the characteristic fields is not required to achieve this coupling. On the other hand, imposition of physical boundary conditions may still rely on (6.16), since this transformation allows one to fix only incoming characteristic modes.

6.3.3 Filtering

Like other nodal (pseudospectral) methods, our scheme may suffer from instabilities driven by aliasing error [124]. *Filtering* is a simple, yet robust remedy. To filter a solution component, such as χ , we use the modal (as opposed to nodal) representation of the solution:

$$\chi_h^k(t, r) = \sum_{j=0}^N \chi(t, r_j^k) \ell_j^k(r) = \sum_{j=0}^N \hat{\chi}_j^k(t) P_j(r), \quad (6.38)$$

where $P_j(r)$ is the j th Legendre polynomial. Let $\eta_j = j/N$, and define the filter function

$$\sigma(\eta_j) = \begin{cases} 1 & \text{for } 0 \leq \eta_j \leq N_c/N \\ \exp\left(-\epsilon\left(\frac{\eta_j - N_c/N}{1 - N_c/N}\right)^{2s}\right) & \text{for } N_c/N \leq \eta_j \leq 1. \end{cases} \quad (6.39)$$

At each timestep we modify our solution component according to

$$\chi_h^k \rightarrow (\chi_h^k)^{\text{filtered}} = \sum_{j=0}^N \sigma(\eta_j) \hat{\chi}_j^k(t) P_j(r). \quad (6.40)$$

Evidently, the modification only affects the top $N - N_c$ modes, and is sufficient to control the type of weak instability driven by aliasing [121]. The numerical parameters N_c and ϵ are problem dependent. For our simulations, we have taken $\epsilon \simeq -\log(\varepsilon_{\text{mach}}) = 36$, where $\varepsilon_{\text{mach}}$ is machine accuracy in double precision.

6.3.4 Model System

To better illustrate the basic properties of our method, we consider a toy model. Namely, the following spatially second-order system:

$$\partial_t u = u' + av - u^3 + g(t, x) \quad (6.41a)$$

$$\partial_t v = u'' + v' - (u + v)(u')^2 + v^2 u^2 + h(t, x), \quad (6.41b)$$

where $a \geq 1$ is constant and g and h are analytic source terms to be specified. In contrast to (6.5), here u , v , and $Q = u'$ are scalars rather than vectors. System (6.41) admits a first-order reduction in which u' is defined as an extra variable. Since this first-order reduction is strongly hyperbolic, the spatially second-order system (6.41) is also strongly hyperbolic by one of the definitions considered in [111]. The

characteristic fields X^\pm and speeds μ^\pm are

$$X^+ = \sqrt{a}v - u', \quad \mu^+ = \sqrt{a} - 1; \quad X^- = \sqrt{a}v + u', \quad \mu^- = -(\sqrt{a} + 1). \quad (6.42)$$

To construct a local dG scheme for this system, we first rewrite it as

$$\partial_t u = Q + av - u^3 + g(t, x) \quad (6.43a)$$

$$\partial_t v = Q' + v' - (u + v)Q^2 + v^2u^2 + h(t, x) \quad (6.43b)$$

$$Q = u'. \quad (6.43c)$$

Evidently, $f = -(Q + v)$ is the v -component of the physical flux vector

$$F(v, Q) \equiv \begin{pmatrix} F_u \\ F_v \end{pmatrix} = \begin{pmatrix} 0 \\ f \end{pmatrix}. \quad (6.44)$$

Note that F has the same structure as $(u, v)^T$. Borrowing from the presentation for the GBSSN system, we write the analogous semidiscrete scheme on each subdomain D^k for the model system:

$$\partial_t \mathbf{u} = \mathbf{Q} + a\mathbf{v} - \mathbf{u}^3 + \mathbf{g}(t) \quad (6.45a)$$

$$\partial_t \mathbf{v} = D\mathbf{Q} + D\mathbf{v} - (\mathbf{u} + \mathbf{v})\mathbf{Q}^2 + \mathbf{v}^2\mathbf{u}^2 + \mathbf{h}(t) + M^{-1}\boldsymbol{\ell}^k(f_h - f^*) \Big|_{a^k}^{b^k}, \quad (6.45b)$$

$$\mathbf{Q} = D\mathbf{u} + M^{-1}\boldsymbol{\ell}^k(u^* - u_h) \Big|_{a^k}^{b^k}. \quad (6.45c)$$

Here, we have suppressed the subinterval label k from all variables except for the vector $\boldsymbol{\ell}^k$ of Lagrange polynomial values. Moreover, following the guidelines discussed above, the numerical fluxes are given by

$$f^* = \{\{f_h\}\} + \frac{1 + \sqrt{a}}{2} [[v_h]]_{\mathbf{n}}, \quad u^* = \{\{u_h\}\} - \frac{1}{2} [[u_h]]_{\mathbf{n}}. \quad (6.46)$$

Next we will analyze the stability of our scheme, for a more general numerical flux choice, as applied to (6.41) with the nonlinear and source terms dropped.

6.3.5 Stability of the Model System

The following stability analysis for the model system (6.41) has been inspired by [226, 227]. After dropping all nonlinear source terms, the system (6.41) becomes

$$\partial_t u = u' + av \tag{6.47a}$$

$$\partial_t v = u'' + v'. \tag{6.47b}$$

This section analyzes the stability of (6.47), considering both the continuum system itself as well as its semi-discrete dG approximation. The latter analysis offers some insight into the empirically observed stability of our dG scheme for the spherically reduced GBSSN equations. For the nonlinear systems (6.3) and (6.41), we do not attempt a formal stability proof. Nevertheless, the results of this proof have served as a guide for our choices of penalty parameters (i.e. numerical flux). Chapter 3 offers an extended discussion of stability, and Sec. 3.1.1 introduces much of the notation used here. Integration measures are suppressed throughout.

Analysis for a Single Interval

For the continuum model we will establish the following estimate:

$$\|u'(T, \cdot)\|_{\mathbb{D}}^2 + a\|v(T, \cdot)\|_{\mathbb{D}}^2 \leq C(T) (\|u'(0, \cdot)\|_{\mathbb{D}}^2 + a\|v(0, \cdot)\|_{\mathbb{D}}^2), \tag{6.48}$$

where the time-dependent constant $C(T)$ is determined solely by the choice of boundary conditions. To show (6.48), we first change variables with $\hat{v} = \sqrt{av}$, thereby rewriting (6.47) in the following symmetric form:

$$\partial_t u = u' + \sqrt{a}\hat{v} \quad (6.49a)$$

$$\partial_t \hat{v} = \sqrt{a}u'' + \hat{v}'. \quad (6.49b)$$

Equations (6.49a,b) then imply

$$\frac{1}{2}\partial_t \int_{\mathbf{D}} (u')^2 = \int_{\mathbf{D}} u'(u'' + \sqrt{a}\hat{v}') = \int_{\mathbf{D}} \sqrt{a}u'\hat{v}' + \frac{1}{2} \int_{\partial\mathbf{D}} (u')^2 \quad (6.50a)$$

$$\frac{1}{2}\partial_t \int_{\mathbf{D}} (\hat{v})^2 = \int_{\mathbf{D}} \hat{v}(\sqrt{a}u'' + \hat{v}') = - \int_{\mathbf{D}} \sqrt{a}u'\hat{v}' + \frac{1}{2} \int_{\partial\mathbf{D}} (\hat{v}^2 + 2\sqrt{a}u'\hat{v}). \quad (6.50b)$$

Here $\hat{v}\hat{v}'$ and $u'u''$ have been expressed as exact derivatives and then integrated to boundary terms, the second equation employs an extra integration by parts, and with only one space dimension $\int_{\partial\mathbf{D}}$ denotes a difference of endpoint evaluations. Addition of Eqs. (6.50a,b) gives

$$\frac{1}{2}\partial_t \int_{\mathbf{D}} [\hat{v}^2 + (u')^2] = \frac{1}{2} \int_{\partial\mathbf{D}} [\hat{v}^2 + (u')^2 + 2\sqrt{a}u'\hat{v}]. \quad (6.51)$$

Substitutions with the identities

$$[\hat{v}^2 + (u')^2] = \frac{1}{2}[(\hat{v} + u')^2 + (\hat{v} - u')^2], \quad 2u'\hat{v} = \frac{1}{2}[(\hat{v} + u')^2 - (\hat{v} - u')^2] \quad (6.52)$$

and replacements to recover the original variable $v = \hat{v}/\sqrt{a}$ yield

$$\frac{1}{2}\partial_t \int_{\mathbf{D}} [av^2 + (u')^2] = \frac{1 + \sqrt{a}}{4} \int_{\partial\mathbf{D}} (\sqrt{a}v + u')^2 + \frac{1 - \sqrt{a}}{4} \int_{\partial\mathbf{D}} (\sqrt{a}v - u')^2. \quad (6.53)$$

From (6.53) we deduce that the time-dependent constant $C(T)$ in (6.48) must satisfy

$$\left| 1 + \frac{\int_0^T \left[\frac{1+\sqrt{a}}{2} \int_{\partial\mathbb{D}} (\sqrt{a}v + u')^2 + \frac{1-\sqrt{a}}{2} \int_{\partial\mathbb{D}} (\sqrt{a}v - u')^2 \right] dt}{\|u'(0, \cdot)\|^2 + a\|v(0, \cdot)\|^2} \right| \leq C(T). \quad (6.54)$$

For periodic boundary conditions, we may choose $C(T) = 1$. Moreover, if $a \geq 1$ and $u' = -\sqrt{a}v$ is specified at $\partial\mathbb{D}^+$, then $\|u'(t, \cdot)\|^2 + a\|v(t, \cdot)\|^2$ decays.

Still working on a single interval (subdomain), we now consider the semi-discrete scheme for (6.49), i. e. (6.45) with all nonlinear source terms dropped, and with v replaced by \hat{v}/\sqrt{a} . Derivation of a formula analogous to (6.53) is our first step toward establishing L_2 stability of the semi-discrete scheme. While (6.45) features vectors, for example $\mathbf{u}(t)$, taking values at the Legendre-Gauss-Lobatto nodal points, here we work with the numerical solution as a polynomial, for example $u_h(t, x)$. These two representations are related by the Lagrange interpolating polynomials for the nodal set, here taken to span both the space of test functions and the space of basis functions. Our scheme is

$$\int_{\mathbb{D}^k} \psi \partial_t u_h = \int_{\mathbb{D}^k} \psi (Q_h + \sqrt{a} \hat{v}_h) \quad (6.55a)$$

$$\int_{\mathbb{D}^k} \xi \partial_t \hat{v}_h = - \int_{\mathbb{D}^k} \xi' (\sqrt{a} Q_h + \hat{v}_h) + \int_{\partial\mathbb{D}^k} \xi (\sqrt{a} Q^* + \hat{v}^*) \quad (6.55b)$$

$$\int_{\mathbb{D}^k} \varphi Q_h = \int_{\mathbb{D}^k} \varphi u'_h + \int_{\partial\mathbb{D}^k} \varphi (u^* - u_h), \quad (6.55c)$$

where ψ , ξ , and φ are polynomial test functions. These test functions are arbitrary, except that they must be degree- N polynomials. In (6.55) the variables u_h , \hat{v}_h and Q_h should also carry a superscript k , but we have suppressed this. Derivation of a formula analogous to (6.53) is complicated by the fact that Q_h is not evolved. Nevertheless, at a given instant t we can assemble Q_h from (6.55c).

Mimicking the calculation (6.50b) from the continuum case, we first use (6.55b) with $\xi = \hat{v}_h$ to write

$$\begin{aligned} \frac{1}{2} \partial_t \int_{\mathbb{D}^k} \hat{v}_h^2 &= - \int_{\mathbb{D}^k} (\sqrt{a} Q_h + \hat{v}_h) \hat{v}_h' + \int_{\partial \mathbb{D}^k} (\sqrt{a} Q^* + \hat{v}^*) \hat{v}_h \\ &= - \int_{\mathbb{D}^k} \sqrt{a} Q_h \hat{v}_h' + \frac{1}{2} \int_{\partial \mathbb{D}^k} [2(\sqrt{a} Q^* + \hat{v}^*) \hat{v}_h - \hat{v}_h^2]. \end{aligned} \quad (6.56)$$

The right-hand side of (6.50a) is analogous to

$$\frac{1}{2} \partial_t \int_{\mathbb{D}^k} Q_h^2 = \int_{\mathbb{D}^k} Q_h \partial_t Q_h. \quad (6.57)$$

However, since Q_h is not evolved, the term $\partial_t Q_h$ must be given a suitable interpretation. On the right hand side of (6.55c) only u_h , u_h' , and u^* necessarily depend on time, since the test function φ need not be time-dependent. Furthermore, u^* is explicitly given as a linear combination of u_h , as seen in Eq. (6.66c) below. Choosing $\varphi = \ell_j$, taking the time derivative of (6.55c), and appealing to the commutivity of mixed partial derivatives, we therefore arrive at

$$\int_{\mathbb{D}^k} \ell_j \partial_t Q_h = \int_{\mathbb{D}^k} \ell_j (\partial_t u_h)' + \int_{\partial \mathbb{D}^k} \ell_j ((\partial_t u)^* - \partial_t u_h), \quad (6.58)$$

where $(\partial_t u)^*$ depends on $\partial_t u_h$ in precisely the same way that u^* depends on u_h . We have written ℓ_j rather than φ in the last equation to emphasize that the result also holds for any linear combination of ℓ_j (for example φ), and even for *time-dependent* combinations. Since Q_h is itself such a combination, we obtain

$$\begin{aligned} \frac{1}{2} \partial_t \int_{\mathbb{D}^k} Q_h^2 &= \int_{\mathbb{D}^k} Q_h (\partial_t u_h)' + \int_{\partial \mathbb{D}^k} ((\partial_t u)^* - \partial_t u_h) Q_h \\ &= \int_{\mathbb{D}^k} Q_h (Q_h' + \sqrt{a} \hat{v}_h') + \int_{\partial \mathbb{D}^k} ((\partial_t u)^* - \partial_t u_h) Q_h \\ &= \int_{\mathbb{D}^k} \sqrt{a} Q_h \hat{v}_h' + \frac{1}{2} \int_{\partial \mathbb{D}^k} [2((\partial_t u)^* - \partial_t u_h) Q_h + Q_h^2]. \end{aligned} \quad (6.59)$$

Addition of (6.56) and (6.59) gives

$$\frac{1}{2} \partial_t \int_{\mathbf{D}^k} (Q_h^2 + \hat{v}_h^2) = \frac{1}{2} \int_{\partial \mathbf{D}^k} [Q_h^2 - \hat{v}_h^2 + 2(\sqrt{a}Q^* + \hat{v}^*)\hat{v}_h + 2((\partial_t u)^* - \partial_t u_h)Q_h], \quad (6.60)$$

the aforementioned analog of (6.53). This formula holds on a single subdomain \mathbf{D}^k , and we now combine multiple copies of it, one for each value of k .

Analysis for Multiple Intervals

To facilitate combination of (6.60) over all k , we change notation. At every subdomain interface $\mathbf{l}^{k+1/2} \equiv \partial \mathbf{D}^k \cap \partial \mathbf{D}^{k+1}$, let the superscripts L and R denote field values respectively taken from the left and right. Then the fields evaluated at $\mathbf{l}^{k+1/2}$ which belong to \mathbf{D}^k will be $u_{k+1/2}^L$, $\hat{v}_{k+1/2}^L$, and $Q_{k+1/2}^L$, while those belonging to \mathbf{D}^{k+1} will be $u_{k+1/2}^R$, $\hat{v}_{k+1/2}^R$, and $Q_{k+1/2}^R$. However, at $\mathbf{l}^{k-1/2}$ the values taken from \mathbf{D}^k are $u_{k-1/2}^R$, $\hat{v}_{k-1/2}^R$, and $Q_{k-1/2}^R$. Note that we have also replaced the subscript h , denoting a numerical solution, with $k \pm 1/2$, denoting the location of the endpoint value of the numerical solution. With this notation, we define

$$\Delta_\alpha^L = \frac{1}{2} [(Q_\alpha^L)^2 - (\hat{v}_\alpha^L)^2] + (\sqrt{a}Q_\alpha^* + \hat{v}_\alpha^*) \hat{v}_\alpha^L + [(\partial_t u_\alpha)^* - \partial_t u_\alpha^L] Q_\alpha^L, \quad (6.61)$$

and similarly for Δ_α^R . The same numerical fluxes appear in both Δ_α^L and Δ_α^R (i.e. each numerical flux takes the same value on either side of an interface), whence fluxes like Q_α^* do not carry an L or R superscript. In terms of these definitions (6.60) becomes

$$\frac{1}{2} \partial_t \int_{\mathbf{D}^k} (Q_h^2 + \hat{v}_h^2) = \Delta_{k+1/2}^L - \Delta_{k-1/2}^R. \quad (6.62)$$

Summation over all \mathbf{D}^k yields

$$\begin{aligned} \frac{1}{2} \partial_t \sum_{k=1}^K \int_{\mathbf{D}^k} (Q_h^2 + \hat{v}_h^2) &= \sum_{k=1}^{K-1} (\Delta_{k+1/2}^L - \Delta_{k+1/2}^R) + \Delta_{K+1/2}^L - \Delta_{1/2}^R \\ &= \sum_{k=1}^{K-1} (\Delta_h^L - \Delta_h^R)|_{\mathbf{l}^{k+1/2}} + \Delta_{K+1/2}^L - \Delta_{1/2}^R. \end{aligned} \quad (6.63)$$

We have reverted to h -notation denoting the numerical solution, since the L, R superscripts indicate unambiguously the relevant domain used for evaluation at $\mathbf{l}^{k+1/2}$.

We again seek an estimate of the form

$$\sum_{k=1}^K (\|Q_h(T, \cdot)\|_{\mathbf{D}^k}^2 + a \|v_h(T, \cdot)\|_{\mathbf{D}^k}^2) \leq C(T) \sum_{k=1}^K (\|Q_h(0, \cdot)\|_{\mathbf{D}^k}^2 + a \|v_h(0, \cdot)\|_{\mathbf{D}^k}^2), \quad (6.64)$$

that is essentially the same as the one (6.48) considered in the continuum case. Assume that the chosen boundary conditions ensure $\Delta_{K+1/2}^L - \Delta_{1/2}^R$ is bounded by a time-dependent constant which does not depend on the numerical parameters N and h (subdomain width). Establishment of stability then amounts to showing that the remaining sum over interface terms in (6.63) is non-positive; whence this remaining sum is consistent with $C(T) \leq 1$, although the boundary conditions may give rise to a different bound. In fact, we will choose the numerical fluxes such that each individual interface term is non-positive. At interface $\mathbf{l}^{k+1/2}$ and in L, R notation, the jump and average of \hat{v}_h , for example, are

$$\frac{1}{2} (\hat{v}^+ + \hat{v}^-) \equiv \{\{\hat{v}_h\}\} = \frac{1}{2} (\hat{v}_{k+1/2}^L + \hat{v}_{k+1/2}^R) \quad (6.65a)$$

$$\mathbf{n}^- \hat{v}^- + \mathbf{n}^+ \hat{v}^+ \equiv [[\hat{v}_h]]_{\mathbf{n}} = \hat{v}_{k+1/2}^L - \hat{v}_{k+1/2}^R. \quad (6.65b)$$

Consider numerical fluxes of the form

$$Q^* = \{\{Q_h\}\} - \frac{\tau_Q}{2} [[Q_h]]_{\mathbf{n}} \quad (6.66a)$$

$$\hat{v}^* = \{\{\hat{v}_h\}\} - \frac{\tau_v}{2} [[\hat{v}_h]]_{\mathbf{n}} \quad (6.66b)$$

$$u^* = \{\{u_h\}\} - \frac{\tau_u}{2} [[u_h]]_{\mathbf{n}} \quad (6.66c)$$

$$(\partial_t u)^* = \{\{\partial_t u_h\}\} - \frac{\tau_u}{2} [[\partial_t u_h]]_{\mathbf{n}}, \quad (6.66d)$$

where (6.66c) induces (6.66d) and where the penalty parameters τ_u , τ_v , and τ_Q are real numbers. The fluxes defined in (6.46) correspond to $\tau_u = 1$, $\tau_v = 1 + \sqrt{a}$, and $\tau_Q = 0$. In terms of these quantities the k th interface contribution in (6.63) is

$$\begin{aligned} (\Delta_h^L - \Delta_h^R)|_{|k+1/2} &= \frac{1}{2} ([[Q_h^2]]_{\mathbf{n}} - [[\hat{v}_h^2]]_{\mathbf{n}}) + \{\{\hat{v}_h\}\} [[\hat{v}_h]]_{\mathbf{n}} - \frac{\tau_v}{2} [[\hat{v}_h]]_{\mathbf{n}}^2 \\ &\quad + \sqrt{a} \{\{Q_h\}\} [[\hat{v}_h]]_{\mathbf{n}} - \frac{\sqrt{a}\tau_Q}{2} [[Q_h]]_{\mathbf{n}} [[\hat{v}_h]]_{\mathbf{n}} - \{\{Q_h\}\} [[\partial_t u_h]]_{\mathbf{n}} - \frac{\tau_u}{2} [[\partial_t u_h]]_{\mathbf{n}} [[Q_h]]_{\mathbf{n}}, \end{aligned} \quad (6.67)$$

where we have suppressed the k dependence of the right-hand side. Now consider the term $[[\partial_t u_h]]_{\mathbf{n}}$. Because $\partial_t u_h$ and $Q_h + \sqrt{a}\hat{v}_h$ are both polynomials of degree N , Eq. (6.55a) implies the vector equation $\partial_t \mathbf{u} = \mathbf{Q} + \sqrt{a}\hat{\mathbf{v}}$, that is *pointwise* equivalence on the nodal points of \mathbf{D}^k , which in turn implies $[[\partial_t u_h]]_{\mathbf{n}} = [[Q_h + \sqrt{a}\hat{v}_h]]_{\mathbf{n}}$. Upon substituting this identity into the last equation, we arrive at an expression which features only \hat{v}_h and Q_h ,

$$\begin{aligned} (\Delta_h^L - \Delta_h^R)|_{|k+1/2} &= \frac{1}{2} ([[Q_h^2]]_{\mathbf{n}} - [[\hat{v}_h^2]]_{\mathbf{n}}) + \{\{\hat{v}_h\}\} [[\hat{v}_h]]_{\mathbf{n}} - \frac{\tau_v}{2} [[\hat{v}_h]]_{\mathbf{n}}^2 \\ &\quad + \sqrt{a} \{\{Q_h\}\} [[\hat{v}_h]]_{\mathbf{n}} - \frac{\sqrt{a}\tau_Q}{2} [[Q_h]]_{\mathbf{n}} [[\hat{v}_h]]_{\mathbf{n}} \\ &\quad - \{\{Q_h\}\} [[Q_h + \sqrt{a}\hat{v}_h]]_{\mathbf{n}} - \frac{\tau_u}{2} [[Q_h + \sqrt{a}\hat{v}_h]]_{\mathbf{n}} [[Q_h]]_{\mathbf{n}}. \end{aligned} \quad (6.68)$$

The identities $\{\{\hat{v}_h\}\} [[\hat{v}_h]]_{\mathbf{n}} = \frac{1}{2} [[\hat{v}_h^2]]_{\mathbf{n}}$ and $[[Q_h + \sqrt{a}\hat{v}_h]]_{\mathbf{n}} = [[Q_h]]_{\mathbf{n}} + \sqrt{a} [[\hat{v}_h]]_{\mathbf{n}}$

then simplify (6.68) to

$$(\Delta_h^L - \Delta_h^R)|_{|k+1/2} = -\frac{\tau_v}{2} [[\hat{v}_h]]_{\mathbf{n}}^2 - \frac{\sqrt{a}(\tau_u + \tau_Q)}{2} [[Q_h]]_{\mathbf{n}} [[\hat{v}_h]]_{\mathbf{n}} - \frac{\tau_u}{2} [[Q_h]]_{\mathbf{n}}^2. \quad (6.69)$$

The role of a penalty parameter is now clear. Positive values of τ_v penalize jumps in \hat{v}_h through a negative contribution to the energy. Likewise, positive values of τ_u penalize jumps in Q_h through a negative contribution to the energy. However, because the sign of $[[Q_h]]_{\mathbf{n}} [[\hat{v}_h]]_{\mathbf{n}}$ can be positive or negative, only the choice $\tau_Q = -\tau_u$ yields an expression for $(\Delta_h^L - \Delta_h^R)|_{|k+1/2}$ which is manifestly negative for $\tau_u \geq 0$ and $\tau_v \geq 0$. A simple estimate based on Young's inequality with ε (that is, $2\alpha\beta \leq \varepsilon^{-1}\alpha^2 + \varepsilon\beta^2$, where $\alpha, \beta \geq 0$ and $\varepsilon > 0$) shows that for $\tau_Q = 0$ the choice $\tau_v \geq a\tau_u/4$ also yields stability. Numerical verification of (6.69) is provided in Sec. 6.4.2.

For the GBSSN system (6.3), u , v , and Q are block indices [cf. Eq. (6.5)]. Similar to the model problem, we have penalized Q with $\tau_u = 1$, with τ_v chosen large enough to heuristically overcome the cross-terms of indefinite size that arise from $\tau_Q = 0$ (we interpret equations like $\tau_u = 1$ componentwise). An analogous choice “ $\tau_Q = -\tau_u$ ” for the GBSSN system might be possible, but would be considerably more complicated. Indeed, such a choice likely entails a *matrix* of penalty parameters, but we do not give the details here.

6.4 Results from Numerical Simulations

This section presents results found by numerically solving both the model system (6.41) and GBSSN system (6.3) with the dG scheme presented in the previous section.

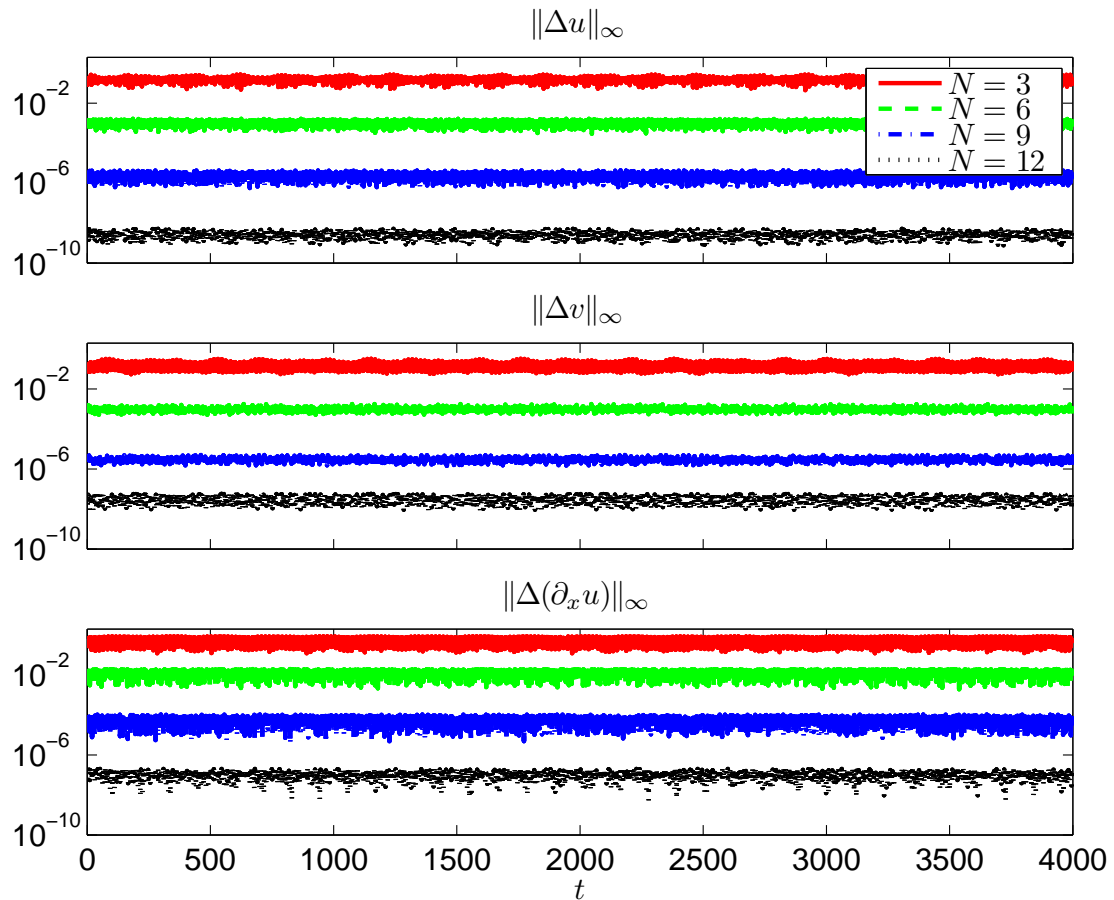


Figure 6.1: SPECTRAL CONVERGENCE OF FIELDS FOR MODEL PDE. Respectively, for $N = 3, 6, 9, 12$, a timestep of $\Delta t = 0.0578, 0.0178, 0.0084, 0.0049$ has been chosen for stability and accuracy. In the title headings, for example, $\Delta u \equiv u_{\text{numer}} - u_{\text{exact}}$.

6.4.1 Simulations of the Model System

The semi-discrete scheme (6.45) has been integrated with the classical fourth-order Runge-Kutta method. When integrating this system, we have first constructed \mathbf{Q} at each Runge-Kutta stage, and then substituted into the evolution equations (6.45a,b) for \mathbf{u} and \mathbf{v} . The problem has been solved on a computational domain $[0, 4\pi]$ comprised of two subdomains with a timestep chosen small enough for stability. The initial data has been taken from the following exact solution to (6.41):

$$u'_{\text{exact}}(t, x) = \frac{1}{2} [\sin(x - \mu^- t) - \sin(x - \mu^+ t)] \quad (6.70a)$$

$$v_{\text{exact}}(t, x) = \frac{1}{2\sqrt{a}} [\sin(x - \mu^- t) + \sin(x - \mu^+ t)] \quad (6.70b)$$

$$g(t, x) = u_{\text{exact}}^3 \quad (6.70c)$$

$$h(t, x) = (u_{\text{exact}} + v_{\text{exact}})(u'_{\text{exact}})^2 - v_{\text{exact}}^2 u_{\text{exact}}^2, \quad (6.70d)$$

where the speeds μ^\pm are found in (6.42). Specification of the boundary condition at a physical endpoint amounts to choosing the external state at that point. We have considered two possibilities: (i) the analytic state $(Q^+, v^+) = (Q_{\text{exact}}, v_{\text{exact}})$ and (ii) an upwind state. For example, at $x = 4\pi$ the upwind state is⁸

$$\begin{aligned} Q^+ &= Q_{\text{upwind}} = \frac{1}{2} [(X^-)_{\text{exact}} - (X^+)_{\text{numer}}], \\ v^+ &= v_{\text{upwind}} = \frac{1}{2\sqrt{a}} [(X^-)_{\text{exact}} + (X^+)_{\text{numer}}]. \end{aligned} \quad (6.71)$$

Either choice of (Q^+, v^+) leads to similar results, and the plots here correspond to the analytic state. Figure 6.1 clearly shows spectral convergence with increasing polynomial order N across all fields for the case $a = 2$. Other values of a , including $a = 1$ for which X^+ is a static characteristic field, have also been considered with

⁸We remind the reader that, unfortunately, the \pm on X^\pm means something different than the \pm indicating exterior/interior dG states [cf. footnote 7].

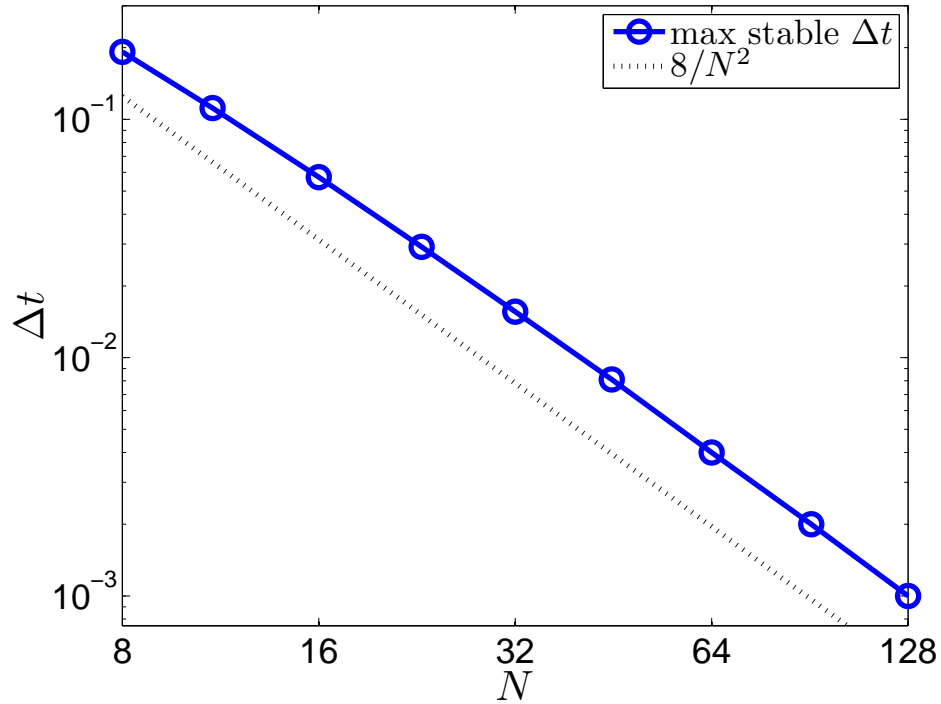


Figure 6.2: SCALING OF MAXIMUM STABLE Δt WITH N FOR MODEL PDE.

similar results.

Section 6.3.5 demonstrates that our proposed scheme for the system (6.45) with nonlinear and source terms dropped is stable in a semi-discrete sense. Nevertheless, the fully discrete scheme, obtained via temporal discretization by the fourth-order Runge-Kutta method, is still subject to the standard absolute stability requirement. Namely, if μ_h is any eigenvalue corresponding to the (linearized) discrete spatial operator, then a necessary condition for stability is that $\mu_h \Delta t$ lies in *absolute stability region* for Runge-Kutta 4. Here, we empirically show that the associated timestep restriction scales like N^{-2} , i.e. $\Delta t = O(N^{-2})$ for stability. We note that such scaling is welcome in light of the second-order spatial operators which appear in the system, and suggest a possible worse scaling like N^{-4} . Fig. 6.2 plots the maximum stable timestep for a range of N , demonstrating the N^{-2} scaling, in line with behavior known from analysis of first-order systems [121]. This scaling also holds for the

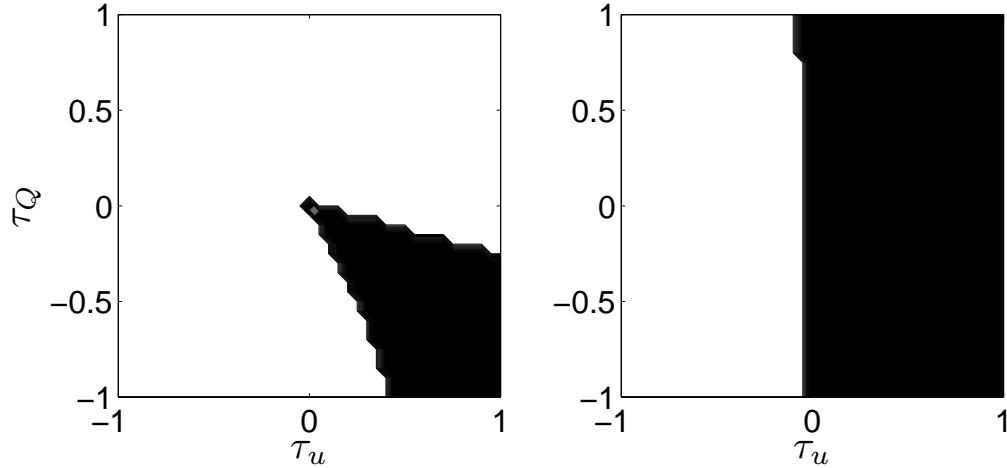


Figure 6.3: STABLE EVOLUTIONS FOR THE MODEL SYSTEM. For fixed $\tau_v = 10^{-6}$ and $\tau_v = 1 + \sqrt{2}$ respectively, the left and right plots depict stable choices (determined empirically) of τ_u and τ_Q for the linear model system (6.47). The stable regions are colored black, but the jagged edges result from the discretization of the (τ_u, τ_Q) -plane.

GBSSN system.

6.4.2 Semi-Discrete Stability of Model PDE

We now verify the theoretical stability result (6.69) given in Sec. 6.3.5. Figure 6.3 depicts certain choices of stable penalty parameters for the *linear* model system evolved to $t_{\text{final}} = 1000$ (with $a = 2$, $N = 10$, and $\Delta t \simeq 0.0553$), as determined empirically with simulations similar to those described in Sec. 6.4.1. The left plot corresponds to a small $\tau_v = 10^{-6}$, for which the choice $\tau_u = 1$, $\tau_Q = 0$ is not stable, as expected from the theoretical analysis. However, the right plot corresponds to $\tau_v = 1 + \sqrt{a}$, for which $\tau_u = 1$, $\tau_Q = 0$ is stable. Motivated by the numerical flux choices (6.34,6.37) used for the GBSSN system (6.3), we have (as mentioned above) set $\tau_u = 1$, $\tau_v = 1 + \sqrt{a}$, and $\tau_Q = 0$ in simulations of the nonlinear model (6.41). For the nonlinear model system (6.41), the theoretically motivated choice $\tau_Q = -\tau_u$ also yields numerically stable evolutions when $\tau_u \geq 0$ and $\tau_v \geq 0$.

6.4.3 Simulations of the GBSSN System

This subsection documents results for simulations of the unit-mass-parameter ($M = 1$) Schwarzschild solution (6.2.4) expressed in terms of ingoing Kerr-Schild coordinates. Since the solution is stationary, temporal integration of the semi-discrete scheme has been carried out with the forward Euler method which the dissipation in our method allows. The r -coordinate domain $[0.4, 3.4]$ has been split into three equally spaced subdomains, and we have set $\eta = 10$, $\lambda = 0.1$, and $C = 2$ [cf. Eq. (6.36)]. For all simulations Δt has been chosen for stability. With the chosen λ , the inner physical boundary $r_{\min} = 0.4$ is an excision surface. At each timestep we have applied an (order $2s = 20$) exponential filter on the top two-thirds of the modal coefficient set for all fields *except* for g_{rr} and $g_{\theta\theta}$. *For stability, we have empirically observed that g_{rr} and $g_{\theta\theta}$ must not be filtered.* A detailed understanding of this is still lacking.

Issues related to physical boundary conditions are similar to the one encountered in Sec. 6.4.1 for the model problem. Similar to before, we have retained Eqs. (6.34,6.37) as the choice of numerical flux even at the endpoints. Therefore, at an endpoint the specification of the boundary condition amounts to the choice W^+ of external state. We have typically chosen the inner boundary of the radial domain as an excision boundary, and in this case $W^+ = W^-$ is enforced at the inner physical boundary. At the outer physical boundary, for W^+ we have again considered two choices: (i) W_{exact} and (ii) W_{upwind} . To enforce choice (ii) the inverse transformation (6.16) must be used with incoming characteristic fields fixed to their exact values, similar to (6.71). We have tried various versions of choice (ii), and in all cases the resulting simulations have been unstable. We therefore present results corresponding to choice (i). Although the choice of an analytical external state W_{exact} at the

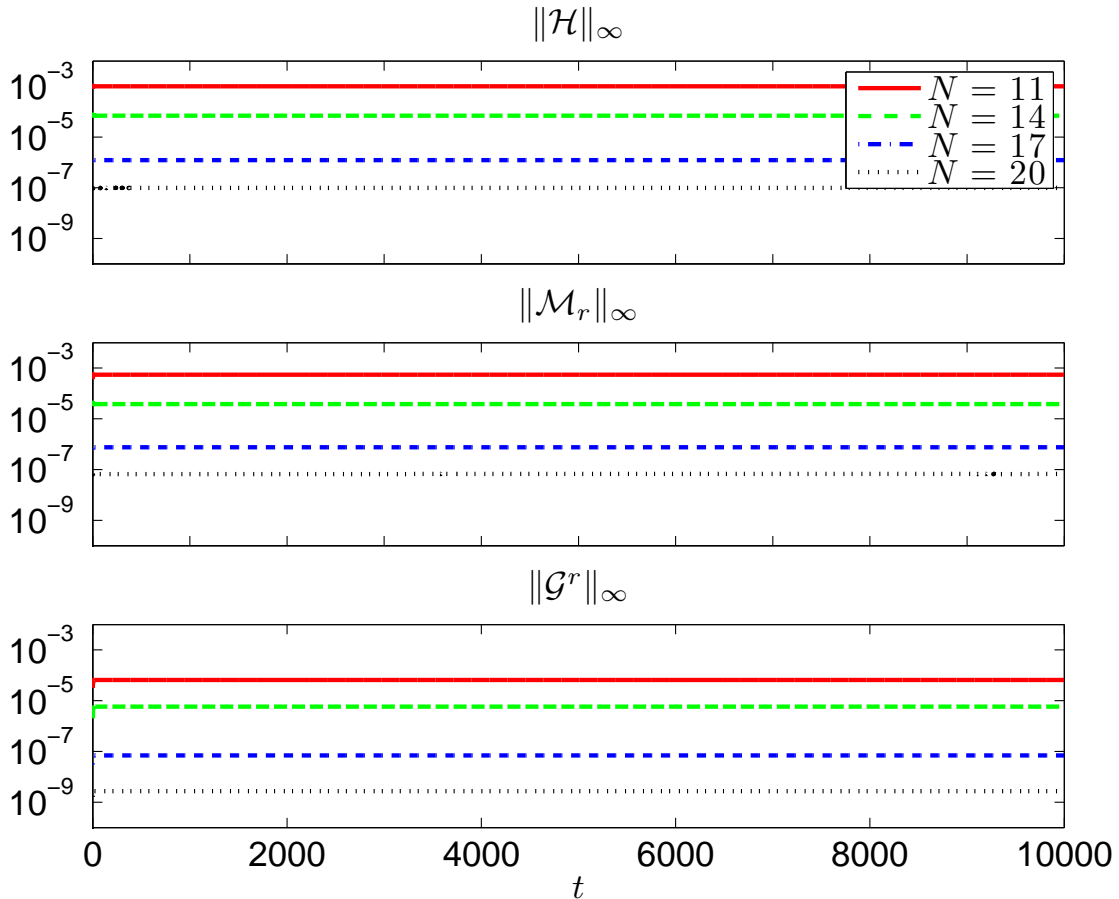


Figure 6.4: SPECTRAL CONVERGENCE OF CONSTRAINT VIOLATIONS FOR $M = 1$ KERR-SCHILD INITIAL DATA. Respectively, for $N = 11, 14, 17, 19$, a timestep of $\Delta t \simeq 0.0041, 0.0026, 0.0018, 0.0013$ has been chosen for stability and accuracy.

outer boundary is stable for our problem, such a boundary condition is unlikely to generalize to more complicated scenarios involving dynamical fields. Indeed, the issue of outer boundary conditions for the (G)BSSN system is an active area of research, with a proper treatment requiring fixation of incoming radiation, control of the constraints, and specification of gauge (see Ref. [171] for a recent analysis).

For GBSSN simulations, our main diagnostic is to monitor the Hamiltonian, momentum, and conformal connection constraints. Figure 6.4 depicts long-time histories of constraint violations, whereas Figs. 6.5 and 6.6 depict long-time error histories for the individual GBSSN field components. From the middle plot in Fig. 6.6, we in-

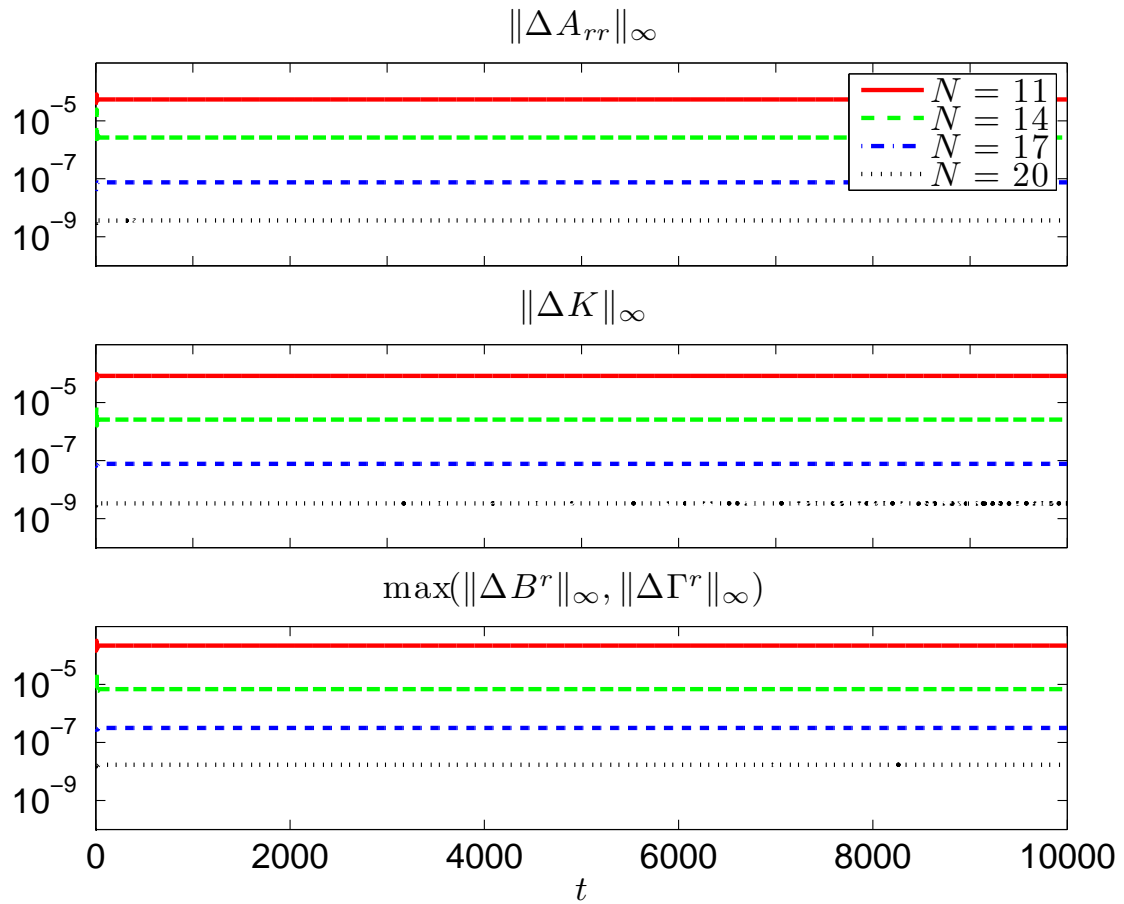


Figure 6.5: SPECTRAL CONVERGENCE OF SOLUTION FOR $M = 1$ KERR-SCHILD INITIAL DATA. Timestep choices are described in the caption for Fig. 6.4. In the title headings, for example, $\Delta A_{rr} \equiv (A_{rr})_{\text{numer}} - (A_{rr})_{\text{exact}}$.

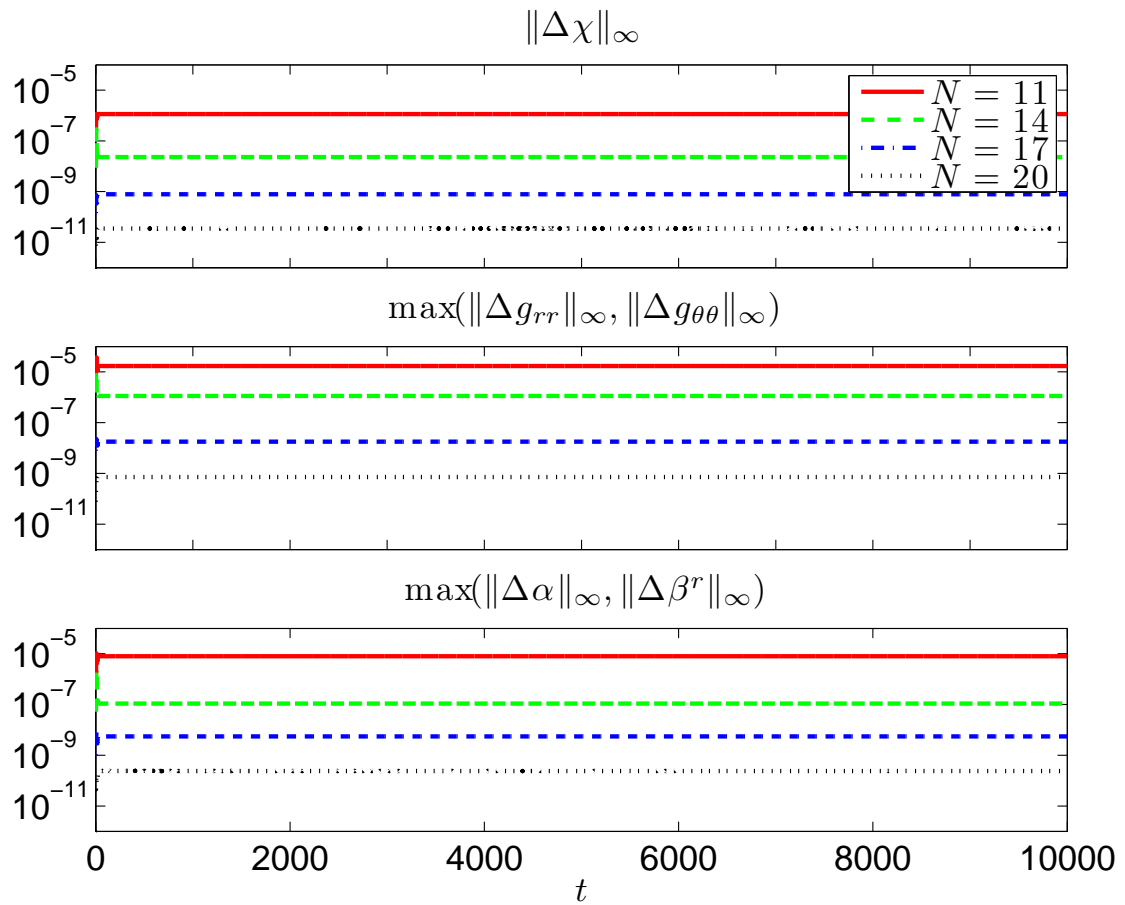


Figure 6.6: SPECTRAL CONVERGENCE OF SOLUTION VIOLATIONS FOR $M = 1$ KERR-SCHILD INITIAL DATA. See the caption of Fig. 6.5 for details.

fer that, up to the indicated numerical error, the factor $g/\sin^2\theta = g_{rr}(g_{\theta\theta})^2$ remains at its initial fixed profile r^4 throughout the evolution. These figures indicate that the proposed scheme is stable for long times, and exhibits spectral convergence with increased polynomial order N . Similar results are recovered from $M = 0$ Minkowski initial data. The stability documented in these plots does not appear to rely on inordinate parameter tuning. For example, with the fixed parameters described above, we obtain similar plots if we individually vary (i) r_{\min} over $\{0.325, 0.35, 0.4, 0.475\}$ (values still corresponding to an excision surface for the given choice of λ), (ii) η over $\{1, 3, 7, 10\}$, (iii) s over $\{8, 9, 10\}$. With the polynomial order N ranging over $\{23, 26, 29, 31\}$, both stability and qualitatively similar exponential convergence is achieved with a single subdomain. Likewise, adoption of a larger coordinate domain with more subdomains does not significantly impact our results. However, for much larger r_{\max} stability requires a smaller time step or a time stepper better suited for wave problems (e.g. Runge Kutta 4). Finally, we have considered the addition of random noise to all field components at the initial time. Precisely, with the system component χ as an example, we have set

$$\boldsymbol{\chi}(0) \mapsto \boldsymbol{\chi}(0) + \delta\boldsymbol{\chi}(0), \quad (6.72)$$

where each component (nodal value) of $\delta\boldsymbol{\chi}(0)$ is 10^{-5} times a random variable drawn from a standard normal distribution. Such perturbed initial data also gives rise to stable evolutions.

CHAPTER SEVEN

Reduced Basis Methods and Parameterized Problems

This dissertation should provide the groundwork for exploring genuinely new opportunities dG methods offer. Here we consider reduced basis methods as an efficient means of dealing with the high-dimensional parameterized problems ubiquitous in binary simulations. This chapter should be viewed as a preliminary report, and as such it will combine both work we have carried out as well as speculation and discussion.

Matched filtering, the main tool used in gravitational wave searches, requires a (typically large) catalog of waveform templates to search over. In section 7.1 we motivate the large catalog problem as the main hurdle we hope to overcome, discussing the standard catalog construction technique and suggest reduced basis methods as a novel approach to the problem. We introduce a reduced basis approach for post-Newtonian (PN) waveforms in section 7.2 and construct catalogs which are orders of magnitude smaller than those produced by standard methods. In this setting the waveforms are analytically given, yet the greedy algorithm and functional space framework transfers to a dG scheme. Section 7.3 begins with discussion on how to adapt the algorithm of sec. 7.2 to a dG scheme for time-dependent problems. We report on preliminary work towards this goal and highlight the challenges as well as potential benefits. We conclude with numerical evidence for the existence of a compact reduced basis space for an EMRB problem considered.

7.1 Gravitational Wave Searches and Catalogs

7.1.1 Generic Bottlenecks of High Dimensional Systems

Astrophysical binary systems constitute a parameterized problem. Most of the relevant parameters have been introduced in previous chapters: orbital eccentricity, orbital semi-latus rectum, and masses of the compact objects. For a continuous range of parameters let \mathcal{H} be the space of all waveforms generated by a binary system, where any plausible model¹ could be used to generate these waveforms. From \mathcal{H} we select a discrete number of waveform *templates* h (or equivalently parameter points) to populate a *catalog* C . The catalog must be a robust approximation to \mathcal{H} for successful gravitational wave searches using matched filtering.

Matched filtering is employed to extract weak signals buried in detector noise, but assumes we have a priori knowledge of the signal’s shape. A known gravitational waveform template $h \in C$ is correlated with the detector’s data s through the matched filtering statistic

$$\langle h, s \rangle_{MF} = 4\text{Re} \int_{f_L}^{f_U} \frac{h(f)\bar{s}(f)}{S_n(f)} df, \quad (7.1)$$

where h normalized, f is the frequency, \bar{s} is the complex conjugate of s , and $S_n(f)$ is the power spectral density (PSD) of the detector’s expected noise [76]. Initial LIGO [4], advanced LIGO [4], and advanced Virgo [190] are three PSDs considered in this chapter. A “detection” occurs when $\langle h, s \rangle_{MF}$ is greater than some threshold value, although in realistic searches this is just one of many triggers [9]. The *minimal*

¹These might be post-Newtonian waveforms, effective one body waveforms, phenomenological waveforms, solutions to Einstein’s equation, or even an alternative theory of gravity. The point being that whatever mechanism we choose to map parameters to waveforms will result in some space \mathcal{H} that is presently under consideration.

match measures the closeness of a catalog C with respect to the continuum \mathcal{H}

$$MM \equiv \min_{s \in \mathcal{H}} \max_{h \in C} \langle h, s \rangle_{MF} \leq 1, \quad (7.2)$$

where we assume normalized waveforms $\langle h, h \rangle_{MF} = 1$, and robust catalogs will typically have $MM > .97$.

Current techniques for generating a catalog result in tens or hundreds of thousands of templates to achieve a $MM > .97$ when the relevant parameters are the binary's masses m_1 and m_2 [17]. Furthermore, the number of templates needed grows rapidly with the dimension P of the parameter space (as $(1 - MM)^{-P/2}$ [173]). In addition to the burden of computing thousands of templates (when solving PDEs), once a catalog is constructed, there is a significant computational cost in performing an actual search (i.e. matched filtering integrations) for gravitational waves due to the size of the catalog. This could adversely affect the physics one performs, for example, real-time analysis of the data is critical to generate alerts to search for electromagnetic counterparts and enable multimessenger astronomy [135, 50].

The template metric approach [173, 17] is currently used by LIGO for template placement [17]. The following example highlights how the algorithm works. Suppose we model gravitational waves by a restricted post-Newtonian waveform at 2nd order. The parameter space is two-dimensional, the binary's masses m_1 and m_2 , and the inspiral gravitational waveform is [9],

$$h(f) = \mathcal{A} f^{-7/6} \exp \left(-i\pi/4 + \frac{3i}{128\eta} \left[v^{-5} + \left(\frac{3715}{756} + \frac{55}{9}\eta \right) v^{-3} - 16\pi v^{-2} + \left(\frac{15293365}{508032} + \frac{27145}{504}\eta + \frac{3085}{72}\eta^2 \right) v^{-1} \right] \right), \quad (7.3)$$

$$v = \left(\frac{GM}{c^3} \pi f \right)^{1/3}$$

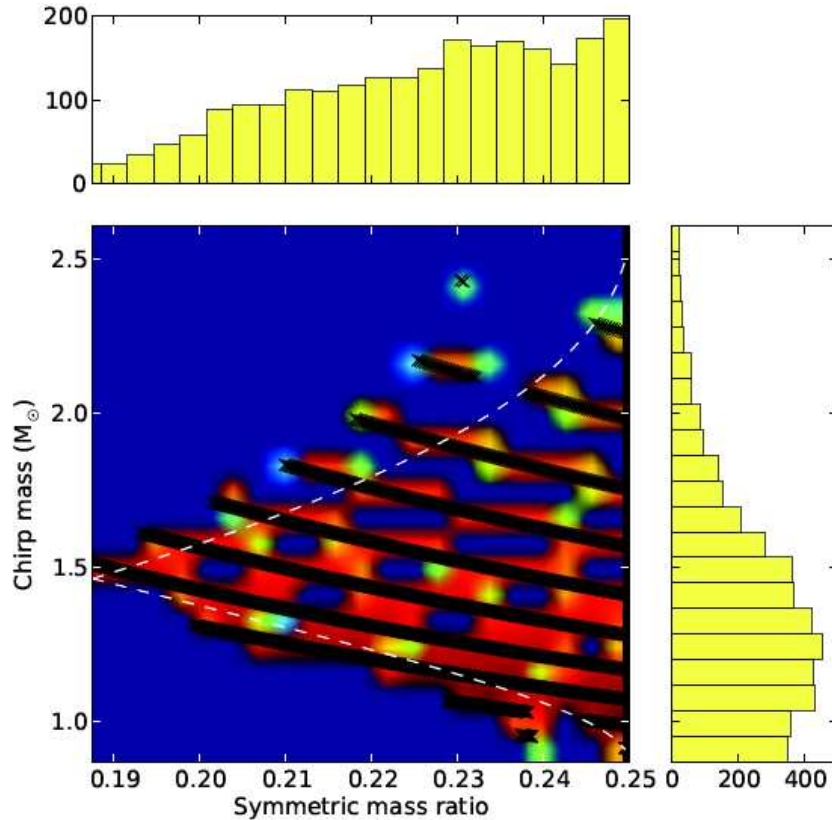


Figure 7.1: The points show the parameter values chosen by the template metric method for the catalog of BNS and Initial LIGO. The density of parameter values is shown using a coloramp as well as histograms. The algorithm selects templates from outside of the parameter range to cover signals near the boundary.

Here \mathcal{A} depends on the distance and orientation of the source and we have defined the total mass $M = m_1 + m_2$ and symmetric mass ratio $\eta = m_1 m_2 / M^2$. A Taylor expansion of (7.3) in η and M is carried out and in each local region of parameter space we ensure $MM > .97$ by plugging Taylor expansions of infinitesimally separated waveforms into the matched filtering inner product (7.1). The algorithm outputs a set of selected parameter values such that the resulting catalog's minimal match is above a set threshold, the details are found in Ref. [17]. For binary neutron star (BNS) inspirals, with which we always assume mass components in the range $[1-3]M_\odot$, Fig. 7.1 shows the chosen parameter values in the chirp mass vs. symmetric mass ratio plane and a density plot of the number of templates, where the chirp mass is $M_c = \eta^{3/5} M$.

7.1.2 A Reduced Basis to the Rescue

The RB framework [186] constructs a global basis rather than using local methods and can be seen as an application-specific spectral expansion. In such an approach one seeks to enable a rapid online evaluation of the reduced model at the expense of having to build the basis prior to the application. It has the following advantageous features over standard model reduction techniques such as Singular Value Decomposition (SVD) (see [185] for a general review of these methods and [118, 59] for applications to GWs, see also [36]):

1. It is applicable to situations in which one must choose the most relevant parameters on the fly.
2. It yields nested, hierarchically constructed catalogs² which can be easily extended. If $C_N = \{h_1, \dots, h_N\}$ is a catalog from the RB method then adding additional waveforms for higher accuracy implies that the resulting catalogs contain the previous ones, $C_N \subset C_{N+1} \subset C_{N+2} \dots$.
3. It is computationally efficient. The cost of adding a new member to an existing catalog of size N is independent of N . Hence, the total cost of generating a catalog of size N scales linearly with N , in contrast to many other approaches.
4. It yields catalogs that are nearly optimal in terms of the error in approximating the whole spectrum of GWs by a compact set of basis elements. Furthermore, this error ensures a strict upper bound over the entire parameter space.

²The term catalog has a slightly different meaning in the context of reduced basis and template metric methods. In both settings, the elements of a catalog are used for matched filtering integrals. In the template metric approach the members of a catalog are the waveforms and the matched filtering integral has physical meaning. For a reduced basis approach the members of a catalog are basis functions of the reduced basis space $W_N = \text{span}(C_N)$, thus only specific linear combinations of the basis functions correspond to physical waveforms. The distinction should become clear throughout the Chapter.

To introduce the RBM we consider two cases. First, we work with analytic waveforms given by the PN approximation (7.3) and compare with existing results. There are no equations to solve, and our task is the construction of a compact linear *reduced basis space* which accurately approximates \mathcal{H} and is of low dimension³. We must decide how to build this space and relatedly how to select points in the parameter space which are optimal in a suitable sense. Our approach has immediate consequences for searches, and in fact we demonstrate improvement over the standard template metric approach. Second, we consider gravitational waveforms as solutions to a PDE, and discuss approaches to accelerate a dG scheme when faced with a parameterized PDE.

7.2 A Reduced Basis Method for PN Waveforms

7.2.1 Theoretical Description

Suppose our frequency dependent gravitational wave template is a function of the P parameters $\vec{\mu} = \{\mu_1, \dots, \mu_P\}$ associated with the source. We denote each of them simply by $h_{\vec{\mu}}$ and do not explicitly write the time or frequency dependence. Although \mathcal{H} is not a linear space, we show that it can be represented by a linear reduced basis space with arbitrarily high accuracy.

We are interested in approximating \mathcal{H} by the best linear combinations of members $\Psi_i \equiv h_{\vec{\mu}=\vec{\mu}_i}$ of a catalog $C_N = \{\Psi_i\}_{i=1}^N$. All such linear combinations form the reduced basis space $W_N = \text{span}(C_N)$. The waveforms that make up this catalog could be optimally chosen so that the error in representing \mathcal{H} with W_N is minimized over the

³The dimension is simply the number of basis functions in C_N .

choice of N catalog members. Such an optimal error is given by the Kolmogorov N -width [176],

$$d_N(\mathcal{H}) = \min_{C_N} \max_{\vec{\mu}} \min_{u \in W_N} \|u - h_{\vec{\mu}}\|. \quad (7.4)$$

That is, one computes the error in the best approximation of $h_{\vec{\mu}}$ by a member of W_N , then finds the parameter $\vec{\mu}$ yielding the largest error, and lastly finds the smallest such error for all possible N -member catalogs. Here, the norm in Eq. (7.4) is calculated from the weighted complex inner product $\langle \cdot, \cdot \rangle$, which is related to the matched filtering integral by $4\Re[\langle \cdot, \cdot \rangle]$, such that for two waveforms F and G in Fourier space,

$$\langle F, G \rangle \equiv \int_{f_L}^{f_U} \frac{\bar{F}(f)G(f)}{S_n(f)} df. \quad (7.5)$$

Finding a catalog that exactly achieves the N -width is a computationally demanding optimization problem. Instead, we use a greedy approach, which is an inexpensive and practical procedure for hierarchically generating catalogs that *nearly* satisfy the N -width [30].

One constructs a catalog by first choosing a waveform for an arbitrary parameter value. A basis vector e_1 is then identified with this waveform, $e_1 = h_{\vec{\mu}_1}$, and the catalog is $C_1 = \{\Psi_1 = h_{\vec{\mu}_1}\}$. To add another waveform to the catalog, one seeks the parameter value $\vec{\mu}_2$ that maximizes $\|h_{\vec{\mu}_2} - P_1(h_{\vec{\mu}_2})\|$ where $P_1(h_{\vec{\mu}_2}) = e_1 \langle e_1, h_{\vec{\mu}_2} \rangle$ is the (orthogonal) projection of $h_{\vec{\mu}_2}$ onto W_1 . We call this step a *greedy sweep*. The waveform corresponding to $\vec{\mu}_2$ is added to the catalog so that $C_2 = \{\Psi_1, \Psi_2\}$. The new basis vector e_2 is then constructed via Gram-Schmidt orthonormalization. Notice that $C_1 \subset C_2$, which demonstrates the hierarchical nature of the catalogs generated.

Additional members of the reduced basis catalog are generated by mathematical induction.

It can be shown [30] that if the decay of the N -width with N can be bounded by an exponential,

$$d_N(\mathcal{H}) \leq Ae^{-cN^\alpha} \quad (7.6)$$

then the decay of the maximum error for a catalog C_N generated by this approach, which we call the *greedy error* ε_N , is also exponential,

$$\varepsilon_N \equiv \max_{\vec{\mu}} \|h_{\vec{\mu}} - P_N(h_{\vec{\mu}})\| \leq \tilde{A}e^{-dN^\beta}. \quad (7.7)$$

where $P_N(h_{\vec{\mu}}) = \sum_{i=1}^N \langle e_i, h_{\vec{\mu}} \rangle e_i$. Note that ε_N is a bound on the error between a waveform and its representation, and that

$$\varepsilon_N^2 = \max_{\vec{\mu}} (1 - \Re[\langle h_{\vec{\mu}}, P_N(h_{\vec{\mu}}) \rangle]), \quad (7.8)$$

so that ε_N^2 is an error comparable to $(1 - MM)$. Given that GWs appear to depend smoothly on the parameters $\vec{\mu}$, we expect $d_N(\mathcal{H})$, and hence the greedy error ε_N , to decay rapidly (in fact exponentially) with N , which is a key feature of this method. Notice that (7.7) implies that any waveform can be represented as $h_{\vec{\mu}} = P_N(h_{\vec{\mu}}) + \delta h_{\vec{\mu}}$ where $\|\delta h_{\vec{\mu}}\| \leq \varepsilon_N$. Therefore, if ε_N is of the order of numerical round-off then, in practice, the projection of $h_{\vec{\mu}}$ onto W_N equals the waveform itself. In addition, the number of RBs needed to represent any $h_{\vec{\mu}}$ is comparatively small (see below). In any greedy approach, the maximum over $\vec{\mu}$ is searched for, in practice, using a *training space* Ξ of samples $\vec{\mu}$. However, since this is done as part of the offline process, the training space can be finely sampled and one can take advantage of

the observation that evaluations for different parameters values are decoupled and, hence, embarrassingly parallel. Algorithm (1) highlights the essential steps.

Algorithm 1 Greedy algorithm for building a reduced basis space

- 1: Input: training space Ξ and waveforms sampled at training space \mathcal{H}_Ξ
 - 2: Randomly select some $\vec{\mu}_1 \in \Xi$
 - 3: $C_1 = \{h_{\vec{\mu}_1}\}$
 - 4: $N = 1$
 - 5: $\varepsilon = 1$ ▷ We use normalized waveforms
 - 6: **while** $\varepsilon \geq \text{Tolerance}$ **do**
 - 7: **for** $\vec{\mu} \in \Xi$ **do**
 - 8: Compute $\text{Err}(\vec{\mu}) = \|h_{\vec{\mu}} - P_N(h_{\vec{\mu}})\|$
 - 9: **end for**
 - 10: Choose $\vec{\mu}_{N+1} = \arg \max_{\vec{\mu} \in \Xi} \text{Err}(\vec{\mu})$
 - 11: $C_{N+1} = \{h_{\vec{\mu}_1}, \dots, h_{\vec{\mu}_N}, h_{\vec{\mu}_{N+1}}\}$
 - 12: $\varepsilon = \text{Err}(\vec{\mu}_{N+1})$
 - 13: $N = N + 1$
 - 14: **end while**
 - 15: $\varepsilon_N = \varepsilon$
 - 16: Output: Greedy error ε_N , C_N , representations $P_N(h_{\vec{\mu}}) \in W_N = \text{span}(C_N)$
-

If one attempted a matched filter search with a RB catalog C_N by filtering each basis function against the data and maximizing over arbitrary linear combinations of these filter outputs, one would of course get a very high false alarm rate. Instead, it is important to allow only linear combinations that correspond to physical waveforms. In fact, the coefficients of these combinations, $\langle e_i, h_{\mu_j} \rangle$, are directly provided by the greedy algorithm. In this way, the RB can compute the overlap between the data and every member of the training space with many fewer inner product integrals and no increase in the false alarm rate.

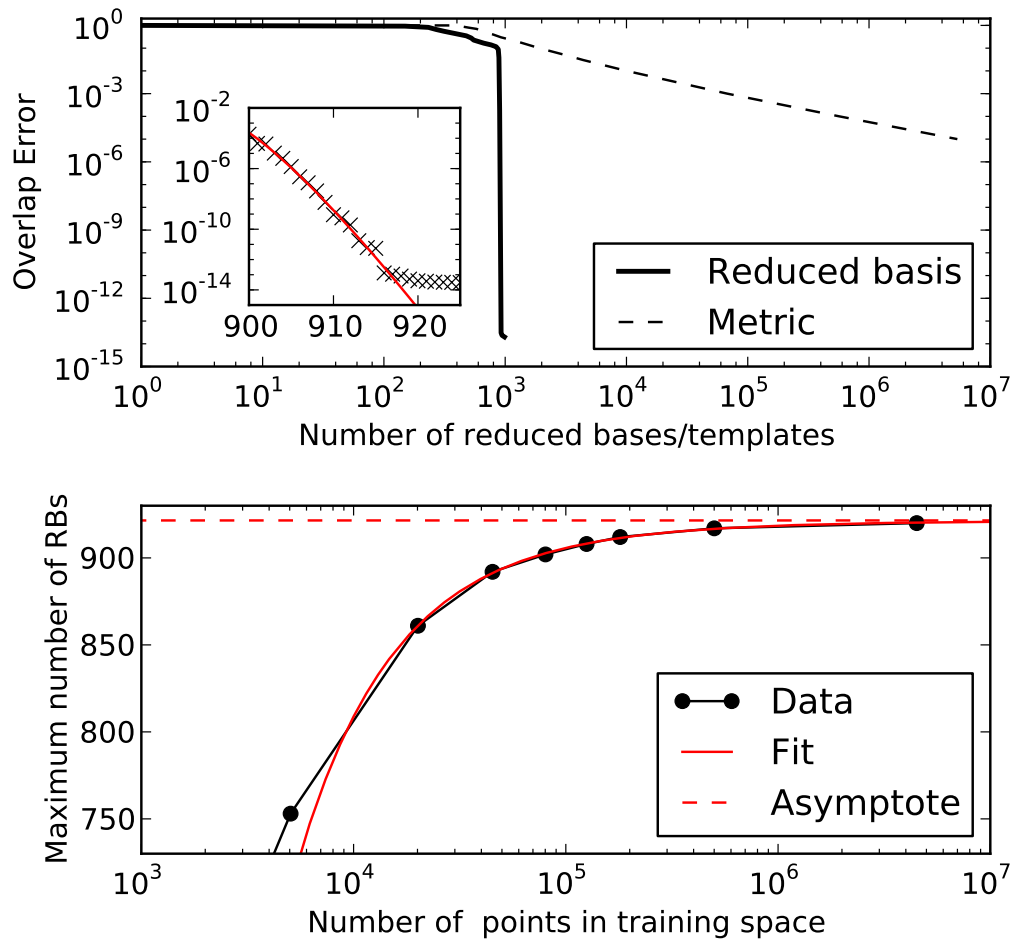


Figure 7.2: Error in approximating the space of waveforms by a discrete catalog for BNS inspirals with Initial LIGO. For reduced basis, the overlap error is the square of the greedy error (7.7) while for metric placement the error is $(1 - MM)$ with MM the minimal match. The lower panel shows the extrapolation of the maximum number of RBs generated for an infinitely large training space. The fit shown (red) excludes the two points with largest x , which change the asymptotic value by 0.2.

7.2.2 Results for PN Waveforms

We discuss our results for constructing reduced bases for “chirp” gravitational waveforms for binary inspirals without spins [32, 231]. We use the 2nd order post-Newtonian waveforms (7.3) normalized to satisfy $\langle h, h \rangle = 1$.

Fig. 7.2 shows results for the greedy error using a reduced basis model for inspirals of BNS (for Initial LIGO with a lower frequency cutoff at $f_L = 40$ Hz) compared with the standard metric template placement method [173]. After a slowly decaying region, the reduced basis model gives very fast exponential convergence decay, which can be fitted by $\varepsilon_N^2 = ae^{-bN^p}$ with $a = 9.65 \times 10^{-4}$, $b = 0.598$, $p = 1.25$. The metric method yields approximately linear decay for a two-dimensional parameter space. As already mentioned, this decay becomes slower as the dimensionality P of the parameter space increases. The fast decay of the reduced basis model allows a representation of the whole set of gravitational waves for these sources and mass ranges to within machine precision. We have found the same feature in all mass ranges that we have explored. This leads to the rather remarkable finding that for all practical purposes the set of relevant gravitational waveforms in compact parameter regions appears to be *finite* dimensional. When increasing the number of samples x in the training set we find the following fit for the number of RB for machine precision error, $N = a + bx^{-1/2} + cx^{-1}$ with $a = 921$, $b = -2090$, $c = -9.18 \times 10^5$ for the case of Fig. 7.2. In particular, in the limit $x \rightarrow \infty$ only 921 bases are needed to represent, within numerical accuracy, the full space of waveforms \mathcal{H} for this range of masses for BNS inspirals.

Fig. 7.3 shows the chosen parameter values in the chirp mass vs. symmetric mass ratio plane and a density plot of the number of RBs. The histograms highlight that most values are picked for (nearly) equal mass systems of low chirp mass, which

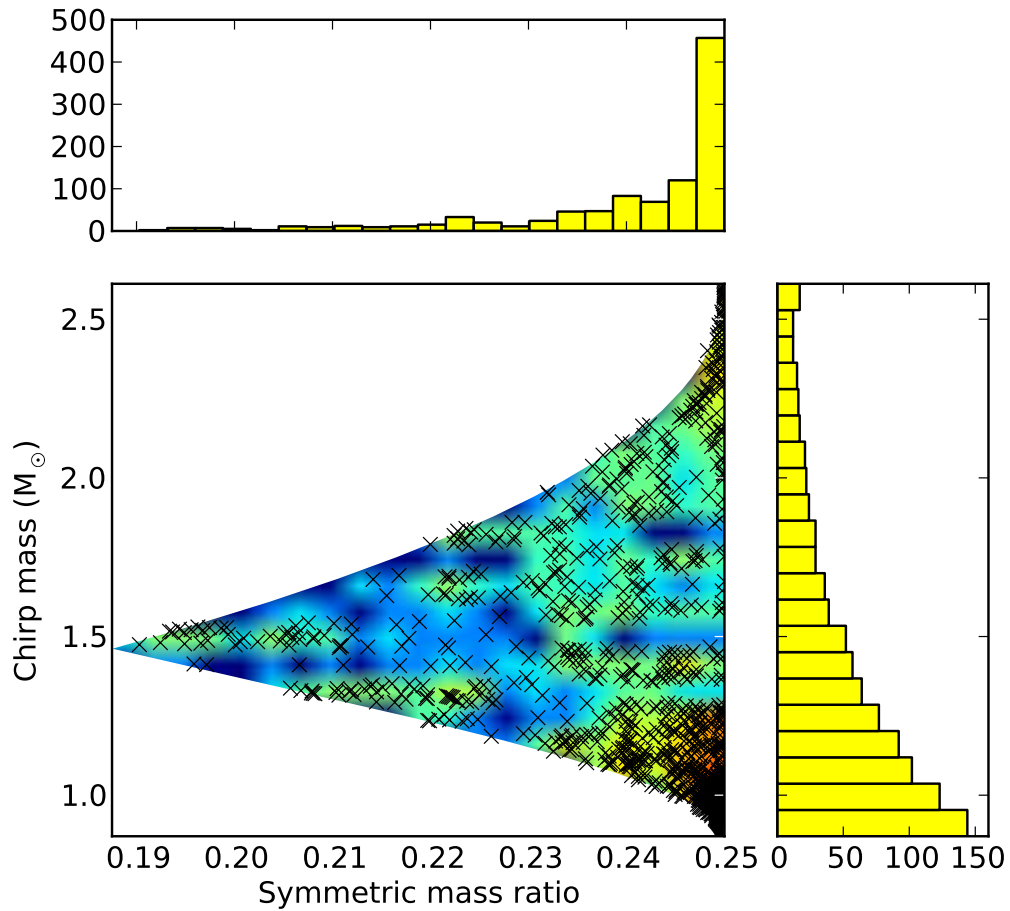


Figure 7.3: The points show the parameter values chosen for the catalog of BNS and Initial LIGO. The density of parameter values is shown using a colormap as well as histograms.

is qualitatively different from the values picked by the template metric algorithm shown in Fig. 7.1.

Tab. 7.1 shows the number of RB that we need to represent inspirals of BNS and stellar size binary black holes (BBH) with mass components in the range $[3-30]M_{\odot}$. The limit $x \rightarrow \infty$ is not taken here for simplicity so the RB values listed in Tab. 7.1 are slightly underestimated.

Detector	Overlap Error	BBH		BNS	
		RB	TM	RB	TM
InitLIGO	10^{-2}	165	2,450	898	10,028
	10^{-5}	170	1.2×10^6	904	4.3×10^6
	2.5×10^{-13}	182	5.9×10^{12}	917	1.4×10^{13}
AdvLIGO	10^{-2}	1,058	19,336	5,395	72,790
	10^{-5}	1,687	1.5×10^7	8,958	4.9×10^7
	2.5×10^{-13}	1,700	2.3×10^{14}	8,976	5.6×10^{14}
AdvVirgo	10^{-2}	1,395	42,496	7,482	156,127
	10^{-5}	1,690	3.1×10^7	8,960	8.3×10^7
	2.5×10^{-13}	1,703	4.8×10^{14}	8,977	6.0×10^{14}

Table 7.1: Number of reduced bases/templates for different target accuracies with the reduced basis (RB) and template metric (TM) approaches for binary neutron stars (BNS) and binary black holes (BBH), using spin-less chirp waveforms. We assume a lower frequency cutoff of 40 Hz for Initial LIGO and 10 Hz for Advanced LIGO and Virgo. The overlap error is given by ε_N^2 for RB and $(1 - MM)$ for TM.

7.3 Preliminary Look at RBM for RWZ Equations

Gravitational waveforms (7.3) considered in Sec. 7.2 were given as the Fourier transform of a time series recorded at some a fixed spatial location. Let us now consider solutions to a dG scheme at a fixed time t . Recall (see Sec. 3.3.2) that our dG scheme seeks a numerical solution $\Psi_h^k \in V_N^k$, where V_N^k is the space of degree N polynomials defined on \mathcal{D}^k . Let $V^{\text{dG}} = \bigoplus_{k=1}^K V_N^k$ be the global solution space of the dG solver, and thus a solution $\Psi_h \in V^{\text{dG}}$ at a fixed t is given by a linear combination of basis element of V^{dG} . In this setting the reduced basis space we seek is a carefully constructed subspace $V^{\text{RB}} \subset V^{\text{dG}}$ such that at a fixed t a reduced basis solution $\Psi_h^{\text{RB}} \in V^{\text{RB}}$ can be quickly recovered. The trade off is a less accurate solution $\|\Psi - \Psi_h\| \leq \|\Psi - \Psi_h^{\text{RB}}\|$, and for the method to be worthwhile the accuracy should not be significantly reduced $\|\Psi_h - \Psi_h^{\text{RB}}\| < \varepsilon_N$.

Adapting the PN algorithm (1) to this scenario will require two new ingredients. First, to build V^{RB} we must be able to find an accurate error estimate for $\|\Psi_h - \Psi_h^{\text{RB}}\|$. By assumption Ψ_h^{RB} can be quickly found, but solving for Ψ_h is an expensive process

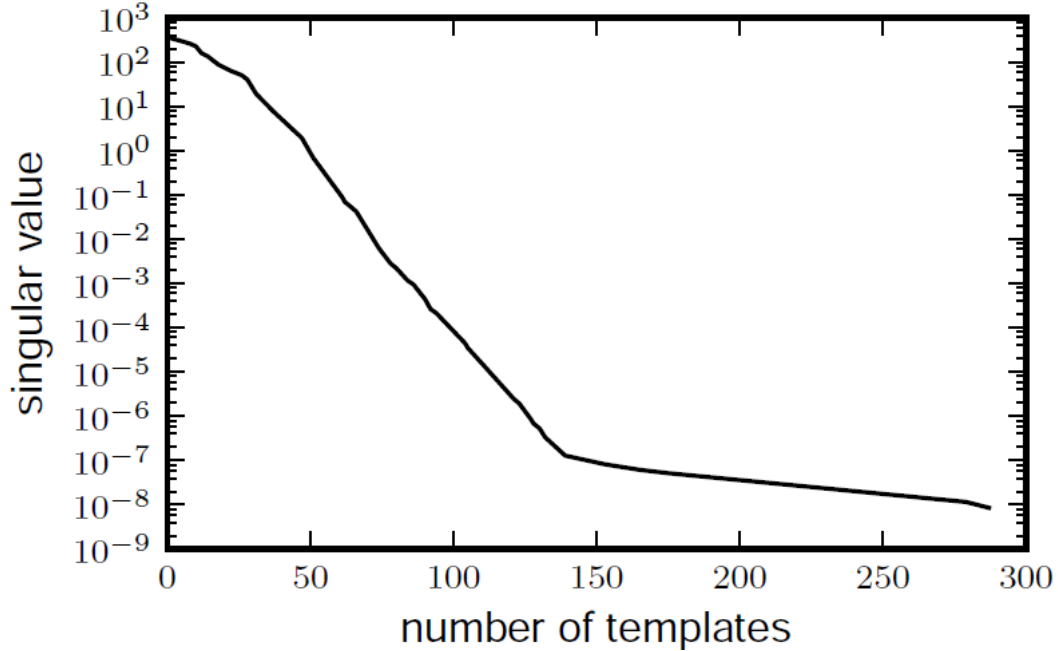


Figure 7.4: The magnitude of the singular value decomposition as a function of the rank of the singular values, which corresponds to the number of templates one would use. The plot shows the rapid exponential fall-off in the singular values.

to be avoided. Yet its precisely $\|\Psi_h^{\text{RB}} - \Psi_h\|$ which we evaluate in our greedy selection algorithm for all parameters, and so we instead estimate $\|\Psi_h^{\text{RB}} - \Psi_h\|$ with some numerical residual that does not require Ψ_h [156, 186, 175]. Second, after V^{RB} has been identified we solve for Ψ_h^{RB} simply by making the replacement $V^{\text{dG}} \rightarrow V^{\text{RB}}$ (in both the test and basis space) in our dG solver. Recall a typical dG scheme (3.38): find a $\Psi_h^k \in V_N^k$ such that

$$\int_{a^k}^{b^k} dx [\partial_t \Psi_h^k - (\lambda_i \Psi')_h^k] v - [(\lambda_i \Psi)^* - (\lambda_i \Psi)_h] v \Big|_{a^k}^{b^k} = 0 \quad \forall v \in V_N^k. \quad (7.9)$$

Now let the RB-dG scheme be: find a $\Psi_h^{\text{RB}} \in V^{\text{RB}}$ such that

$$\int_{a^k}^{b^k} dx [\partial_t \Psi_h^{\text{RB}} - (\lambda_i \Psi^{\text{RB}'})_h] v - [(\lambda_i \Psi^{\text{RB}})^* - (\lambda_i \Psi^{\text{RB}})_h] v \Big|_{a^k}^{b^k} = 0 \quad \forall v \in V^{\text{RB}}. \quad (7.10)$$

Perhaps here the parameter is λ_i , for the RWZ equations they explicitly appear on the right hand side of Eq. (4.1).

Although formulating a RB method for say finite difference or finite volume methods could be done, existing RB tools have been primarily developed for dG and finite element solvers. For time-dependent problems the typical approach uses a greedy-SVD strategy where the solution's time history is compressed with an SVD and the aim is to find a RB space which minimizes spacial degrees of freedom in the scheme [84]. For long-time problems, as in the case for EMRBs, what we really would like is a spacetime reduced basis and developing a RB method in this setting could prove useful. Nevertheless, for the time-dependent problem we envision RBMs are still in their infancy, and applying this potentially powerful approach to gravitational wave problems may require new ideas.

We concluded this chapter by providing numerical evidence of a reduced space, indicating the potential utility of a RB-dG scheme. The power of a RB approach requires that solutions for a continuous set of parameters live in a low dimensional space. We have empirically demonstrated this for the analytic PN waveforms, but the computationally intensive nature of a PDE solver may preclude a direct approach. Instead we sample a sliver of the parameter space and then perform an SVD analysis to judge the applicability of the RB technique. The rate at which the singular values decay indicates the degree of linear dependence between solutions over a range of parameters. Fig. 7.4 shows the results of an SVD of the dominate ($\ell = 2, m = 2$) waveform template space using the EMRB solver from chapter 4. The orbital parameters are varied over a range of eccentricity $e \in [0, 0.25]$ and semi-latus rectum $p \in [7.0, 9.2]$. Since the number of templates needed corresponds to the SVD magnitude rank, the exponential fall-off of the singular values implies that the solution space can be spanned by significantly fewer templates, if carefully chosen.

CHAPTER EIGHT

Conclusions

Our work has been motivated by the need for efficient computation of accurate gravitational waves generated from compact binary systems. Throughout this dissertation we have considered a nodal discontinuous Galerkin method for the GBSSN and RWZ equations, two PDEs typically called upon for such computations. Like any scientific undertaking, we confronted unexpected observations (e.g. Jost junk solutions) and challenges (e.g. construction of a stable numerical flux for the discretized GBSSN system) along the way. We also considered reduced basis methods as a new approach for parameterized waveforms, both in the context of constructing matched filtering catalogs as well as hybrid dG-RB schemes.

We now summarize the main contributions which have been made along with potential future work:

- **Extreme mass ratio binaries and the Regge-Wheller-Zerilli equation:**

We have presented a high-order accurate dG method for computing gravitational waveforms from EMRBs. Time-domain approaches for computing such waveforms have been hampered by the presence of distributional source terms (which include both a moving Dirac delta function and its derivative) in the governing master equations. By writing a distributional master equation as a first order system, we have treated the source term physically through an appropriate modification to the numerical flux function. Our method maintains spectral convergence without requiring additional procedures (e.g. filtering), even pointwise in the immediate vicinity of the moving discontinuity. Through the use of convolution radiation boundary conditions, we have read-off waveforms at outer boundaries, thereby reducing computational cost without spoiling the high-order accuracy of our method. Accurate (read-off) waveforms, often with a relative error of better than 10^{-8} , have been routinely observed

in the course of our simulations. Although we have not computed self-force corrected trajectories, we have demonstrated that our method allows very accurate self-force computations to be carried out.

We believe that the central ideas of our approach might apply to many of these more sophisticated models. In particular, we hope to use our method in tandem with self-force corrections based on regularization of gauge-invariant quantities, at least for quasi-circular orbits. Finally, we remark on the applicability of our dG method to perturbations of the Kerr metric. Now the relevant wave equation, the forced Teukolsky equation, is inherently 2+1 dimensional in the time-domain. In this case we would need to ensure that the particle always lies on an edge between adjacent subdomains (in this case triangles). Clearly, this is a geometrically different problem, but Fan *et al* [88] have also considered 2+1 problems, and one might pursue the Kerr problem along similar lines.

- **Trivial initial data and Jost junk solutions:** We have shown that impulsive starting conditions are inadequate for time-domain modeling of EMRBs. Such conditions result in more dynamical junk, evident in self-force calculations, and potentially a static Jost junk solution which persists indefinitely. Although each effect is small compared to the physical solution, such systematic errors will corrupt studies which require high accuracy. For example, computation of waveforms accurate to second order in the mass ratio requires reconstruction of the first order perturbations. Since these first order terms act as sources for the wave equations describing the second order masterfunctions, the presence of a Jost junk solution will affect second order waveforms. When studying eccentric orbits, errors arising from the persistent junk solution appear to corrupt studies requiring even modest accuracy. Minimization of dynamical and Jost junk by smoothing the source terms during start-up will improve waveform templates and self-force techniques with minimal computa-

tional and human effort.

- **GBSSN system with second order operators:** We have introduced a dG method for solving the spherically reduced GBSSN system with second-order spatial operators. The key ingredient of a stable dG scheme is an appropriate choice of numerical flux, and our particular choice has been motivated by the analysis presented in Sec. 6.3.5. When used to evolve the Schwarzschild solution in Kerr-Schild coordinates, our numerical implementation of the GBSSN system (6.3) is robustly stable and converges to the analytic solution exponentially with increased polynomial order. By approximating the spatially second-order form of the GBSSN system, we have not introduced extra fields which are *evolved*. Evolved auxiliary fields result in new constraints which may spoil stability. Our main goal has been stable evolution of the spherically reduced GBSSN system as a first step towards understanding how a dG method might be applied to the full BSSN system. Towards that goal, we now discuss treatment of singularities and generalization of the described dG method to higher space dimension.

To deal with the fixed Schwarzschild singularity, we have used excision which is easy in the context of the spherically reduced BSSN system. However, excision for the binary black hole problem in full general relativity requires attention to the technical challenge of horizon tracking. State-of-the-art BSSN codes avoid such complication, relying instead on the moving-puncture technique. While the moving-puncture technique does involve mild central singularities, it may still prove amenable to spectral methods. Indeed, spectral methods for non-smooth problems is well-developed in both theory and for complex applications. Since the moving-puncture technique can be performed in spherical symmetry [42], a first-step toward a spectral moving-puncture code would be to implement a moving puncture with the nodal dG method described here.

Such an implementation may adopt Legendre-Gauss-Radau nodes on the innermost subdomain, thereby ensuring that the physical singularity does not lie on a nodal point (in much the same way finite difference codes use a staggered grid). Beyond traditional excision and moving punctures, one might construct smooth initial data via the turducken approach to singularities. However, in combination with 1+log slicing and the Gamma-driver shift condition, turduckened initial data will evolve towards a “trumpet” geometry [48, 47].

DG methods for hyperbolic problems in two and three space dimensions are well-developed. A generalization of the method described here to three dimensions and the full BSSN system would likely rely on an unstructured mesh. Appropriate local polynomial expansions for the subdomains are well-understood, as are choices for the numerical fluxes which would now live on two-dimensional faces rather than single points. Whether or not it would ultimately prove successful, generalization of our dG method to a higher dimension would rely on an established conceptual framework. Further computational advances of relevance to a generalization of our dG method to the full BSSN system (possibly including matter) may include mesh *hp*-adaptivity, local timestepping, shock capturing and slope limiting techniques [121]. Moreover, recent work [38] indicates that enhanced performance would be expected were our scheme implemented on graphics processor units.

- **Reduced basis approach for parameterized problems:** We have considered the development and use of a reduced basis method to template catalog construction and found rapid exponential convergence of the waveform catalog over the full parameter space. The catalog is computationally cheap to derive, hierarchical (i.e. if a more accurate catalog is required, elements can be added), can be extended for a computational cost that is independent of N , and one can show it is robust under changes in a detector’s noise [92]. Currently, the

computational and mathematical framework for generating a catalog entirely from numerical waveforms is absent. Using a combined dG–RB approach could allow for such catalogs, and we have pointed out some approaches and challenges towards this goal. Additionally, we have found that the space of PN gravitational waveforms considered are essentially finite-dimensional for any finite range of physical parameters. We conjecture that it is in general the case and provide corroborating evidence from EMRB systems.

Appendices

APPENDIX ONE

Derivation of the GBSSN System

A.1 Outline of Approach

The GBSSN system is relatively new, having been first derived in 2005 [41] by an action principle, and presented in spherical symmetry for a vanishing stress–energy tensor in 2008 [42]. The derivation given in this appendix will employ straightforward but tedious tensor operations, and for a non–zero stress–energy tensor. We have defined the GBSSN variables in Sec. 2.6.1. In this appendix these variables are differentiated, and using ADM equations (2.84,2.85) results in the GBSSN evolution and constraint system. The straightforward but tedious approach was also used by Refs. [43, 44], although for brevity few details were given. To the best of my knowledge this is the first time these steps have been spelled out in detail.

A.2 GBSSN Evolution and Constraint Equations

We begin by deriving evolution equations for the determinant of the spatial metric, $\gamma \equiv \det(\gamma_{ij})$, and inverse metric γ^{ij} . From the ADM equations, γ evolves according to

$$\mathcal{L}_n \ln \sqrt{\gamma} = \frac{1}{2} \gamma^{ij} \mathcal{L}_n \gamma_{ij} = -K \tag{A.1}$$

and the inverse metric satisfies

$$\begin{aligned}
\mathcal{L}_n \gamma^{ij} &= (n^\alpha \gamma^{ij}{}_{;\alpha} - \gamma^{jk} n^i{}_{;k} - \gamma^{ik} n^j{}_{;k}) \\
&= -(n^{i;j} + n^{j;i}) \\
&= 2\gamma^{im} \gamma^{jn} K_{mn} \\
&= 2K^{ij}.
\end{aligned} \tag{A.2}$$

These two equations will be used frequently throughout this appendix.

A.2.1 GBSSN Constraints

The ADM Hamiltonian constraint (2.85a) can be expressed with GBSSN variables after rewriting the term $K_{ij}K^{ij}$ as

$$K_{ij}K^{ij} = \left(\bar{A}_{ij} + \frac{1}{3}\bar{\gamma}_{ij}K \right) \left(\bar{A}^{ij} + \frac{1}{3}\bar{\gamma}^{ij}K \right) = \bar{A}_{ij}\bar{A}^{ij} + \frac{1}{3}K^2, \tag{A.3}$$

which gives

$$\mathcal{H} = R - \bar{A}_{ij}\bar{A}^{ij} + \frac{2}{3}K^2 = 16\pi\rho. \tag{A.4}$$

The contravariant momentum constraint (2.85b) \mathcal{M}^k can also be expressed with GBSSN variables

$$\begin{aligned}
\mathcal{M}^k &= 8\pi\gamma^{ki}j_i = \gamma^{ki}D_jK^j_i - \gamma^{ki}D_iK \\
&= D_jK^{jk} - \gamma^{ki}D_iK \\
&= D_j\left(A^{jk} + \frac{1}{3}\gamma^{jk}K\right) - \gamma^{ki}D_iK \\
&= D_jA^{jk} - \frac{2}{3}\gamma^{ki}D_iK.
\end{aligned} \tag{A.5}$$

Multiplying by χ^{-n} and integrating by parts leads to

$$8\pi\chi^{-n}j^k = D_j\bar{A}^{jk} + n\bar{A}^{jk}\chi^{-1}\chi_{,j} - \frac{2}{3}\bar{\gamma}^{ki}D_iK. \tag{A.6}$$

Next the covariant derivative of \bar{A}_{jk} is rewritten as

$$\begin{aligned}
D_j\bar{A}^{kj} &= \partial_j\bar{A}^{kj} + \Gamma_{jn}^k\bar{A}^{nj} + \Gamma_{jn}^j\bar{A}^{kn} \\
&= \partial_j\bar{A}^{kj} + \bar{A}^{nj}\left(\bar{\Gamma}_{jn}^k - \frac{n}{2}\chi^{-1}[\delta^k_j\chi_{,n} + \delta^k_n\chi_{,j} - \bar{\gamma}^{km}\bar{\gamma}_{jn}\chi_{,m}]\right) \\
&\quad + \bar{A}^{kn}\left(\bar{\Gamma}_{jn}^j - \frac{n}{2}\chi^{-1}[\delta^j_j\chi_{,n} + \delta^j_n\chi_{,j} - \bar{\gamma}^{jm}\bar{\gamma}_{jn}\chi_{,m}]\right) \\
&= \partial_j\bar{A}^{kj} + \bar{A}^{nj}\bar{\Gamma}_{jn}^k + \bar{A}^{kn}\bar{\Gamma}_{jn}^j - \frac{n}{2}\chi^{-1}(4\bar{A}^{nk}\chi_{,n} + 2\bar{A}^{kj}\chi_{,j} - \bar{A}^{km}\chi_{,m}) \\
&= \partial_j\bar{A}^{kj} + \bar{A}^{nj}\bar{\Gamma}_{jn}^k + \bar{A}^{kn}\bar{\Gamma}_{jn}^j - n\frac{5}{2}\chi^{-1}\bar{A}^{kn}\chi_{,n}.
\end{aligned} \tag{A.7}$$

Noticing that $\bar{\gamma}^{jm}[\bar{\gamma}_{nm,j} - \bar{\gamma}_{jn,m}] = 0$, the term $\bar{A}^{kn}\bar{\Gamma}_{jn}^j$ becomes

$$\bar{A}^{kn}\bar{\Gamma}_{jn}^j = \bar{A}^{kn}\left[\frac{1}{2}\bar{\gamma}^{jm}(\bar{\gamma}_{nm,j} + \bar{\gamma}_{jm,n} - \bar{\gamma}_{jn,m})\right] = \frac{1}{2}\bar{A}^{kn}\partial_n\ln\bar{\gamma}. \tag{A.8}$$

Finally, the momentum constraint is

$$\chi^{-n}\mathcal{M}^i = 8\pi\chi^{-n}j^i = \partial_j\bar{A}^{ij} + \bar{A}^{kj}\bar{\Gamma}_{jk}^i + \frac{1}{2}\bar{A}^{ij}\partial_j\ln\bar{\gamma} - n\frac{3}{2}\chi^{-1}\bar{A}^{ij}\partial_j\chi - \frac{2}{3}\bar{\gamma}^{ij}\partial_jK. \quad (\text{A.9})$$

Additionally, a new constraint arises from the introduction of conformal connection functions

$$\mathcal{G}^i = \bar{\Gamma}^i - \bar{\gamma}^{jk}\bar{\Gamma}_{jk}^i. \quad (\text{A.10})$$

A.2.2 Evolution Equation: Trace of the Extrinsic Curvature

First we derive the evolution equation for the extrinsic curvature trace K

$$\mathcal{L}_nK = \gamma^{ij}\mathcal{L}_nK_{ij} + K_{ij}\mathcal{L}_n\gamma^{ij} = I + II. \quad (\text{A.11})$$

The first part may be found by contracting the components of ADM equation (2.84)

$$I = -\frac{1}{\alpha}D^2\alpha + (R - 2K^{ij}K_{ij} + K^2) + 4\pi(S - 3\rho). \quad (\text{A.12})$$

Using (A.2) we find

$$II = 2K^{ij}K_{ij}. \quad (\text{A.13})$$

Adding $I + II$, and using the Hamiltonian constraint (A.4) yields

$$\mathcal{L}_nK = -\frac{1}{\alpha}D^2\alpha + \bar{A}_{ij}\bar{A}^{ij} + \frac{1}{3}K^2 + 4\pi(S + \rho). \quad (\text{A.14})$$

A.2.3 Evolution Equation: Conformal Factor

First write $\chi = (\bar{\gamma}/\gamma)^{1/(3n)}$ (cf. Sec. 2.6.2), then compute the Lie derivative as

$$\begin{aligned}
 \mathcal{L}_n \ln \chi &= \frac{1}{3n} \mathcal{L}_n \ln (\bar{\gamma}/\gamma) \\
 &= \frac{1}{3n} [\mathcal{L}_n \ln \bar{\gamma} - \mathcal{L}_n \ln \gamma] \\
 &= \frac{1}{3n} [\mathcal{L}_n \ln \bar{\gamma} - 2\mathcal{L}_n \ln \sqrt{\gamma}] \\
 &= \frac{1}{3n} [\mathcal{L}_n \ln \bar{\gamma} + 2K], \tag{A.15}
 \end{aligned}$$

where Eq. (A.1) was used in the last line. Taking a derivation of the natural logarithm produces the desired equation

$$\mathcal{L}_n \chi = \frac{\chi}{3n} (\mathcal{L}_n \ln \bar{\gamma} + 2K). \tag{A.16}$$

A.2.4 Evolution Equation: Conformal Spatial Metric

Using the evolution equations for χ and γ_{ij} results in

$$\begin{aligned}
 \mathcal{L}_n \bar{\gamma}_{ij} &= \gamma_{ij} \mathcal{L}_n \chi^n + \chi^n \mathcal{L}_n \gamma_{ij} \\
 &= n\gamma_{ij} \chi^{n-1} \mathcal{L}_n \chi - 2\chi^n K_{ij} \\
 &= \frac{1}{3} \bar{\gamma}_{ij} (\mathcal{L}_n \ln \bar{\gamma} + 2K) - 2 \left(\bar{A}_{ij} + \frac{1}{3} \bar{\gamma}_{ij} K \right) \\
 &= \frac{1}{3} \bar{\gamma}_{ij} \mathcal{L}_n \ln \bar{\gamma} - 2\bar{A}_{ij}. \tag{A.17}
 \end{aligned}$$

A.2.5 Evolution Equation: Traceless Part of the Extrinsic Curvature

Taking a Lie derivative of Eq. (2.89) with respect to the normalized timelike vector n produces

$$\begin{aligned}
\mathcal{L}_n A_{ij} &= \mathcal{L}_n K_{ij} - \frac{1}{3} (\gamma_{ij} \mathcal{L}_n K + K \mathcal{L}_n \gamma_{ij}) \\
&= -\frac{1}{\alpha} D_i D_j \alpha + R_{ij} - 2K_{ik} K^k_j + K K_{ij} - 8\pi S_{ij} + 4\pi \gamma_{ij} (S - \rho) \\
&\quad - \frac{1}{3} \left(\gamma_{ij} \left[-\frac{1}{\alpha} D^2 \alpha + \bar{A}_{mn} \bar{A}^{mn} + \frac{1}{3} K^2 + 4\pi (S + \rho) \right] - 2K K_{ij} \right). \quad (\text{A.18})
\end{aligned}$$

With the Hamiltonian constraint (A.4) we remove $\frac{1}{3} (\bar{A}_{mn} \bar{A}^{mn} + 16\pi\rho)$. Many of the remaining terms group into the trace-free expressions

$$-\frac{1}{\alpha} (D_i D_j \alpha)^{\text{TF}} = -\frac{1}{\alpha} D_i D_j \alpha + \frac{1}{3\alpha} \gamma_{ij} D^2 \alpha \quad (\text{A.19})$$

$$-8\pi S_{ij}^{\text{TF}} = -8\pi S_{ij} + 8\pi \frac{1}{3} \gamma_{ij} S \quad (\text{A.20})$$

$$R_{ij}^{\text{TF}} = R_{ij} - \frac{1}{3} \gamma_{ij} R, \quad (\text{A.21})$$

which gives

$$\mathcal{L}_n A_{ij} = -\frac{1}{\alpha} (D_i D_j \alpha)^{\text{TF}} - 8\pi S_{ij}^{\text{TF}} + R_{ij}^{\text{TF}} - 2K_{ik} K^k_j - \frac{1}{3} \gamma_{ij} K^2 + \frac{5}{3} K K_{ij}. \quad (\text{A.22})$$

Using

$$\begin{aligned}
K_{ik}K^k{}_j &= K_{ik}\gamma^{km}K_{mj} \\
&= \left(A_{ik} + \frac{1}{3}\gamma_{ik}K\right)\gamma^{km}\left(A_{mj} + \frac{1}{3}\gamma_{mj}K\right) \\
&= \left(A_{ik} + \frac{1}{3}\gamma_{ik}K\right)\left(A^k{}_j + \frac{1}{3}\delta^k{}_jK\right) \\
&= A_{ik}A^k{}_j + \frac{1}{3}A_{ij}K + \frac{1}{3}A_{ij}K + \frac{1}{9}\gamma_{ij}K^2 \\
&= A_{ik}A^k{}_j + \frac{2}{3}A_{ij}K + \frac{1}{9}\gamma_{ij}K^2
\end{aligned} \tag{A.23}$$

we may write

$$-2K_{ik}K^k{}_j - \frac{1}{3}\gamma_{ij}K^2 + \frac{5}{3}KK_{ij} = -2A_{ik}A^k{}_j + \frac{1}{3}A_{ij}K. \tag{A.24}$$

Finally, we arrive at

$$\mathcal{L}_n A_{ij} = \frac{1}{3}K A_{ij} - 2A_{ik}A^k{}_j + \left(R_{ij} - \frac{1}{\alpha}D_i D_j \alpha - 8\pi S_{ij}\right)^{\text{TF}}. \tag{A.25}$$

A.2.6 Evolution Equation: Conformal and Traceless Part of the Extrinsic Curvature

With the evolution equation for A_{ij} at hand, straightforward computation reveals

$$\begin{aligned}
\mathcal{L}_n \bar{A}_{ij} &= A_{ij}\mathcal{L}_n \chi^n + \chi^n \mathcal{L}_n A_{ij} \\
&= nA_{ij}\chi^{n-1}\mathcal{L}_n \chi + \frac{1}{3}K\bar{A}_{ij} - 2\bar{A}_{ik}\bar{A}^k{}_j + \chi^n \left(R_{ij} - \frac{1}{\alpha}D_i D_j \alpha - 8\pi S_{ij}\right)^{\text{TF}} \\
&= \frac{1}{3}\bar{A}_{ij}\mathcal{L}_n \ln \bar{\gamma} + K\bar{A}_{ij} - 2\bar{A}_{ik}\bar{A}^k{}_j + \chi^n \left(R_{ij} - \frac{1}{\alpha}D_i D_j \alpha - 8\pi S_{ij}\right)^{\text{TF}}.
\end{aligned} \tag{A.26}$$

A.2.7 Evolution Equation: Conformal Connection Function

Care is required when deriving an evolution equation for $\bar{\Gamma}^i$ which has no definite tensorial type. Introduce $\hat{\partial}_0 = \alpha \mathcal{L}_n = \partial_t - \mathcal{L}_\beta$, and note that $\hat{\partial}_0$ and ∂_j commute [41].

We now compute $\hat{\partial}_0 \bar{\Gamma}^i$ as

$$\begin{aligned} -\hat{\partial}_0 \bar{\Gamma}^i &= \hat{\partial}_0 \left[\bar{\gamma}^{-1/2} (\bar{\gamma}^{1/2} \bar{\gamma}^{ij})_{,j} \right] \\ &= -\frac{1}{2} \bar{\gamma}^{-3/2} (\bar{\gamma}^{1/2} \bar{\gamma}^{ij})_{,j} \hat{\partial}_0 \bar{\gamma} + \bar{\gamma}^{-1/2} \left(\frac{1}{2} \bar{\gamma}^{-1/2} \bar{\gamma}^{ij} \hat{\partial}_0 \bar{\gamma} + \bar{\gamma}^{1/2} \hat{\partial}_0 \bar{\gamma}^{ij} \right)_{,j}. \end{aligned} \quad (\text{A.27})$$

The first term simplifies as

$$-\frac{1}{2} \bar{\gamma}^{-3/2} (\bar{\gamma}^{1/2} \bar{\gamma}^{ij})_{,j} \hat{\partial}_0 \bar{\gamma} = -\frac{1}{2} \bar{\gamma}^{-1/2} (\bar{\gamma}^{1/2} \bar{\gamma}^{ij})_{,j} \hat{\partial}_0 \ln \bar{\gamma} = \frac{1}{2} \bar{\Gamma}^i \hat{\partial}_0 \ln \bar{\gamma}. \quad (\text{A.28})$$

Using $\mathcal{L}_n \bar{\gamma}^{ij} = -\frac{1}{3} \bar{\gamma}^{ij} \mathcal{L}_n \ln \bar{\gamma} + 2 \bar{A}^{ij}$, the last two terms are

$$\begin{aligned} \left(\frac{1}{2} \bar{\gamma}^{-1/2} \bar{\gamma}^{ij} \hat{\partial}_0 \bar{\gamma} + \bar{\gamma}^{1/2} \hat{\partial}_0 \bar{\gamma}^{ij} \right)_{,j} &= \left(\frac{1}{2} \bar{\gamma}^{-1/2} \bar{\gamma}^{ij} \hat{\partial}_0 \bar{\gamma} + \bar{\gamma}^{1/2} \left[-\frac{1}{3} \bar{\gamma}^{ij} \hat{\partial}_0 \ln \bar{\gamma} + 2\alpha \bar{A}^{ij} \right] \right)_{,j} \\ &= \left(\frac{1}{2} \bar{\gamma}^{1/2} \bar{\gamma}^{ij} \hat{\partial}_0 \ln \bar{\gamma} - \frac{1}{3} \bar{\gamma}^{1/2} \bar{\gamma}^{ij} \hat{\partial}_0 \ln \bar{\gamma} + 2\alpha \bar{\gamma}^{1/2} \bar{A}^{ij} \right)_{,j} \\ &= \left(\frac{1}{6} \bar{\gamma}^{1/2} \bar{\gamma}^{ij} \hat{\partial}_0 \ln \bar{\gamma} + 2\alpha \bar{\gamma}^{1/2} \bar{A}^{ij} \right)_{,j} \\ &= \frac{1}{6} \bar{\gamma}^{1/2} (\bar{\gamma}^{ij} \hat{\partial}_0 \ln \bar{\gamma})_{,j} + \frac{1}{6} \bar{\gamma}_{,j}^{1/2} \bar{\gamma}^{ij} \hat{\partial}_0 \ln \bar{\gamma} \\ &\quad + 2\alpha \bar{\gamma}^{1/2} \bar{A}_{,j}^{ij} + 2\alpha \bar{\gamma}_{,j}^{1/2} \bar{A}^{ij} + 2\alpha_{,j} \bar{\gamma}^{1/2} \bar{A}^{ij}. \end{aligned} \quad (\text{A.29})$$

The divergence of A_{ij} can be removed by using the momentum constraint (A.9)

$$\begin{aligned} -\hat{\partial}_0 \bar{\Gamma}^i &= \frac{1}{2} \bar{\Gamma}^i \hat{\partial}_0 \ln \bar{\gamma} + \frac{1}{6} (\bar{\gamma}^{ij} \hat{\partial}_0 \ln \bar{\gamma})_{,j} \\ &\quad + \frac{1}{6} \bar{\gamma}^{-1/2} \bar{\gamma}_{,j}^{1/2} \bar{\gamma}^{ij} \hat{\partial}_0 \ln \bar{\gamma} + 2\alpha \bar{\gamma}^{-1/2} \bar{\gamma}_{,j}^{1/2} \bar{A}^{ij} + 2\alpha_{,j} \bar{A}^{ij} \\ &\quad + 2\alpha \left[8\pi \chi^{-n} j^i - \bar{A}^{nj} \bar{\Gamma}_{jn}^i - \frac{1}{2} \bar{A}^{in} \partial_n \ln \bar{\gamma} + n \frac{3}{2} \chi^{-1} \bar{A}^{in} \chi_{,n} + \frac{2}{3} \bar{\gamma}^{ji} \partial_j K \right]. \end{aligned} \quad (\text{A.30})$$

The fourth and eighth terms cancel while the second and third terms are

$$\begin{aligned}
\frac{1}{6} \left(\bar{\gamma}^{ij} \hat{\partial}_0 \ln \bar{\gamma} \right)_{,j} + \frac{1}{6} \bar{\gamma}^{-1/2} \bar{\gamma}_{,j}^{1/2} \bar{\gamma}^{ij} \hat{\partial}_0 \ln \bar{\gamma} = \\
\frac{1}{6} \bar{\gamma}_{,j}^{ij} \hat{\partial}_0 \ln \bar{\gamma} + \frac{1}{6} \bar{\gamma}^{ij} \partial_j \hat{\partial}_0 \ln \bar{\gamma} + \bar{\gamma}^{-1} \frac{1}{12} \bar{\gamma}_{,j} \bar{\gamma}^{ij} \hat{\partial}_0 \ln \bar{\gamma} = \\
\frac{1}{6} \bar{\gamma}^{ij} \partial_j \hat{\partial}_0 \ln \bar{\gamma} - \frac{1}{6} \bar{\Gamma}^i \hat{\partial}_0 \ln \bar{\gamma}.
\end{aligned} \tag{A.31}$$

We finally arrive at

$$\begin{aligned}
\hat{\partial}_0 \bar{\Gamma}^i = & -\frac{1}{3} \bar{\Gamma}^i \hat{\partial}_0 \ln \bar{\gamma} - \frac{1}{6} \bar{\gamma}^{ij} \partial_j \hat{\partial}_0 \ln \bar{\gamma} - 2 \bar{A}^{ij} \partial_j \alpha \\
& - 2\alpha \left[8\pi \chi^{-n} j^i - \bar{A}^{jk} \bar{\Gamma}_{jk}^i + n \frac{3}{2} \chi^{-1} \bar{A}^{ij} \partial_j \chi + \frac{2}{3} \bar{\gamma}^{ji} \partial_j K \right].
\end{aligned} \tag{A.32}$$

APPENDIX TWO

Distributional RWZ Jump Conditions

The jump conditions' (4.19) derivation is as follows. Using the selection properties of $\delta'(u)$ as a distribution, we first rewrite (4.1) as

$$\begin{aligned} -\partial_t^2\Psi + \partial_x^2\Psi - V(r)\Psi &= f_p(t)F(t, r_p(t))\delta'(r - r_p(t)) \\ &+ [f_p(t)G(t, r_p(t)) - g_p(t)F(t, r_p(t)) - f_p(t)F_r(t, r_p(t))]\delta(r - r_p(t)), \end{aligned} \quad (\text{B.1})$$

using the shorthand notations from (4.20). Next, with L for “left” and R for “right”, we let

$$\Psi(t, r) = \Psi^L(t, r)\theta(r_p(t) - r) + \Psi^R(t, r)\theta(r - r_p(t)), \quad (\text{B.2})$$

where the step function $\theta(u)$ obeys $\theta(u) = 0$ for $u < 0$, and $\theta(u) = 1$ for $u > 0$. We view the functions $\Psi^{L,R}$ as everywhere satisfying the homogeneous PDE

$$-\partial_t^2\Psi^{L,R} + \partial_x^2\Psi^{L,R} - V(r)\Psi^{L,R} = 0, \quad (\text{B.3})$$

even across the particle location $r_p(t)$.

To complete our derivation of (4.19), we calculate the distributional derivatives of Ψ as given in (B.2), insert them into (B.1), and then compare terms. Using $\partial/\partial x = f\partial/\partial r$, the identity $\theta'(u) = \delta(u)$, and the argument symmetry of $\delta(u)$, we first compute

$$\partial_x\Psi = \Psi_x^L\theta(r_p(t) - r) + \Psi_x^R\theta(r - r_p(t)) - f\Psi^L\delta(r - r_p(t)) + f\Psi^R\delta(r - r_p(t)), \quad (\text{B.4})$$

where on the right-hand side we have switched to subscript notation for partial

derivatives. The second x -derivative of (B.2) is then

$$\begin{aligned}\partial_x^2 \Psi &= \Psi_{xx}^L \theta(r_p(t) - r) + \Psi_{xx}^R \theta(r - r_p(t)) - 2f^2 \Psi_r^L \delta(r - r_p(t)) + 2f^2 \Psi_r^R \delta(r - r_p(t)) \\ &\quad - f f' \Psi^L \delta(r - r_p(t)) + f f' \Psi^R \delta(r - r_p(t)) - f^2 \Psi^L \delta'(r - r_p(t)) + f^2 \Psi^R \delta'(r - r_p(t)).\end{aligned}\tag{B.5}$$

Expressed compactly, the last formula is

$$\begin{aligned}\partial_x^2 \Psi &= \Psi_{xx}^L \theta(r_p(t) - r) + \Psi_{xx}^R \theta(r - r_p(t)) + f_p^2(t) [[\Psi_r]] \delta(r - r_p(t)) \\ &\quad - f_p(t) g_p(t) [[\Psi]] \delta(r - r_p(t)) + f_p^2(t) [[\Psi]] \delta'(r - r_p(t)),\end{aligned}\tag{B.6}$$

where the definition (4.21) is here $[[\Psi]](t) \equiv \Psi^R(t, r_p(t)) - \Psi^L(t, r_p(t))$. To reach Eq. (B.6) from the previous line, we have used the selection properties of $\delta'(u)$. Next, we similarly compute

$$\begin{aligned}\partial_t^2 \Psi &= \Psi_{tt}^L \theta(r_p(t) - r) + \Psi_{tt}^R \theta(r - r_p(t)) + 2\dot{r}_p \Psi_t^L \delta(r - r_p(t)) - 2\dot{r}_p \Psi_t^R \delta(r - r_p(t)) \\ &\quad + \ddot{r}_p \Psi^L \delta(r - r_p(t)) - \ddot{r}_p \Psi^R \delta(r - r_p(t)) - \dot{r}_p^2 \Psi^L \delta'(r - r_p(t)) + \dot{r}_p^2 \Psi^R \delta'(r - r_p(t)).\end{aligned}\tag{B.7}$$

The last formula may be written in the succinct form

$$\begin{aligned}\partial_t^2 \Psi &= \Psi_{tt}^L \theta(r_p(t) - r) + \Psi_{tt}^R \theta(r - r_p(t)) - 2\dot{r}_p(t) [[\Psi_t]] \delta(r - r_p(t)) \\ &\quad - \ddot{r}_p(t) [[\Psi]] \delta(r - r_p(t)) - \dot{r}_p^2(t) [[\Psi_r]] \delta(r - r_p(t)) + \dot{r}_p^2(t) [[\Psi]] \delta'(r - r_p(t)),\end{aligned}\tag{B.8}$$

again by using the properties of $\delta'(u)$. Finally, with $\partial_t [[\Psi]] = [[\Psi_t]] + \dot{r}_p(t) [[\Psi_r]]$,

we rewrite the last expression as

$$\begin{aligned} \partial_t^2 \Psi &= \Psi_{tt}^L \theta(r_p(t) - r) + \Psi_{tt}^R \theta(r - r_p(t)) - 2\dot{r}_p(t) (\partial_t [[\Psi]]) \delta(r - r_p(t)) \\ &\quad - \ddot{r}_p(t) [[\Psi]] \delta(r - r_p(t)) + \dot{r}_p^2(t) [[\Psi_r]] \delta(r - r_p(t)) + \dot{r}_p^2(t) [[\Psi]] \delta'(r - r_p(t)). \end{aligned} \tag{B.9}$$

Substitution of (B.6) and (B.9) into (B.1), along with the fact that Ψ^R and Ψ^L solve the homogeneous PDE (B.3), then yields Eqs. (4.19a) and (4.19b).

APPENDIX THREE

Exact Solutions to the Forced 1+1 Wave Equations

C.1 Problem Setup

This appendix presents exact solutions to the distributionally forced 1+1 wave equation. Precisely, we consider the equation

$$-\partial_t^2 \Psi + \partial_x^2 \Psi = G(t)\delta(x - vt) + F(t)\delta'(x - vt), \quad (\text{C.1})$$

where either $F(t) = 0, G(t) = \cos t$ or $F(t) = \cos t, G(t) = 0$. In analyzing both cases, we make use of the following distributional identities:

$$\partial_u |u| = \text{sgn } u, \quad \partial_u \text{sgn } u = 2\delta(u), \quad (\text{sgn } u)^2 = 1, \quad (\text{C.2})$$

with $\text{sgn } u \equiv u/|u|$ the sign function. Throughout, the particle location $x_p(t) = vt$ has linear time dependence, with corresponding speed $|v| < 1$.

C.2 Solution for $F(t) = 0, G(t) = \cos t$

Following analysis similar to that presented in Section 4.2.4 [or by substituting the correspondences $x_p(t) = r_p(t)$, $x = r$, $f(r) = 1$, $f'(r) = 0$, and $\ddot{r}(t) = 0$ into the general jumps (4.19)], we find the jump relations

$$[[\Psi]]_{x=vt} = 0, \quad [[\partial_x \Psi]]_{x=vt} = \gamma^2 \cos t, \quad [[\partial_t \Psi]]_{x=vt} = -v\gamma^2 \cos t, \quad (\text{C.3})$$

where $\gamma = (1 - v^2)^{-1/2}$ is the usual relativistic factor. The particular solution

$$\Psi(t, x) = -\frac{1}{2} \sin \vartheta, \quad \vartheta = \gamma^2(t - xv - |x - vt|) \quad (\text{C.4})$$

to Eq. (C.1) possess the jumps listed in (C.3). Using the identities (C.2), let us verify that (C.4) indeed solves (C.1) for $F(t) = 0$ and $G(t) = \cos t$. Straightforward computation of the first and second order t -derivatives yields

$$\partial_t \Psi = -\frac{1}{2}\gamma^2[1 + v \operatorname{sgn}(x - vt)] \cos \vartheta \quad (\text{C.5})$$

$$\partial_t^2 \Psi = \frac{1}{2}\gamma^4[1 + v \operatorname{sgn}(x - vt)]^2 \sin \vartheta + v^2\gamma^2\delta(x - vt) \cos \vartheta. \quad (\text{C.6})$$

while for the x -derivatives we similarly find

$$\partial_x \Psi = \frac{1}{2}\gamma^2[v + \operatorname{sgn}(x - vt)] \cos \vartheta \quad (\text{C.7})$$

$$\partial_x^2 \Psi = \frac{1}{2}\gamma^4[v + \operatorname{sgn}(x - vt)]^2 \sin \vartheta + \gamma^2\delta(x - vt) \cos \vartheta. \quad (\text{C.8})$$

Forming $-\partial_t^2 \Psi + \partial_x^2 \Psi = \delta(x - vt) \cos \vartheta$, we then appeal to the selection property of the delta function in order to reach the desired result, $-\partial_t^2 \Psi + \partial_x^2 \Psi = \delta(x - vt) \cos t$.

C.3 Solution for $F(t) = \cos t$, $G(t) = 0$

The jump relations for this case are

$$[[\Psi]]_{x=vt} = \gamma^2 \cos t, \quad [[\partial_x \Psi]]_{x=vt} = 2v\gamma^4 \sin t, \quad [[\partial_t \Psi]]_{x=vt} = -(1 + v^2)\gamma^4 \sin t. \quad (\text{C.9})$$

Now a particular solution to (C.1) is

$$\Psi(t, x) = \frac{1}{2}\gamma^2[v + \operatorname{sgn}(x - vt)] \cos \vartheta, \quad \vartheta = \gamma^2(t - xv - |x - vt|). \quad (\text{C.10})$$

To verify that (C.10) indeed solves (C.1) for $F(t) = \cos t$ and $G(t) = 0$, we first calculate

$$\partial_t \Psi = -\frac{1}{2}\gamma^4[2v + (1 + v^2) \operatorname{sgn}(x - vt)] \sin \vartheta - v\gamma^2 \delta(x - vt) \cos \vartheta \quad (\text{C.11})$$

$$\begin{aligned} \partial_t^2 \Psi &= v^2 \gamma^2 \delta'(x - vt) \cos \vartheta + \gamma^4[2v + v^3 + v^2 \operatorname{sgn}(x - vt)] \delta(x - vt) \sin \vartheta \\ &\quad - \frac{1}{2}\gamma^6[3v + v^3 + (3v^2 + 1) \operatorname{sgn}(x - vt)] \cos \vartheta, \end{aligned} \quad (\text{C.12})$$

and then likewise compute

$$\partial_x \Psi = \gamma^2 \delta(x - vt) \cos \vartheta + \frac{1}{2}\gamma^4[1 + v^2 + 2v \operatorname{sgn}(x - vt)] \sin \vartheta \quad (\text{C.13})$$

$$\begin{aligned} \partial_x^2 \Psi &= \gamma^2 \delta'(x - vt) \cos \vartheta + \gamma^4[3v + \operatorname{sgn}(x - vt)] \delta(x - vt) \sin \vartheta \\ &\quad - \frac{1}{2}\gamma^6[3v + v^3 + (3v^2 + 1) \operatorname{sgn}(x - vt)] \cos \vartheta. \end{aligned} \quad (\text{C.14})$$

Combination of Eqs. (C.11) and (C.13) yields

$$-\partial_t^2 \Psi + \partial_x^2 \Psi = \delta'(x - vt) \cos \vartheta + \gamma^2[v + \operatorname{sgn}(x - vt)] \delta(x - vt) \sin \vartheta. \quad (\text{C.15})$$

By the selection properties of $\delta'(u)$, we have

$$\delta'(x - vt) \cos \vartheta = \delta'(x - vt) \cos t - \gamma^2[v + \operatorname{sgn}(x - vt)] \delta(x - vt) \sin t. \quad (\text{C.16})$$

Substituting this result into (C.15), using the selection property of $\delta(u)$, and realizing that $\delta(u) \operatorname{sgn} u = 0$ by symmetry, we arrive at the desired result, $-\partial_t^2 \Psi + \partial_x^2 \Psi = \delta'(x - vt) \cos t$.

APPENDIX FOUR

Time-Independent Master Equations

D.1 Regge-Wheeler Equation

Subject to the *Ansatz* that the solution v is time-independent and in terms of the dimensionless variable $\rho = (2M)^{-1}r$, the homogeneous Regge-Wheeler equation is [83]

$$-\left(1 - \frac{1}{\rho}\right)v'' - \frac{1}{\rho^2}v' + \left[\frac{\ell(\ell+1)}{\rho^2} + \frac{\kappa}{\rho^3}\right]v = 0, \quad (\text{D.1})$$

where $\kappa = 1 - j^2$ in terms of the spin $j = 0, 1, 2$. For gravitational perturbations $j = 2$, but we leave j unspecified for the time being. Expressing the equation in the form

$$v'' + P(\rho)v' + Q(\rho)v = 0$$

$$P(\rho) = \frac{1}{\rho(\rho-1)}, \quad Q(\rho) = -\frac{\ell(\ell+1)\rho + \kappa}{\rho^2(\rho-1)}, \quad (\text{D.2})$$

we find that it has regular singular points at 0, 1, and ∞ , as well as the associated Riemann-Papperitz symbol [161]

$$v = P \left\{ \begin{matrix} 0 & 1 & \infty \\ 1+j & 0 & -(\ell+1) \\ 1-j & 0 & \ell \end{matrix} ; \rho \right\}. \quad (\text{D.3})$$

To obtain the standard normal form, we let $v = \rho^{1+j}u$, so that

$$u = P \left\{ \begin{matrix} 0 & 1 & \infty \\ 0 & 0 & -\ell+j \\ -2j & 0 & \ell+j+1 \end{matrix} ; \rho \right\}, \quad (\text{D.4})$$

where u satisfies the hypergeometric equation

$$\rho(1-\rho)u'' + [c - (a+b+1)\rho]u' - abu = 0, \quad (\text{D.5})$$

with $a = -\ell + j$, $b = \ell + j + 1$, and $c = 1 + 2j$. As one of the two linearly independent solutions based at $\rho = \infty$ (chosen to be the second), we may take

$$u_2(\rho) = \rho^{-\ell-j-1} {}_2F_1(\ell + j + 1, \ell - j + 1; 2(\ell + 1); \rho^{-1}). \quad (\text{D.6})$$

Expressed in terms of the original dependent variable, $v_2 = \rho^{1+j}u_2$, this solution is our axial/right solution $v_2(\rho) = v_R^{\text{axial}}(\rho)$ given in (5.10b). To obtain series solutions based at 1 which are nevertheless valid on $(1, \infty)$, we follow Leaver [144] and consider the transformation $\eta = (\rho - 1)/\rho$. Then with $w(\eta) = v(1/(1 - \eta))$, we get

$$\begin{aligned} w'' + \mathcal{P}(\eta)w' + \mathcal{Q}(\eta)w &= 0 \\ \mathcal{P}(\eta) &= \frac{1 - 3\eta}{\eta(1 - \eta)}, \quad \mathcal{Q}(\eta) = -\frac{\ell(\ell + 1) + \kappa(1 - \eta)}{\eta(1 - \eta)^2}, \end{aligned} \quad (\text{D.7})$$

which has the P -symbol

$$w = P \left\{ \begin{array}{ccc} 0 & 1 & \infty \\ 0 & -(\ell + 1) & 1 + j \\ 0 & \ell & 1 - j \end{array} ; \eta \right\}. \quad (\text{D.8})$$

Now let $w = (\eta - 1)^\ell y$ so that

$$y = P \left\{ \begin{array}{ccc} 0 & 1 & \infty \\ 0 & 0 & 1 + \ell + j \\ 0 & -(2\ell + 1) & 1 + \ell - j \end{array} ; \eta \right\} \quad (\text{D.9})$$

solves

$$\eta(1 - \eta)y'' + [C - (A + B + 1)\eta]y' - AB y = 0, \quad (\text{D.10})$$

with $A = \ell - j + 1$, $B = \ell + j + 1$, and $C = 1$. Therefore, we choose $v_1(\rho) = v_L^{\text{axial}}(\rho)$ given in (5.10a) as both a first linearly independent solution and the axial/left one

of interest.

D.2 Zerilli Equation

In dimensionless form, the time-independent Zerilli equation is

$$-\left(1 - \frac{1}{\rho}\right)v'' - \frac{1}{\rho^2}v' + \left[\frac{8n^2(n+1)\rho^3 + 12n^2\rho^2 + 18n\rho + 9}{\rho^3(2n\rho + 3)^2}\right]v = 0, \quad (\text{D.11})$$

again where $n = \frac{1}{2}(\ell - 1)(\ell + 2)$. In standard form, the equation is

$$\begin{aligned} v'' + P(\rho)v' + Q(\rho)v &= 0, & P(\rho) &= \frac{1}{\rho(\rho - 1)} \\ Q(\rho) &= -\left[\frac{8n^2(n+1)\rho^3 + 12n^2\rho^2 + 18n\rho + 9}{\rho^2(\rho - 1)(2n\rho + 3)^2}\right]. \end{aligned} \quad (\text{D.12})$$

This equation has regular singular points at 0 , 1 , ∞ , and $-3/(2n)$, with the following associated pairs of indicial exponents: $\{1, 1\}$, $\{0, 0\}$, $\{\ell, -(\ell + 1)\}$, $\{2, -1\}$. The general second order homogeneous ODE with regular singular points at z_0 , z_1 , z_2 , and ∞ has the form $y'' + R(z)y' + S(z)y = 0$, with

$$\begin{aligned} R(z) &= \frac{A_0}{z - z_0} + \frac{A_1}{z - z_1} + \frac{A_2}{z - z_2} \\ S(z) &= \frac{B_0}{(z - z_0)^2} + \frac{B_1}{(z - z_1)^2} + \frac{B_2}{(z - z_2)^2} + \frac{C_0}{z - z_0} + \frac{C_1}{z - z_1} + \frac{C_2}{z - z_2}, \end{aligned} \quad (\text{D.13})$$

where the A_i , B_i , and C_i are all constants subject to $C_0 + C_1 + C_2 = 0$ and the requirement that for each $i = 0, 1, 2$ at least one member of the triple A_i , B_i , and C_i must be non-zero (for otherwise z_i would be an ordinary point). By expressing all constants A_i , B_i , C_i except C_0 in terms of the indicial exponents $\{\{\lambda_k, \lambda'_k\} : k =$

$0, 1, 2, \infty\}$, we find

$$\begin{aligned}
 R(z) &= \frac{1 - \lambda_0 - \lambda'_0}{z - z_0} + \frac{1 - \lambda_1 - \lambda'_1}{z - z_1} + \frac{1 - \lambda_2 - \lambda'_2}{z - z_2} \\
 S(z) &= \frac{\lambda_0 \lambda'_0}{(z - z_0)^2} + \frac{\lambda_1 \lambda'_1}{(z - z_1)^2} + \frac{\lambda_2 \lambda'_2}{(z - z_2)^2} \\
 &+ \frac{\lambda_\infty \lambda'_\infty - \lambda_0 \lambda'_0 - \lambda_1 \lambda'_1 - \lambda_2 \lambda'_2}{(z - z_1)(z - z_2)} \\
 &+ \frac{C_0(z_0 - z_1)(z_0 - z_2)}{(z - z_0)(z - z_1)(z - z_2)}.
 \end{aligned} \tag{D.14}$$

Here $-C_0$ is the *accessory parameter* [203], and the generalized Riemann scheme [203] associated with the equation is

$$\left[\begin{array}{cccc|c}
 1 & 1 & 1 & 1 & \\
 z_0 & z_1 & z_2 & \infty & ; z \\
 \lambda_0 & \lambda_1 & \lambda_2 & \lambda_\infty & ; -C_0 \\
 \lambda'_0 & \lambda'_1 & \lambda'_2 & \lambda'_\infty &
 \end{array} \right]. \tag{D.15}$$

The notation is similar to the P -symbol, but also indicates the type of singular points in the first row (regular singular points are indicated by a 1). We find the scheme

$$\left[\begin{array}{cccc|c}
 1 & 1 & 1 & 1 & \\
 0 & 1 & -3/(2n) & \infty & ; \rho \\
 1 & 0 & 2 & -(\ell + 1) & ; 0 \\
 1 & 0 & -1 & \ell &
 \end{array} \right]. \tag{D.16}$$

for the specific case of the time-independent Zerilli equation (D.11).

Upon transforming the ODE specified by (D.14) to normal form, we find the new

accessory parameter

$$q = -C_0 + \frac{\lambda_0(\lambda'_1 - 1) + \lambda_1(\lambda'_0 - 1)}{z_0 - z_1} + \frac{\lambda_0(\lambda'_2 - 1) + \lambda_2(\lambda'_0 - 1)}{z_0 - z_2}, \quad (\text{D.17})$$

as well as the transformed scheme

$$\left[\begin{array}{cccc|c} 1 & 1 & 1 & 1 & \\ z_0 & z_1 & z_2 & \infty & ; z \\ 0 & 0 & 0 & \lambda_\infty + \lambda_0 + \lambda_1 + \lambda_2 & ; q \\ \lambda'_0 - \lambda_0 & \lambda'_1 - \lambda_1 & \lambda'_2 - \lambda_2 & \lambda'_\infty + \lambda_0 + \lambda_1 + \lambda_2 & \end{array} \right]. \quad (\text{D.18})$$

With the assumptions $z_0 = 0$ and $z_1 = 1$, this scheme corresponds to the Heun equation $G'' + P(z)G' + Q(z)G = 0$ in normal form, where

$$\begin{aligned} P(z) &= \frac{c}{z} + \frac{d}{z-1} + \frac{1+a+b-c-d}{z-z_2} \\ Q(z) &= \frac{ab}{(z-1)(z-z_2)} - \frac{qz_2}{z(z-1)(z-z_2)}. \end{aligned} \quad (\text{D.19})$$

Here the transformed scheme

$$\left[\begin{array}{cccc|c} 1 & 1 & 1 & 1 & \\ 0 & 1 & z_2 & \infty & ; z \\ 0 & 0 & 0 & a & ; q \\ 1-c & 1-d & c+d-a-b & b & \end{array} \right] \quad (\text{D.20})$$

is expressed in terms of the constants a , b , c , and d which may be related to the

above exponent pairs $\{\lambda_k, \lambda'_k\}$. The normal form of (D.11) then has the scheme

$$\begin{bmatrix} 1 & 1 & 1 & 1 \\ 0 & 1 & -3/(2n) & \infty & ; \rho \\ 0 & 0 & 0 & 2 - \ell & ; 1 - 4n/3 \\ 0 & 0 & -3 & \ell + 3 \end{bmatrix}. \quad (\text{D.21})$$

While the preceding analysis both addresses the structure of the time-independent Zerilli equation and reveals the asymptotic behavior of the solutions near any given singular point, it does not provide concrete analytical expressions for the solutions $v_{L,R}^{\text{polar}}$ considered in the main text. To obtain such expressions, we use the intertwining operators [12]

$$D_{\pm} = \left(1 - \frac{1}{\rho}\right) \frac{d}{d\rho} \pm \left[\frac{2}{3}n(n+1) + \frac{3(\rho-1)}{\rho^2(3+2n\rho)}\right]. \quad (\text{D.22})$$

Using our earlier solutions $v_{L,R}^{\text{axial}}(\rho)$ to the time-independent Regge-Wheeler equation, we then get corresponding solutions $v_{L,R}^{\text{polar}}(\rho) \equiv D_+ v_{L,R}^{\text{axial}}(\rho)$ to (D.11) by direct application of D_+ and the identity

$$\frac{d}{dz} {}_2F_1(a, b; c; z) = \frac{ab}{c} {}_2F_1(a+1, b+1; c+1; z). \quad (\text{D.23})$$

Therefore, we have also expressed the relevant polar solutions in terms of the Gauss-hypergeometric function ${}_2F_1$. The analysis above then shows that we are likewise able to express solutions to a particular instance of the Heun equation in terms of hypergeometric functions.

APPENDIX FIVE

Hyperbolicity of the First-order GBSSN System

This appendix analyzes the matrix $\mathcal{A}(u)$ appearing in (6.9) in order to construct the characteristic fields (6.13). In matrix form the sector (6.7) of the principal part of (6.9) reads as follows¹:

$$\partial_t \begin{bmatrix} B^r \\ A_{rr} \\ K \\ \Gamma^r \\ Q_\chi \\ Q_{g_{rr}} \\ Q_{g_{\theta\theta}} \\ Q_\alpha \\ Q_{\beta^r} \end{bmatrix} = \begin{bmatrix} \beta^r & 0 & -\frac{4\lambda\alpha}{3g_{rr}} & 0 & 0 & \frac{\lambda\beta^r}{6(g_{rr})^2} & \frac{\lambda\beta^r}{3g_{\theta\theta}g_{rr}} & 0 & \frac{4\lambda}{3g_{rr}} \\ 0 & \beta^r & 0 & \frac{2}{3}g_{rr}\alpha\chi & \frac{1}{3}\alpha & -\frac{\alpha\chi}{3g_{rr}} & \frac{\alpha\chi}{3g_{\theta\theta}} & -\frac{2}{3}\chi & 0 \\ 0 & 0 & \beta^r & 0 & 0 & 0 & 0 & -\frac{\chi}{g_{rr}} & 0 \\ 0 & 0 & -\frac{4\alpha}{3g_{rr}} & \beta^r & 0 & \frac{\beta^r}{6(g_{rr})^2} & \frac{\beta^r}{3g_{\theta\theta}g_{rr}} & 0 & \frac{4}{3g_{rr}} \\ 0 & 0 & \frac{2}{3}\alpha\chi & 0 & \beta^r & -\frac{\beta^r\chi}{3g_{rr}} & -\frac{2\beta^r\chi}{3g_{\theta\theta}} & 0 & -\frac{2}{3}\chi \\ 0 & -2\alpha & 0 & 0 & 0 & \frac{2}{3}\beta^r & -\frac{2g_{rr}\beta^r}{3g_{\theta\theta}} & 0 & \frac{4}{3}g_{rr} \\ 0 & \frac{g_{\theta\theta}\alpha}{g_{rr}} & 0 & 0 & 0 & -\frac{g_{\theta\theta}\beta^r}{3g_{rr}} & \frac{1}{3}\beta^r & 0 & -\frac{2}{3}g_{\theta\theta} \\ 0 & 0 & -2\alpha & 0 & 0 & 0 & 0 & \beta^r & 0 \\ \frac{3}{4} & 0 & 0 & 0 & 0 & 0 & 0 & 0 & \beta^r \end{bmatrix} \begin{bmatrix} B^r \\ A_{rr} \\ K \\ \Gamma^r \\ Q_\chi \\ Q_{g_{rr}} \\ Q_{g_{\theta\theta}} \\ Q_\alpha \\ Q_{\beta^r} \end{bmatrix}' \quad (\text{E.1})$$

which defines the matrix $\tilde{A}(u)$ appearing in (6.8), and so also the matrix $\mathcal{A}(u)$ in (6.9). Note that in the last equation the matrix within the square brackets is $-\tilde{A}(u)$. For certain configurations of u and λ , the system (6.9) is strongly hyperbolic [140], that is $\mathcal{A}(u)$ has a complete set of eigenvectors and real eigenvalues. Indeed, five eigenpairs

¹We remind the reader that in Chapter 6 $g_{\alpha\beta}$ is used for the spatial metric and conformal quantities have no ‘bar’ (cf. footnote 1).

of $\mathcal{A}(u)$ are trivially recovered upon inspection of $\mathcal{A}(u)$'s leading 5×5 diagonal block. These correspond to eigenvalue 0 and the left eigenspace $\{\xi_j = e_j^T : 1 \leq j \leq 5\}$, where e_j are the canonical basis vectors. Since each component of u arises as $e_j^T W$, each is also a characteristic field.

The remaining nine eigenpairs are determined by $\tilde{A}(u)$. The eigenvalues of $\tilde{A}(u)$ are

$$\begin{aligned} \mu_1 &= 0, & \mu_{2,3} &= -\beta^r, & \mu_4^\pm &= -\beta^r \pm \sqrt{\frac{2\alpha\chi}{g_{rr}}}, \\ \mu_5^\pm &= -\beta^r \pm \alpha\sqrt{\frac{\chi}{g_{rr}}}, & \mu_6^\pm &= -\beta^r \pm \sqrt{\frac{\lambda}{g_{rr}}}, \end{aligned} \quad (\text{E.2})$$

and the corresponding left eigenvectors are

$$x_1 = (0, 0, 0, 0, 0, g_{\theta\theta}, 2g_{rr}, 0, 0) \quad (\text{E.3a})$$

$$x_2 = \left(0, 0, 0, g_{rr}, \frac{2}{\chi}, -\frac{1}{2g_{rr}}, -\frac{1}{g_{\theta\theta}}, 0, 0\right) \quad (\text{E.3b})$$

$$x_3 = \left(\frac{g_{rr}}{\lambda}, 0, 0, 0, \frac{2}{\chi}, -\frac{1}{2g_{rr}}, -\frac{1}{g_{\theta\theta}}, 0, 0\right) \quad (\text{E.3c})$$

$$x_4^\pm = \left(0, 0, \pm\sqrt{\frac{2\alpha g_{rr}}{\chi}}, 0, 0, 0, 0, 1, 0\right) \quad (\text{E.3d})$$

$$x_5^\pm = \left(0, \mp\frac{3}{\sqrt{g_{rr}\chi}}, \pm 2\sqrt{\frac{g_{rr}}{\chi}}, 2g_{rr}, \frac{1}{\chi}, -\frac{1}{g_{rr}}, \frac{1}{g_{\theta\theta}}, 0, 0\right) \quad (\text{E.3e})$$

$$\begin{aligned} x_6^\pm &= \left(-\frac{3}{4}\frac{g_{rr}}{\lambda}, 0, \pm\frac{\alpha\sqrt{\lambda g_{rr}}}{(2\alpha\chi - \lambda)}, 0, 0, -\frac{\beta^r}{8(\beta^r g_{rr} \mp \sqrt{\lambda g_{rr}})}, \right. \\ &\quad \left. -\frac{\beta^r g_{rr}}{4g_{\theta\theta}(\beta^r g_{rr} \mp \sqrt{\lambda g_{rr}})}, \frac{\alpha\chi}{(2\alpha\chi - \lambda)}, \pm\sqrt{\frac{g_{rr}}{\lambda}}\right), \end{aligned} \quad (\text{E.3f})$$

where for example $x_5^\pm \tilde{A}(u) = \mu_5^\pm x_5^\pm$. Assuming that g_{rr} , $g_{\theta\theta}$, χ , and α are everywhere strictly positive, the eigenvalues are real and the eigenvectors are linearly independent provided that (6.14) holds. These eigenvectors are easily extended to eigenvectors of $\mathcal{A}(u)$, e. g. as $x_6^\pm \rightarrow (0_{1 \times 5}, x_6^\pm)$. Then, for example, the characteristic

field

$$X_6^\pm \equiv (0_{1 \times 5}, x_6^\pm)W = x_6^\pm W_{v:Q}, \quad (\text{E.4})$$

and similarly $X_j^\pm = x_j^\pm W_{v:Q}$ for $j = 4, 5$ and $X_k = x_k W_{v:Q}$ for $k = 1, 2, 3$. The characteristic speeds for these fields are μ_k and μ_j^\pm . With this convention the speeds listed in Table 6.1 correspond to the X_k and X_j^\pm in (6.13).

APPENDIX SIX

Reduction of the GBSSN System to Spherical Symmetry

F.1 Problem Setup

A conformal–traceless decomposition of each spacelike 3–surface’s geometry is presented in Section 2.6. Variables associated with this decomposition satisfy the GBSSN evolution (2.91) and constraint (2.92) equations. We now carry out a reduction of the evolution and constraint equations for a spherically symmetric spacetime,

$$ds^2 = -\alpha^2 dt^2 + \chi^{-1} \bar{\gamma}_{rr} (dr + \beta^r dt)^2 + \chi^{-1} \bar{\gamma}_{\theta\theta} (d\theta^2 + \sin^2 \theta d\phi^2), \quad (\text{F.1})$$

along with the spherically symmetric *Ansatz*:

$$\bar{\Gamma}^a = \begin{pmatrix} \bar{\Gamma}^r \\ -\cos \theta / (\bar{\gamma}_{\theta\theta} \sin \theta) \\ 0 \end{pmatrix}, \quad \bar{A}_{ab} = \bar{A}_{rr} \begin{pmatrix} 1 & 0 & 0 \\ 0 & -\bar{\gamma}_{\theta\theta} / (2\bar{\gamma}_{rr}) & 0 \\ 0 & 0 & -\bar{\gamma}_{\theta\theta} \sin^2 \theta / (2\bar{\gamma}_{rr}) \end{pmatrix}. \quad (\text{F.2})$$

for the conformal–traceless extrinsic curvature and conformal connection functions. The GBSSN system variables are χ , $\bar{\gamma}_{rr}$, $\bar{\gamma}_{\theta\theta}$, \bar{A}_{rr} , K , $\bar{\Gamma}^r$, α , β^r and B^r , and all are functions of t and r . Then the non–zero conformal connection components are computed as

$$\begin{aligned} \bar{\Gamma}_{rr}^r &= \frac{\bar{\gamma}'_{rr}}{2\bar{\gamma}_{rr}}, & \bar{\Gamma}_{\theta r}^\theta &= \frac{\bar{\gamma}'_{\theta\theta}}{2\bar{\gamma}_{\theta\theta}}, & \bar{\Gamma}_{\phi r}^\phi &= \frac{\bar{\gamma}'_{\theta\theta}}{2\bar{\gamma}_{\theta\theta}}, & \bar{\Gamma}_{\theta\theta}^r &= -\frac{\bar{\gamma}'_{\theta\theta}}{2\bar{\gamma}_{rr}}, \\ \bar{\Gamma}_{\phi\phi}^r &= \sin^2 \theta \bar{\Gamma}_{\theta\theta}^r, & \bar{\Gamma}_{\phi\phi}^\theta &= -\sin \theta \cos \theta, & \bar{\Gamma}_{\phi\theta}^\phi &= \frac{\cos \theta}{\sin \theta}. \end{aligned} \quad (\text{F.3})$$

Here, and throughout this appendix, the prime stands for partial r -differentiation.

Recall that the conformal metric’s determinant evolves according to a Lagrangian condition (see Sec. 2.6.3). In spherical symmetry and expressed with the GBSSN

system variables, this condition is

$$\begin{aligned}\alpha\mathcal{L}_n\ln\bar{\gamma} &= -2\bar{D}_a\beta^a = -2(\partial_a\beta^a + \bar{\Gamma}_{ac}^a\beta^c) \\ &= -2\beta^{r'} - \frac{\bar{\gamma}'_{rr}\beta^r}{\bar{\gamma}_{rr}} - \frac{2\bar{\gamma}'_{\theta\theta}\beta^r}{\bar{\gamma}_{\theta\theta}},\end{aligned}\tag{F.4}$$

where the Lagrangian condition $\partial_t(\ln\bar{\gamma}) = 0$ has been used in the first equality.

Eq. (F.4) will be used to replace $\mathcal{L}_n\ln\bar{\gamma}$ throughout the GBSSN system (2.91).

F.2 Physical Ricci Tensor and Scalar

In this subsection we seek expressions for R_{rr}^{TF} and R with conformal (GBSSN) variables. To accomplish this task, we first construct expressions built from physical variables and later substitute for the conformal ones.

Components R_{rr} and $R_{\theta\theta}$ are directly computed via the spatial (i.e. Latin index) version of (2.15):

$$\begin{aligned}R_{rr} &= -\frac{\gamma''_{\theta\theta}}{\gamma_{\theta\theta}} + 2(\Gamma_{r\theta}^\theta)^2 - 2\frac{\gamma_{rr}}{\gamma_{\theta\theta}}\Gamma_{rr}^r\Gamma_{\theta\theta}^r \\ &= -\frac{\gamma''_{\theta\theta}}{\gamma_{\theta\theta}} + \frac{(\gamma'_{\theta\theta})^2}{2\gamma_{\theta\theta}^2} + \frac{\gamma'_{rr}\gamma'_{\theta\theta}}{2\gamma_{rr}\gamma_{\theta\theta}}\end{aligned}\tag{F.5}$$

$$\begin{aligned}R_{\theta\theta} &= -\frac{1}{2}\gamma^{\phi\phi}\gamma_{\phi\phi,\theta\theta} - \frac{1}{2}\gamma^{rr}\gamma''_{\theta\theta} + \frac{\gamma_{\theta\theta}}{\gamma_{rr}}(\Gamma_{r\theta}^\theta)^2 + (\Gamma_{\theta\phi}^\phi)^2 - \Gamma_{rr}^r\Gamma_{\theta\theta}^r - \frac{\gamma_{rr}}{\gamma_{\theta\theta}}(\Gamma_{\theta\theta}^r)^2 \\ &= 1 - \frac{\gamma''_{\theta\theta}}{2\gamma_{rr}} + \frac{\gamma'_{rr}\gamma'_{\theta\theta}}{4\gamma_{rr}^2}.\end{aligned}\tag{F.6}$$

Noting $R_{\phi\phi} = \sin^2 \theta R_{\theta\theta}$, we compute the Ricci scalar as

$$\begin{aligned} R &= \frac{R_{rr}}{\gamma_{rr}} + 2 \frac{R_{\theta\theta}}{\gamma_{\theta\theta}} \\ &= -\frac{2\gamma''_{\theta\theta}}{\gamma_{rr}\gamma_{\theta\theta}} + \frac{(\gamma'_{\theta\theta})^2}{2\gamma_{rr}\gamma_{\theta\theta}^2} + \frac{\gamma'_{rr}\gamma'_{\theta\theta}}{\gamma_{rr}^2\gamma_{\theta\theta}} + \frac{2}{\gamma_{\theta\theta}}. \end{aligned} \quad (\text{F.7})$$

Comparing (F.7) and (F.5), observe that

$$R_{rr} = \frac{1}{2}\gamma_{rr}R + \frac{(\gamma'_{\theta\theta})^2}{4\gamma_{\theta\theta}^2} - \frac{\gamma_{rr}}{\gamma_{\theta\theta}}, \quad (\text{F.8})$$

which allows the trace-free component to take on a particularly useful form

$$R_{rr}^{\text{TF}} = \frac{1}{6}\gamma_{rr}R + \frac{(\gamma'_{\theta\theta})^2}{4\gamma_{\theta\theta}^2} - \frac{\gamma_{rr}}{\gamma_{\theta\theta}}. \quad (\text{F.9})$$

Finally, substituting for conformal variables produces the desired result

$$R = -\frac{2\bar{\gamma}''_{\theta\theta}\chi}{\bar{\gamma}_{rr}\bar{\gamma}_{\theta\theta}} + \frac{(\bar{\gamma}'_{\theta\theta})^2\chi}{2\bar{\gamma}_{rr}\bar{\gamma}_{\theta\theta}^2} + \frac{\bar{\gamma}'_{rr}\bar{\gamma}'_{\theta\theta}\chi}{\bar{\gamma}_{rr}^2\bar{\gamma}_{\theta\theta}} + \frac{2\chi}{\bar{\gamma}_{\theta\theta}} + \frac{2\chi''}{\bar{\gamma}_{rr}} - \frac{5(\chi')^2}{2\bar{\gamma}_{rr}\chi} + 2\frac{\chi'\bar{\gamma}'_{\theta\theta}}{\bar{\gamma}_{\theta\theta}\bar{\gamma}_{rr}} - \frac{\chi'\bar{\gamma}'_{rr}}{\bar{\gamma}_{rr}^2}, \quad (\text{F.10})$$

$$\chi R_{rr}^{\text{TF}} = -\frac{\bar{\gamma}''_{\theta\theta}\chi}{3\bar{\gamma}_{\theta\theta}} + \frac{(\bar{\gamma}'_{\theta\theta})^2\chi}{3\bar{\gamma}_{\theta\theta}^2} + \frac{\bar{\gamma}'_{rr}\bar{\gamma}'_{\theta\theta}\chi}{6\bar{\gamma}_{rr}\bar{\gamma}_{\theta\theta}} - \frac{2\chi\bar{\gamma}_{rr}}{3\bar{\gamma}_{\theta\theta}} + \frac{\chi''}{3} - \frac{(\chi')^2}{6\chi} - \frac{\chi'\bar{\gamma}'_{\theta\theta}}{6\bar{\gamma}_{\theta\theta}} - \frac{\chi'\bar{\gamma}'_{rr}}{6\bar{\gamma}_{rr}}. \quad (\text{F.11})$$

These expressions are substituted for the appropriate terms found in the Hamiltonian constraint equation and the right-hand side of $\partial_t \bar{A}_{rr}$.

F.3 Reduced Constraint Equations

The Hamiltonian constraint (2.92a) is found using an expression for the term

$$\bar{A}_{ij}\bar{A}^{ij} = (\bar{\gamma}^{rr}\bar{A}_{rr})^2 + (\bar{\gamma}^{\theta\theta}\bar{A}_{\theta\theta})^2 + (\bar{\gamma}^{\phi\phi}\bar{A}_{\phi\phi})^2 = \frac{3\bar{A}_{rr}^2}{2\bar{\gamma}_{rr}^2} \quad (\text{F.12})$$

along with the Ricci scalar (F.10). To recover the r -component of the covariant momentum constraint, first apply $\chi\gamma_{rr} = \bar{\gamma}_{rr}$ directly to (A.9). Carrying out the tensor operations, while noting $\bar{A}^{ri}\partial_i\ln\bar{\gamma} = \bar{A}^{rr}\bar{\gamma}^{jk}\partial_r\bar{\gamma}_{jk}$, gives the desired result. The conformal connection function constraint is easily computed from the conformal connection functions' definition (2.90) and constraints (2.92c). Subject to spherical symmetry, the GBSSN system constraints are as follows:

$$\begin{aligned} \mathcal{H} = & -\frac{3\bar{A}_{rr}^2}{2\bar{\gamma}_{rr}^2} + \frac{2K^2}{3} - \frac{5(\chi')^2}{2\chi\bar{\gamma}_{rr}} + \frac{2\chi''}{\bar{\gamma}_{rr}} + \frac{2\chi}{\bar{\gamma}_{\theta\theta}} - \frac{2\chi\bar{\gamma}_{\theta\theta}''}{\bar{\gamma}_{rr}\bar{\gamma}_{\theta\theta}} \\ & + \frac{2\chi'\bar{\gamma}_{\theta\theta}'}{\bar{\gamma}_{rr}\bar{\gamma}_{\theta\theta}} + \frac{\chi\bar{\gamma}_{rr}'\bar{\gamma}_{\theta\theta}'}{\bar{\gamma}_{rr}^2\bar{\gamma}_{\theta\theta}} - \frac{\chi'\bar{\gamma}_{rr}'}{\bar{\gamma}_{rr}^2} + \frac{\chi(\bar{\gamma}_{\theta\theta}')^2}{2\bar{\gamma}_{rr}\bar{\gamma}_{\theta\theta}^2} \end{aligned} \quad (\text{F.13a})$$

$$\mathcal{M}_r = \frac{\bar{A}'_{rr}}{\bar{\gamma}_{rr}} - \frac{2K'}{3} - \frac{3\bar{A}_{rr}\chi'}{2\chi\bar{\gamma}_{rr}} + \frac{3\bar{A}_{rr}\bar{\gamma}'_{\theta\theta}}{2\bar{\gamma}_{rr}\bar{\gamma}_{\theta\theta}} - \frac{\bar{A}_{rr}\bar{\gamma}'_{rr}}{\bar{\gamma}_{rr}^2} \quad (\text{F.13b})$$

$$\mathcal{G}^r = -\frac{\bar{\gamma}'_{rr}}{2\bar{\gamma}_{rr}^2} + \frac{\bar{\gamma}'_{\theta\theta}}{\bar{\gamma}_{rr}\bar{\gamma}_{\theta\theta}} + \bar{\Gamma}^r. \quad (\text{F.13c})$$

These expressions agree with the ones listed by Brown in [42].

F.4 Reduced Evolution Equations

F.4.1 Trace of the Extrinsic Curvature

Consider the K component of (2.91). We seek to express

$$D^i D_i \alpha = \gamma^{ij} D_j D_i \alpha = \gamma^{ij} [\partial_j \partial_i \alpha - \Gamma_{ij}^k \partial_k \alpha] = \gamma^{rr} \partial_r \partial_r \alpha - \gamma^{ij} \Gamma_{ij}^r \partial_r \alpha \quad (\text{F.14})$$

with GBSSN variables. The relevant connection components are found with the help of (2.87)

$$\Gamma_{rr}^r = \bar{\Gamma}_{rr}^r - \frac{\chi'}{2\chi}, \quad \Gamma_{\theta\theta}^r = \bar{\Gamma}_{\theta\theta}^r + \frac{\chi' \bar{\gamma}^{rr} \bar{\gamma}_{\theta\theta}}{2\chi}, \quad \Gamma_{\phi\phi}^r = \sin^2 \theta \Gamma_{\theta\theta}^r, \quad (\text{F.15})$$

and we have

$$D^i D_i \alpha = \frac{\chi}{\bar{\gamma}_{rr}} \alpha'' - \left(\frac{\chi \bar{\gamma}'_{rr}}{2\bar{\gamma}_{rr}^2} - \frac{\chi \bar{\gamma}'_{\theta\theta}}{\bar{\gamma}_{\theta\theta} \bar{\gamma}_{rr}} + \frac{\chi'}{2\bar{\gamma}_{rr}} \right) \alpha'. \quad (\text{F.16})$$

Noting Eq. (F.12), the spherically reduced equation for K is

$$\begin{aligned} \partial_t K &= \frac{1}{3} \alpha K^2 + \alpha \frac{3\bar{A}_{rr}^2}{2\bar{\gamma}_{rr}^2} - \frac{\chi}{\bar{\gamma}_{rr}} \alpha'' \\ &+ \left(\frac{\chi \bar{\gamma}'_{rr}}{2\bar{\gamma}_{rr}^2} - \frac{\chi \bar{\gamma}'_{\theta\theta}}{\bar{\gamma}_{\theta\theta} \bar{\gamma}_{rr}} + \frac{\chi'}{2\bar{\gamma}_{rr}} \right) \alpha' + \beta^r K' + 4\pi (S + \rho). \end{aligned} \quad (\text{F.17})$$

F.4.2 Conformal and Traceless Part of the Extrinsic Curvature

Next, consider the \bar{A}_{rr} component of the system (2.91). The first three terms are straightforward to compute, while the $D^i D_i \alpha$ piece of the trace-free term

$$\begin{aligned}
(D_r D_r \alpha)^{\text{TF}} &= D_r D_r \alpha - \frac{1}{3} \gamma_{rr} D^i D_i \alpha \\
&= \alpha'' - \left(\frac{\bar{\gamma}'_{rr}}{2\bar{\gamma}_{rr}} - \frac{\chi'}{2\chi} \right) \alpha' - \frac{\bar{\gamma}_{rr}}{3\chi} \left[\frac{\chi}{\bar{\gamma}_{rr}} \alpha'' - \left(\frac{\chi \bar{\gamma}'_{rr}}{2\bar{\gamma}_{rr}^2} - \frac{\chi \bar{\gamma}'_{\theta\theta}}{\bar{\gamma}_{\theta\theta} \bar{\gamma}_{rr}} + \frac{\chi'}{2\bar{\gamma}_{rr}} \right) \alpha' \right] \\
&= \frac{2}{3} \alpha'' + \left(-\frac{\bar{\gamma}'_{rr}}{3\bar{\gamma}_{rr}} - \frac{\bar{\gamma}'_{\theta\theta}}{3\bar{\gamma}_{\theta\theta}} + \frac{2\chi'}{3\chi} \right) \alpha'
\end{aligned} \tag{F.18}$$

is expression (F.16). By adding a multiple of the conformal connection constraint's derivative (F.13c) to χR_{rr}^{TF} (given by (F.11)) we may change the principle part. Using

$$\bar{\Gamma}^{r'} = \frac{\bar{\gamma}''_{rr}}{2\bar{\gamma}_{rr}^2} - \frac{\bar{\gamma}''_{\theta\theta}}{\bar{\gamma}_{rr} \bar{\gamma}_{\theta\theta}} - \frac{(\bar{\gamma}'_{rr})^2}{\bar{\gamma}_{rr}^3} + \frac{(\bar{\gamma}'_{\theta\theta})^2}{\bar{\gamma}_{rr} \bar{\gamma}_{\theta\theta}^2} + \frac{\bar{\gamma}'_{\theta\theta} \bar{\gamma}'_{rr}}{\bar{\gamma}_{rr}^2 \bar{\gamma}_{\theta\theta}}, \tag{F.19}$$

χR_{rr}^{TF} is rewritten as

$$\begin{aligned}
\chi R_{rr}^{\text{TF}} &= \frac{2\chi(\bar{\gamma}'_{rr})^2}{3\bar{\gamma}_{rr}^2} - \frac{\chi(\bar{\gamma}'_{\theta\theta})^2}{3\bar{\gamma}_{\theta\theta}^2} - \frac{(\chi')^2}{6\chi} + \frac{2}{3} \bar{\gamma}_{rr} \chi \bar{\Gamma}^{r'} - \frac{\chi \bar{\gamma}'_{rr} \bar{\gamma}'_{\theta\theta}}{2\bar{\gamma}_{rr} \bar{\gamma}_{\theta\theta}} \\
&\quad - \frac{\bar{\gamma}'_{rr} \chi'}{6\bar{\gamma}_{rr}} - \frac{\bar{\gamma}'_{\theta\theta} \chi'}{6\bar{\gamma}_{\theta\theta}} - \frac{\chi \bar{\gamma}''_{rr}}{3\bar{\gamma}_{rr}} + \frac{\chi \bar{\gamma}''_{\theta\theta}}{3\bar{\gamma}_{\theta\theta}} - \frac{2\bar{\gamma}_{rr} \chi}{3\bar{\gamma}_{\theta\theta}} + \frac{\chi''}{3}.
\end{aligned} \tag{F.20}$$

Bringing together these results, we arrive at an expression

$$\begin{aligned}
\partial_t \bar{A}_{rr} &= \beta^r \bar{A}'_{rr} + \frac{4}{3} \bar{A}_{rr} \beta^{r'} - \frac{\beta^r \bar{\gamma}'_{rr} \bar{A}_{rr}}{3\bar{\gamma}_{rr}} - \frac{2\beta^r \bar{\gamma}'_{\theta\theta} \bar{A}_{rr}}{3\bar{\gamma}_{\theta\theta}} + \frac{2\alpha\chi(\bar{\gamma}'_{rr})^2}{3\bar{\gamma}_{rr}^2} - \frac{\alpha\chi(\bar{\gamma}'_{\theta\theta})^2}{3\bar{\gamma}_{\theta\theta}^2} \\
&\quad - \frac{\alpha(\chi')^2}{6\chi} + \frac{2}{3} \bar{\gamma}_{rr} \alpha \chi \bar{\Gamma}^{r'} - \frac{\alpha\chi \bar{\gamma}'_{rr} \bar{\gamma}'_{\theta\theta}}{2\bar{\gamma}_{rr} \bar{\gamma}_{\theta\theta}} + \frac{\chi \bar{\gamma}'_{rr} \alpha'}{3\bar{\gamma}_{rr}} + \frac{\chi \bar{\gamma}'_{\theta\theta} \alpha'}{3\bar{\gamma}_{\theta\theta}} - \frac{\alpha \bar{\gamma}'_{rr} \chi'}{6\bar{\gamma}_{rr}} \\
&\quad - \frac{\alpha \bar{\gamma}'_{\theta\theta} \chi'}{6\bar{\gamma}_{\theta\theta}} - \frac{2}{3} \alpha' \chi' + \frac{\alpha \chi''}{3} - \frac{2}{3} \chi \alpha'' - \frac{\alpha \chi \bar{\gamma}''_{rr}}{3\bar{\gamma}_{rr}} + \frac{\alpha \chi \bar{\gamma}''_{\theta\theta}}{3\bar{\gamma}_{\theta\theta}} - \frac{2\alpha \bar{A}_{rr}^2}{\bar{\gamma}_{rr}} \\
&\quad + K \alpha \bar{A}_{rr} - \frac{2\bar{\gamma}_{rr} \alpha \chi}{3\bar{\gamma}_{\theta\theta}} - 8\pi \alpha \chi S_{ij}^{\text{TF}}
\end{aligned} \tag{F.21}$$

which describes the evolution of \bar{A}_{rr} .

F.4.3 Spherically Symmetric GBSSN System

The remaining GBSSN equations (Lagrangian choice for $\mathcal{L}_n \ln \bar{\gamma}$) readily reduce to spherical symmetry using the results of this section, and we arrive at¹:

$$\partial_t \alpha = \beta^r \alpha' - 2\alpha K \quad (\text{F.22a})$$

$$\partial_t \beta^r = \beta^r \beta^{r'} + \frac{3}{4} B^r \quad (\text{F.22b})$$

$$\partial_t B^r = \beta^r B^{r'} + \partial_t \bar{\Gamma}^r - \beta^r \bar{\Gamma}^{r'} - \eta B^r \quad (\text{F.22c})$$

$$\partial_t \chi = \beta^r \chi' + \frac{2}{3} K \alpha \chi - \frac{\beta^r \bar{\gamma}'_{rr} \chi}{3 \bar{\gamma}_{rr}} - \frac{2 \beta^r \bar{\gamma}'_{\theta\theta} \chi}{3 \bar{\gamma}_{\theta\theta}} - \frac{2}{3} \beta^{r'} \chi \quad (\text{F.22d})$$

$$\partial_t \bar{\gamma}_{rr} = \frac{2}{3} \beta^r \bar{\gamma}'_{rr} + \frac{4}{3} \bar{\gamma}_{rr} \beta^{r'} - 2 \bar{A}_{rr} \alpha - \frac{2 \bar{\gamma}_{rr} \beta^r \bar{\gamma}'_{\theta\theta}}{3 \bar{\gamma}_{\theta\theta}} \quad (\text{F.22e})$$

$$\partial_t \bar{\gamma}_{\theta\theta} = \frac{1}{3} \beta^r \bar{\gamma}'_{\theta\theta} + \frac{\bar{A}_{rr} \bar{\gamma}_{\theta\theta} \alpha}{\bar{\gamma}_{rr}} - \frac{\bar{\gamma}_{\theta\theta} \beta^r \bar{\gamma}'_{rr}}{3 \bar{\gamma}_{rr}} - \frac{2}{3} \bar{\gamma}_{\theta\theta} \beta^{r'} \quad (\text{F.22f})$$

$$\begin{aligned} \partial_t \bar{A}_{rr} = & \beta^r \bar{A}'_{rr} + \frac{4}{3} \bar{A}_{rr} \beta^{r'} - \frac{\beta^r \bar{\gamma}'_{rr} \bar{A}_{rr}}{3 \bar{\gamma}_{rr}} - \frac{2 \beta^r \bar{\gamma}'_{\theta\theta} \bar{A}_{rr}}{3 \bar{\gamma}_{\theta\theta}} + \frac{2 \alpha \chi (\bar{\gamma}'_{rr})^2}{3 \bar{\gamma}_{rr}^2} - \frac{\alpha \chi (\bar{\gamma}'_{\theta\theta})^2}{3 \bar{\gamma}_{\theta\theta}^2} \\ & - \frac{\alpha (\chi')^2}{6 \chi} + \frac{2}{3} \bar{\gamma}_{rr} \alpha \chi \bar{\Gamma}^{r'} - \frac{\alpha \chi \bar{\gamma}'_{rr} \bar{\gamma}'_{\theta\theta}}{2 \bar{\gamma}_{rr} \bar{\gamma}_{\theta\theta}} + \frac{\chi \bar{\gamma}'_{rr} \alpha'}{3 \bar{\gamma}_{rr}} + \frac{\chi \bar{\gamma}'_{\theta\theta} \alpha'}{3 \bar{\gamma}_{\theta\theta}} - \frac{\alpha \bar{\gamma}'_{rr} \chi'}{6 \bar{\gamma}_{rr}} \\ & - \frac{\alpha \bar{\gamma}'_{\theta\theta} \chi'}{6 \bar{\gamma}_{\theta\theta}} - \frac{2}{3} \alpha' \chi' + \frac{\alpha \chi''}{3} - \frac{2}{3} \chi \alpha'' - \frac{\alpha \chi \bar{\gamma}''_{rr}}{3 \bar{\gamma}_{rr}} + \frac{\alpha \chi \bar{\gamma}''_{\theta\theta}}{3 \bar{\gamma}_{\theta\theta}} - \frac{2 \alpha \bar{A}^2_{rr}}{\bar{\gamma}_{rr}} \\ & + K \alpha \bar{A}_{rr} - \frac{2 \bar{\gamma}_{rr} \alpha \chi}{3 \bar{\gamma}_{\theta\theta}} - 8 \pi \alpha \chi S_{ij}^{\text{TF}} \end{aligned} \quad (\text{F.22g})$$

$$\partial_t K = \beta^r K' + \frac{\chi \bar{\gamma}'_{rr} \alpha'}{2 \bar{\gamma}_{rr}^2} - \frac{\chi \bar{\gamma}'_{\theta\theta} \alpha'}{\bar{\gamma}_{rr} \bar{\gamma}_{\theta\theta}} + \frac{\alpha' \chi'}{2 \bar{\gamma}_{rr}} - \frac{\chi \alpha''}{\bar{\gamma}_{rr}} + \frac{3 \alpha \bar{A}^2_{rr}}{2 \bar{\gamma}_{rr}^2} + \frac{1}{3} \alpha K^2 + 4 \pi (S + \rho) \quad (\text{F.22h})$$

$$\begin{aligned} \partial_t \bar{\Gamma}^r = & \beta^r \bar{\Gamma}^{r'} + \frac{\bar{A}_{rr} \alpha \bar{\gamma}'_{\theta\theta}}{\bar{\gamma}_{rr}^2 \bar{\gamma}_{\theta\theta}} + \frac{2 \beta^{r'} \bar{\gamma}'_{\theta\theta}}{3 \bar{\gamma}_{rr} \bar{\gamma}_{\theta\theta}} + \frac{\bar{A}_{rr} \alpha \bar{\gamma}'_{rr}}{\bar{\gamma}_{rr}^3} - \frac{4 \alpha K'}{3 \bar{\gamma}_{rr}} - \frac{2 \bar{A}_{rr} \alpha'}{\bar{\gamma}_{rr}^2} - \frac{3 \bar{A}_{rr} \alpha \chi'}{\bar{\gamma}_{rr}^2 \chi} \\ & + \frac{4 \beta^{r''}}{3 \bar{\gamma}_{rr}} - \frac{\beta^r (\bar{\gamma}'_{\theta\theta})^2}{\bar{\gamma}_{rr} (\bar{\gamma}_{\theta\theta})^2} + \frac{\beta^r \bar{\gamma}''_{rr}}{6 (\bar{\gamma}_{rr})^2} + \frac{\beta^r \bar{\gamma}''_{\theta\theta}}{3 \bar{\gamma}_{\theta\theta} \bar{\gamma}_{rr}} - \frac{16 \pi \alpha}{\chi} j^r, \end{aligned} \quad (\text{F.22i})$$

¹For this system the determinant $\bar{\gamma} = \bar{\gamma}_{rr} (\bar{\gamma}_{\theta\theta})^2 \sin^2 \theta$ is not unity.

To keep with convention, $\bar{\Gamma}^r$ has been removed from the right hand side of the $\partial_t \bar{\Gamma}^r$ equation using \mathcal{G}^r (F.13c). The vacuum Eqs. (F.22d-i) are recovered by the condition $j^r = S_{ij}^{\text{TF}} = S = \rho = 0$, these are precisely Brown's Eqs. (9a-f) listed in [42] and subject to the Lagrangian condition (corresponding to $v = 1$ in Brown's equations). The first three equations (F.22a-c) comprise the gauge sector, these are spherically symmetric versions of the standard 1+log and Γ -driver conditions.

Bibliography

- [1] A. Abrahams, A. Anderson, Y. Choquet-Bruhat, and J. W. York, Jr., *Einstein and Yang-Mills Theories in Hyperbolic Form without Gauge Fixing*, Phys. Rev. Lett. 75, 3377-3381 (1995).
- [2] A. M. Abrahams and C. R. Evans, *Reading off gravitational radiation waveforms in numerical relativity calculations: Matching to linearized gravity*, Phys. Rev. D 37, 318-332 (1988).
- [3] A. M. Abrahams and C. R. Evans, *Gauge-invariant treatment of gravitational radiation near the source: Analysis and numerical simulations*, Phys. Rev. D 42, 2585-2594 (1990).
- [4] P. Ajith and S. Bose, *Estimating the parameters of nonspinning binary black holes using ground-based gravitational-wave detectors: Statistical errors*, Phys. Rev. D 79, 084032 (2009) (21 pages).
- [5] S. Akcay, *A Fast Frequency-Domain Algorithm for Gravitational Self-Force: I, Circular Orbits in Schwarzschild Spacetime*, <http://arxiv.org/abs/1012.5860> (2010).
- [6] M. Alcubierre, B. Brügmann, P. Diener, M. Koppitz, D. Pollney, E. Seidel, and R. Takahashi, *Gauge conditions for long-term numerical black hole evolutions*

- without excision*, Phys. Rev. D 67, 084023 (2003) (18 pages).
- [7] M. Alcubierre, B. Brügmann, M. Miller, and W.-M. Suen, *Conformal hyperbolic formulation of the Einstein equations*, Phys. Rev. D 60, 064017 (1999) (4 pages).
- [8] R. López-Alemán, G. Khanna, J. Pullin, *Perturbative evolution of particle orbits around Kerr black holes: time domain calculation*, Class. Quantum Grav. 20, 3259-3268 (2003).
- [9] B. Allen, W. G. Anderson, P. R. Brady, D. A. Brown, J. D. E. Creighton, *FINDCHIRP: an algorithm for detection of gravitational waves from inspiraling compact binaries*, <http://arxiv.org/abs/gr-qc/0509116> (2005).
- [10] B. Alpert, L. Greengard, and T. Hagstrom, *Rapid Evaluation of Nonreflecting Boundary Kernels for Time-Domain Wave Propagation*, SIAM J. Numer. Anal. 37, 1138-1164 (2000).
- [11] A. Anderson, Y. Choquet-Bruhat, and J. W. York, *Einstein-Bianchi hyperbolic system for general relativity*, Topol. Meth. Nonlinear Anal. 10, 353-373 (1997).
- [12] A. Anderson and R. H. Price, *Intertwining of the equations of black-hole perturbations*, Phys. Rev. D 43, 3147-3154 (1991).
- [13] A. Anderson and J. W. York, Jr., *Fixing Einstein's Equations*, Phys. Rev. Lett. 82, 4384-4387 (1999).
- [14] T. A. Apostolatos, C. Cutler, G. J. Sussman, and K. S. Thorne, *Spin-induced orbital precession and its modulation of the gravitational waveforms from merging binaries*, Phys. Rev. D 49, 62746297 (1994).
- [15] D. N. Arnold, F. Brezzi, B. Cockburn, and L. D. Marini, *Unified analysis of discontinuous Galerkin methods for elliptic problems*, SIAM J. Numer. Anal. 39, no. 5, 17491779 (2002).
- [16] R. Arnowitt, S. Deser, and C. W. Misner, *The Dynamics of General Relativity*, in *Gravitation: an introduction to current research*, edited by L.

- Witten (Wiley, New York, 1962), Chapter 7, 227-265. Also available as <http://arxiv.org/pdf/gr-qc/0405109>.
- [17] S. Babak, R. Balasubramanian, D. Churches, T. Cokelaer, and B. S. Sathyaprakash, *A template bank to search for gravitational waves from inspiralling compact binaries: I. Physical models*, *Class. Quantum Grav.* 23, 5477-5504 (2006).
- [18] L. Baiotti, T. Damour, B. Giacomazzo, A. Nagar, and L. Rezzolla, *Accurate numerical simulations of inspiralling binary neutron stars and their comparison with effective-one-body analytical models*, <http://arxiv.org/abs/1103.3874> (2011).
- [19] L. Barack, Y. Mino, H. Nakano, A. Ori, and M. Sasaki, *Calculating the Gravitational Self-Force in Schwarzschild Spacetime*, *Phys. Rev. Lett.* 88, 091101 (2002) (4 pages).
- [20] L. Barack and C. O. Lousto, *Perturbations of Schwarzschild black holes in the Lorenz gauge: Formulation and numerical implementation* *Phys. Rev. D* 72, 104026 (2005) (25 pages).
- [21] L. Barack, *Gravitational self-force in extreme mass-ratio inspirals*, *Class. Quantum Grav.* 26, 213001 (2009) (56 pages).
- [22] L. Barack and N. Sago, *Gravitational self-force on a particle in circular orbit around a Schwarzschild black hole*, *Phys. Rev. D* 75, 064021 (2007) (25 pages).
- [23] L. Barack, A. Ori, and N. Sago, *Frequency-domain calculation of the self force: the high-frequency problem and its resolution*, *Phys. Rev. D* 78, 084021 (2008) (17 pages).
- [24] J. L. Barton, D. J. Lazar, D. J. Kennefick, G. Khanna, L. M. Burko, *Computational Efficiency of Frequency- and Time-Domain Calculations of Extreme Mass-Ratio Binaries: Equatorial Orbits*, *Phys. Rev. D* 78, 064042 (2008) (15 pages).

- [25] F. Bassi and S. Rebay, *A High-Order Accurate Discontinuous Finite Element Method for the Numerical Solution of the Compressible Navier-Stokes Equations*, J. Comp. Phys. 131, issue 2, 267-279 (1997).
- [26] J. G. Baker, J. Centrella, D.-I. Choi, M. Koppitz, and J. van Meter, *Gravitational-Wave Extraction from an Inspiral Configuration of Merging Black Holes*, Phys. Rev. Lett. 96, 111102 (2006) (4 pages).
- [27] T. W. Baumgarte and S. L. Shapiro *Numerical Relativity and Compact Binaries*, Phys. Rept. 376, 41-131 (2003). Also available as <http://arxiv.org/abs/gr-qc/0211028>.
- [28] T. W. Baumgarte and S. L. Shapiro, *Numerical integration of Einstein's field equations*, Phys. Rev. D 59, 024007 (1998) (7 pages).
- [29] T. W. Baumgarte and S. G. Naculich, *Analytical representation of a black hole puncture solution*, Phys. Rev. D 75, 067502 (2007) (4 pages).
- [30] P. Binev, A. Cohen, W. Dahmen, R. Devore, G. Petrova, and P. Wojtaszczyk, *Convergence Rates for Greedy Algorithms in Reduced Basis Methods*, <http://www.dfg-spp1324.de/download/preprints/preprint047.pdf> (2010).
- [31] L. Blanchet, S. Detweiler, A. Le Tiec, B. F. Whiting, *Post-Newtonian and numerical calculations of the gravitational self-force for circular orbits in the Schwarzschild geometry*, Phys. Rev. D 81, 064004 (2010) (22 pages).
- [32] L. Blanchet, T. Damour, I. Thibault, and R. Bala, *Gravitational waves from inspiralling compact binaries: Energy loss and wave form to second-post-Newtonian order*, Phys. Rev. D 51, 53605386 (1995).
- [33] C. Bona, J. Massó, E. Seidel, and J. Stela, *New Formalism for Numerical Relativity*, Phys. Rev. Lett. 75, 600-603 (1995).
- [34] M. Á. G. Bonilla, *Symmetric hyperbolic systems for Bianchi equations*, Class. Quantum Grav. 15, 2001-2005 (1998).

- [35] L. Boyle, M. Kesden, and S. Nissanke, *Binary-Black-Hole Merger: Symmetry and the Spin Expansion*, Phys. Rev. Lett. 100, 151101 (2008) (4 pages).
- [36] P. R. Brady and S. R. -Majumder, *Incorporating information from source simulations into searches for gravitational-wave bursts*, Class. Quantum Grav. 21, S1839-S1848 (2004).
- [37] F. Brezzi, G. Manzini, D. Marini, P. Pietra, and A. Russo, *Discontinuous finite elements for diffusion problems*, in *Atti Convegno in onore di F. Brioschi (Milan, 1997)*, 197-217. Istituto Lombardo, Accademia di Scienze e Lettere, Milan, Italy, 1999.
- [38] A. Klöckner, T. Warburton, J. Bridge, and J. S. Hesthaven, *Nodal discontinuous Galerkin methods on graphics processors*, J. Comp. Phys. 228, issue 21, 7863-7882 (2009).
- [39] D. Brill and J. Hartle *Method of the Self-Consistent Field in General Relativity and its Application to the Gravitational Geon*, Phys. Rev. 135, B271B278 (1964).
- [40] D. Brizuela, J. M. Martin-Garcia, and M. Tiglio, *A complete gauge-invariant formalism for arbitrary second-order perturbations of a Schwarzschild black hole*, Phys. Rev. D 80, 024021 (2009) (14 pages).
- [41] J. D. Brown, *Conformal invariance and the conformal-traceless decomposition of the gravitational field*, Phys. Rev. D 71, 104011 (2005) (12 pages).
- [42] J. D. Brown, *BSSN in spherical symmetry*, Class. Quantum Grav. 25, 205004 (2008) (23 pages).
- [43] J. D. Brown, *Covariant formulations of BSSN and the standard gauge*, Phys. Rev. D 79, 104029 (2009) (6 pages)
- [44] J. D. Brown, personal correspondence.
- [45] J. D. Brown, *Probing the puncture for black hole simulations*, Phys. Rev. D 80, 084042 (2009) (24 pages).

- [46] J. D. Brown, *Puncture evolution of Schwarzschild black holes*, Phys. Rev. D 77, 044018 (2008) (5 pages).
- [47] D. Brown, P. Diener, O. Sarbach, E. Schnetter, and M. Tiglio, *Turduckening black holes: An analytical and computational study*, Phys. Rev. D 79, 044023 (2009) (19 pages).
- [48] D. Brown, O. Sarbach, E. Schnetter, M. Tiglio, P. Diener, I. Hawke, and D. Pollney, *Excision without excision*, Phys. Rev. D 76, 081503(R) (2007) (5 pages).
- [49] B. Brüggmann, J. A. González, M. Hannam, S. Husa, U. Sperhake, and W. Tichy, *Calibration of moving puncture simulations*, Phys. Rev. D 77, 024027 (2008) (25 pages).
- [50] D. Buskulic, LIGO and Virgo Scientific Collaboration, *Very low latency search pipeline for low mass compact binary coalescences in the LIGO S6 and Virgo VSR2 data*, Class. Quantum Grav. 27, 194013.
- [51] G. Calabrese, J. Pullin, O. Sarbach and M. Tiglio, *Convergence and stability in numerical relativity*, Phys. Rev. D 66, 041501(R) (2002) (4 pages).
- [52] M. Campanelli, C. O. Lousto, and Y. Zlochower, *Last orbit of binary black holes*, Phys. Rev. D 73, 061501(R) (2006) (5 pages).
- [53] M. Campanelli, C. O. Lousto, P. Marronetti, and Y. Zlochower, *Accurate Evolutions of Orbiting Black-Hole Binaries without Excision*, Phys. Rev. Lett. 96, 111101 (2006) (4 pages).
- [54] M. Campanelli and C. O. Lousto, *The imposition of Cauchy data to the Teukolsky equation. I. The nonrotating case*, Phys. Rev. D 58, 024015 (1998) (8 pages).
- [55] M. Campanelli, W. Krivan, and C. O. Lousto, *The imposition of Cauchy data to the Teukolsky equation. II. Numerical comparison with the Zerilli-Moncrief approach to black hole perturbations*, Phys. Rev. D 58, 024016 (1998) (7 pages).
- [56] P. Cañizares and C. F. Sopuerta, *Simulations of Extreme–Mass–Ratio Inspirals Using Pseudospectral Methods*, J. Phys. Conf. Series 154 012053 (2009) (6 pages).

- [57] P. Cañizares and C. F. Sopuerta, *Efficient pseudospectral method for the computation of the self-force on a charged particle: Circular geodesics around a Schwarzschild black hole*, Phys. Rev. D 79, 084020 (2009) (15 pages).
- [58] P. Cañizares, C. F. Sopuerta, and J. L. Jaramillo, *Pseudospectral collocation methods for the computation of the self-force on a charged particle: Generic orbits around a Schwarzschild black hole*, Phys. Rev. D 82, 044023 (2010) (19 pages).
- [59] K. Cannon, A. Chapman, C. Hanna, D. Keppel, A. C. Searle, and A. J. Weinstein, *Singular value decomposition applied to compact binary coalescence gravitational-wave signals*, Phys. Rev. D 82, 044025 (2010) (6 pages).
- [60] S. Carroll, *Spacetime and Geometry: An Introduction to General Relativity*, (Addison-Wesley, New York, 2003). As available as <http://arxiv.org/abs/gr-qc/9712019>
- [61] D. Chakraborty, J.-H. Jung, G. Khanna, *A multi-domain hybrid method for head-on collision of black holes in particle limit*, <http://arxiv.org/abs/1103.1551> (2011).
- [62] S. Chandrasekhar, *The mathematical theory of black holes*, (Oxford University Press, New York, 1992).
- [63] Y. Cheng and C.-W. Shu, *A discontinuous Galerkin finite element method for time dependent partial differential equations with higher order derivatives*, Math. Comp. 77, no. 262, 699-730 (2007).
- [64] M. Chirvasa, *Finite difference methods for 1st Order in time, 2nd order in space, hyperbolic systems used in numerical relativity*, <http://www.scientificcommons.org/57150453>.
- [65] Y. Choquet-Bruhat and J. W. York, *Geometrical well posed systems for the Einstein equations*, C. R. Acad. Sci. Paris, t. 321, Série I, 1089-1095 (1995).

- [66] P. L. Chrzanowski, *Vector potential and metric perturbations of a rotating black hole*, Phys. Rev. D 11, 2042-2062 (1975).
- [67] B. Cockburn and C.-W. Shu, *The local discontinuous Galerkin method for time-dependent convection-diffusion systems*, SIAM J. Numer. Anal. 35, no. 6, 2440-2463 (1998).
- [68] B. Cockburn and C. W. Shu, *TVB Runge–Kutta Local Projection Discontinuous Galerkin Finite Element Method for Conservation Laws II: General Framework*, Math. Comp. 52, 411-435 (1989).
- [69] B. Cockburn, S. Hou, and C. W. Shu, *The Runge-Kutta local projection discontinuous Galerkin finite element method for conservation laws IV: The multidimensional case*, Math. Comp. 54, 545-581 (1990).
- [70] B. Cockburn and C. W. Shu, *The Runge–Kutta Discontinuous Galerkin Method for Conservation Laws V: Multidimensional Systems*, J. Comp. Phys. 141, Issue 2, 199-224 (1998).
- [71] B. Cockburn, F. Li, and C. W. Shu, *Locally divergence-free discontinuous Galerkin methods for the Maxwell equations*, J. Comp. Phys. 194, Issue 2, 588-610 (2004).
- [72] G. Cohen, X. Ferrieres, and S. Pernet, *A spatial high-order hexahedral discontinuous Galerkin method to solve Maxwell's equations in time domain* J. Comp. Phys. 217, Issue 2, 340-363 (2006).
- [73] C. T. Cunningham, R. H. Price, and V. Moncrief, *Radiation from collapsing relativistic stars. I - Linearized odd-parity radiation* Astrophys. J. 224 643-667 (1978).
- [74] C. T. Cunningham, R. H. Price, and V. Moncrief, *Radiation from collapsing relativistic stars. II - Linearized even-parity radiation* Astrophys. J. 230 870-892 (1979).

- [75] C. Cutler, D. Kennefick, and E. Poisson, *Gravitational radiation reaction for bound motion around a Schwarzschild black hole*, Phys. Rev. D 50, 3816-3835 (1994).
- [76] C. Cutler, E. E. Flanagan, *Gravitational radiation reaction for bound motion around a Schwarzschild black hole*, Phys. Rev. D 49, 26582697 (1994).
- [77] T. Damour, *Gravitational self-force in a Schwarzschild background and the effective one-body formalism*, Phys. Rev. D 81, 024017 (2010) (22 pages).
- [78] M. Davis, R. Ruffini, W. H. Press, and R. H. Price, *Gravitational Radiation from a Particle Falling Radially into a Schwarzschild Black Hole*, Phys. Rev. Lett. 27, 1466-1469 (1971).
- [79] S. Detweiler, *Perspective on gravitational self-force analyses*, Class. Quantum Grav. 22, S681 (2005) (39 pages).
- [80] S. Detweiler, *Consequence of the gravitational self-force for circular orbits of the Schwarzschild geometry*, Phys. Rev. D 77, 124026 (2008) (15 pages).
- [81] S. Detweiler and B. F. Whiting, *Self-force via a Green's function decomposition*, Phys. Rev. D 67, 024025 (2003) (5 pages).
- [82] P. Diener, F. Herrmann, D. Pollney, E. Schnetter, E. Seidel, R. Takahashi, J. Thornburg, and J. Ventrella, *Accurate Evolution of Orbiting Binary Black Holes*, Phys. Rev. Lett. 96, 121101 (2006) (4 pages).
- [83] R. Donniger, W. Schlag, and A. Soffer, *A proof of Price's Law on Schwarzschild black hole manifolds for all angular momenta*, <http://arxiv.org/abs/0908.4292>.
- [84] J. L. Eftang, A. T. Patera, and E. M. Ronquist, *An hp Certified Reduced Basis Method for Parametrized Parabolic Partial Differential Equations*, Spectral and High Order Methods for Partial Differential Equations, Lecture Notes in Computational Science and Engineering, 2011, Volume 76, 179-187.

- [85] F. B. Estabrook, R. S. Robinson, and H. D. Wahlquist, *Hyperbolic equations for vacuum gravity using special orthonormal frames*, *Class. Quantum Grav.* 14, 1237-1247 (1997).
- [86] Z. B. Etienne, J. A. Faber, Y. T. Liu, S. L. Shapiro, and T. W. Baumgarte, *Filling the holes: Evolving excised binary black hole initial data with puncture techniques*, *Phys. Rev. D* 76, 101503(R) (2007) (5 pages).
- [87] L. C. Evans, *Partial Differential Equations*, (American Mathematical Society, Providence, 1998).
- [88] K. Fan, W. Cai, and X. Ji, *A generalized discontinuous Galerkin (GDG) method for Schrödinger equations with nonsmooth solutions*, *J. Comp. Phys.* 227 2387-2410 (2008).
- [89] S. E. Field, J. S. Hesthaven, and S. R. Lau, *Discontinuous Galerkin method for computing gravitational waveforms from extreme mass ratio binaries*, *Class. Quantum Grav.* 26 165010 (2009) (28 pages).
- [90] S. E. Field, J. S. Hesthaven, and S. R. Lau, *Persistent junk solutions in time-domain modeling of extreme mass ratio binaries*, *Phys. Rev. D* 81, 124030 (2010) (14 pages).
- [91] S. E. Field, J. S. Hesthaven, S. R. Lau, and A. H. Mroue, *Discontinuous Galerkin method for the spherically reduced Baumgarte–Shapiro–Shibata–Nakamura system with second-order operators*, *Phys. Rev. D* 82, 104051 (2010) (19 pages).
- [92] S. E. Field, C. R. Galley, F. Herrmann, J. S. Hesthaven, E. Ochsner, and M. Tiglio, *Reduced basis catalogs for gravitational wave templates*, <http://arxiv.org/abs/1101.3765>.
- [93] V. Fock, *The Theory of Space Time and Gravitation* (Pergamon Press, New York, 1959).
- [94] G. B. Folland, *Introduction to Partial Differential Equations*, (Princeton University Press, Princeton, 1995).

- [95] H. Friedrich, *Hyperbolic reductions for Einstein's equations*, Class. Quantum Grav. 13, 1451-1469 (1996).
- [96] S. Frittelli and O. Reula, *On the Newtonian Limit of General Relativity*, Commun. Math. Phys. 166, 221-235 (1994).
- [97] S. Frittelli and O. A. Reula, *First-Order Symmetric Hyperbolic Einstein Equations with Arbitrary Fixed Gauge*, Phys. Rev. Lett. 76, 4667-4670 (1996).
- [98] S. Frittelli and O. A. Reula, *Well-posed forms of the 3+1 conformally-decomposed Einstein equations* J. Math. Phys. 40, 5143-5156 (1999).
- [99] H. Friedrich and A. Rendall, *The Cauchy problem for the Einstein equations*, in *Einstein's Field Equations and their Physical Implications*, edited by B. G. Schmidt, Springer Lecture Notes in Physics, vol. 540, pp. 127-223 (Springer-Verlag, Berlin, 2000).
- [100] H. Friedrich and A. D. Rendall, *The Cauchy Problem for the Einstein Equations*, Lec. Notes Phys. 540, 127-224 (2000). Also available as [arXiv:gr-qc/0002074v1](https://arxiv.org/abs/gr-qc/0002074v1).
- [101] C. R. Galley and B. L. Hu, *Self-force on extreme mass ratio inspirals via curved spacetime effective field theory*, Phys. Rev. D 79, 064002 (2009) (18 pages).
- [102] C. R. Galley and M. Tiglio, *Radiation reaction and gravitational waves in the effective field theory approach*, Phys. Rev. D 79, 124027 (2009) (19 pages).
- [103] U. H. Gerlach and U. K. Sengupta, *Gauge invariant coupled gravitational, acoustical, and electromagnetic modes on most general spherical spacetimes*, Phys. Rev. D 22, 1300-1312 (1980).
- [104] R. J. Gleiser, C. O. Nicasio, R. H. Price, and J. Pullin, *Gravitational radiation from Schwarzschild black holes: The second order perturbation formalism*, Phys. Rept. 325 41-81 (2000).
- [105] N. Gödel, S. Schomann, T. Warburton, and M. Clemens, *Local timestepping discontinuous Galerkin methods for electromagnetic RF field problems*, Proceed-

- ings of the Third European Conference on Antennas and Propagation, Berlin, Germany, 21492153 (2009).
- [106] G. H. Golub and C. F. Van Loan, *Matrix Computations*, third edition (John Hopkins University Press, Baltimore and London, 1996).
- [107] M. J. Grote, A. Schneebeli, and D. Schötzau, *Discontinuous Galerkin finite element method for the wave equation*, SIAM J. Numer. Anal. 44, no. 6, 2408-2431 (2006).
- [108] M. J. Grote, A. Schneebeli, and D. Schötzau, *Interior penalty discontinuous Galerkin method for Maxwell's equations: Energy norm error estimates*, J. Comp. Appl. Math. 204, issue 2, 375-386 (2007).
- [109] C. Gundlach, G. Calabrese, I. Hinder and J. M. Martín-García, *Constraint damping in the Z_4 formulation and harmonic gauge*, Class. Quantum Grav. 22, 3767-3773 (2005).
- [110] C. Gundlach and J. M. Martin-Garcia, *Symmetric hyperbolic form of systems of second-order evolution equations subject to constraints*, Phys. Rev. D 70, 044031 (2004) (14 pages).
- [111] C. Gundlach, J. M. Martin-Garcia, *Hyperbolicity of second-order in space systems of evolution equations*, Class. Quantum Grav. 23, S387-S404 (2006).
- [112] B. Gustafsson, H. O. Kreiss and J. Olinger, *Time dependent problems and difference methods*, (Wiley, New York, 1995).
- [113] R. Haberman *Elementary Applied Partial Differential Equations*, (Prentice Hall, New Jersey, 1998).
- [114] G. Hagstrom and T. Hagstrom, *Grid stabilization of high-order one-sided differencing. I. First-order hyperbolic systems*, J. Comp. Phys. 223 316-340 (2007).
- [115] M. Hannam, S. Husa, D. Pollney, B. Brügmann, and N. Ó Murchadha, *Geometry and Regularity of Moving Punctures*, Phys. Rev. Lett. 99, 241102 (2007) (4 pages).

- [116] M. Hannam, S. Husa, B. Brügmann, J. A. González, U. Sperhake, and N. Ó Murchadha, *Where do moving punctures go?*, J. Phys.: Conf. Ser. 66, 012047 (2007) (9 pages).
- [117] M. Hannam, S. Husa, F. Ohme, B. Brügmann, and N. Ó Murchadha, *Wormholes and trumpets: the Schwarzschild spacetime for the moving-puncture generation*, Phys. Rev. D 78, 064020 (2008) (19 pages).
- [118] I. S. Heng, *Rotating stellar core-collapse waveform decomposition: A principal component analysis approach*, Class. Quantum Grav. 26, 105005 (2009).
- [119] F. Herrmann, I. Hinder, D. Shoemaker, and P. Laguna, *Unequal mass binary black hole plunges and gravitational recoil*, Class. Quantum Grav. 24, S33-S42 (2007).
- [120] S. D. Hern, *Numerical Relativity and Inhomogeneous Cosmologies*, Ph.D. dissertation, University of Cambridge, 1999. Also available as <http://arxiv.org/abs/gr-qc/0004036>.
- [121] J. S. Hesthaven and T. Warburton, *Nodal Discontinuous Galerkin Methods: Algorithms, Analysis, and Applications* (Springer, New York, 2008).
- [122] J. S. Hesthaven and T. Warburton, *Nodal High-Order Methods on Unstructured Grids. I. Time-Domain Solution of Maxwell's Equations*, J. Comp. Phys. 181, issue 1, 186-221 (2002).
- [123] J. S. Hesthaven and T. Warburton, *High-Order Accurate Methods for Time-domain Electromagnetics*, Comp. Mod. Engin. Sci. 5 395-408 (2004).
- [124] J. S. Hesthaven, S. Gottlieb, and D. Gottlieb, *Spectral Methods for Time-Dependent Problems* (Cambridge University Press, Cambridge UK, 2007).
- [125] S. Hopper and C. R. Evans *Gravitational perturbations and metric reconstruction: Method of extended homogeneous solutions applied to eccentric orbits on a Schwarzschild black hole*, Phys. Rev. D 82, 084010 (2010) (21 pages).

- [126] S. A. Hughes, *Lisa sources and science*, Proceedings of the 7th Edoardo Amaldi Conference on Gravitational Waves, <http://arxiv.org/abs/0711.0188> (2007).
- [127] M. S. Iriondo, E. O. Leguizamón, and O. A. Reula, *Einstein's Equations in Ashtekar's Variables Constitute a Symmetric Hyperbolic System*, Phys. Rev. Lett. 79, 4732-4735 (1997).
- [128] R. A. Isaacson, *Gravitational radiation in the limit of high frequency I: The linear approximation and geometrical optics* Phys. Rev. 166, 12631271 (1968).
- [129] R. A. Isaacson, *Gravitational radiation in the limit of high frequency II: Non-linear terms and the effective stress tensor*, Phys. Rev. 166, 12721280 (1968).
- [130] J. D. Jackson, *Classical Electrodynamics*, (Wiley, New York, 1975).
- [131] G. B. Jacobs, and J. S. Hesthaven, *High-order nodal discontinuous Galerkin particle-in-cell method on unstructured grids*, J. Comp. Phys. 214, Issue 1, 96-121 (2006).
- [132] J. L. Jaramillo, C. F. Sopuerta, and P. Canizares, *Are Time-Domain Self-Force Calculations Contaminated by Jost Solutions?*, (2011), <http://arxiv.org/abs/1101.2324>.
- [133] S. Jhingan and T. Tanaka, *Improvement on the metric reconstruction scheme in Regge-Wheeler-Zerilli formalism* Phys. Rev. D 67, 104018 (2003) (9 pages).
- [134] J.-H. Jung, G. Khanna, and I. Nagle, *A spectral collocation approximation of one-dimensional head-on collisions of black-holes*, to appear in Int. J. Mod. Phys. C, <http://arxiv.org/abs/0711.2545> (2007).
- [135] J. Kanner et al., *LOOC UP: Locating and observing optical counterparts to gravitational wave bursts*, Class. Quantum Grav. 25, 84034 (2008).
- [136] L. E. Kidder, M. A. Scheel and S. A. Teukolsky, *Extending the lifetime of 3D black hole computations with a new hyperbolic system of evolution equations*, Phys. Rev. D 64, 064017 (2001) (13 pages).

- [137] L. E. Kidder, M. A. Scheel, S. A. Teukolsky, E. D. Carlson, and G. B. Cook, *Black hole evolution by spectral methods*, Phys. Rev. D 62, 084032 (2000) (20 pages).
- [138] L. E. Kidder, M. A. Scheel, S. A. Teukolsky, *Extending the lifetime of 3D black hole computations with a new hyperbolic system of evolution equations*, Phys. Rev. D 64, 064017 (2001) (13 pages).
- [139] A. Klöckner, T. Warburton, J. S. Hesthaven, *Title: Viscous Shock Capturing in a Time-Explicit Discontinuous Galerkin Method*, <http://arxiv.org/abs/1102.3190> (2011).
- [140] H.-O. Kreiss and J. Lorenz, *Initial-Boundary Value Problems and the Navier-Stokes Equations*, SIAM Classics in Applied Mathematics (SIAM, Philadelphia, 2004).
- [141] M. D. Kruskal, *Maximal extension of Schwarzschild metric*, Phys. Rev. 119, 1743-1745 (1960).
- [142] L. D. Landau and E. M. Lifshitz, *The Classical Theory of Fields*, (Pergamon Press, Oxford, 1975).
- [143] S. R. Lau, *Analytic structure of radiation boundary kernels for blackhole perturbations*, J. Math. Phys. 46 102503 (2005) (21 pages).
- [144] E. W. Leaver, *Solutions to a generalized spheroidal wave equation: Teukolsky's equations in general relativity, and the two-center problem in molecular quantum mechanics*, J. Math. Phys. 27 1238-1265 (1986).
- [145] F. Li, and C. -W. Shu, *Locally Divergence-Free Discontinuous Galerkin Methods for MHD Equations*, J. Sci. Comp. 22-23, Numbers 1-3, 413-442 (2005).
- [146] A. P. Lightman, W. H. Press, R. H. Price, and S. A. Teukolsky, *Problem Book in Relativity and Gravitation* (Princeton University Press, Princeton, 1975).

- [147] L. Lindblom, M. A. Scheel, L. E. Kidder, R. Owen, and O. Rinne, *A new generalized harmonic evolution system*, *Class. Quantum Grav.* 23, S447-S462 (2006).
- [148] G. Lin, and G. E. Karniadakis, *A discontinuous Galerkin method for two-temperature plasmas*, *Comput. Methods Appl. Mech. Eng.* 195, Issues 25-28, 3504-03527 (2006).
- [149] L. Liu, X. Li, and Fang. Q. Hu, *Nonuniform time-step Runge-Kutta discontinuous Galerkin method for Computational Aeroacoustics*, *J. Comp. Phys.* 229, 19 6874-6897 (2010).
- [150] I. Lomtev, G. E. Karniadakis, *A discontinuous Galerkin method for the Navier-Stokes equations*, *Int. J. Num. Methods Fluids* 29, 587-603 (1999).
- [151] C. O. Lousto, *Reconstruction of black hole metric perturbations from Weyl curvature: II. The Regge-Wheeler gauge*, *Class. Quantum Grav.* 22, S569-S587 (2005).
- [152] C. O. Lousto, R. H. Price, *Understanding initial data for black hole collisions* *Phys. Rev. D* 56, 6439-6457 (1997).
- [153] C. O. Lousto, *A time-domain fourth-order-convergent numerical algorithm to integrate black hole perturbations in the extreme-mass-ratio limit*, *Class. Quantum Grav.* 22, S543-S568 (2005).
- [154] C. O. Lousto and Y. Zlochower, *Orbital Evolution of Extreme-Mass-Ratio Black-Hole Binaries with Numerical Relativity*, *Phys. Rev. Lett.* 106, 041101 (2011).
- [155] M. H. P. M. van Putten and D. M. Eardley, *Nonlinear wave equations for relativity*, *Phys. Rev. D* 53, 3056-3063 (1996).
- [156] Y. Maday, A. T. Patera, and G. Turinici, *A Priori convergence theory for reduced-basis approximations of single-parameter elliptic partial differential equations*, *J. of Sci. Comp.* 17 437-446 (2002).

- [157] K. Martel, *Gravitational waveforms from a point particle orbiting a Schwarzschild black hole*, Phys. Rev. D 69, 044025 (2004) (20 pages).
- [158] K. Martel and E. Poisson, *One-parameter family of time-symmetric initial data for the radial infall of a particle into a Schwarzschild black hole*, Phys. Rev. D 66 084001 (2002) (16 pages).
- [159] K. Martel and E. Poisson, *Gravitational perturbations of the Schwarzschild spacetime: A practical covariant and gauge-invariant formalism*, Phys. Rev. D 71, 104003 (2005) (13 pages). Expanded version available as <http://arxiv.org/abs/gr-qc/0502028>.
- [160] P. Marronetti, W. Tichy, B. Brügmann, J. González, M. Hannam, S. Husa and U. Sperhake, *Binary black holes on a budget: simulations using workstations*, Class. Quantum Grav. 24 S43-S58 (2007).
- [161] J. Mathews and R. L. Walker, *Methods of Mathematical Physics* (W. A. Benjamin, Inc., New York, 1965).
- [162] Y. Mino, M. Sasaki, and T. Tanaka, *Gravitational radiation reaction to a particle motion*, Phys. Rev. D 55, 457-3476 (1997).
- [163] C. W. Misner, K. S. Thorne, and J. A. Wheeler, *Gravitation*, (Freeman, San Francisco, 1973).
- [164] V. Moncrief, *Gravitational Perturbations of Spherically Symmetric Systems: The Exterior Problem*, Annals of Physics, 88 323-342 (1974).
- [165] V. Moncrief, *Odd-parity stability of a Reissner-Nordström black holes*, Phys. Rev. D 9, 2707-2709 (1974).
- [166] V. Moncrief, *Stability of a Reissner-Nordström black hole*, Phys. Rev. D 10, 1057-1059 (1974).
- [167] A. H. Mroue, personal correspondence.
- [168] A. Nagar, T. Damour, and A. Tartaglia, *Binary black hole merger in the extreme-mass-ratio limit*, Class. Quantum Grav. 24 S109-S123 (2007).

- [169] Current website for the project: <http://lisa.nasa.gov/>
- [170] B. O'Neill, *Semi-Riemannian Geometry with Applications to Relativity*, (Academic Press, San Diego, 1983).
- [171] D. Núñez and O. Sarbach, *Boundary conditions for the Baumgarte-Shapiro-Shibata-Nakamura formulation of Einstein's field equations*, Phys. Rev. D 81, 044011 (2010) (16 pages).
- [172] R. Owen, *Constraint damping in first-order evolution systems for numerical relativity*, Phys. Rev. D 76, 044019 (2007) (11 pages).
- [173] B. J. Owen, *Search templates for gravitational waves from inspiraling binaries: Choice of template spacing* Phys. Rev. D 53, 67496761 (1996).
- [174] N. Yunes, A. Buonanno, S. A. Hughes, M. C. Miller, Y. Pan, *Modeling Extreme Mass Ratio Inspirals within the Effective-One-Body Approach*, Phys. Rev. Lett. 104 091102 (2010) (4 pages).
- [175] A. T. Patera, and G. Rozza, *Reduced Basis Approximation and A Posteriori Error Estimation for Parametrized Partial Differential Equations*, to appear in (tentative rubric) MIT Pappalardo Graduate Monographs in Mechanical Engineering. http://augustine.mit.edu/methodology/methodology_bookPartI.htm
- [176] A. Pinkus, *N-widths in approximation theory*, (Springer, Amsterdam, 1985).
- [177] E. Poisson, *Absorption of mass and angular momentum by a black hole: Time-domain formalisms for gravitational perturbations, and the small-hole or slow-motion approximation*, Phys. Rev. D 70, 084044 (2004) (36 pages).
- [178] E. Poisson, *Gravitational radiation from a particle in circular orbit around a black hole. I. Analytical results for the nonrotating case*, Phys. Rev. D 47, 1497-1510 (1993).
- [179] E. Poisson, *The Motion of Point Particles in Curved Spacetime*, Living Reviews in Relativity, <http://www.livingreviews.org/lrr-2004-6>

- [180] F. Pretorius, *Evolution of Binary Black-Hole Spacetimes*, Phys. Rev. Lett. 95, 121101 (2005) (4 pages).
- [181] F. Pretorius, *Simulation of binary black hole spacetimes with a harmonic evolution scheme*, Class. Quantum Grav. 23, S529-S552 (2006).
- [182] F. Pretorius, *Numerical relativity using a generalized harmonic decomposition*, Class. Quantum Grav. 22, 425-451 (2005).
- [183] F. Pretorius <http://www.sns.ias.edu/pitp/index2009final.html> PITP lectures
- [184] R. H. Price and L. M. Burko, *Late time tails from momentarily stationary, compact initial data in Schwarzschild spacetimes*, Phys. Rev. D 70, 084039 (2004) (6 pages).
- [185] R. Pinnau, *Model Order Reduction: Theory, Research Aspects and Applications*, eds. Boc et al., (Springer Berlin 2008),
- [186] C. Prud'homme, D. V. Rovas, K. Veroy, L. Machiels, Y. Maday, A. T. Patera, and G. Turinici, *Reliable Real-Time Solution of Parametrized Partial Differential Equations: Reduced-Basis Output Bound Methods*, J. Fluids Engin. 124, 70-80 (2002).
- [187] J. Qiu, and C. -W. Shu, *Hermite WENO schemes and their application as limiters for Runge-Kutta discontinuous Galerkin method II: Two dimensional case*, Computers and Fluids 34, Issue 6, 642-663 (2005).
- [188] T. C. Quinn and R. M. Wald, *Axiomatic approach to electromagnetic and gravitational radiation reaction of particles in curved spacetime*, Phys. Rev. D 56, 33813394 (1997).
- [189] D. Radice and L. Rezzolla, *Discontinuous Galerkin methods for general-relativistic hydrodynamics: formulation and application to spherically symmetric spacetimes*, <http://arxiv.org/abs/1103.2426> (2011).

- [190] C. Reisswig, S. Husa, L. Rezzolla, E. N. Dorband, D. Pollney, and J. Seiler, *Gravitational-wave detectability of equal-mass black-hole binaries with aligned spins*, Phys. Rev. D 80, 124026 (2009) (19 pages).
- [191] W. H. Reed, and T. R. Hill, *Triangular mesh methods for the neutron transport equation*, Los Alamos Scientific Laboratory Report, LA-UR-73-479, (1973).
- [192] T. Regge and J. Wheeler, *Stability of a Schwarzschild Singularity*, Phys. Rev. 108, 1063-1069 (1957).
- [193] N. Sago, L. Barack, and S. Detweiler, *Two approaches for the gravitational self-force in black hole spacetime: Comparison of numerical results*, Phys. Rev. D 78, 124024 (2008) (9 pages).
- [194] N. Sago and L. Barack, in preparation; *Calculation of the gravitational self-force in Schwarzschild spacetime*, presentation given by N. Sago at the 12th Capra Meeting on Radiation Reaction, www.astro.indiana.edu/~jthorn/capra12/.
- [195] O. Sarbach and M. Tiglio, *Gauge invariant perturbations of Schwarzschild black holes in horizon-penetrating coordinates* Phys. Rev. D 64, 084016 (2001) (15 pages).
- [196] O. Sarbach and M. Tiglio, *Continuum and discrete initial-boundary-value problems and Einstein's field equations*, in preperation.
- [197] M. A. Scheel, H. P. Pfeiffer, L. Lindblom, L E. Kidder, O. Rinne, and S. A. Teukolsky, *Solving Einstein's Equations With Dual Coordinate Frames*, Phys. Rev. D 74, 104006 (2006) (13 pages).
- [198] M. A. Scheel, M. Boyle, T. Chu, L. E. Kidder, K. D. Matthews, and H. P. Pfeiffer, *High-accuracy waveforms for binary black hole inspiral, merger, and ring-down*, Phys. Rev. D 79, 024003 (2009) (14 pages).

- [199] A. Schneebeli, *Interior Penalty Discontinuous Galerkin Methods for Electromagnetic and Acoustic Wave Equations*, Ph.D. dissertation, University of Basel, 2006. Also available as http://edoc.unibas.ch/diss/DissB_7760.
- [200] M. Shibata and T. Nakamura, *Evolution of three-dimensional gravitational waves: Harmonic slicing case*, Phys. Rev. D 52, 5428-5444 (1995).
- [201] T. Tanaka, M. Shibata, M. Sasaki, H. Tagoshi, and T. Nakamura, *Gravitational Wave Induced by a Particle Orbiting around a Schwarzschild Black Hole*, Prog. Theo. Phys. 90 65-83 (1993).
- [202] H. Shinkai and G. Yoneda, *Hyperbolic formulations and numerical relativity: experiments using Ashtekar's connection variables*, Class. Quantum Grav. 17, 4799-4822 (2000).
- [203] S. Y. Slavyanov and W. Lay, *Special Functions: A Unified Theory Based on Singularities* (Oxford University Press, Oxford, 2000).
- [204] C. F. Sopuerta and P. Laguna, *Finite element computation of the gravitational radiation emitted by a pointlike object orbiting a nonrotating black hole*, Phys. Rev. D 73, 044028 (2006) (17 pages).
- [205] Spectral Einstein Code <http://www.black-holes.org/SpEC.html>
- [206] U. Sperhake, *Binary black-hole evolutions of excision and puncture data*, Phys. Rev. D 76, 104015 (2007) (20 pages).
- [207] P. A. Sundararajan, G. Khanna, and S. A. Hughes, *Towards adiabatic waveforms for inspiral into Kerr black holes: A new model of the source for the time domain perturbation equation*, Phys. Rev. D 76, 104005 (2007) (20 pages).
- [208] K. Shahbazi, *An explicit expression for the penalty parameter of the interior penalty method*, J. Comp. Phys. 205, issue 2, 401-407 (2005).
- [209] P. A. Sundararajan, G. Khanna, S. A. Hughes and S. Drasco, *Towards adiabatic waveforms for inspiral into Kerr black holes. II. Dynamical sources and generic orbits*, Phys. Rev. D 78, 024022 (2008) (13 pages).

- [210] B. Szilágyi, D. Pollney, L. Rezzolla, J. Thornburg, and J. Winicour, *An explicit harmonic code for black-hole evolution using excision*, *Class. Quantum Grav.* 24, S275-S293 (2007).
- [211] M. E. Taylor, *Partial Differential Equations I-III*, (Springer, New York, 1996).
- [212] N. W. Taylor, L. E. Kidder, and S. A. Teukolsky, *Spectral methods for the wave equation in second-order form*, *Phys. Rev. D* 82, 024037 (2010) (16 pages).
- [213] N. W. Taylor, personal communication.
- [214] W. Tichy, *Black hole evolution with the BSSN system by pseudospectral methods*, *Phys. Rev. D* 74, 084005 (2006) (10 pages).
- [215] W. Tichy, *Long term black hole evolution with the BSSN system by pseudospectral methods*, *Phys. Rev. D* 80, 104034 (2009) (10 pages).
- [216] J. Thornburg, *Adaptive Mesh Refinement for Characteristic Grids*, (2009), <http://arxiv.org/abs/0909.0036>.
- [217] J. Thornburg, *The Capra Research Program for Modelling Extreme Mass Ratio Inspirals*, (2010), <http://arxiv.org/abs/1102.2857v1>.
- [218] J. Thornburg, *Highly accurate and efficient self-force computations using time-domain methods: Error estimates, validation, and optimization*, <http://arxiv.org/abs/1006.3788>.
- [219] K. S. Thorne, *Multipole expansions of gravitational radiation*, *Rev. Mod. Phys.* 52 299-339 (1980).
- [220] K. S. Thorne, *300 Years in Gravitation*, edited by S. W. Hawking and W. Israel (Cambridge University Press, Cambridge, 1987), (pages 330-458).
- [221] S. A. Teukolsky, *Perturbations of a Rotating Black Hole. I. Fundamental Equations for Gravitational, Electromagnetic, and Neutrino-Field Perturbations*, *Astrophys. J.* 185 635-647 (1973).
- [222] K. Tomita, *Prog. Theor. Phys.* 52, 1188 (1974).

- [223] K. Tomita and N. Tajima, *Prog. Theor. Phys.* 56, 551 (1976).
- [224] S. Tu and S. Aliabadi, *A slope limiting procedure in discontinuous Galerkin finite element method for gasdynamic applications*, *Int. J. Numer. Anal. Model.* 2 163-178 (2005).
- [225] C. V. Vishveshwara, *Stability of the Schwarzschild Metric*, *Phys. Rev. D* 1, 2870-2879 (1970).
- [226] Y. Xu and C.-W. Shu, *Local discontinuous Galerkin methods for nonlinear Schrödinger equations*, *J. Comp. Phys.* 205, Issue 1, 72-97 (2005).
- [227] Y. Xu and C.-W. Shu, *Local discontinuous Galerkin methods for the Kuramoto-Sivashinsky equations and the Ito-type coupled KdV equations*, *Comp. Methods Appl. Mech. Engin.* 195, 3430-3447 (2006).
- [228] I. Vega and S. Detweiler, *Regularization of fields for self-force problems in curved spacetime: Foundations and a time-domain application*, *Phys. Rev. D* 77, 084008 (2008) (14 pages).
- [229] I. Vega, P. Diener, W. Tichy, and S. Detweiler, *Self-force with (3+1) codes: A primer for numerical relativists*, *Phys. Rev. D* 80, 084021 (2009) (22 pages).
- [230] T. C. Warburton and G. E. Karniadakis, *A Discontinuous Galerkin Method for the Viscous MHD Equations*, *J. Comp. Phys.* 152, Issue 2, 608-641 (1999).
- [231] C. M. Will, A. G. Wiseman, *Gravitational radiation from compact binary systems: gravitational waveforms and energy loss to second post-Newtonian order*, *Phys. Rev. D* 54, 4813-4848 (1996).
- [232] G. Yoneda and H. Shinkai, *Symmetric Hyperbolic System in the Ashtekar Formulation*, *Phys. Rev. Lett.* 82, 263-266 (1999).
- [233] G. Yoneda and H. Shinkai, *Constructing Hyperbolic Systems in the Ashtekar Formulation of General Relativity*, *Int. J. Mod. Phys. D* 9, 13-34 (2000).

- [234] G. Yoneda and H. Shinkai, *Hyperbolic formulations and numerical relativity: II. asymptotically constrained systems of Einstein equations*, *Class. Quantum Grav.* 18, 441-462 (2001).
- [235] J. W. York Jr., *Kinematics and Dynamics of General Relativity*, in *Sources of Gravitational Radiation*, edited by L. L. Smarr (Cambridge University Press, Cambridge, 1979).
- [236] S. Weinberg, *Gravitation and Cosmology: Principles and Applications of the General Theory of Relativity*, (John Wiley and Sons, New York, 1972).
- [237] A. Zenginoglu, *Asymptotics of black hole perturbations*, *Class. Quantum Grav.* 27 045015 (2010) (15 pages).
- [238] F. J. Zerilli, *Effective Potential for Even-Parity Regge-Wheeler Gravitational Perturbation Equations*, *Phys. Rev. Lett.*, 24 737-738 (1970).
- [239] F. J. Zerilli, *Gravitational Field of a Particle Falling in a Schwarzschild Geometry Analyzed in Tensor Harmonics*, *Phys. Rev. D* 2, 21412160 (1970).
- [240] Z. Xu, Y. Liu, and C. W. Shu, *Hierarchical reconstruction for discontinuous Galerkin methods on unstructured grids with a WENO-type linear reconstruction and partial neighboring cells*, *J. Comp. Phys.* 228, Issue 6, 2194-2212 (2009).
- [241] G. Zumbusch, *Finite Element, Discontinuous Galerkin, and Finite Difference evolution schemes in spacetime*, *Class. Quantum Grav.* 26, 175011 (2009).